A STUDY OF PRE-IGNITION AND KNOCK IN AN OPTICAL SPARK IGNITION ENGINE

Hassan Vafamehr

Department of Mechanical, Aerospace and Civil Engineering

College of Engineering, Design and Physical Sciences

Brunel University London

Dissertation submitted to the Brunel University London in accordance with the requirements of the degree of Doctor of Philosophy

May 2018

This thesis is dedicated to my parents Ali and Azimeh

And my wife Fatemeh

ABSTRACT

The currently reported work involved fundamental study of auto-ignition under unusually high knock intensities in an optical spark ignition engine. The single cylinder research engine adopted included full bore overhead optical access capable of withstanding continuous peak in-cylinder pressure and knock intensity of up to 150 bar and 60 bar respectively. Heavy knock was deliberately induced under relatively low loads (5 bar IMEP) using inlet air heating up to 66 °C and a primary reference fuel blend of reduced octane rating (75 RON). High speed chemiluminescence natural light imaging was used together with simultaneous heat release analysis to evaluate the combustion events.

The key out comes of this study could be listed as follow:

- Proof and improved understanding of multi centred auto-ignition events under high KIs
- Improved understanding of the potential pitfalls of over-fuelling for heavy knock suppression
- Optical validation of ‘natural’ oil droplet release and on-off behaviour of knocking cycles

Multiple centred auto-ignition events were regularly observed to lead in to violent knocking events, with knock intensities above 140 bar observed. The ability to directly image the events associated with such high magnitude of knock is believed to be a world first in a full bore optical engine. The multiple centred events were in good agreement with the developing detonation theory to be the key mechanism leading to

heavy knock in modern downsized SI engines. The accompanying thermodynamic analysis indicated lack of relation between knock intensity and the remaining unburned mass fraction burned at the onset of the auto-ignition. Spatial analysis of the full series of images captured demonstrated random location of the first captured auto-ignition sites during developing auto-ignition events. Under such circumstances new flame kernels formed at these sites, with initial steady growth sometimes observed to suppress the growth of the earlier spark initiated main flame front prior to violent end gas auto-ignition. It was found that pre-ignition most commonly initiated in the area surrounding the exhaust valve head and resulted in a deflagration that caused the overall combustion phasing to be over advanced. In the cycles after heavy knock, droplets of what appeared to be lubricant were sometimes observed moving within the main charge and causing pre-ignition. These released lubricant droplets were found to survive within the combustion chamber for multiple cycles and were associated with a corresponding "on-off" knocking combustion pattern that has been so widely associated with super-knock in real downsized spark ignition engines.

This research also concerned with improving understanding of the competing effects of latent heat of vaporization and auto-ignition delay times of different ethanol blended fuels during heaving knocking combustion. Under normal operation the engine was operated under port fuel injection with a stoichiometric air-fuel mixture. Additional excess fuel of varied blend was then introduced directly into the end-gas in short transient bursts. As the mass of excess fuel was progressively increased a trade-off was apparent, with knock intensity first increasing by up to 60% before lower unburned gas temperatures suppressed knock under extremely rich conditions (γ=0.66). This trade-off is not usually observed during conventional low intensity knock suppression via over-

fuelling and has been associated with the reducing auto-ignition delay times outweighing the influence of charge cooling and ratio of specific heats. Ethanol had the highest latent heat of vaporization amongst the other fuels directly injected and was more effective to reduce knock intensity albeit still aggravating knock under slightly rich conditions. Overall, the results demonstrate the risks in employing excess fuel to suppress knock deep within a heavy knocking combustion regime (potentially including a Super-Knock regime).

ACKNOWLEDGEMENTS

First and foremost I would like to thank God for giving me the opportunity and the talents to complete this thesis.

This has been a long journey and many people supported me to achieve this goal.

I wish to sincerely thank my supervisor, Professor Alasdair Cairns, for his invaluable guidance and help during this work. He was the only reason I moved from Birmingham to Brunel for my studies. He was not only a boss, but also a leader and a role model for me. He always concerns about his students and treats them like a family member.

Prof. Cairns, thank you so much for all the support that you have given me during the project, wise guidance, prompt communications either via numerous email exchange, phone calls or meetings. Your reassurance when the going got tough will forever be in my mind. I learned a lot from you. I couldn't have asked for better supervisor.

I would also like to thanks my second supervisor, Professor Hua Zhao for his support.

Also I hereby convey my appreciation to Dr. Apostolos Pesiridis for his advice and supports during my studies.

Special thanks to Dr. Simon Dingle who helped me a lot at the beginning of my PhD.

I am also eternally grateful of my colleagues, Dr. Apostolos Karvountzis, Dr. Thompson Lanzanova, Dr. Jack Justus and Sheykh Khalifa. Huge thanks to the brilliant technicians Chris Allan, Willian, Eamon and Andy Selway.

Many thanks to my friends Dr. Mohsen Alamuti, Mohsen Moslemin, Dr. Shahrazad, Dr. Khodapanah, Dr. Salman Rouhani, Dr. Omid Dustdar and Ms. Sameaha Parker.

A special thanks to my parents and my family. Words cannot describe how grateful I am to my parents for their unwavering and unconditional love and support throughout my entire life. My thanks and gratitude to other members of my family, brothers, my parents in law, Captain Aghdaie, Mrs. Ayani, Capitan Mohammad Aghdaie and Ali for their continued love and support.

Finally, thanks to my wonderful wife, Fatemeh, who has supported me and put up with long distance and stressed days while I've written this work.

LIST OF PUBLICATIONS

[1] H. Vafamehr, A. Cairns, O. Sampson, and M. M. Koupaie, “The competing chemical and physical effects of transient fuel enrichment on heavy knock in an optical spark ignition engine,” Appl. Energy, vol. 179, pp. 687–697, 2016.

[2] H. Vafamehr and A. Cairns, “The Effects of Transient Over-Fuelling on Heavy Knock in an Optical Spark Ignition (SI) Engine,” in 3rd Biennial International Conference on Powertrain Modelling and Control, 2016.

[3] H. Vafamehr and A. Cairns, and Moslemin Koupaie, M., "The Competing Chemical and Physical Effects of Transient Fuel Enrichment During Heavy Knock in an Optical SI Engine Using Ethanol Blends," SAE Technical Paper 2017-01-0665, 2017, doi:10.4271/2017-01-0665

[4] H. Vafamehr, A. Cairns, and H. Ebne-Abbasi, “A study of transient over-fuelling during heavy knock in an optical spark ignition engine,” Int. J. Powertrains, vol. 7, no. 1–3, 2018.

[5] M. Moslemin Koupaie, A. Cairns, H. Vafamehr, and T. Lanzanova, “Cyclically Resolved Flame and Flow Imaging in an SI Engine Operating with Future Ethanol Fuels,” SAE Tech. Pap., vol. 2017–March, no. March, 2017.

[6] K.I. Bureshaid, Feng, D., Vafamehr, H., and Zhao, H., “In-Cylinder Study of Combustion and Knocking Tendency of Gasoline, Anhydrous Ethanol and Wet Ethanol in an Optical Engine,” SAE Technical Paper 2017-01-0665, 2017, doi:10.4271/2017-01-0665

[7] O. Sampson, H. Vafamehr, and A. Cairns, “Effects of direct injection (DI) on knocking combustion in spark ignition (SI) engine operated on 75-RON and Ethanol Fuels,” Soc. Pet. Eng., 2018.

CONTENTS

LIST OF TABLES

LIST OF FIGURES

LIST OF ABBREVIATIONS AND SYMBOLS

AFR	air-fuel ratio
aTDC	after top dead centre
API	American Petroleum Institute
BDC	bottom dead centre
BLD	borderline detonation
BMEP	brake mean effective pressure
BSFC	brake specific fuel consumption
aTDCnf	after top dead centre, non-fired
bTDC	before top dead centre
C_2	carbon-carbon
CA_dP/dCA_max	location of the maximum average in-cylinder pressure gradient with respect to crank angle
CA0	crank angle at the start of combustion
CA2	crank angle at 2% mass fraction burned
CA10	crank angle at 10% mass fraction burned
CA50	crank angle at 50% mass fraction burned

CA90	crank angle at 90% mass fraction burned
CAD	computer aided design
CA Pmax	crank angle location of maximum in-cylinder pressure
CCV	cycle-by-cycle variations
CFD	computational fluid dynamics
CII	calculated ignition index
CO_2	carbon dioxide
COV	coefficient of variation
DAQ	data acquisition
DI	direct injection / direct injector
ECU	engine control unit
EGR	exhaust gas recirculation
EGT	exhaust gas temperature
EMOP	exhaust valve maximum open position
EU	European Union
EVC	exhaust valve close
EVO	exhaust valve open

fps	frame per second
GDI	gasoline direct injection
HC	hydro-carbon
IMEP	indicated mean effective pressure
IMEPnet	net indicated mean effective pressure
IMOP	inlet valve maximum open position
IQT	ignition quality test
IVC	inlet valve close
IVO	inlet valve open
KI	knock intensity
LSPI	low-speed pre-ignition
MBT	maximum brake torque
MEP	mean effective pressure
MFB	mass fraction burned
MON	motored octane number
NEDC	new European drive cycle
PC	personal computer

PFI	port fuel injection
Pmax	maximum in-cylinder pressure
PRF75	primary reference fuel with research octane number of 75
ROHR	rate of heat release
RON	research octane number
rpm	revolutions per minute
SI	spark ignition
SOI	start of injection
TDC	top dead centre
TDCnf	non-fired top dead centre
UEGO	universal exhaust gas oxygen (sensor)
UHC	unburned hydrocarbons
ULG	Unleaded Gasoline
USB	universal serial bus
ZnDTP	zinc dialkyldithiophosphates
AFR	air-fuel ratio

1 INTRODUCTION

1.1 Aims and Objectives

The main aims and objectives of this study could be listed as follow:

- Imaging and analysis of auto-ignition and heavy knock
- Understanding of the chemical and physical trade-offs when employing transient over-fuelling to control auto-ignition
    - Faster Chemistry (auto-ignition delay) Versus Charge Cooling
- Improving understanding fuel stratification under heavy knocking combustion using both DI and PFI

1.2 General Background

The global rise in oil prices and increasing concerns about the environmental effects of rising carbon dioxide (CO2) emissions are enforcing governments and automotive manufacturers to minimise tailpipe CO2 emissions and other pollutant emissions. The CO2 emissions from passenger cars are currently limited to 130gCO2/km for 80% of new vehicle registrations in the European Union (EU) and will decrease to 95gCO2/km by 2020 [1]. Overall, diesel engines have lower CO2 emission levels and over the last decade or so most European countries decreased fuel tax to encourage the growth of the diesel market share [2]. However, in the last few years the diesel engine has fallen from favour due to concerns over real world pollutant emissions, particularly with respect to

NOx [3]. In addition, several European governments including the UK [4] have proposed to ban the sale of 'conventional' ICE vehicles, meaning all vehicles without some form of hybridisation. The electrification of passenger cars is undoubtedly one viable method of reducing CO2 and pollutant emissions but only if remaining grand challenges concerning green electricity production and energy storage, battery manufacture and recycling and charging infrastructure can be suitably addressed. Due to such remaining issues, over the next few decades the IC engine will remain the key source of road car propulsion as recently acknowledged by the UK Automotive Council[5].

As a result of the 'demonization' of the diesel, the gasoline engine is more likely to be a main source of automotive propulsion for next decades, with more technologically advanced forms of evolved fuels, combustion strategies and supplementary hybrid technology.

Over the last decade, engine downsizing technique was the point of interest for most automotive OEMs. The main advantage of this technique is to reduce CO2 emissions while maintaining or increasing the full-load engine performance. By employing this technique, fuel consumption is reduced under lower loads as the engine displacement is reduced. Maximum engine and in-vehicle performance is maintained through boosting the intake pressure. Less engine displacement has some impacts on increasing the specific engine load for a fixed power output, notably lower levels of pumping losses under part load cruising. Additionally, overall frictional losses may be decreased by a reduction in the number of cylinders and by down-speeding (albeit cylinder specific

friction may increase due to higher in-cylinder pressures). The technique is now a widely established method for reducing CO2 emissions from gasoline passenger vehicles.

While part-load efficiency is significantly increased, high in-cylinder pressures and temperatures ultimately result in the need for the combustion phasing to be highly retarded at low engine speed in order to prevent auto-ignition and knock. As the degree of downsizing has been developed a new auto-ignition regime has been defined [6] often referred to as Low Speed Pre-ignition (LSPI) and super-knock [7]. The auto-ignition regime is typically characterised by multiple uncontrollable pre-ignition sites followed by high-intensity knocking combustion. Following pre-ignition, knocking intensities exceeding 100bar with peak in-cylinder pressures in excess of 200 bar have been noted [8] . In order to reduce or mitigate the damage caused by such high-intensity knocking events, some automotive manufacturers have proposed increasing the fuelling in regions of the speed-load map where LSPI most likely occurs. This has the effect of reducing the air-fuel mixture temperature and has been reported to greatly reduce the frequency of such occurrences [9], [10]. However, this method increases fuel consumption and CO2 emissions, and is not favourable to the main goal of engine downsizing. Therefore, it is of great benefit to the automotive industry to have a better understanding of the super-knock phenomena, its causes and the solution to knock mitigation.

1.3 Thesis Outline

The currently reported research is concerned with improving fundamental understanding of auto-ignition and heavy knock in an optical spark ignition engine. In

Chapter 2, a literature review is presented. This includes an overview of the common efficiency losses in gasoline spark ignition engines, engine downsizing as a technique for improving efficiency over the drive cycles and the super-knock phenomena. Within this chapter a review of the current and future trend for vehicle electrification presented. Chapter 3 provided the details of the equipment used in this study, including the design details of a cylinder head, the fuel delivery system and combustion imaging instrumentation. Chapter 4 delivers details of the thermodynamic data collection techniques used within this study. Also this chapter covers the data analysis techniques. Flame imaging technics and analysis covered in chapter 5. The difficulties and problems occurred during flame imaging is also included in this chapter. In Chapter 6, the results of the pre-ignition and heavy-knock study are presented and discussed. In Chapter 7 and analysis of the competing chemical and physical effects of transient fuel enrichment during heavy knock is presented. Finally the conclusions of the presented work and recommendations for further work are reported in Chapter 8.

2 LITERATURE REVIEW

2.1 Chapter Outline

The main aim of this chapter is to underpin current understanding of the fundamentals and limitations of auto-ignition and knock in modern IC engines. Firstly, a concise history of the internal combustion engine (ICE) is provided, followed by discussion on 'normal' operation of spark-ignition engines, the major causes of efficiency losses and the primary ways in which automotive manufacturers try to reduce the impact of these losses. The established theories of auto-ignition and knock are then reviewed, before moving on to an overview of recently published observations of the 'super-knock' phenomena in modern automotive SI engines. Finally, some discussion is provided on the future of the automotive internal combustion engine in the backdrop of recent intensifying focus upon electrification.

2.2 Definition of Auto-ignition Versus Knock

A large portion of this thesis deals with the concept of abnormal combustion. There are different terms used in the literature to define the concept of such abnormal combustion. However, there is often no alignment in the definitions within different literature sources. Some key fundamental terms will be used throughout this thesis as follows:

Auto-ignition: is defined here as combustion that is initiated by means other than the electrical discharge from the spark plug or by entrainment of unburned charge in to the propagating flame. It often results in knock, but not necessarily.

Pre-Ignition: is defined here as any auto-ignition that occurs prior to the intended spark-timing. It can lead to further auto-ignition events and can lead to knock, but not necessarily.

Knock: is defined here as high-frequency pressure oscillations within the combustion chamber that arise as a result of auto-ignition (whether it be auto-ignition before the spark or afterwards in the end-gas).

Heavy Knock: is defined here as knocking cycles with knock intensity approximately over 7 bar.

2.3 Introduction

Climate change has become a serious issue and an unavoidable reality of recent human evolution. Although this is a cyclic natural phenomenon [1], recent climate change cannot be explained by historical data alone and there is now clear evidence that these changes are driven by human generated greenhouse gas (GHG) emissions such as carbon dioxide, methane and nitrous oxide [2]. A huge share of these emissions results from fossil fuel exploration and burn to meet the energy demand and economic growth. For these reasons, governments have agreed to reduce global greenhouse gases emissions in order to hold the global average temperature through adoption of the Paris Protocol agreement, for example [3]. According to NASA, in 2016 the Earth's average temperature crushed the previous record for hottest year by 0.12°C. That record was set in 2015, which broke the previous record by 0.13°C. That record had been set in 2014, beating out 2010, which in turn had broken the previous record set in 2005 [4].

In recent years, European CO2 emission targets have been met through a high proportion of diesel sales, rising above 50% in some states. However, the distillation of crude oil results in high proportions of both gasoline and diesel fuel, which results in Europe becoming “diesel lean” at times. The need to achieve the future global emissions goals requires adequate plans from the energy researchers and policy makers. Moxey and Cairns [5] suggested that in the short-to-medium term it will be necessary to improve the fuel consumption of the gasoline engine and in the longer term, source sustainable alternatives to crude oil. Substitutes such as electric and hydrogen fuel cell vehicles, hybrid vehicles, and biofuels (e.g., bioethanol and biodiesel) are among the alternatives being investigated. However, considerable hurdles remain regarding the sustainability of these alternatives to meet the global demand of the automotive sector. In electric vehicles the relative high cost and weight of the batteries has proven to be a key barrier in mass adoption, although incremental improvements in energy density and cost continue in Lithium-ion and Lithium-Polymer battery technology [6]. Local government policy must also be taken in to account, where electrification has recently been reported as a widespread solution albeit highly dependent on substantial improvements to electricity production, storage and infrastructure.

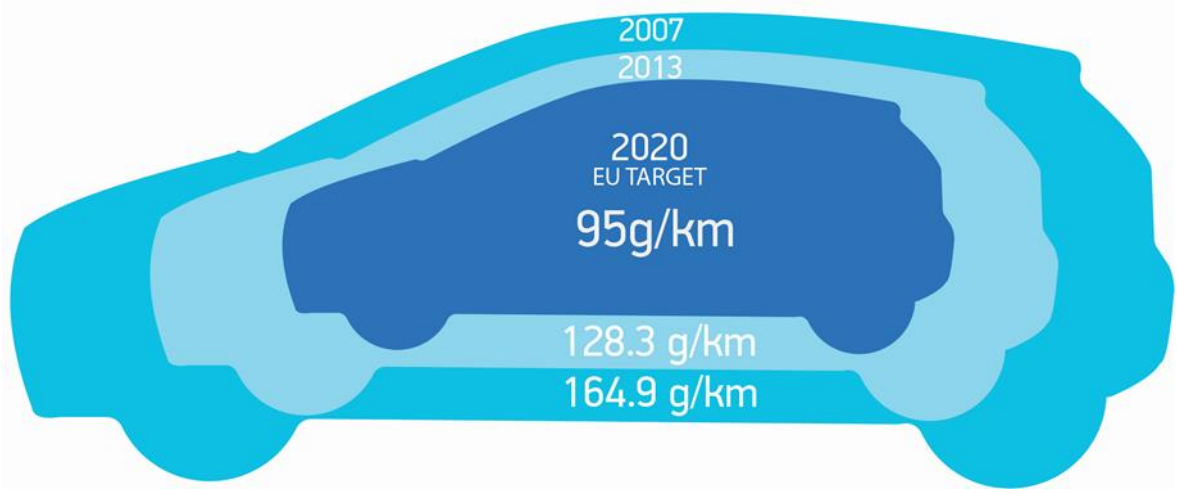

Figure 2-1: EU new car CO2 emissions Landmark [7].

By 2020 the limitation of carbon emissions from passenger cars is planned to reduce to 95 gCO2/km [8] as shown in Figure 2-1. The world's greenhouse gas emissions records of 2004 revealed that transport alone made up approximately 23% of all emissionsas shown in Figure 2-2. The wide adoption of turbo-diesel engines in the EU in the past few years has served as a favourable solution. However, biomass if attained, alcohol fuels can offer a very significant alternative solution. The use of alcohol fuels in internal combustion engines started since the onset of mechanically driven automotive transportation [5]. Most of the alcohols available for current SI engines are gasoline-ethanol blends, with 5-10% volume allowed in current European legislation [9].

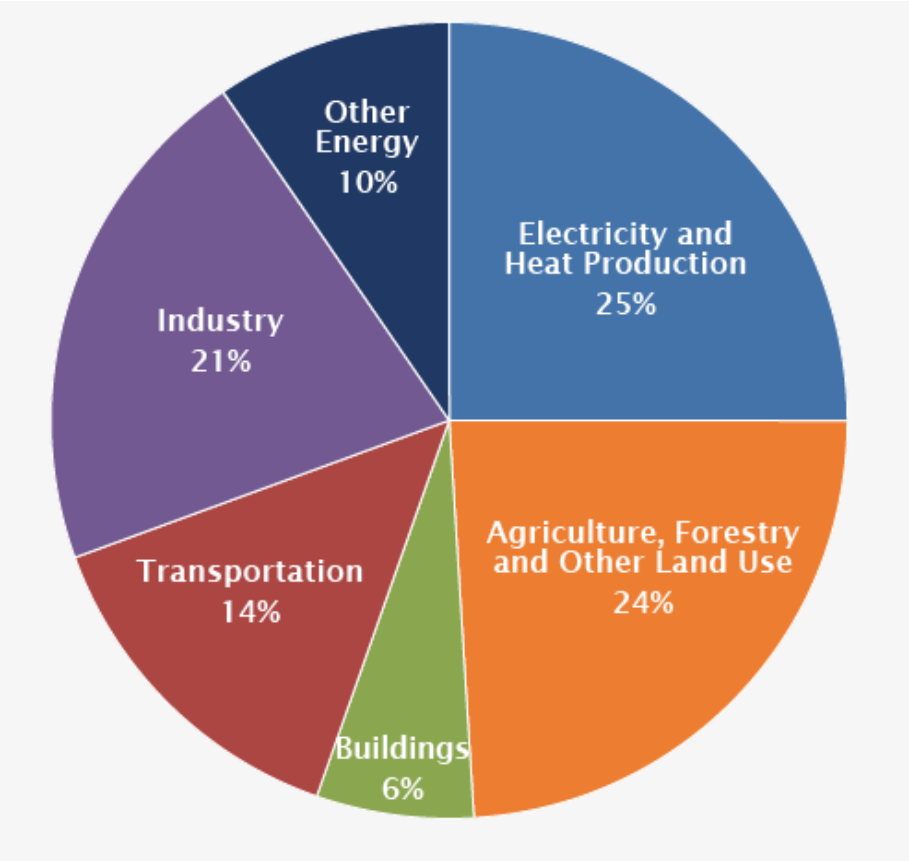

Figure 2-2: Global greenhouse gas emissions by economic sector [6]

In improving SI engine fuel consumption, engine "downsizing" has become widely considered as one of the positive steps taken by automotive manufacturers. The basic principle is to reduce the capacity of the engine. This enforces a large proportion of engine operation to higher loads, where the pumping losses are reduced for a given road load requirement under the wider open throttle (WOT) conditions. In order to maintain vehicle performance and top speed the engine must be fitted with some form of intake air pressure charging, usually combined with direct fuel injection (DI) and variable valve timing to help maximise volumetric efficiency [10]. The DI helps in cooling the charge and optimisation the combustion chamber scavenging process. As demonstrated by Amann and Dingle [11,12], the majority of downsized engines are associated with

some limitations in breathing, combustion and/or performance. These limitations include (but are not limited to) boosting system parasitic losses, unacceptable transient response (‘turbo lag’), unacceptable on-cost (e.g. compound boosting systems) or violent combustion events associated with low speed pre-ignition (LSPI) and heavy knocking/super-knock.

In current SI engines, knocking combustion usually arises due to excessive energy release rate via exothermic centres (or so-called hot spots) in the end gas beyond the entraining edge of the flame. The sporadic release of the chemical energy in the local end gas causes very high local temperature gradients which in turn may result in pressure waves of considerable amplitude resonating across the combustion chamber at the local speed of sound [13]. Increased engine loads under this high temperature and pressure conditions may lead to increased frequency of the unwanted occurrence of auto-ignition of the unburned gas. At low speeds and the highest loads this auto-ignition comes as irregular and uncontrollable pre-ignition with high-intensity knocking combustion [14]. The recent adoption of ethanol blends is widely acknowledged to be beneficial to knock reduction provided the inherent anti-knock benefit is not traded off with the traditional additives [15]. However, the relative effects during LSPI and super-knock remain poorly understood. In both the EU and US, flex-fuel operation via ethanol has gained significant attention in recent years [16]. Moreover, Brazil (with no oil reserves but plentiful sources of vegetation) is already operating an alcohol-fuel policy, where pump grades usually contain substantial amounts of ethanol. Conversely, the effect of the low volumetric energy content of the alcohol must not be neglected while using it as a blend.

2.4 Spark ignition engine operation fundamentals

The theoretical principle behind the operation of the four-stroke engine can be defined through four phases: induction, compression, expansion, and exhaust. These phases happen in 180 crank angle degrees (CAD). With regards to instantaneous valve events, the intake valve opens (IVO) in the top dead centre (TDC) and charge mixture is induced into the cylinder as the piston moves downwards. The intake valve closes (IVC) in the bottom dead centre (BDC) with the charge being delivered to a near isentropic compression while the piston travels upward. At the top dead centre, combustion takes place immediately and adiabatically. The increase in pressure happens due to the exothermic chemical reactions, which result in increased mixture temperature and new molecules or combustion products. The burned gases are isentropically expanded during the expansion stroke while the piston travels downward from TDC to BDC. The exhaust valve opens around BDC and the burned gases are ejected perfectly from the cylinder while the piston moves upward. At TDC the exhaust valves close and intake valves open, starting a new cycle. The theoretical efficiency of the cycle is given by:

$$\eta_{Otto} = 1 - \frac{1}{CR^{\gamma-1}}$$

Equation 1-1

In the above equation, CR represents the compression ratio which is given by the link between in-cylinder volume at BDC and TDC while γ represents the ratio of specific heats. Therefore, higher efficiency could achieve by a higher compression ratio with the highest possible ratio of specific heats.

In a real engine, the combustion process occurs during a finite period, starting some degrees before TDC, and ending well after TDC, with combustion duration and phasing directly influencing the engine output. Various fuels provide different energy by promoting different levels of enthalpy due to high temperature. Particularly during combustion and expansion, due to the wall heat transfer, the available energy to be converted into work is lower.

According to [17], the combustion process within the spark engine happens in four phases as detailed below.

- Stage 1: Spark and flame initiation

At this stage, the rise in the voltage between the spark plug electrodes results in an electrical breakdown, which in turn leads to an electrical arc. The arising ionisation in turn leads to reactive species and the formation of an initial flame kernel between the electrodes

- Stage 2: Initial flame development

This stage accounts for around 30 percent of the aggregate duration of the combustion [18]. The flame kernel between the electrodes is almost immediately influenced by the surrounding in-cylinder flow, both in terms of convection and progressively increased wrinkling of the flame front as the scales of turbulence are encroached [19]. Typically, due to cycle to cycle variations, the FDA (flame development angle) may be defined to occur from the timing of the spark to approximately 5% MFB or 10% MFB [20] .

- Stage 3: Turbulent Flame Propagation

This stage corresponds to the period between 10% and 90% of mass fraction burned. The rate of entrainment of the unburned mass is predominately governed by the turbulence intensity and distribution, local charge mixture composition. in-cylinder geometry The size of the flame front increases from the initial kernel while sustaining its shape until it is quenched close to the wall [20].

- Stage 4: Flame Termination

This is the phase where the flame front touches the cylinder wall and the flame is quenched. Typically there is significant mass entrained but still burning behind the front which continues to burn during the power stroke.

Based on observations by several authors [20], [22], between the four primary combustion phases, the phases linked to the initiation of the flame and development of the kernel are generally important with regards to the cyclic variability of the engine performance. For this reason, the speeding up of the early flame kernel development is inclined to bring down cyclic variability while increasing the maximum charge dilution limit. Furthermore, owing to the fact that the cycle-by-cycle air variability of the intake process changes the local and bulk composition or the in-cylinder charge and flow structures, it has a direct effect on the first stages of combustion and in consequence the IMEP variability.

Bearing in mind the two large in-cylinder flow arrangements swirl and tumble (rotary motion of air about the axis of cylinder in the combustion chamber), studies have concluded that these large bulk fluid motions dismantle into small scales during the compression stage, which results in increased small scale turbulence during combustion

[21]. The tumble movement represents the large-scale fluid movement produced during the intake stoke around an axis at right angles to the centre line of the cylinder. During the time when the cylinder is moving in the direction of TDC, in the process of compression, the tumble initially upsurges as a result of the angular momentum conservation. Later on, during the compression stroke, there is a distortion of the large flow structure as a result of sheer stresses. It then decays into smaller turbulence structures [22,23].

The swirl concept represents the motion of the fluid within the cylinder axis in a rotational manner. Unlike tumble, the motion of the piston has a lesser effect on the bulk flow mean velocity [24]. Hence, it is expected that when the tumble in-cylinder motion increases, higher levels of turbulence will be generated ahead of combustion than the axial swirl case [25,26]. Nevertheless, swirl motion can increase flame growth and convict initial flame growth from the spark electrodes. This could lead to increased growth of the flame kernel as a result lower heat transfer [27].

Tumble has mostly been preferred in four valve engines because of the head symmetry in the valve cylinder while swirl has been employed in two valve diesel and SI engines. Using this type of in-cylinder flow motion is important for lean burn engines but must be carefully balanced, where the benefits of additional flame wrinkling can be outweighed by excessive flame stretch under too high a turbulent flow field. While swirl is maintained during combustion, extreme movement of the fluid could result in the decreased overall performance of the engine because of increased heat losses [21,28].

2.5 Optimum Spark-Ignition Engine Operation

The "island" of minimum Brake Specific Fuel Consumption (BSFC) of a naturally-aspirated spark-ignition engine is typically located somewhere around mid-speed and load. Generally, there are five key mechanisms for increased BSFC (reduced efficiency) as an SI engine's operating conditions are moved away from the region of optimum operation. These are graphically represented in Figure 2-5 and further expanded upon within this section.

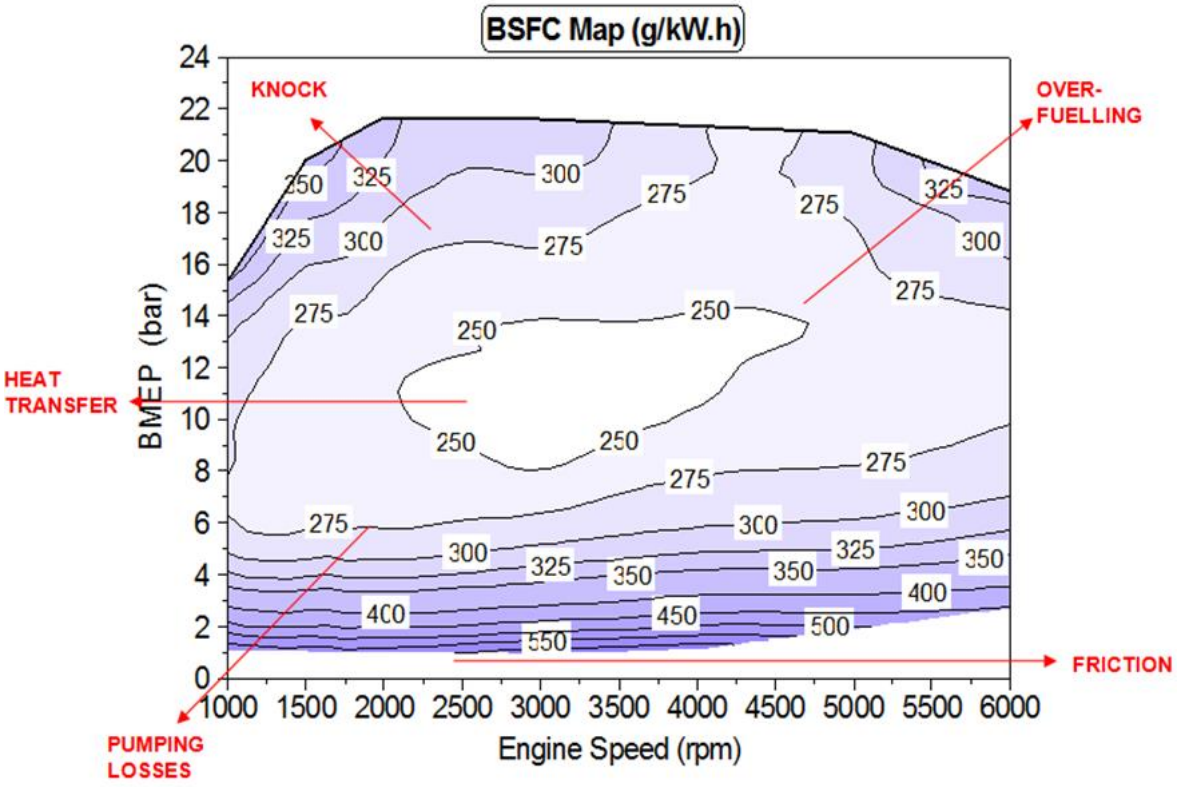

Figure 2-3: Brake Specific Fuel Consumption map (BSFC) for a typical turbocharged gasoline direct fuel injection engine (courtesy of MAHLE Powertrain)

2.5.1 Spark Retard due to Knock Limited Operation

In order to increase thermal efficiency across the speed-load map, the compression ratio is normally increased until the end-gas knock region is incurred at low speeds and high loads. In this condition combustion timing is limited by knock and must be moved away from the Maximum Brake Torque (MBT) phasing by retarding the spark timing [6,13]. The degree of spark retard tolerated at the highest loads is a trade-off between low and high load thermal efficiency and must usually be assessed over a drive cycle.

2.5.2 Fuel Enrichment due to Temperature Limited Operation

In conditions where the loads and speeds are high less time exists for heat rejection to the combustion chamber walls although the aggregate heat rejection to the cylinder is at its peak. Under such conditions, the temperatures of components can go above their safe maximum operating temperature. This could result in failure or lead the component to a state where its temperature could ignite the fuel/air charge to pre-ignition. Parts that are usually susceptible to overheating include spark plugs, turbochargers, sharp combustion chamber edges, pistons, exhaust valves and emissions after-treatment systems. The results of overheated systems within the combustion chamber usually become common locations for surface pre-ignition [13]. On the other hand, the overheating of the turbocharger and exhaust valves leads to failure of these components. Over-fuelling is a common method used to mitigate the risk of high component temperature [29,30]. When fuelling is increased, the gamma value of the charge is reduced, therefore the gas temperature within the cylinder before combustion is lower. This also results in the reduction of the combustion temperature and subsequently the temperature of the exhaust gas. This has the undesirable effect of reducing the efficiency of the engine as is

shown in Figure 2-6. In addition the three-way catalytic converter becomes ineffective leading to vast increase in tailpipe pollutant emissions. The recently introduced RDE assessments are partly aimed at addressing such inefficient and polluting operation.

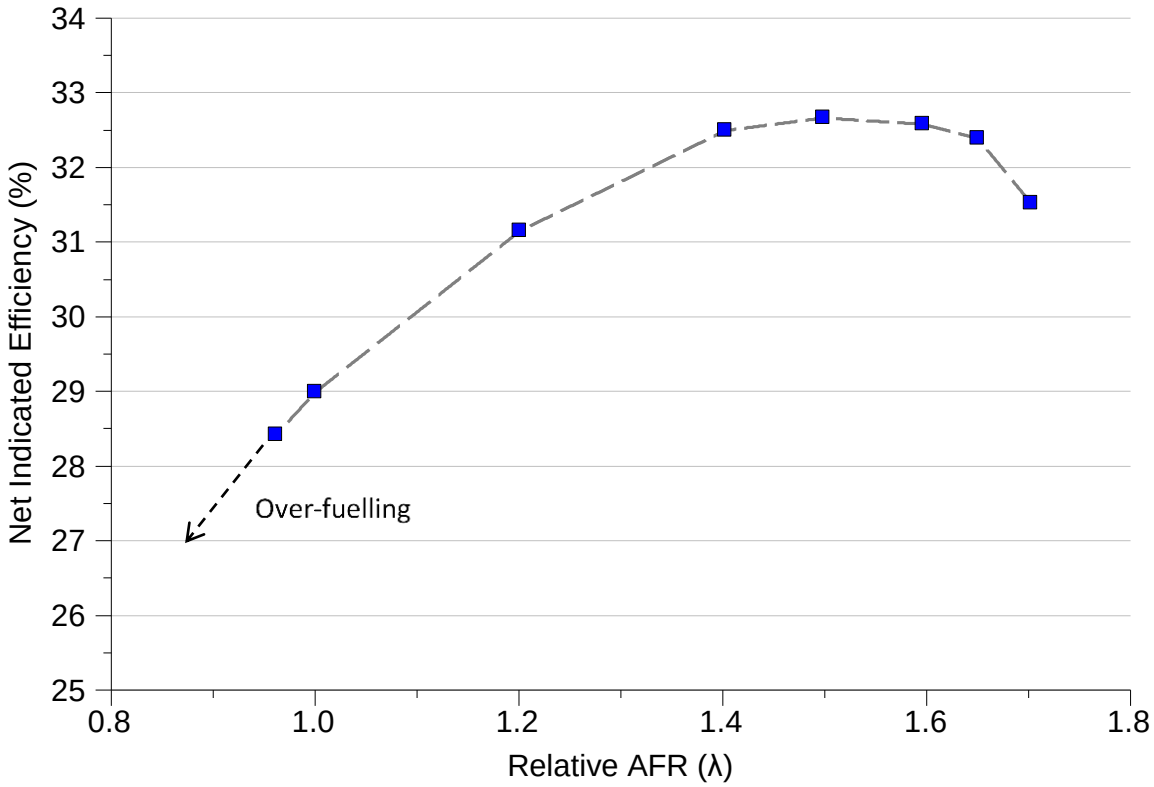

Figure 2-4: Graph showing the effect of relative air-fuel ratio on engine efficiency. Adapted from data published by Ayala et al. [31]

2.5.3 Increased Engine Friction

The consequence of increased engine speed is increased engine frictional losses as a function of the engine speed squared [13]. The outcome of this is a relative increase in the energy needed to overcome the frictional resistance; leading to lowered engine efficiency. This effect is increased also at higher engine loads owing to the increased

combustion pressures leading to an increase in the rubbing function between the inner part of the cylinder and the piston rings. Nevertheless, this is a small effect when compared to engine speed.

2.5.4 Pumping Losses

Normally, in order to maintain acceptable flammability and acceptable catalytic conversion most spark ignition engines operate under stoichiometric and homogenous fuelling conditions. Hence there is a need to proportionally reduce the air mass flow rate with that of the fuel as the demanded load is reduced. The reduction of the mass flow rate is achieved through throttling the engine intake upstream of the intake valve so as to bring down pressure levels within the intake air, falling well below atmospheric at the lowest load. The inhalation of fresh charge under a vacuum and exhalation to atmospheric pressure (or above) leads to inherent ‘pumping losses, as shown graphically below in Figure 2-7.

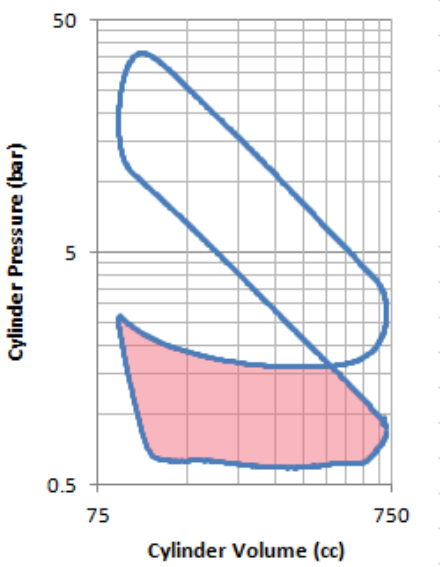

Figure 2-5: diagram of part load engine operation with the pumping loop highlighted [32].

2.5.5 Increased Heat Transfer

If the speed of the engine is reduced below the region of minimum BSFC, the efficiency of the engine is dominated by increase in heat transfer from the working fluid to the in-cylinder walls (cylinder head, liner, piston crown and valves). The increase in heat transfer is the result of more time being available during the cycle at lower speeds as illustrated in Figure 2-8.

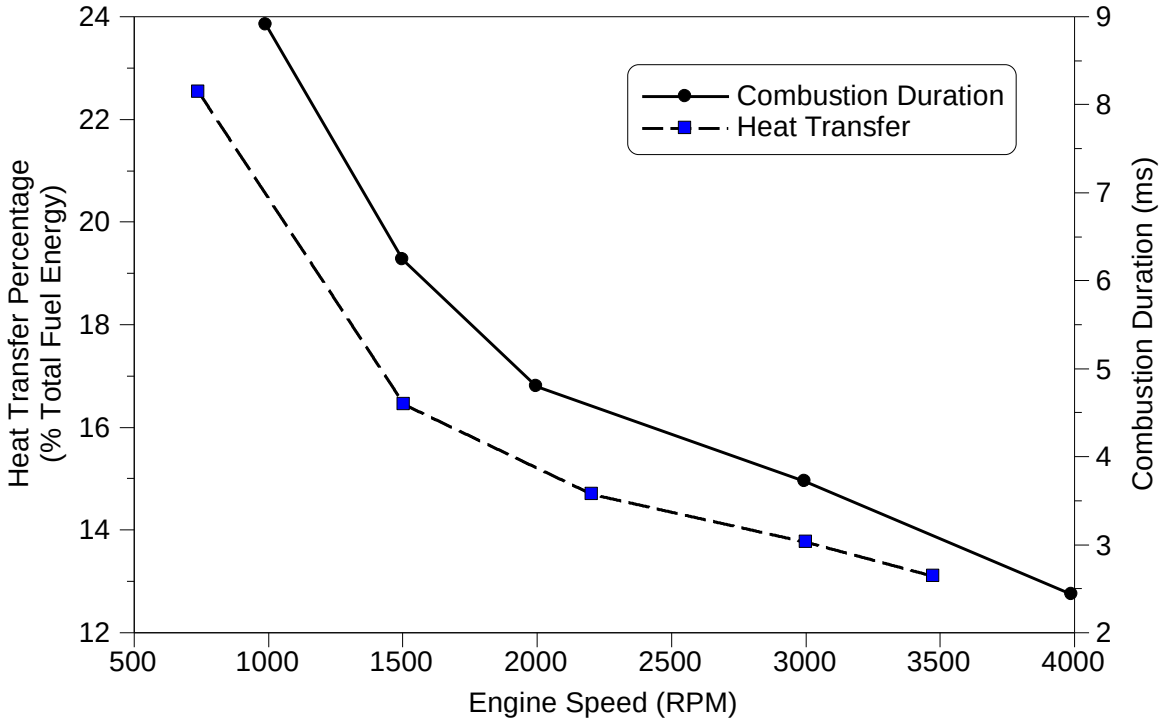

Figure 2-6: Combustion duration and heat transfer against engine speed. Figure created from data published by Hires et al. [33]

2.5.6 Other Losses

Apart from the specific loses outlined above some of the energy in the fuel is lost from the engine to the ambient surroundings, with additional losses incurred through the transmission and vehicle road load.; there are a number of other corridors within the

whole speed-load map where losses can happen. Figure 2-9 is a ‘split of losses’ analysis which indicates these typical inefficiencies. The heat lost to the exhaust typically accounts for 20-30% of the available fuel energy. Additional heat loss to the coolant and oil typically accounts for between 25 and 33%, air drag 5%, mechanical inefficiency 33 to 40%, brakes 5% and rolling friction between 12 and 45%. What this means is that only around 20% of the energy stored in the fuel is ultimately available to propel the car.

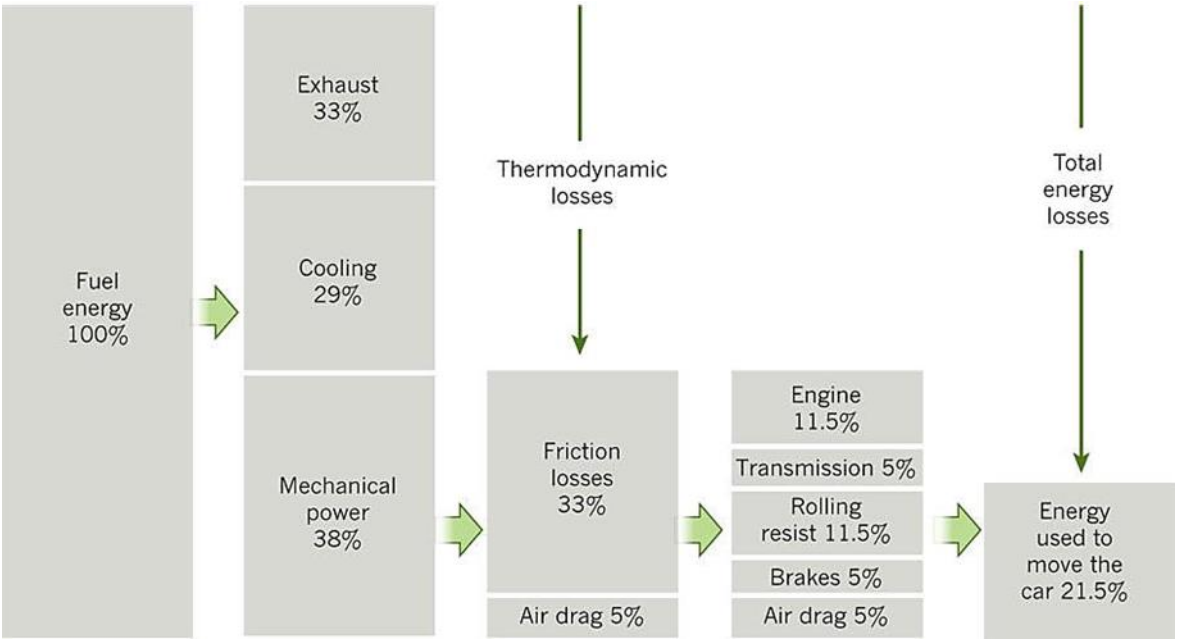

Figure 2-7: A breakdown of the average losses of internal-combustion-engine cars [34].

2.6 Reducing Losses in SI Engines

2.6.1 Pumping Loss Reduction Technologies

2.6.1.1 Variable valve actuation (VVA) mechanisms

The standard throttled load control technique employed in four-stroke gasoline engines that have standard fixed camshafts leads to heightened pumping losses at part load

operation. There is also a significant loss of efficiency compromise to placate effective combustion stability at a broad range of loads and speeds without having to compromise power at wide open throttle (WOT). Hence, the automotive industry has embraced variable valve actuation (VVA) with the aim of increasing not just part load engine efficiency but also engine performance at full load.

Within the past ten years, a number of VVA mechanisms were developed to allow for various levels of valve activation freedom. Even though fully variable valve actuation (FVVA) mechanisms are now accessible for production engines, these systems are still relatively more expensive when compared to simpler ones. This is the reason why the techniques have only been adopted by some pockets of the market. Generally, the level of valve actuation freedom required to assist in meeting legislation regulating CO_2 emissions depends on the size of the vehicle. Hence, mechanisms linked to valve actuation can be grouped into two basic classes: with a camshaft and without a camshaft.

The cam profile switch (CPS) originally suggested by Honda with its VTEC system, is one of the most basic variable valve actuation systems. It contains two separate intake cams with different profiles made to cater for low speed/load (shorter duration accompanied by small lift) and high speed/load (longer duration and high lift) [35]. These systems are able to deliver low load with higher efficiency through partial de-throttling which results in the reduction of pumping work. Here the term de-throttling will represent wider throttle opening. On the other hand the term unthrottled will represent WOT condition where the load control is achieved through other means. Cam phasing is another basic mechanism. This method can increase or decrease valve

overlap through phasing to help control residual content [36–38]. To gain more benefits, some manufacturers have used both systems at the same time [39–41].

Continuously variable valve lift (CVVL) is another system, based on the camshaft, which delivers a greater degree of freedom. These systems can provide freedom between the valve lift freedom and cam phase. A number of other systems have been proposed such as BMW Valvetronic [42,43], Nissan Variable Valve Event and Lift (VVEL) [44–46] and Chrysler's Schaeffler UniAir [47,48]. Other manufacturers including Alfa Romeo and Ferrari [49] have embraced three dimensional cam lobes. Some of the valve strategies made possible by CVVL systems are illustrated in Figure 2-10.

Finally, systems not based on camshafts such as the fully flexible variable actuation (FVVA) have also been suggested. Such systems can be electro-pneumatic [50–56], electro-hydraulic [52–54] or electromagnetic [55] based. They ensure fully independent actuation with reduced throttling at the valve itself by eliminating the traditional valve ramp events, with the option of two and four stroke operation within the same engine [57]. Even though this technology has shown great promise with regards to light duty cars, the only system that has been deployed in high-end production engines is the Freevalve's electro-pneumatic based system [56]. The leading advantages of these systems are the option of any valve strategy actuation, which could consequently improve the efficiency of the engine through its ability to reduce the pumping losses (unthrottled operation) and enhancing combustion.

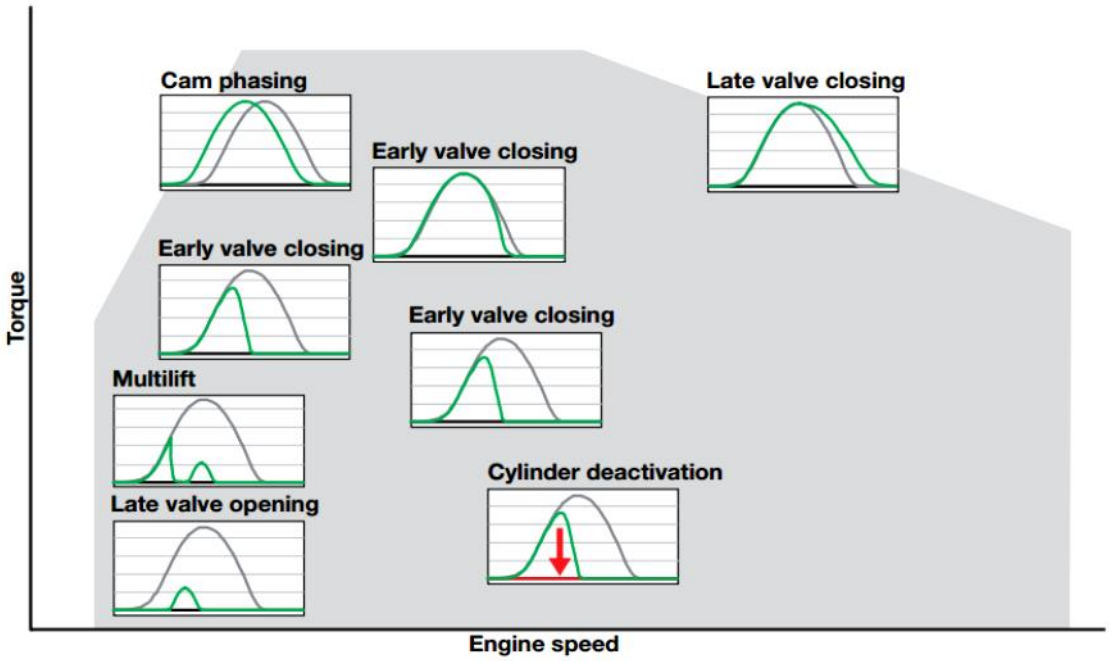

Figure 2-8: Valve strategies according to engine load and speed [58]

2.6.1.2 Lean Burn Combustion

The concept of lean burn represents the burning of fuel that has an excess of air in the internal combustion engine. The air/fuel ratio, in lean burn engines, could be as lean as 65:1 (by mass) while the air/fuel ratio required to combust gasoline stoichiometrically is 14.64:1. The oversupply of air allows for higher ratio of specific heats and high combustion efficiency provided the flammability limits are not exceeded [59]. The challenge is often attaining sufficient speed-load range, with low temperatures inhibiting very low loads and lack of boost limiting higher loads.

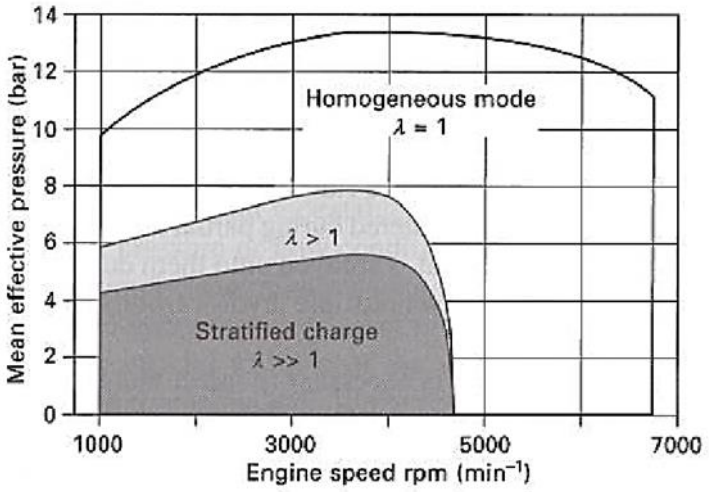

Figure 2-9: Operation map for GDI engines [60]

The engines made for lean-burning have the capacity to deploy higher compression ratios and hence lead to enhanced performance (increased expansion work), more efficient use of fuel and lower hydrocarbon emissions when compared to standard gasoline engines.

A stratified charge engine is a type of IC engine in which the fuel is directly injected into the cylinder just before ignition. Conventionally, a four-stroke Otto Cycle engine, inhales its fuel by drawing a combination of fuel and air into the combustion chamber during the intake stroke (and in the process produces a homogeneous charge) [61].

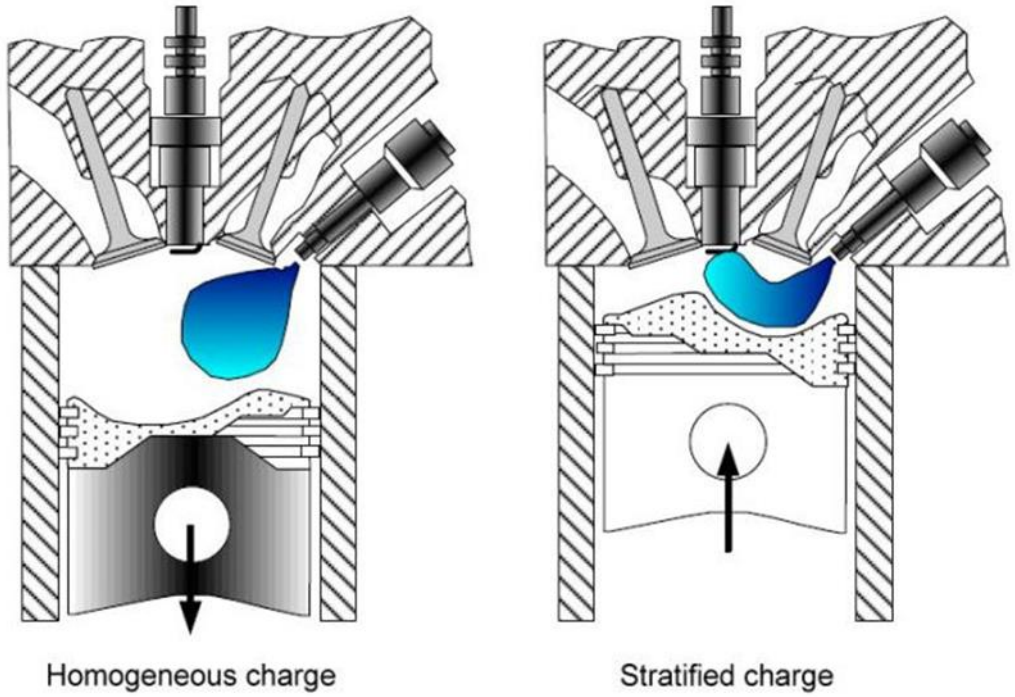

Figure 2-10: stratified charge vs homogeneous charge [62]

2.6.1.3 CAI/HCCI Combustion

Control Auto Ignition (CAI) or Homogenous Charge Compression Ignition (HCCI) is an alternative combustion. Initially, it was identified as a combustion phenomenon when the SI engine goes on running even when the ignition has been turned off [63,64]. Ignition, in CAI/HCCI combustion, takes places in a number of areas at the same time; leading to the air/fuel mixture burning almost instantaneously. Opposed to the spark ignition combustion, the temperature and density of the fuel-air mixture are raised to the level where the reaction of the whole mixture happens at the same time in CAI/HCCI. This permits for a burning of extremely lean or diluted mixture which is both repeatable and uniform within the gasoline engine [65]. Some of the capabilities provided by direct injection technologies include injection timing which is flexible while also permitting for single and multiple injection strategies so that a level of closed-loop control over

this type of combustion processes can be attained while also extending the operational range of CAI/HCCI combustion [66,67].

In HCCI engine fuel and air get compressed to a stage where auto-ignition takes place. It incorporates the features of a CI engine with those of a gasoline one. In gasoline engines a homogeneous charge (HC) is combined with spark ignition (SI), and abbreviated as HCSI. On the other hand, in diesel engines, a stratified charge is combined with the compressed ignition, which is abbreviated as SCCI. [68,69].

In the same manner as happens in HCSI, in HCCI fuel is injected during the intake stroke. However, instead of deploying an electric discharge in the form of a spark to ignite a part of the mixture, HCCI raises temperature and density using compression to the extent when the entire mixture spontaneously reacts.

Stratified charge compression ignition also relies on temperature and density increase resulting from compression. However, it injects fuel later, during the compression stroke. Combustion occurs at the boundary of the fuel and air, producing higher emissions, but allowing a leaner and higher compression burn, producing greater efficiency [70].

Two conditions need to be met in order for one to control HCCI: physical comprehension of the ignition process and microprocessor control. Designs based on HCCI achieve the type of emissions that are like those from gasoline engines while delivering efficiencies comparable to diesel engines. Such engines also have the capacity to attain very low levels of NO_x emissions without the need for a catalytic

converter. Carbon monoxide and hydrocarbon emissions which remain unburned still need to be treated in order to meet regulations for automotive emission.

Research done recently, has concluded that hybrid fuels that mix various reativities, like diesel and gasoline, can assist with the control of burn rates and HCCI ignition. Reactivity Controlled Compression Ignition (RCCI) has been shown to deliver extremely efficient, low emissions when operating over a broad range of speeds and loads [71].

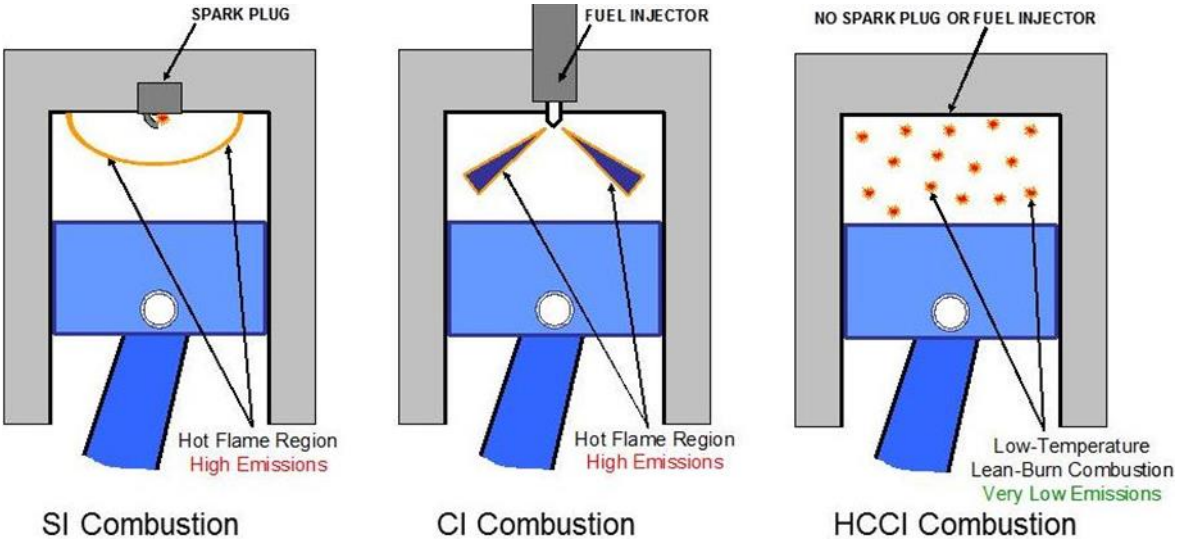

Figure 2-11: Combustion differences between the three modes of IC operation [72].

2.6.1.4 Exhaust Gas Recirculation (EGR)

Historically, EGR has been perceived as the most known type of recirculating exhaust gases in contemporary SI engines. The reason behind this popularity is that it is one of the lowest cost options even though with temporary response limitations. A number of companies including Fiat [73], Ford [74] and Mitsubishi [75] have been observed to

deploy external EGR in the SI engines they manufacture, especially in the US because of the more stern regulations controlling NO_x emissions. The majority, and possibly all, contemporary SI engines also use external EGR with the aim of controlling the Particulate-NO_x and in-cylinder temperature. The capability for inert exhaust gas to bring down levels of fuel consumption is essential as a result of reduced peak in-cylinder temperatures, in-cylinder volume occupation and heat losses. In instances where exhaust gases are returned to the cylinder, they take space that would have otherwise been taken by a new charge. When the available volume for a new charge is restricted by the surplus charge still within the engine, a wider open throttle accompanied by higher manifold and in-cylinder pressures at lower loads and speeds will be forced into the system, resulting in a reduction in pumping loses.

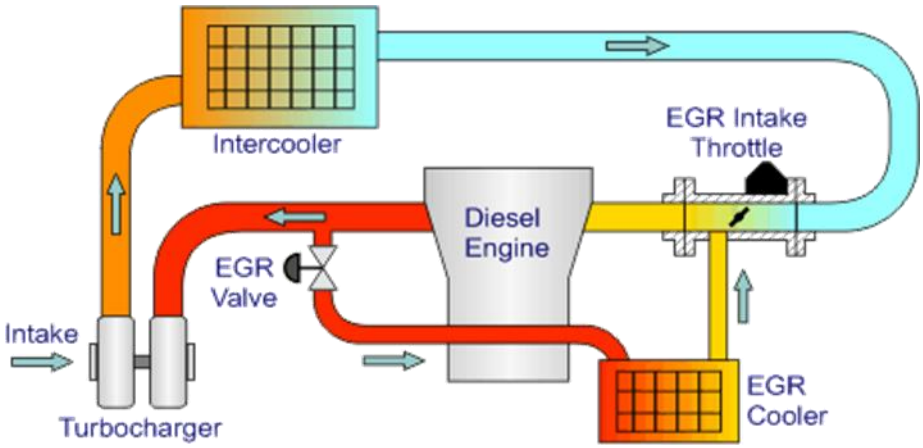

Figure 2-12: Schematic representation of a high-speed passenger car EGR/intake throttle system for Euro 3 application [76]

2.6.2 Pumping Loss Advanced Technologies

2.6.2.1 Engine Downsizing

The main difference in general engine performance between diesel and gasoline engines is the part load pumping loss. This is because of the huge amounts of times that car engines operate at part load. In SI engines, there are basically two primary concepts which can be used for minimising pumping losses. The first one is to get rid of the pumping loss. Basic examples of this idea include spray-guided stratified SI combustion and Controlled Auto-Ignition (CAI) combustion. Between the years 2000 and 2005, CAI combustion attracted the attention of many researchers, with many of them suggesting that it was the sustainable solution to improving the efficiency of gasoline engines [77,78]. However, it was soon discovered that CAI was only a possibility within only a limited range of engine speeds and loads when compared to homogeneous SI combustion [79]. It was also concluded that controlling the rate of auto-ignition and

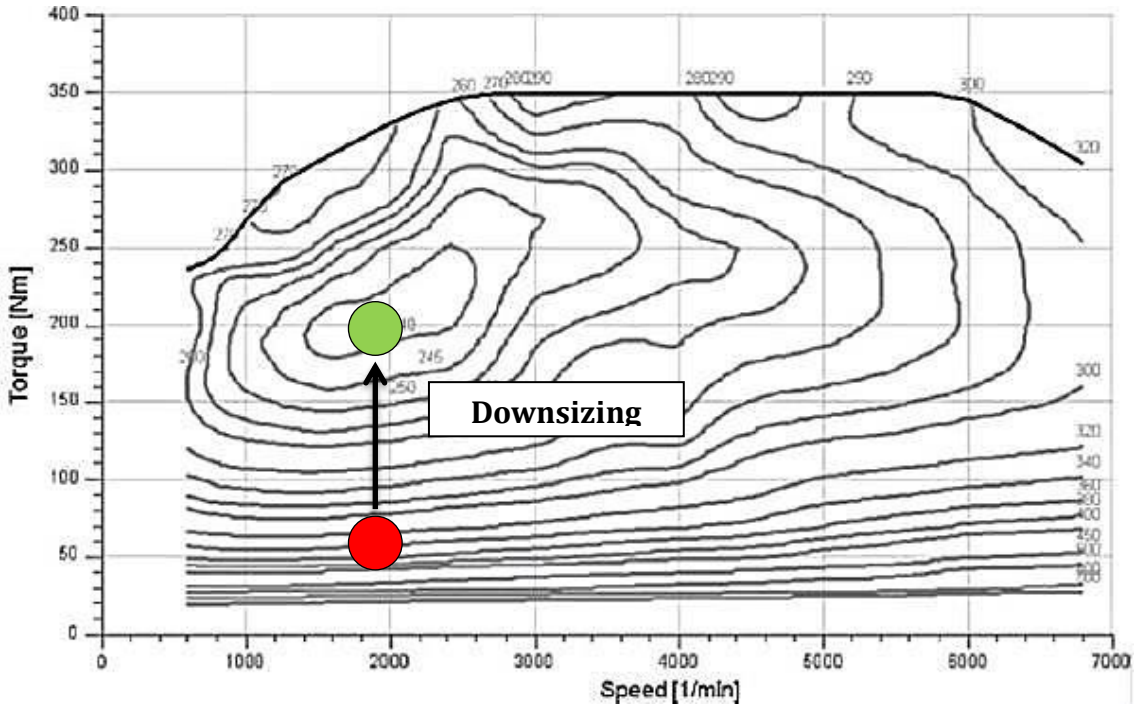

Figure 2-13: Downsizing of a traditional SI Engine to a more efficient region on a BSFC map

timing was a huge problem for production engines [6]. Currently, spray-guided stratified SI combustion is seen as a possible substitute for homogenous SI combustion engines [80]. However, it has not yet reached the stage where it can be implemented on a wide scale owing to some unresolved issues linked to operational robustness and the comparatively high after treatment costs.

The second method for reducing part-load pumping losses is to avoid them by operating the engine nearer the region of minimum BSFC for more of its operating time. This technique has already been applied as a kind of engine design idea referred to as engine downsizing [81]. This idea incorporates a reduction of the engine capacity so that performance is optimized by boosting the intake pressure. This engine capacity reduction means that in the context of a fixed part load (with regards to brake torque), the pressure of the inlet manifold needs to be higher, which would minimise losses associated with preload pumping [6]. The engine load range that is typically optimised for is the range covered by the NEDC[82]. Added to the reduction of losses linked to the reduced part-load pumping, engines which are downsized generally have lower net frictional losses as a consequence of the lower number of cylinders. However, a 25 percent reduction in the number of cylinders will not result in exactly 25 percent of losses linked to friction due to higher operation pressure.

The use of turbo-chargers to improve the intake manifold pressures ensures that some of the heat within the exhaust gases that may otherwise have been lost, is retained. Hence, turbocharging can be a method of reducing CO_2 emissions without having to compromise efficiency. However, it needs to be noted that turbo-chargers result in a delay between load demand and the required enhanced inlet manifold pressure. Turbo-

lag is the name that this delay is often called. Generally, when the demand for power is higher, larger turbo-chargers are needed. Bigger turbochargers also result in longer delay times. With the aim of improving the transient response, some automotive engines which are drastically downsized deploy a two-stage pressure boosting configuration that is comprised of two turbochargers, each of a different size. The smaller one is designed for lower engine speeds with low airflow demands, while the bigger one designed to take care of advanced engine speeds. Including two turbochargers with different sizes delivers a bigger speed load operating window while also enhancing transient response times when compared to one turbocharger. Nonetheless, even after embracing these approaches, there are still issues of performance linked to transient response in engines that are downsized [83].

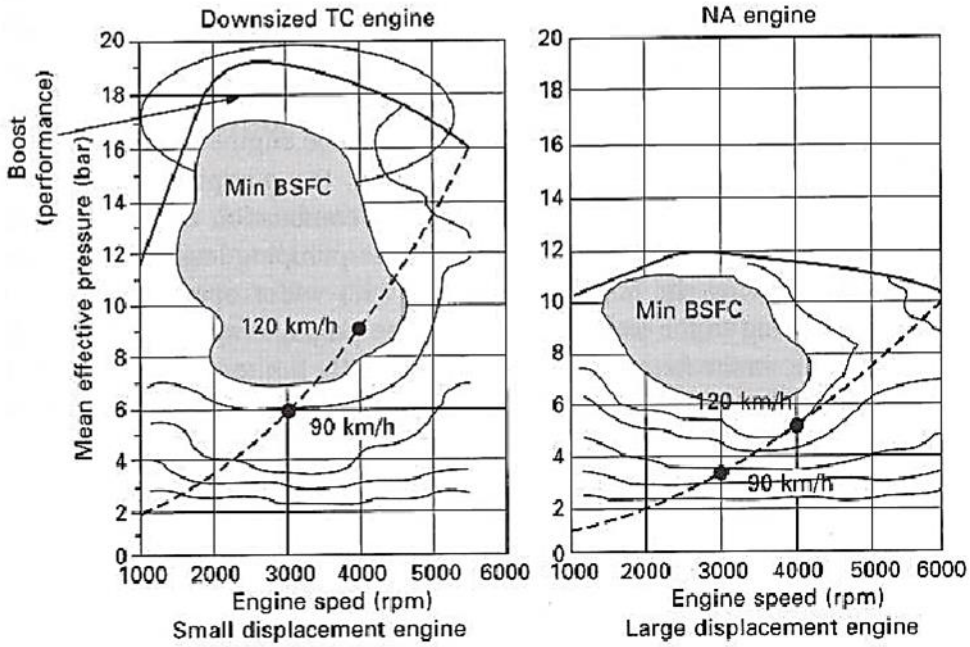

Figure 2-14: Effect of engine downsizing on BSFC [60]

Figure 2-17 and Table 2-1 illustrate the benchmark on the most prominent downsized gasoline engines. They present a comparison using BMEP (MPa) and specific torque units (Nm/dm^3) of all models against conventional four-stroke baseline PFI engines. The level of engine downsizing does not necessarily reflect the engine efficiency in this case, as it may have been penalised by retarded ignition timings to reduce structural stresses and combustion noise. Also, with the aim of bringing down exhaust temperatures, fuel enrichment is often employed, so as to mitigate against the risk of after treatment or turbo damage [84–86].

The baseline 2.0 Litre four-stroke engine model, as illustrated in Figure 2-17, presents the advantage of a full load torque which is almost flat from 1500 to 5500 revolutions per minute. All engines downsized by half such as the Ford EcoBoost, show a maximum torque of at least two and half times higher from 2000 to 3500 revolutions per minute. If a comparison is made to a severely boosted engine with similar displacements, such as the JLR Ultraboost, it delivers up to 3.2 times greater torque. The idea was that this 2.0 dm^3 concept would replace a 5.0 dm^3 naturally aspirated engine, representing a downsizing of 60 percent. It was capable of reaching up to 3.3 MPa BMEP and 257 Nm/dm^3 at 3500 rpm. However, downsizing still represents some limitations, between 1000 rpm and 2000 rpm regarding low-speed torque as is represented in Figure 2-17. The transient response of such engines is also an issue considering that at least 50% of boost build-up is required to meet the transient torque response of a 30% downsized engine [87]. Some promising results have been observed from the adoption of superchargers, two-stage turbocharging, and e-boosters [88]. In order to mitigate against the risk of knocking combustion, improved quality alcohol fuels [89] and gasoline have been used [90]. The use of cooled external EGR at high

speeds and loads helps mitigate against abnormal combustion and reduces the rates of heat release [91]. All the presented downsized engines were operated under stoichiometric conditions, with each having at least one turbocharger. Also, some form of VVA system was used.

Mahle, in 2008, proposed one of the first downsized engines with the capacity to reach 120 kW/dm3 [92]. This engine delivered better fuel efficiency by up to 30 percent when compared to its equivalent 2.4 dm3 engine. The two-cylinder Bosch MBE engine [93], showed performance results in an improvement of 24 percent in fuel consumption when it was compared to a four-cylinder 1.6 dm3 NA engine. In a similar manner, the JLR Ultraboost downsized by 60 percent brought about an improvement in fuel efficiency of 38 percent in particular regions of the NEDC [94] when a comparison is made to a bigger counterpart engine. A 53 percent downsized engine was able to reach almost 3.3 Mpa BMEP, owing to ethanol's higher knock resistance, and it's better cooling effect which is a result of higher heat of vaporisation [98]. In this 1.4 dm3 two-stage turbocharged engine running on E100, a braking efficiency of up to 44 percent was achieved.

Table 2-1: Details of the selected downsized engines [93]

Engine Model	**Number of Cylinders**	**Displacement (L)**	**Year**
Baseline - Ford Duratec	4	2.0	2005
Bosch MPE	2	0.85	2013
Fiat Multiair	4	1.4	2015
Ford EcoBoost	3	1.0	2012
JLR Ultraboost	4	2.0	2014

Mahle	3	1.2	2008
Ricardo HyBoost	3	1.0	2012
Toyota ESTEC	4	1.2	2015

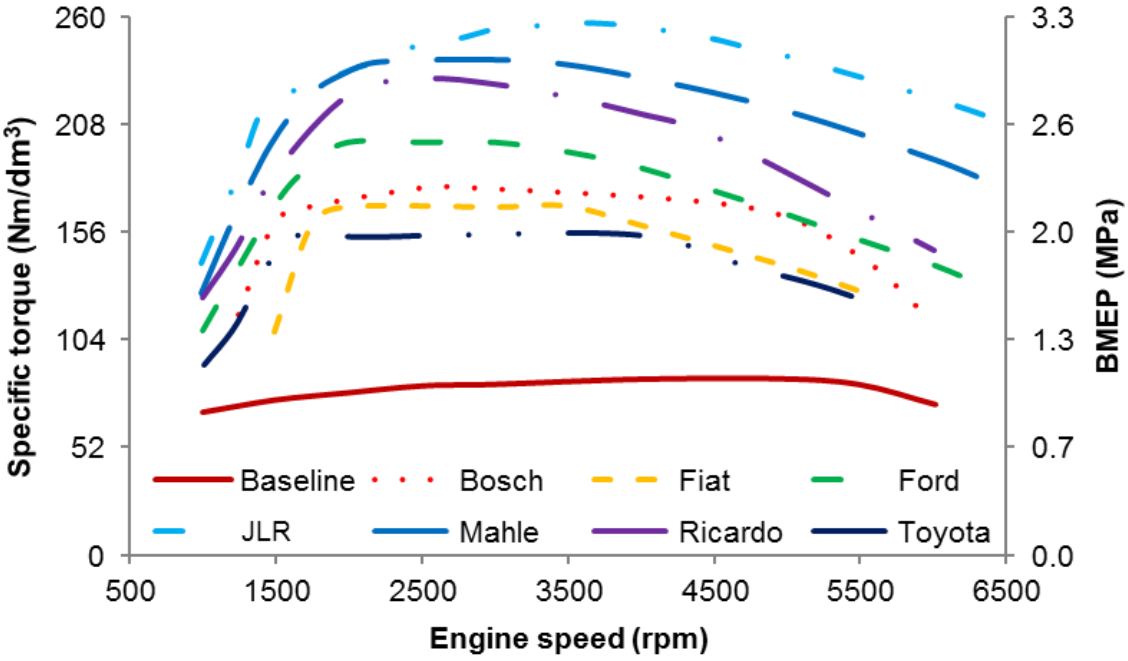

Figure 2-15: Benchmark of contemporary downsized four-stroke engines [93]

2.6.2.2 Rightsizing vs. Downsizing

Manufacturers of automobiles are mitigating the rising fuel prices by producing smaller engines which still deliver the same power as their bigger counterparts. This results not only in better fuel economy but also in fewer emissions. This is appealing, at least in theory. In reality, many people are disappointed as such engines fail to live up to expectation.

Ford is one of the manufacturers that started the downsizing trend. The company introduced the 1.0 litre Ecoboost in April of 2012, as a replacement for the 1.6 naturally aspirated Duratec engine. This was met with some doubt from the public which perceived this engine size as only being suitable for smaller cars such as the Ford Focus and Fiesta. However, these doubts were soon allayed when journalists started praising this as one of the best engines in the market. The engine would later go on to win the best engine under 1-litre award for four consecutive years. This engine was able to perform like bigger engines because of its technical solutions which included the turbochargers and a properly weighted flywheel which ensured smooth running.

This success shown by Ford encouraged other manufacturers to also start experimenting with smaller engines particularly to substitute the naturally aspirated gasoline one. Currently, almost all manufacturers have a small turbocharged gasoline engine in their cars. Most manufacturers have replaced the 1.4 and 1.6 naturally aspirated engine with the 1.0 and 1.2 turbo-charged one. Other manufacturers like Renault and Fiat have even gone as low as 0.9 litres.

The main reason behind engine downsizing was to ensure cars were cheaper to run, while also making them comply with the new legal emissions. However, even if this trend initially targeted the city car, it soon started affecting even the big cars. For instance, Mercedes introduced the 5.5 bi-turbo as a replacement for the 6.3 aspirated, while Audi designed the 4.0 V8 bi-turbo which is also used by Bentley. At BMW, the V10 was replaced by the V8 4.4 bi-turbo while at Ferrari and McLaren the V8 bi-turbo was introduced and delivers more power and torque than its aspirated counterparts.

Within this downsizing era, the cost of manufacturing rises, and also does the cost of new vehicles. Some observers have argued that the whole downsizing idea is a marketing trick where consumers are encouraged to buy something more expensive and complicated. They claim that the benefits of running a smaller engine are actually just an illusion because practically, the aspirated petrol and bigger diesel engines consume less fuel.

The doubts expressed by observers partly make sense as smaller engines can only make the same progress if the driver is raving them hard, which leads to more fuel being consumed. In order to take advantage of the benefits of smaller engines, they need to be driven gently; otherwise, they will have the same consumption like their bigger counterparts. The benefits of such engines are more noticeable during steady throttle driving, such as a motorway. An example is the Ford Fiesta 1.0 Ecoboost which can travel 100 kilometres on 4.5 litres of fuel (62mpg) at an average speed of 100 km/h, while the old naturally aspirated one will only do 5.5 to 6 litres (47 mpg) at a similar speed.

With regards to diesel engines, the concept of downsizing is not as popular as it is in petrol engines. However, manufacturers like Mercedes Benz and Renault have been using a similar downsized 1.6-litre diesel. At Honda, the 2.2-litre diesel was replaced but a 1.6-litre engine. The same happened at Volkswagen where the Polo engine was reduced from 1.6 to 1.4 TDI. BMW has reduced its 2.0-litre engines to 1.5 litres one.

Even though a number of manufacturers seem to think that the answer to improved efficiency and fuel economy lies in downsizing, there is also a number that does not agree. These manufacturers rather believe that the answer lies in rightsizing. One of the

manufacturers who has followed this route is Mazda. In its 2.2-litre diesel engine, which is bigger than the standard 2.0 and 1.6 litres, Mazda has introduced the SkyActive technology to make the engine more economical while also maintaining a wide torque band. For example, the Mazda 2, unlike its counterparts which have resorted to small turbocharged petrol, still uses the 1.5 litres aspirated petrol with 75, 95, and 115 hp. Mini Cooper S. is the other car that has followed the same principle. While the engine size in the old Cooper was 1.6 litres, the new engine has a capacity of 2 litres. According to the manufacturers of the car, this size comes with more torque while also being more economical with the use of fuel. What the above discussion indicates is that downsizing is not the final answer. While no one can dispute the fact that it is effective, it looks like it only does with smaller cars. Its effectiveness really depends on the kind of car where it is being applied [94].

2.6.2.3 Engine Down-Speeding

One of the most notable benefits of using turbochargers and superchargers is its ability to enhance the maximum low-speed engine load [82]. The impact of this is that it reduces the engine speed needed for a particular output. The use of longer gearing can lead to a significant reduction of frictional and pumping loses on an engine that is downsized through a concept known as engine down speeding. The BSFC maps in Figure 2-18 illustrate the impact of the engine down speeding and downsizing. . It can be seen from these maps that for a given gear ratio, engine downsizing alone improves BSFC at motorway cruising speed. It can also be seen that down-speeding by increasing the gear ratio can further improve BSFC. It is also observed that the down-speeding which can be executed mostly relies on the head-room in low-speed torque and can be different depending on the engine in question. However, it has been proved that the use

of this method can lead to improvements in the consumption of fuel over the NEDC [82].

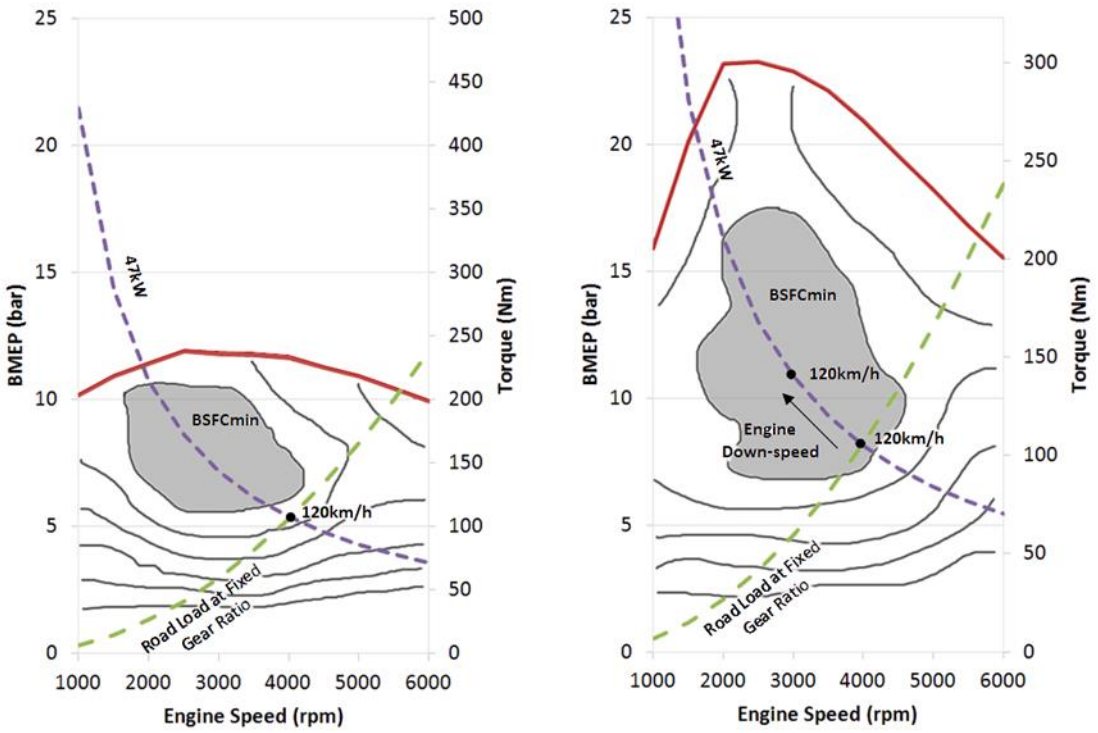

Figure 2-16: Conceptual BSFC maps for a 2.5L naturally-aspirated engine (left) and a 1.6L boosted engine (right). Adapted from Zhao [60] and Stone [6]

2.6.2.4 Engine Stop and Start Systems

Generally, when a car is driven in an urban area, the amount of fuel used while a car is idling has been observed to be around 10 % of the overall consumption [95]. This amount can be reduced significantly by the use of a start and stop system which stops the engine when the vehicle is stationary and then switches it back on when the gear is engaged to move. Even though these systems have been tested since the 1970s, with companies like Toyota introducing an electronic device which would automatically

switch off the engine if it had been stationary(Toyota Crown) [96], the direct injection technologies have brought the potential to realize a fast and efficient engine stop and start system An example of this type of system is the Mazda i-stop. It takes advantage of the direct injection technology which uses combustion to start the engine, within a period of less than half a second. The Japan JC08 mode test cycle has shown that this system improves fuel economy by up to 8%.

2.7 Abnormal Combustion and Knock in Spark-Ignition Engines

As a subject of research, engine knocking has been a popular research topic since the car manufacturing industry started the advanced development of the SI engine [104]. The term knock is derived from the metal “pinging” sound as a result of auto-ignition (spontaneous combustion). Combustion abnormalities of knock and surface ignition are prioritised in research due to their potential for considerable damage and noise [13]. Surface ignition happens through hot spots which can result from carbonaceous deposits inside the cylinder or as a result of a spark plug or valve heating up. Usually, it happens ahead of the spark ignition and is also referred to as pre-ignition. There is a difference between knock and surface ignition as knock is a consequence of auto-ignition of fresh charge. Results produced by research into the high specific output application of engines which are highly downsized indicates that pre-ignition, which is also referred to as Super Knock can be identified when operating at low engine speeds and high loads of more than 20bar BMEP.

2.7.1 Engine Knock

With regards to SI engine, the term knock denotes the sound produced by high-pressure shock waves. The uncontrolled combustion of the whole or part of the charge inside the combustion chamber which has been a design challenge for SI engines for over a century is responsible for these shockwaves [97]. Before extensive work on knock in the early years of the 1990s [98–102], two theories dominated explanations as to the cause of end-gas knock: the detonation theory and homogeneous auto-ignition theory [13,100]. Ricardo [103] was the first to suggest the homogenous auto-ignition theory as the reason responsible for knock in spark-ignition engines and also suggested that it was responsible for limitations on engine efficiency. The detonation theory, proposed that knock is caused by the exponential acceleration of the normal flame leading to detonation. On the other hand, homogeneous auto-ignition theory suggested that knock is the result of consistent auto-ignition of unburned mixture. Even though both the theories are credible to an extent, none of them is able to explain all the observed behaviour associated with knocking combustion [100,104]. Hence, the proposal of the theory of heterogeneous auto-ignition, initiated at discrete points within the end-gas (so-called “hot-spots”) by Konig and Sheppard et al. [98–101].

2.7.2 Knock Intensity

Rassweiler and Withrow [105] produced different images of end-gas auto-ignition that resulted in various magnitudes of knock intensity (including no knock at all) with auto-ignition often occurring a head of the flame front, well within the end-gas region. Konig and Sheppard [98], have in more recent times, made available optical data giving details of the cyclic variation in end gas auto-ignition using an optical engine with full-bore

overhead access. They illustrated an array of auto-ignition intensities starting from no knock to “severe”, with knock intensity measurements of around 35bar. From the recorded images, it could be observed that auto-ignition happened in the end gas and usually, it commenced almost at the same time in different places as is illustrated in Figure 2-19. Miller's [97] declared that knock intensity was not linked to end-gas volume at the point of auto-ignition, were supported by the comparisons between optical data and cylinder pressure data. It was concluded that knock intensity was generally well correlated with the unburned gas temperature at the onset of auto-ignition, but there was no correlation between knock intensity and the mass of fuel remaining at the point of auto-ignition.

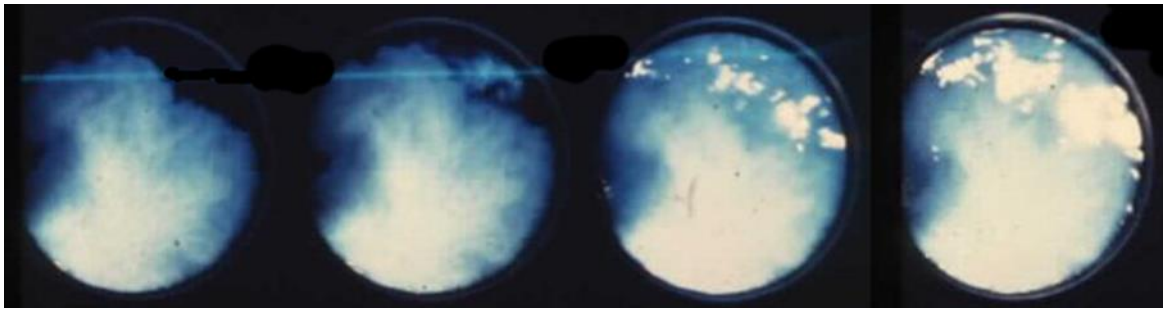

Figure 2-17 : Example of end-gas auto-ignition and knock in an SI engine [97]

2.7.3 End-Gas Auto-Ignition and Exothermic Centres

Konig and Sheppard et al. [99] applied the three modes of exothermic reaction propagation originally developed by Zel’dovich for one-dimensional shock tubes to exothermic centres within a two-dimensional combustion chamber end-gas region. The concept of exothermic centres show restricted areas where auto-ignition will most probably take place as a result of their chemical composition or temperature. They are a result of incomplete mixing of the fuel, air and residual exhaust gas. Each mode of

exothermic reaction propagation was associated with a series of temperature gradients throughout the centre of the exothermic reaction. Table 2-2 outlines the three modes of reaction propagation that Zel'dovich described. A computer code was used in modelling these three distinct cases of temperature gradient and forecast their effect on the pressure of the combustion chamber after auto-ignition. From this model, it was discovered that, for a high-temperature gradient (~125K/mm and higher) at the centre of the exothermic reaction, a deflagration with extremely low-pressure gradients inside the combustion chamber was formed. On the opposite end of the scale, with extremely low (almost homogenous) temperature gradient throughout the centre of the exothermic reaction, a thermal explosion took place. Within this model, this thermal explosion resulted in moderate pressure waves of the same magnitude as a combustion cycle with moderate knock intensity. An intermediate case was modelled between these two extreme cases, and its temperature gradient across the exothermic centre was 12.5K/mm. Regarding this case, a number of shock waves were created. The manner in which these shockwaves interfered with each other was very much representative of the severe knocking combustion illustrated in Figure 2-20. A comparison was then made between these modelled auto-ignition regimes and investigational knocking combustion cycles that highly showed to have the same characteristics with regards to mean end-gas temperature, resulting in flame propagation velocity and fluctuations in pressure. However, it was noted that experimentally observed knocking cycles could not be easily categorised as only displaying a single regime of auto-ignitive flame propagation.

Table 2-2: Overview of Zel'dovich's modes of exothermic reaction propagation and modelled knock intensities by Konig and Sheppard et al. [98]

Type of Flame Reactions	Mean Temperature	Temperature Gradient	Reaction	Knock
Deflagration	Low	High (~125K/mm)	A gentle pressure wave, where the flame advances regularly, even though the combustion shifts to deflagration.	None to Moderate
Detonation ("Thermal explosion")	High	Low (~1.25K/mm)	After ignition, there is an immediate chemical reaction of the gas at a relatively constant temperature.	Moderate
Developing Detonation	Moderate	Moderate (~12.5K/mm)	A substantial shock is generated if a low enough gradient is present, which would institute a strong chemical reaction resulting in a steady state detonation.	Violent

Figure 2-18: Lines of constant pressure within a two-dimensional combustion chamber during a simulated heavy knocking cycle. Adapted from Konig et al. [99]

Eventually, some modifications were made to the 2-D model so that it could incorporate many exothermic reactions focused on different sites and taking place at different times, and also making available results for tracking particles during the process of auto-ignition flame propagation [101]. This was able to describe, more sufficiently, the inhomogeneity and complexity of the end-gas area during combustion. This model was custom-made and correlated against, experimental particle tracking data obtained from a full-bore optical SI engine. From this model, it was concluded that the flame propagation regime of an exothermic reaction with a high temperature gradient across its centre could be modified from a deflagration to a developing detonation by an earlier exothermic reaction also propagating via the deflagration regime. Thereby, it was concluded that the combination of two or more auto-ignition events that would individually create a low knock intensity event could combine together to create a heavy knocking cycle.

The rapid discharge of energy from the auto-ignition has a strong influence on the local temperature and pressure producing a propagation shockwave. In the illustration on Figure 2-21, the measured cylinder pressure is influenced by this shockwave, expansion and reflection.

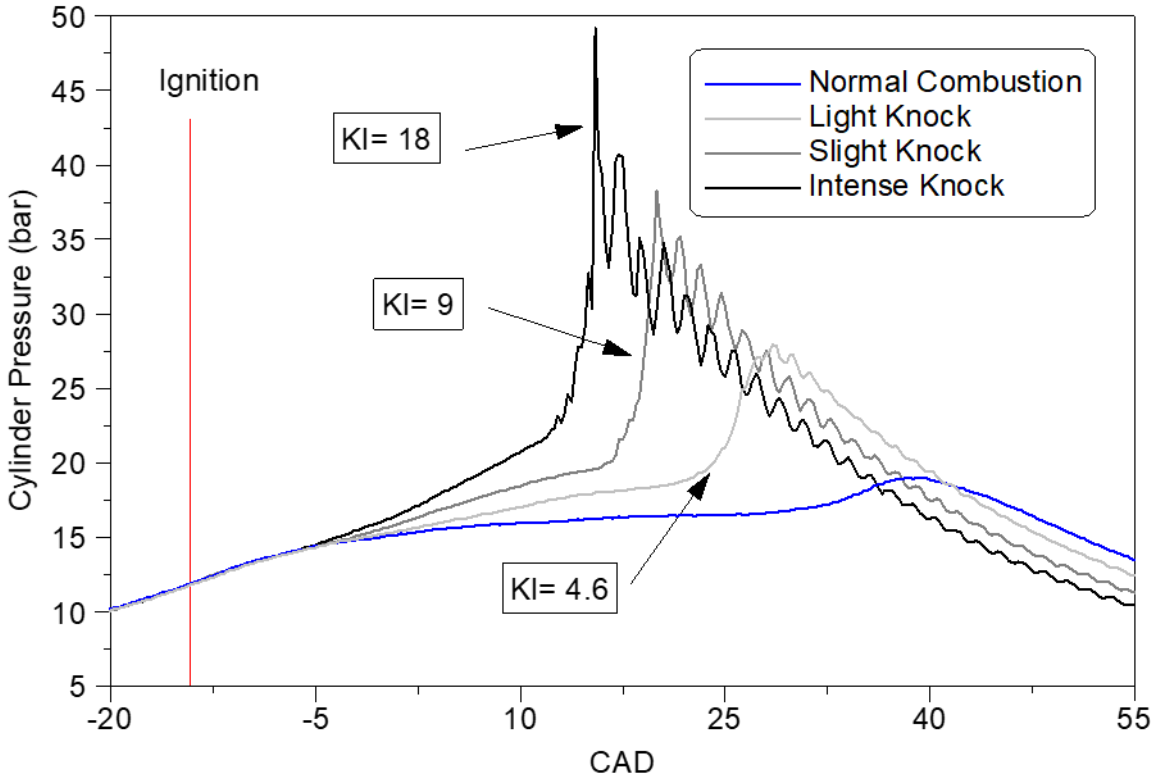

Figure 2-19: Cylinder pressure variation in relation to CA for normal and abnormal combustion

2.7.4 Knock Damage

A diverse range of engines which had failed as a result of a knock prompted component were studied by Nates and Yates [106]. They arrived at the conclusion that the engine failure mechanisms observed were prompted by either erosion damage or heat flux. The increase in heat flux resulted in extreme component expansion and interference; the piston rings being specifically affected. Damage linked to erosion resulted in recurrent pitting of the piston crown and top-land area, causing the piston rings to move excessively and a deficiency of compression caused by excessive blowby.

Maly et al. [100] explain that knock erosion is a result of a combination of thermal and mechanical wall loading caused by shockwaves formed during the auto-ignition of exothermic centres. It is observed that these shock waves move at speeds ranging between 500 and 2000m/s. It has also been observed that the shockwaves have localised areas of maximum pressure and order of magnitude above that which is measured by a dynamic pressure transducer [107]. Hence, it has been indicated via modelling and observation that the correlation between knock damage severity and intensity of knock is minimal. To the contrary, it has been concluded that knock damage depends more on the in-cylinder pressure at the point where the knock begins [102,107].

An experimental study was conducted by Fitton and Nates [107] where they placed an aluminium test specimen in a single cylinder engine's end-gas region. To get an idea of the extent of the knock damage caused, the researchers quantified the amount of material worn in the process of the knocking combustion. The “damage index” is the phrase they used to call this measured value. Knock damage was measured at different spark timings and compression ratios. These scholars arrived at the conclusion that knock damage would not take place if the knock was initiated at cylinder pressures that were sufficiently low.

Figure 2-20: : Samples of knock damage to piston rings and piston crown [108].

2.7.5 The Characteristics of Super-Knock

Owing to Low-Speed Pre-Ignition (LSPI), which is sometimes referred as a Super Knock, the level to which modern high specific power SI engines can be downsized has been restricted. LSPI happens at irregular intervals and can result in a catastrophic failure of the engine even though it happens infrequently [60]. The pre-ignition was initially unanticipated since the events occurred below the typical charge auto-ignition temperature and its infrequent nature. The result of an LSPI event is considered to be a developing detonation flame reaction where low-to-moderate temperature gradients are experienced in the unburned charge. The consequence of this event is numerous waves of pressure which interact at a high frequency.

Super knock has been shown to take place at conditions of high load and has become a common problem of engines that are downsized where engine load is increased through intake pressure charging to loads in excess of 20bar Brake Mean Effective Pressure (BMEP) [82,84]. It has been observed that any further increases to the engine load

could lead to increase of the frequency of super-knock events [11,109]. The speed load graph in Figure 2-24, illustrates the region affected by super-knock.

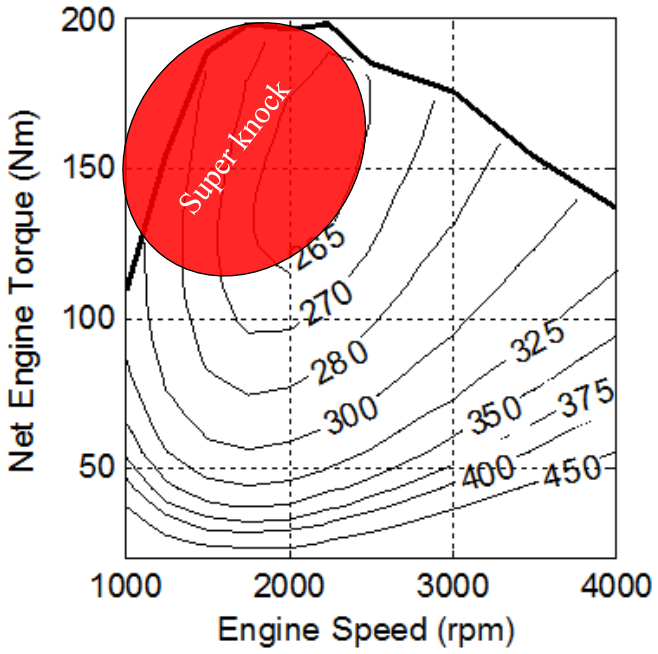

Figure 2-21: Speed-load region commonly affected by super-knock

2.7.6 Knock control strategies

There are a number of strategies available for vehicle OEMs to mitigate against the risk of knock occurrence and the damage that it comes with. During the engine design phase, safety margins such as the octane number, compression ratio and ignition timing are often invoked [106]. These will result in fuel and performance penalties, but are implemented to avoid the occurrence of damages. Real time on-board knock detection is used to allow the electronic control unit (ECU) to adjust appropriately in order to avoid potentially damaging affects by retard spark timing and in extreme cases the calibration may resort to over-fuelling. If the ignition timing takes place too early, knock and

linked damage could occur. However, power could be lost if too retarded, because the piston has moved past the potential peak power position. This results in more fuel remaining unburned and thus higher levels of emission and could also be more likely to overheat. The ECU in modern engines will use electronic control of ignition timing to accommodate differences in pressure, temperature and fuel characteristics, including, where applicable, boosting technologies. To measure the performance of a gasoline fuel, an octane number is used and in diesel fuels, a cetane number is used. If the octane rating is higher, it implies that the fuel has the capacity to withstand higher levels of compression before the ignition. Usually, it is given as a Research Octane Number (RON) that is obtained using a test engine and then doing an analysis of the results together with the fuel content. The use of a lower quality fuel, 95RON instead of 97RON, increases the propensity to knock, and the ECU adapts accordingly, mostly through retardation of the spark timing. Vehicle OEMs rate their engines with a certain kind of fuel. Usually, those engines which are heavily boosted or build to give superior performance are calibrated to deliver their maximum performance when powered by higher-octane fuel. Knock may also be avoided by enriching the air-fuel ratio, reducing engine load and decreasing the manifold pressure and therefore in-cylinder pressure by restricting airflow with the throttle or boost pressure [110]. It needs to be noted that altitude has an effect on air-fuel ratio; usually, this is obtained through use of a barometer to measure ambient pressure and then a different fuelling map calibration on the engine being implemented so that it suites the prevailing conditions. In engines with increased turbulence, knock is less common as this accelerates burning and cooling of the unburned mixture [111]. It also needs to be noted that increased engine speed enhances turbulence.

2.8 Vehicle hybridisation

Figure 2-25 represents a demonstration of the unavoidable powertrain hybridisation path for dealing with CO_2 emission legislation requirements for passenger cars. Pure electric vehicles, sometimes referred to as Battery Electric Vehicles (BEV), are some of the potential answers to reduced emissions. However, their current batteries have an energy density of approximately 0.7 MJ/dm3 [112], while those of gasoline ambient conditions are 32 MJ/dm^3. These limitations still represent a compromise amongst vehicle autonomy weight and cost of production. Using fuel cells to power passenger cars also leads to zero CO_2 emissions, even though the current techniques used to get hydrogen and the distribution grid needed to transmit the energy is still not cost effective [113]. Hence, hybrid units present a possible solution to the reduction of CO_2 emissions within the next few decades. Such units would have an electronic motor(s), batteries, an internal combustion engine (ICE).

Both electronic motor(s) and ICE, in electric hybrid vehicles (EHV), have the capacity to directly provide power to the vehicle, so the propulsion approach will depend on the conditions. EHVs do not require an external connection to the electrical grid; its batteries are charged through methods of regenerative braking and other arrangements included saving energy. While plug-in hybrid electric vehicles (PHEV) have similar features to HEVs, they can also be charged through the use of an external source of power. Greater flexibility of propulsion strategies, such as serial/parallel connection between electric motor(s) and ICE in such vehicles is made possible by the larger capacity batteries [114]. In a parallel connection, both ICE and electric motors provide propulsion to the vehicles when demand increases. In serial mode, an electric generator

is powered by the running ICE, and these deliver energy to the electric motor or batteries. In particular cases, there is no connection between the ICE and driveline which is wholly powered by electric motor(s). In such conditions, the IC engine is a range extender to the electric system and mostly triggered if the energy levels in the battery are at minimum levels [115].

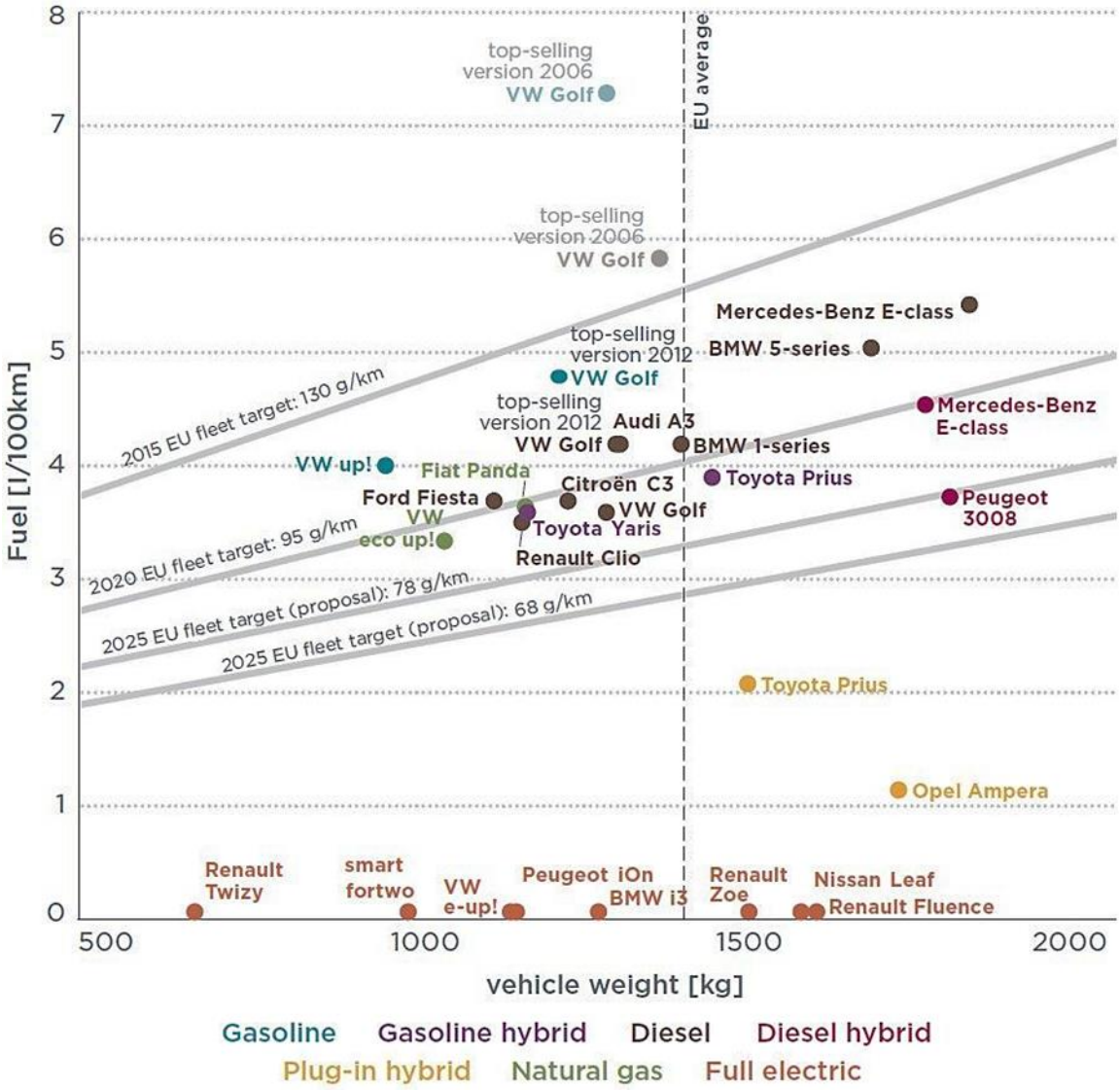

Figure 2-22 : Fuel consumption and weight from selected passenger cars in the EU in 2013. Emissions targets for 2025 not yet confirmed. Adapted from [116].

Figures from 2014 indicate that global sales of electric vehicles (HEV, BEV, and PHEV) reached approximately 300,000. When compared to 2013, this represents an increase of 53%. Norway was the most successful country in embracing electronic vehicles, representing about 13 % of the total fleet. The following country is the Netherlands with around 4 % of the market in 2014 [112]. It is projected that by 2040, the number of new electric vehicles sold will outnumber the light-duty gasoline/diesel vehicles as is represented in Figure 2-26.

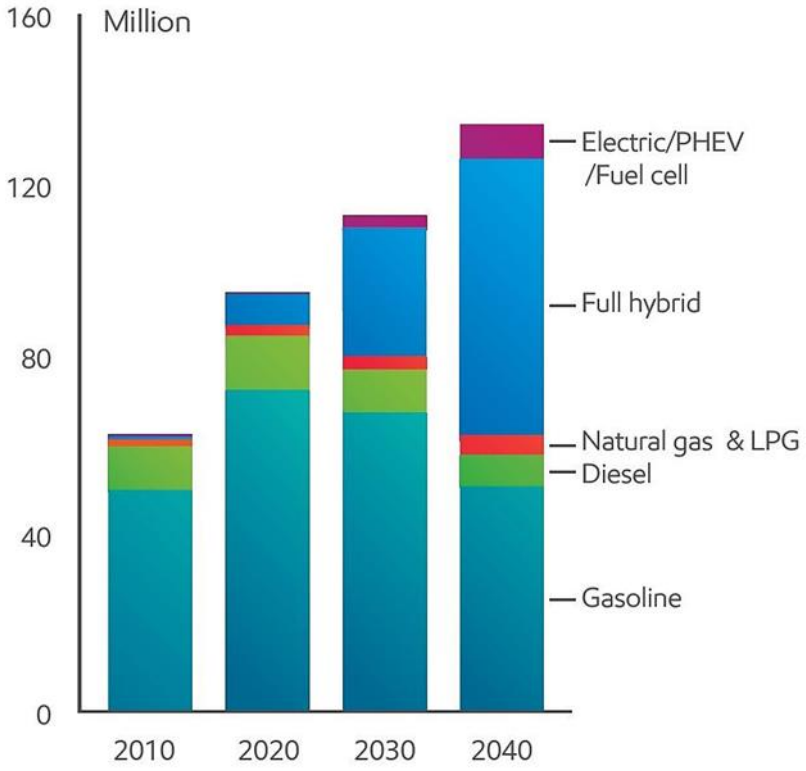

Figure 2-23: Annual world new light-duty vehicle sales, adapted from [4].

2.9 Future of IC engines and automotive electrification

It is difficult to make market projections related to electrified powertrains as has been indicated by past forecasts which have often proved to be off the mark [117]. An important factor here is sheer complexity: if market projections are to be accurate, they will have to be founded on a number of factors including assumptions about the direction of government policy, availability of attractive vehicles with electrified powertrain, statutory instruments, and preferences of customers, incentives and future costs of batteries. On their own, each of these factors has a significant effect on the future of the electrified powertrain while also not being completely independent of each other.

However, what is of interest is the fact that leading manufacturers of cars have in recent times taken a more forceful position on electrification. For instance, the Volkswagen group has indicated that it expects its battery electric vehicle (BEV) share to increase to 25 percent in 2019 and subsequently 50 percent by 2030. The company also announced that this will be based on 30 BEVs that will be launched across the assembly lines of the company by 2025. Within a similar timeframe, Daimler has announced that it will launch 10 BEVs.

Ricardo [117] reports that a high penetration of BEVs is possible, particularly as manufacturers of cars are moving in the direction of attractive cars with spacious interiors and a unique design language which the bespoke BEV platforms and modular kits are making possible. Even though BEVs have higher real-world ranges, the biggest issues that need to be attended to is the well-timed introduction of infrastructure for

charging which will alleviate the anxieties linked to queuing of both the private and fleet buyers.

Available realistic reports forecast that by 2030, almost 70 percent of all cars sold across the world will still have an ICE component [117]. However, over the coming years, it is expected that a substantial increase in the electrification content of new vehicles will take place. This will be driven by the car manufacturing industry striving to comply with the environmental restrictions set by governments and regulators across the world. It is expected that emission limits and certification process will become tighter going into the future. However, it is likely to be accompanied by further vital changes in the manner of regulation, whose aim will be to embrace both life-cycle analysis and well-to-wheels concepts. This is a challenge that industry will have to meet, while at the same time ensuring that the products they make are both desirable and affordable to the consumer.

Currently, there are substantial research efforts aimed at the development of new battery cells systems and chemistries, which will make it possible for pure electric vehicles to be cost-effective when compared to traditional vehicles. However, even when this breakthrough takes place, there are expected to be further challenges related to infrastructure, which cannot just be wished away. Pure BEVs will surely form a much larger proportion of the market than they do now, but perhaps less than many observers are predicting.

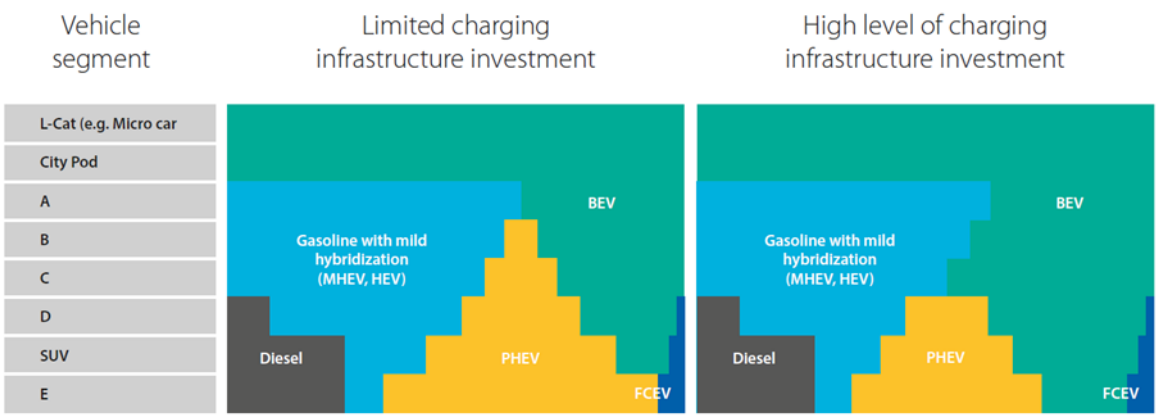

Figure 2-24: Ricardo view of the 2030 passenger car electrified powertrain mix in Europe [117]

3 ENGINE DESIGN & INSTRUMENTATION

3.1 Introduction

The engine used in this study was a Lister Petter TS-1 at the Centre for Advanced Powertrain and Fuels Research (CAPF) at Brunel. The engine originally was produced for a diesel canal-boat powertrain but was employed here with a fully redesigned cylinder head. This new head allowed for full-bore overhead optical access to the combustion chamber. The redesigned engine was capable of operating in PFI or DI mode. The following section includes details of the design and experimental methodology, covering the engine, data acquisition system and associated test cell infrastructure.

3.2 Test Rig Requirements

The desire was to construct an engine that would allow for full-bore optical access and withstand heavy knocking cycles repeatedly and consistently introduced. Moreover, full-bore optical access was required to the combustion chamber in order to have full direct visual observation of the combustion events and flame behaviour, which complicates the design. Prior reverse engineering analysis and validation established that the unit adopted throughout the currently reported study was capable of withstanding in-cylinder gas pressures of up to 150 bar [12].

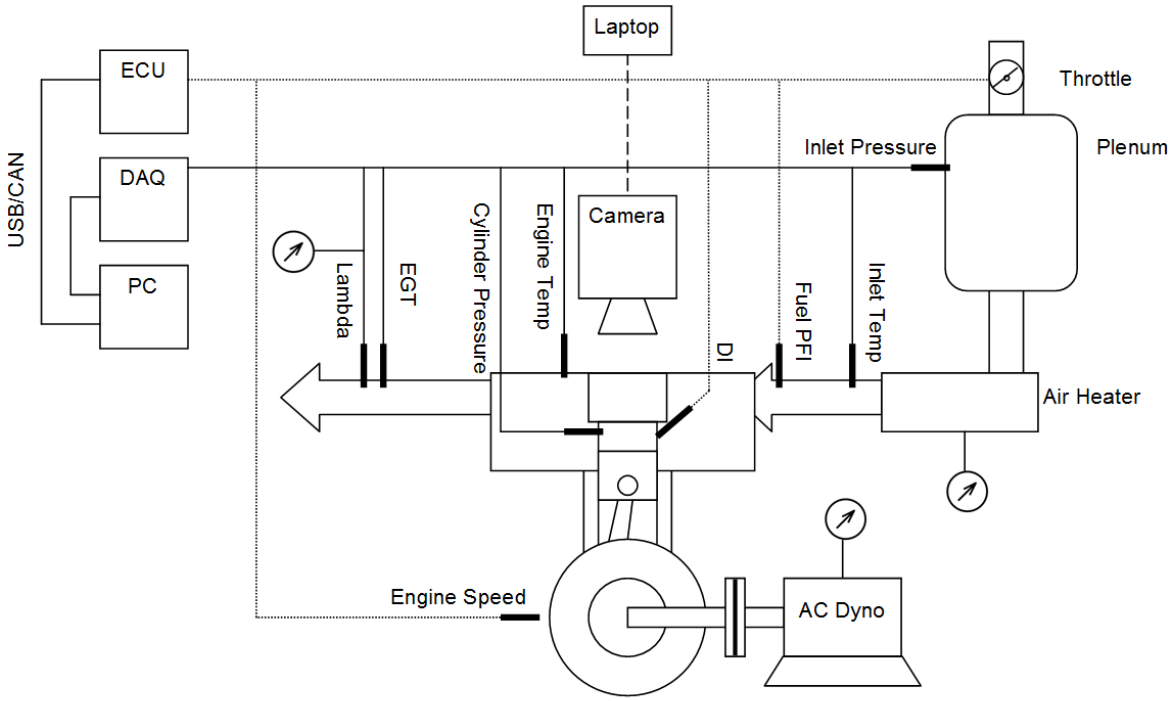

Figure 3-1: Schematic of the experimental set-up.

3.3 Engine Design

The engine used throughout this study was a combination of a Lister Petter TS1 diesel engine and fully redesigned gasoline cylinder head. The bottom of the engine was almost entirely unchanged. The TS1 was designed to withstand the high combustion pressures present in diesel engines; therefore the bottom end of the TS1 was extremely strong and robust for knocking combustion testing. Diesel engines are usually designed to have relatively low maximum speeds compared to gasoline engines, however this issue was not considered to be limiting for the planned research as knock and super-knock typically occur at low engine speed.

The original engine was used for diesel experiments [118] and later upgraded for EGR entrainment and HCCI studies [118–121]. In 2002 the unit was first modified by

Williams [122] for studying the effect of charge stratification on the combustion and emissions of a spark-ignition internal combustion engine. The unit was altered again in 2013 when the cylinder head was completely redesigned by Dingle who was studying lubricant induced pre-ignition in an optical spark ignition engine [123].

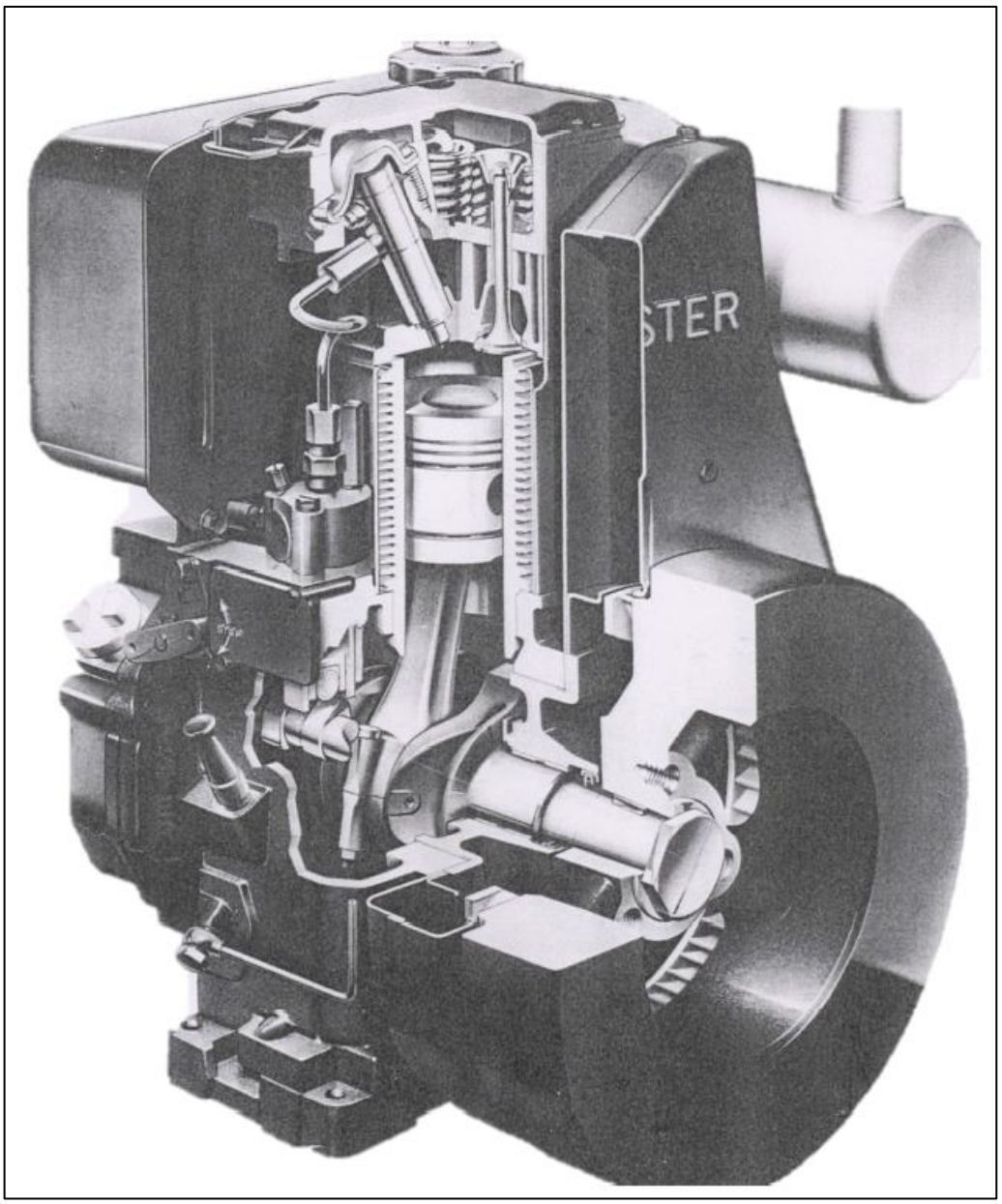

Figure 3-2: Original Lister Petter TS-1 engine.

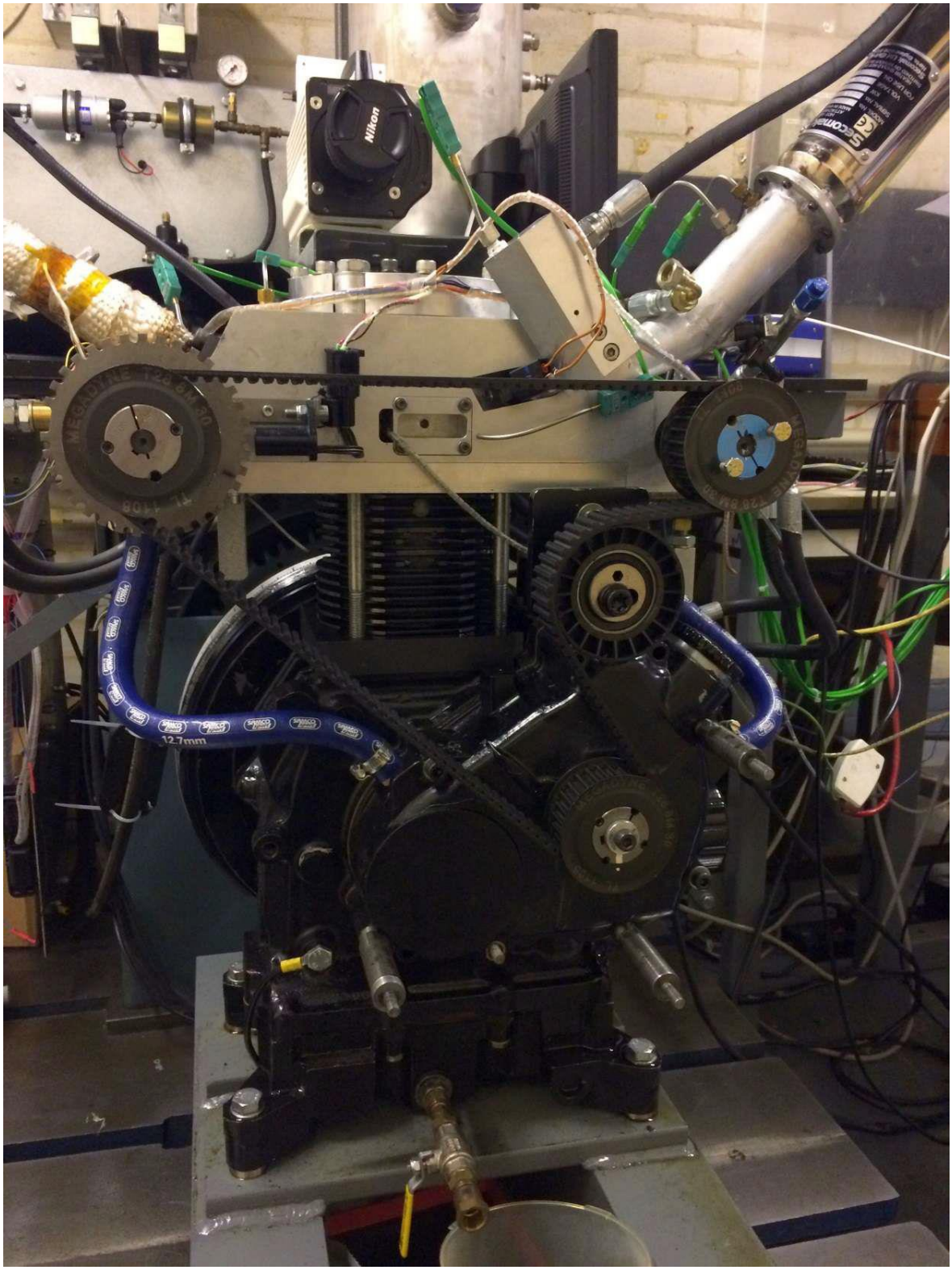

Figure 3-3: Current engine with modified cylinder head on top.

3.3.1 Basic Engine Geometry

The original Lister Petter TS1 was a single cylinder research engine with capacity of 600 cc. After cylinder head modification, the engine capacity increased to 630 cc with a bore of 95mm, stroke of 89mm and compression ratio decreased to 8.4:1. The original air-cooled liner provided a suitable bottom-end for the modified optical cylinder head. Generally, the modified unit could be considered to offer a relatively robust platform, with recent FEA analysis and validation proving the current unit to be capable of withstanding continuous in-cylinder gas pressures of up to 150 bar and instantaneous peak pressures of 200 bar, which is unique for an overhead optical research engine. A table of key baseline engine geometry is presented in Table 3-1.

Table 3-1: Table of key engine geometric parameters.

Parameter	Value
Bore (mm)	95
Stroke (mm)	89
Swept Volume (cc)	631
Clearance Height (mm)	9
Geometric Compression Ratio	8.4:1
Exhaust Duration (deg. CA)	230
Exhaust MOP (°bTDC)	105
Exhaust Valve Lift (mm)	5
Standard Valve Overlap (deg. CA)	25
Intake Duration (deg. CA)	230
Inlet MOP (°aTDC)	100
Con-Rod Length (mm)	165.16

3.3.2 Cylinder Head Design

3.3.2.1 Optical Access

In order to study the flame structure and auto-ignition combustion characteristics full bore optical access was essential. Due to the unpredictable nature of knocking combustion, full-bore optical access was needed to examine the auto ignition sites and end gas knock near to the cylinder wall. Moreover, the location of pre ignition and knock occurrence was not known, nor is it possible to know if these effects occur in the same location during different test runs. Therefore, full bore optical access increased the amount of information recorded and prevented the loss of vital information due to incomplete optical access. It should be noted that the valves were recessed in deep pockets but that these were usually covered during the timing of the auto-ignition events.

The design of the cylinder head allowed for two partial side optical accesses in addition to the overhead window. These were mainly to be used for future laser sheet testing and as a result the side windows were replaced with metal blanks (identical aluminium material to the head) throughout the currently reported work. A full schematic of top and side optical accesses is presented in Figure 3-4.

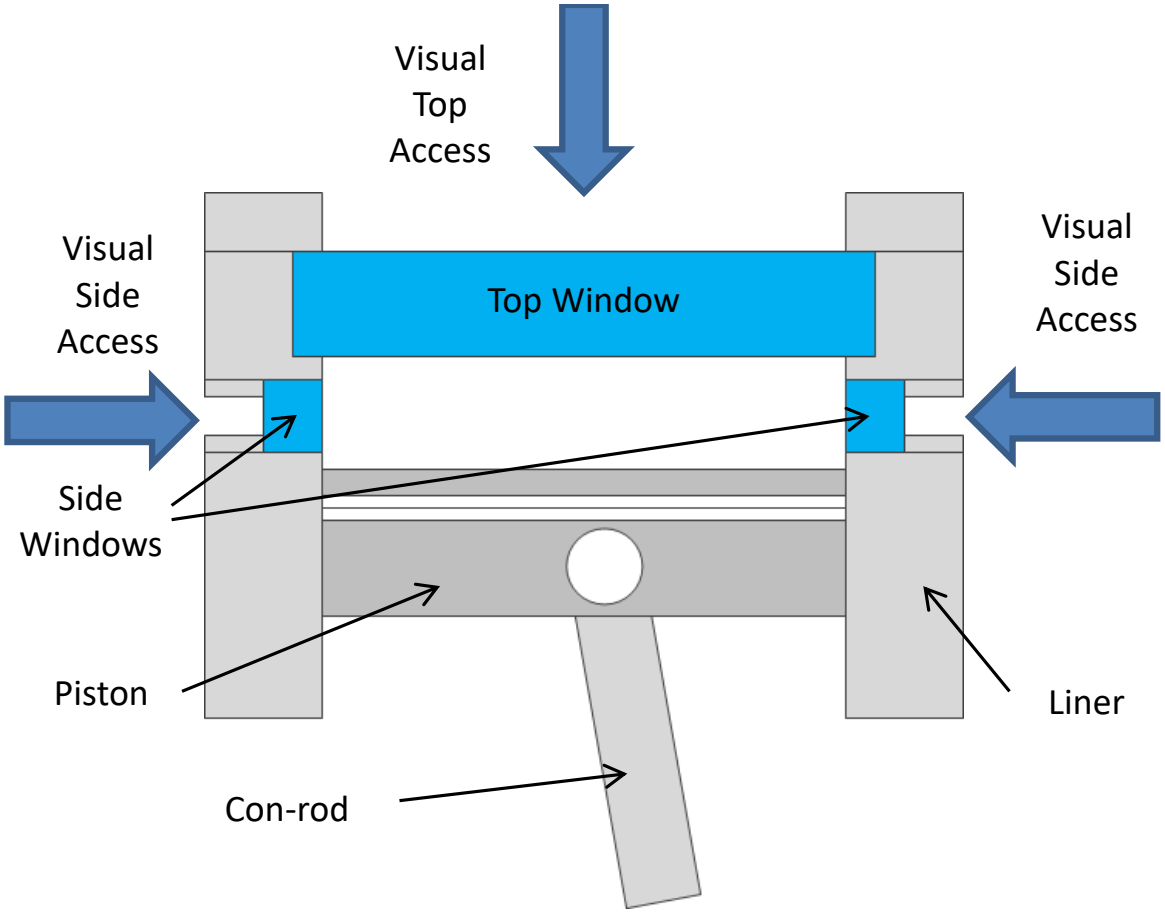

Figure 3-4: Schematic of optical access for overhead window concept.

3.3.2.2 Concept

The cylinder head design concept was based on side valve full overhead optical access. This was selected in preference to the more conventional Bowditch piston as it allows the full bore to be visualised while still attaining a valve arrangement that leads to a tumbling intake air motion (albeit with an abrupt pancake shaped chamber in place of the typical pent roof).

As the engine was naturally aspirated, and due to the potentially high load application of the engine, it was decided that four valves (two intakes and two exhausts) would be necessary to provide the air needed for sufficient engine breathing. While the valves were mounted on the opposite sides of the combustion chamber, two camshafts were required to operate all four ports. Likewise the spark plug was moved to the side of the head in order to maintain complete optical access to the combustion chamber and piston crown within the top window. Also, by moving the spark plug to the side it becomes easier to record the end gas knock phenomena [124]. The purpose of the side-mounted spark plug was to maintain complete optical access to the piston crown. A direct injector was included on the opposite side of spark plug for two purposes; firstly to provide a potential means of injecting excess fuel into the combustion chamber to study the effect of charge cooling on knock reduction [125–127], and secondly to allow the possibility of adopting a dual fuel strategy in future studies (with late stratified injection into the end-gas). Additionally, a rapid gas sampling access was provided in the side wall of the combustion chamber in order to be used by fast response analyser for cyclic variation studies.

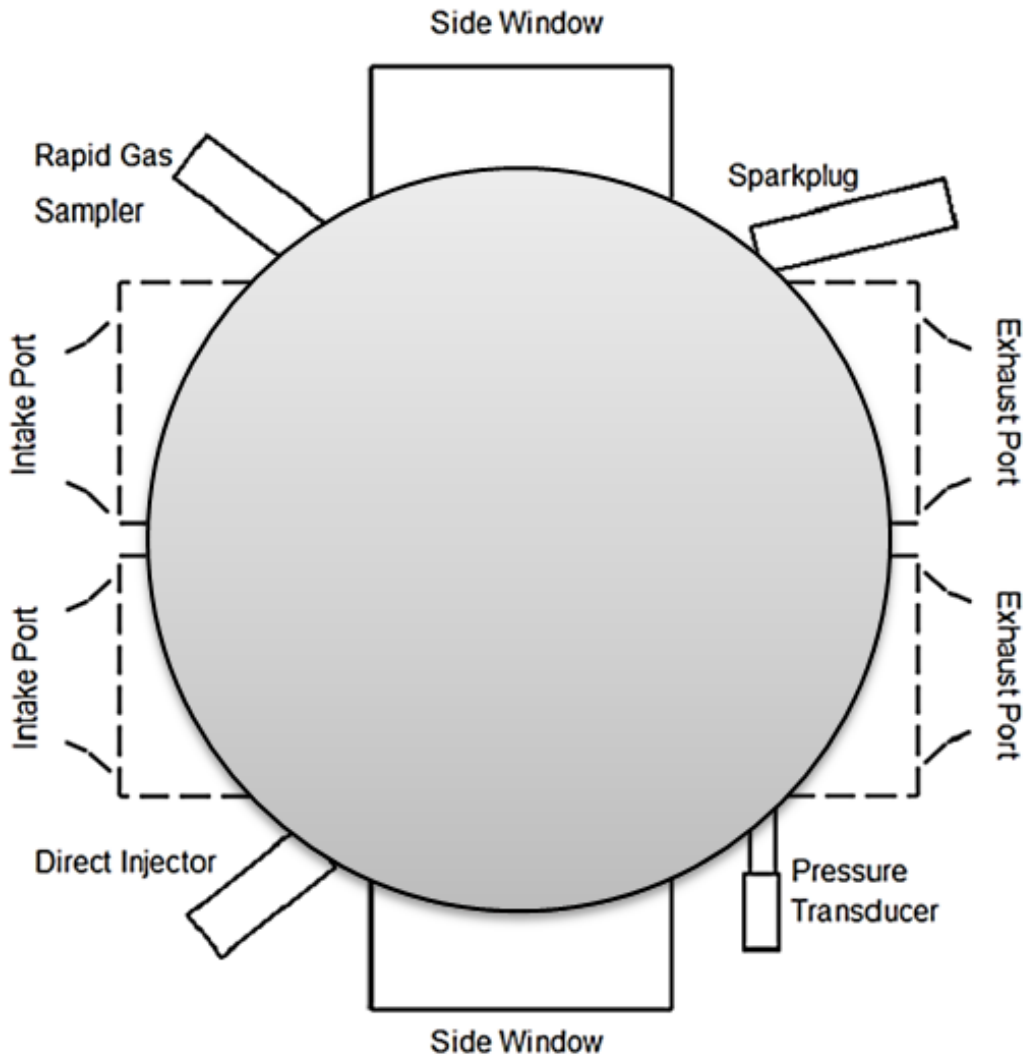

Figure 3-5: Overhead schematic of the cylinder head concept at Brunel University, where the valves moved to the sides

3.3.3 Optical Window Design: Materials and Installation

Full bore access to the combustion chamber requires a robust glass mounting at the top of the cylinder head. The engine was originally a diesel with a large bore diameter of 95mm, and area of 7088mm^2; this increased the complexity of the engine design

process. The engine was designed to withstand the harsh conditions of 150 bar in-cylinder pressure continuously.

The highest recorded knocking cycle in terms of both the maximum in-cylinder pressure and the knocking intensity was captured during fast over-fuelling testing with PRF75. This cycle is presented in Figure 3-8. The engine was running in optical mode with the side-mounted spark plug and the overhead optical window. However, the high-speed camera was not activated and the cycle was not captured optically. The cycle is presented in Figure 3-8 in terms of the in-cylinder pressure against crank angle. Following this cycle, the bottom-end, combustion chamber and optical access window were inspected in detail and it was found that no damage had been caused. This suggests that the engine was capable of surviving severe end-gas knock without damage (albeit given the unpredictable nature of knock such running was not to be deliberately invoked).

The top window was made from Corning 7890 HPFS silica and supplied by Gooch & Housego (UK). The material is a highly pure form of synthetic amorphous silicon dioxide manufactured using flame deposition technology.

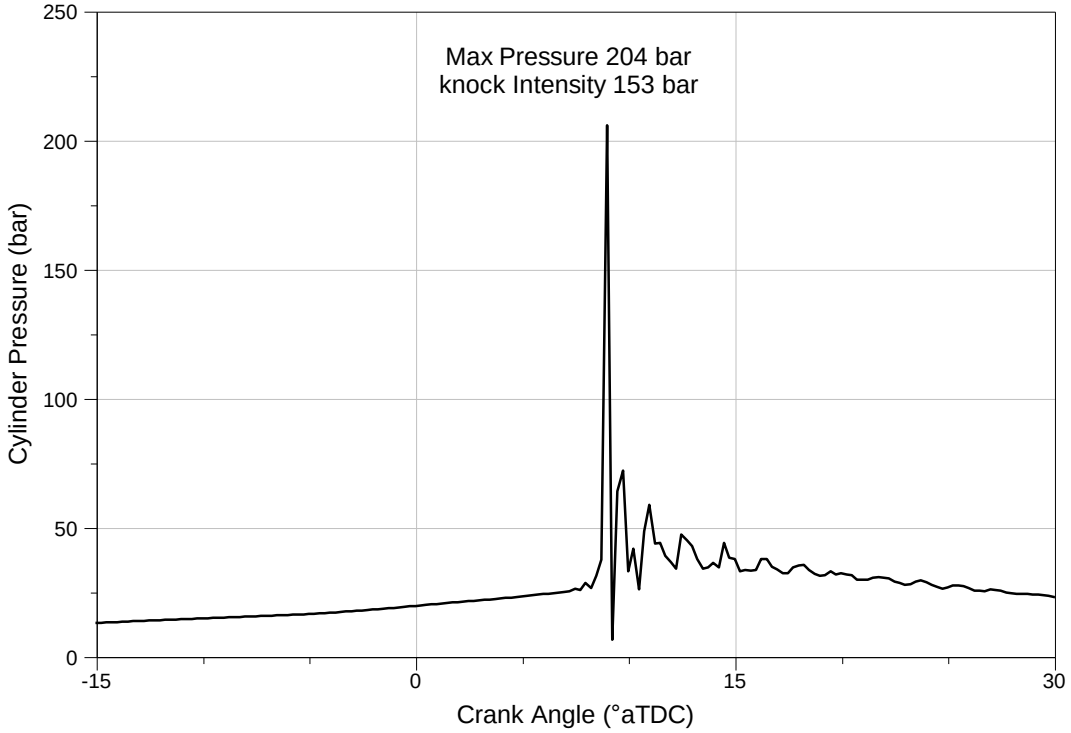

Figure 3-6: Plot of in-cylinder pressure against crank angle, showing the heaviest recorded knocking cycle in terms of both Pmax and KI.

The top window must be clamped into the cylinder head in order to resist the force and pressure exerted upon it. The clamp had to be robust enough to hold the window without yielding, and stiff enough to fix the position of the window evenly without breaking the glass. In the initial design, the window was manually lowered directly into the position, with a steel ring gasket between the glass and cylinder head that was then fixed by using eight M8 bolts.

During preliminary testing it was discovered that due to the expansion of the ring gasket, the force between them did not distribute equally and caused localised stresses. As a result, the shoulder area of the window was damaged where there was a contact between the glass and ring. Upon further investigation it was discovered that the

window was loose. This problem was solved by encasing the window in an aluminium jacket and sealing with an Elring Klinger C4400 soft cut gasket and high-temperature silicone-based sealant (with the sealant effectively providing a gas seal but periodically requiring replacement). This solution avoided metal to glass contact, and reduced the heat transfer. This design made the access to the window easier for the purpose of cleaning. This solution was highly successful, with no window failures after using the engine continuously for 4 years on heavy knock studies. Relevant photos of the damage glass and the aluminium gasket are presented in figure 3-9.

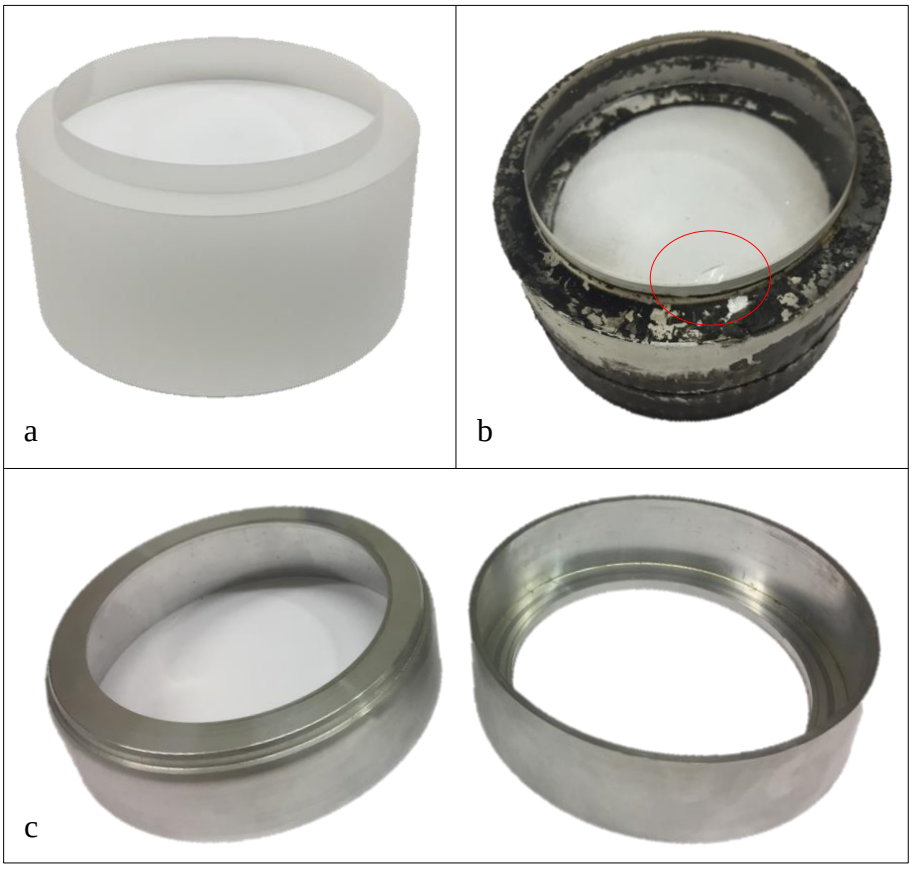

Figure 3-7: a) Original glass received from supplier, b) Damage to the window highlighted by the red circle, c) Upper and lower aluminium jackets

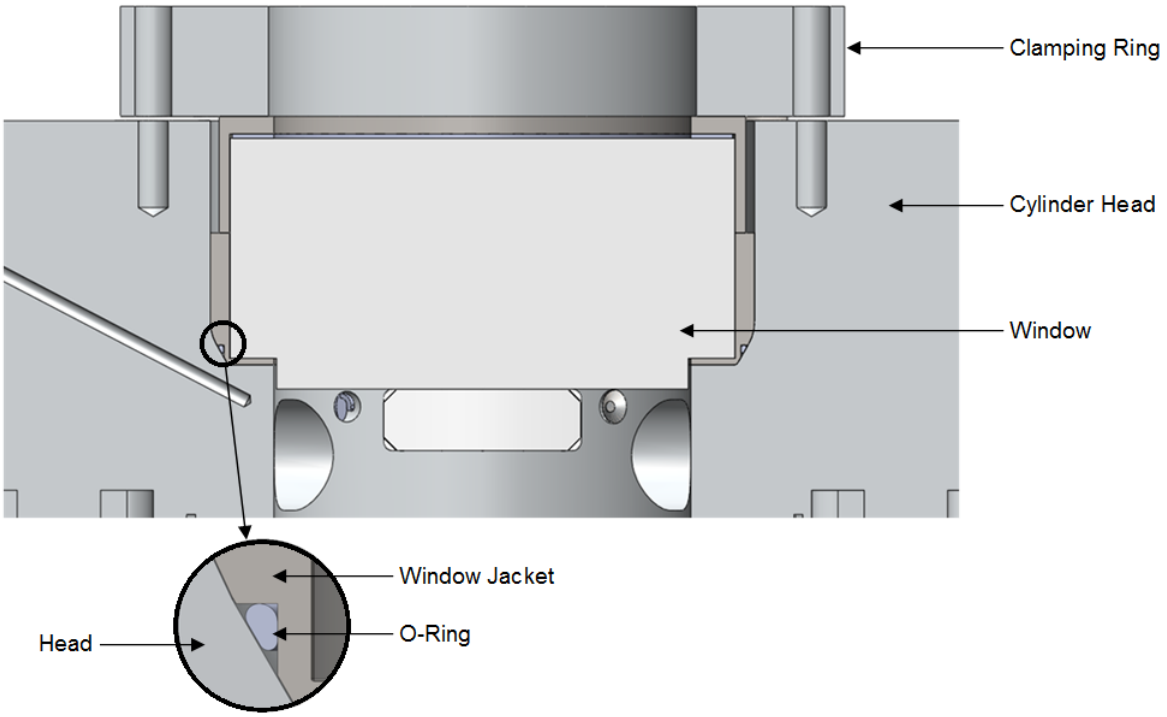

Figure 3-8: CAD image of the installed window and jacket assembly.

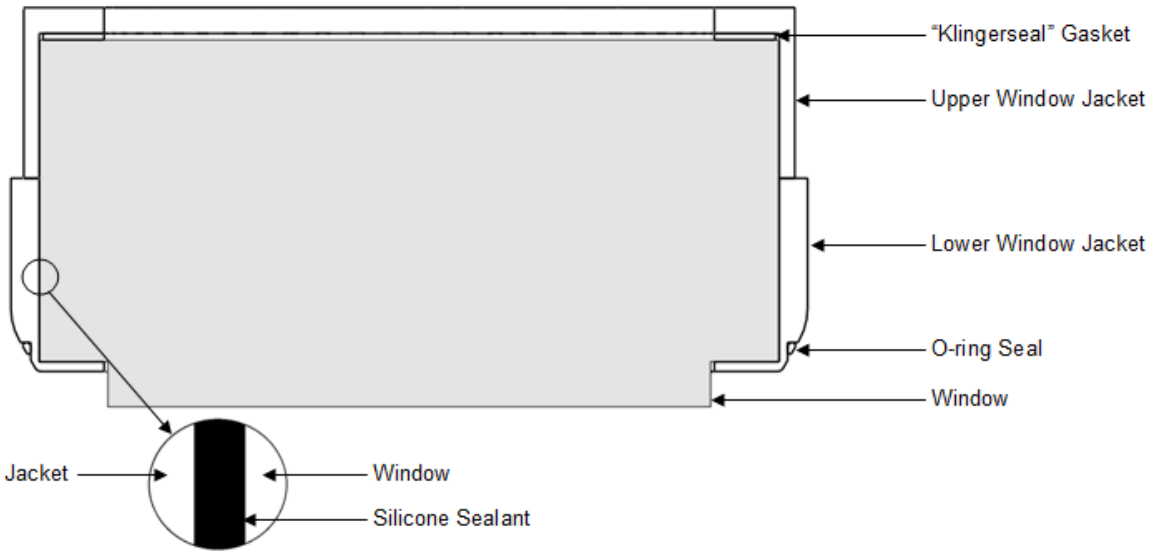

Figure 3-9: Schematic of the window and jacket assembly.

For further studies on 3D flow and flame propagation using a planar laser sheet, 2 side windows were considered in the original design. Due to the design, the thickness of the window was not sufficient to resist the high pressure of the heavy knocking cycles, so aluminium blanks of identical geometry were fabricated for the side windows.

3.3.4 Ports Design and Valvetrain

The cylinder head was mostly machined from an aluminium billet and the complex parts, such as the ports, were created by spark erosion. This process was found to be the most economical way to fabricate the new cylinder head. However, several limitations were imposed to the port runner design.

Usually the inlet runner has a curved shape for the purpose of improved discharge coefficient, but due to the manufacturing limits (the ports must be turned or milled), straight port design was selected [128]. In order to maximize the air flow and mixing effects, the ports were designed with tight angle and tapered runner.

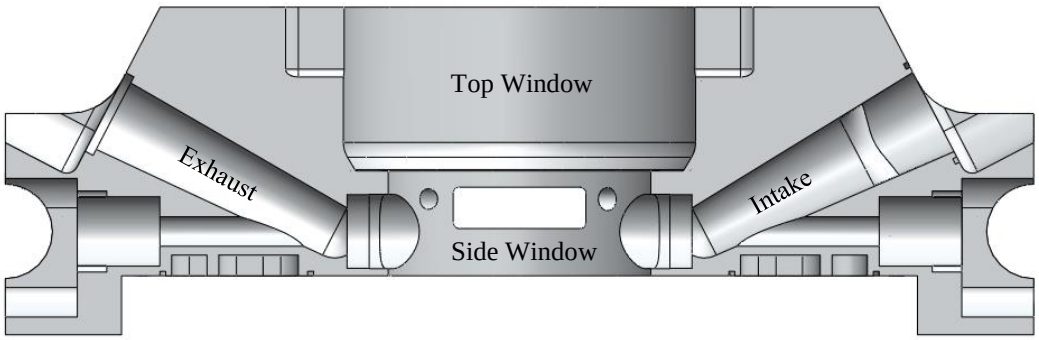

Figure 3-10: Cylinder head with cross-section through ports.

Due to the low clearance height between the upper window and the piston the diameter of the valve seat was limited. In the previous study by Dingle[123], the relationship

between choked flow engine speed, diameter of the valve head and the geometric compression ratio was found. Valves of 22mm were selected as a best option for the engine based on this analysis. For ease of maintenance, supply and reduction in running costs Fiat Multijet valves were selected for the engine since the dimensions were the same.

As the Engine was designed to have fixed valve timing, a compromise had to be made between the overlap period and the engine speeds at different loads. When the engine is idling, a retarded IVO is advantageous as it allows for a lower residual gas fraction and therefore a more complete burn in the next cycle. In higher speed operation, the same valve timing can cause excessive knock. However, if IVO was advanced at the higher speeds this would result in better intake charge flow and raise the volumetric efficiency and increase the power and torque.

For this set of experiments, the valve timing was selected to give ideal scavenging and induction at 1500RPM with a starting point of 230°CA duration (end-of-ramp to end-of-ramp) and overlap of 10°CA (symmetrical around TDC). These assumptions replicate the valve timing of a modern SI engine at lower engine speeds. From this starting position, many valve-lift profiles were trialled (checked for clash and estimated choked engine speeds). To estimate the choked mass-flow rate of air through the ports during each crank revolution, Dingle [123] studied the equations published by Heywood [13] for estimating air flow across a valve at a specific lift, and used them as the basis for a spreadsheet that modelled engine breathing. The spreadsheet performed the calculations for each crank angle when given a valve lift profile, and estimated the engine speed at which the valves would be fully choked. Then Valve lift profiles were created using a

spreadsheet provided by MAHLE Powertrain to produce a precise cam profile with acceptable acceleration and forces.

After preliminary studies, the valve timing and duration was later altered with a final valve lift duration retained at 230° CA (end-of-ramp to end-of-ramp), with a maximum lift of 5mm and the nominal overlap period of 20°CA symmetrical about TDC.

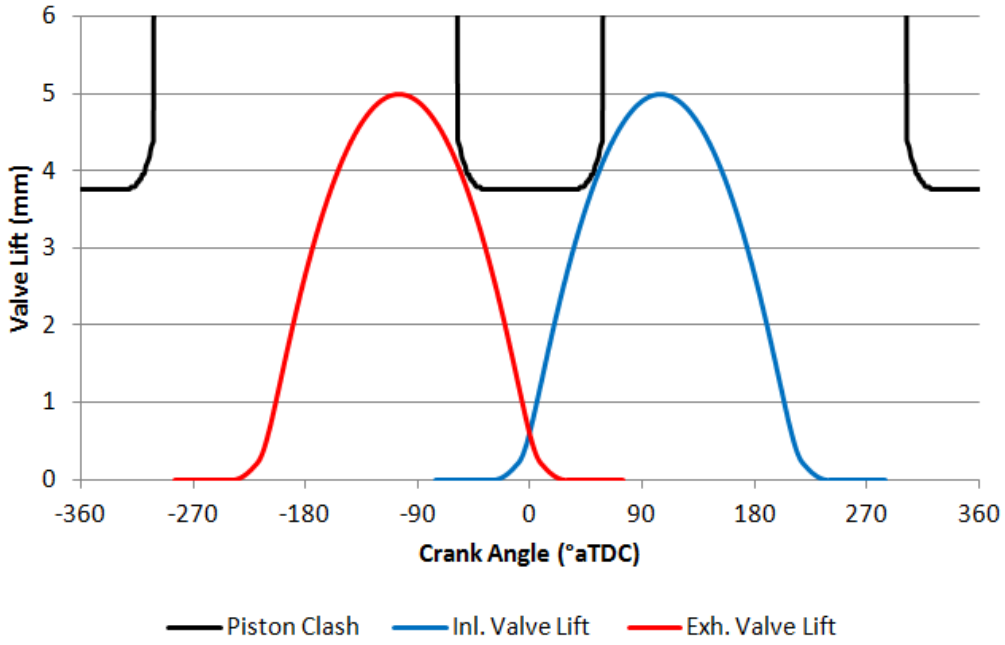

Figure 3-11: Selected valve timing

As the top window was installed in the combustion chamber roof, this forced the location of the entire valvetrain system to the sides. As a result the two valve events (intake and exhaust) were split into two separate camshafts placed diametrically opposed. A 30mm wide simple pulley and toothed belt system linked the two cylinder head camshafts to the crankshaft using 28-tooth taper lock pulleys fitted to the relevant shafts, which could be removed to allow for valve timing adjustment.

Two camshafts were supplied by Piper Cams, a specialist camshaft manufacturer. They were turned and ground from EN40B steel and then hardened in Nitride. Finally the cam profile was ground as the last manufacturing step. The camshafts were held in the cylinder head by a pair of taper-roller bearings (SKF NU2203ECP) per camshaft.

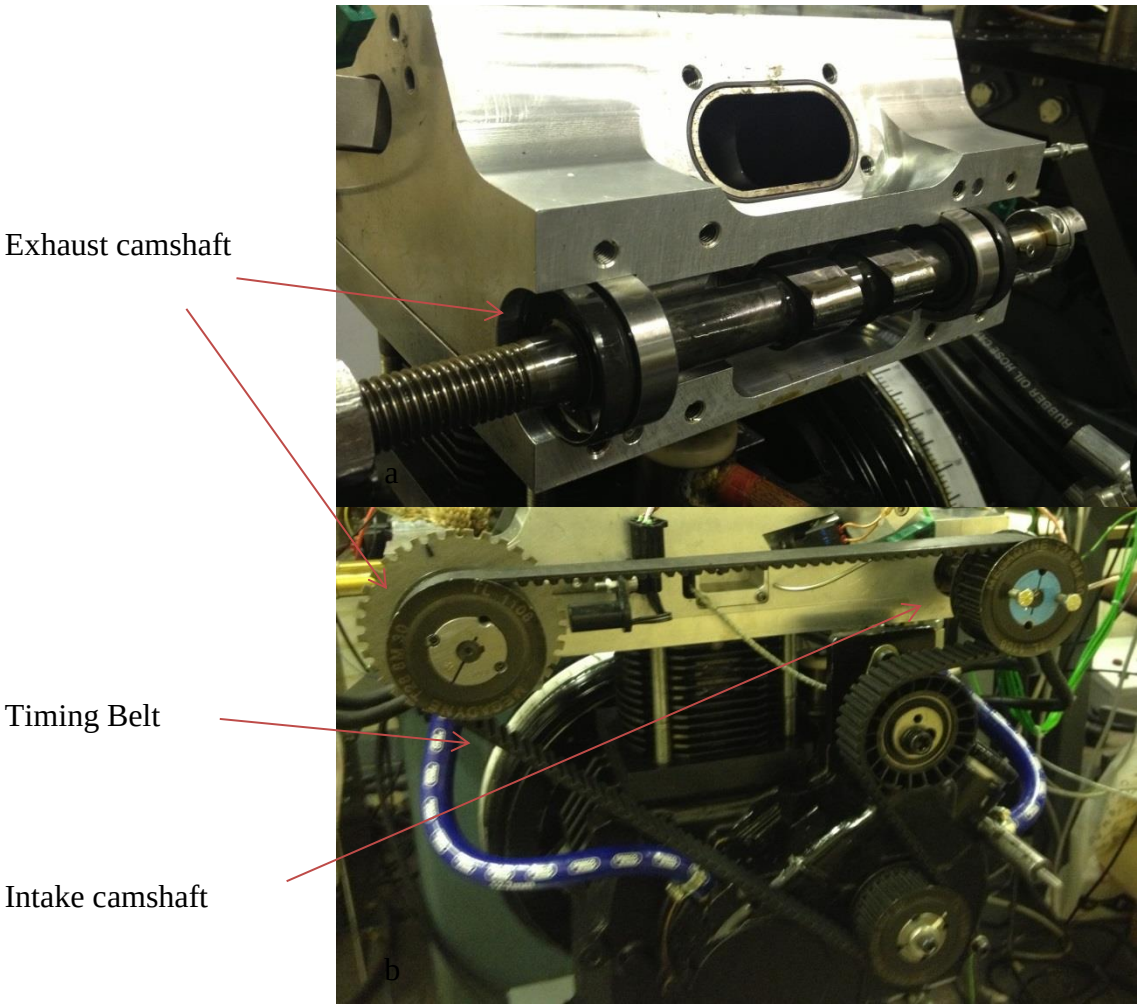

Figure 3-12: An image of the engine showing the belt and pulley arrangement with the intake cam (a), the belt is driven off a pulley connected to the crankshaft via a toothed gear (b).

3.3.5 Throttle

The throttle was a 40mm fly-by-wire Bosch EGAS, commonly found in the 2010 VW Golf and installed before the intake plenum. The throttle was designed to control the mass flow rate of air and the engine load. The throttle was a butterfly type, and the throttle angle was operated by a Pulse width Modulation (PWM) servo motor that was controlled by the Electronic Control Unit (ECU). It was subsequently found that the throttle diameter was too large, with too little sensitivity in throttle control as initially it was designed for a boosted IC engine of higher capacity . Consequently a mechanically actuated AT Power throttle of 24mm diameter was installed in its place.

Downstream of the throttle, the airflow entered an intake plenum with a capacity of 50 litres. This was designed to allow the intake air to collect, and to reduce any pressure waves that could occur; particularly at lower engine speeds where excessive time between breathing events in a single cylinder engine can cause difficulties in maintaining a constant flow rate and pressure. The pressure of the gas was logged from the plenum. Also, the temperature of the inlet air was controlled using a closed loop k-type thermocouple attached to the heater with PID control as described below

3.3.6 Inlet Air Heater

In order to control and raise the inlet air temperature, a 2kW Secomac 571/4 air heater was fitted after plenum, immediately upstream of the port fuel injector. The inlet air temperature was controlled by a closed loop PID temperature controller and k-type thermocouple attached to the heater and inlet port. The heater was able to heat the air to a desired maximum constant temperature of 70±2 °C.

3.3.7 Fuel Delivery

The unique design of the engine made it possible to use both direct injector (DI) and port fuel injector (PFI) separately or in combination. The PFI was mainly used to inject gasoline or 75 RON primary reference fuel during heavy knock tests, while DI was used to inject other fuels (or engine lubricant for Super Knock studies) directly into the combustion chamber.

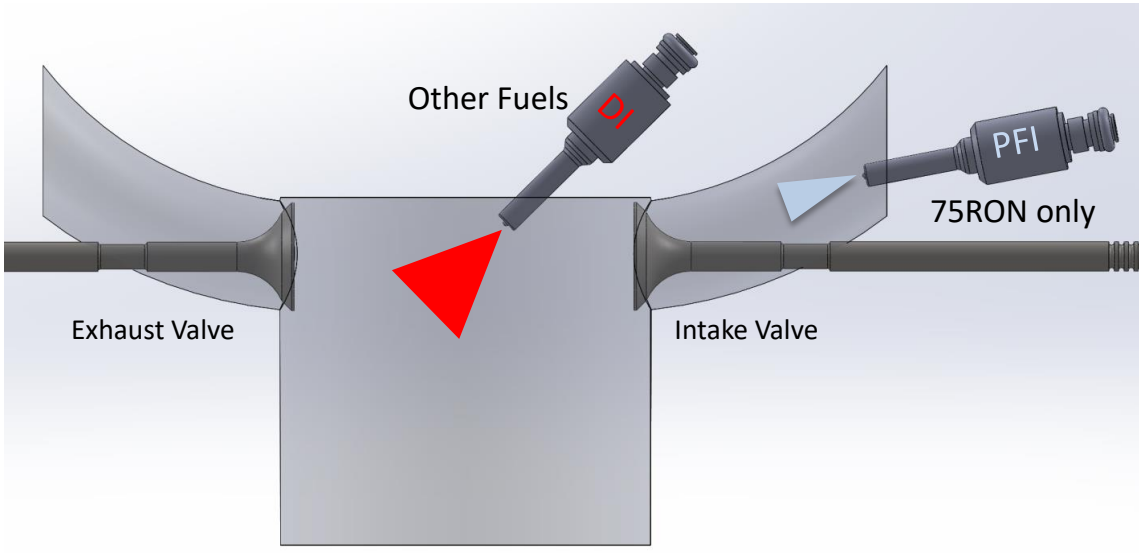

Figure 3-13: Schematic of the fuel delivery system.

The fuel for the tests was not taken from the lab's common supply, but was stored in a 5 litre tank located near the engine. It was decided to adopt Primary Reference Fuels (PRF), which eliminated variations in fuel content and octane rating when using pump gasoline. The iso-octane and n-heptane were obtained from a chemical supplier, with water content guaranteed to fall below 0.02%. Iso-octane was used as the replacement main constituent in creating a "75RON" fuel blend (75% iso-octane+25% n-heptane). W5E10 (0.5% water +9.5% Ethanol +90% iso-Octane) and pure Ethanol were also

evaluated as additional fuels, but only injected as supplementary to the base PRF blend via the direct injector.

3.3.7.1 Port Fuel Injector

The fuel pump was used to raise the pressure of the fuel rail to 3bar gauge. Then fuel pressure was regulated using a mechanical regulator, which returned excess fuel back to the tank. A fuel filter was fitted just before the pump to remove most of particulates from the fuel before it was injected in to the engine cylinder. Due to the low speed and displacement of the single cylinder engine, the 5 litre fuel reservoir was sufficient to store the required fuel for at least one day of engine testing.

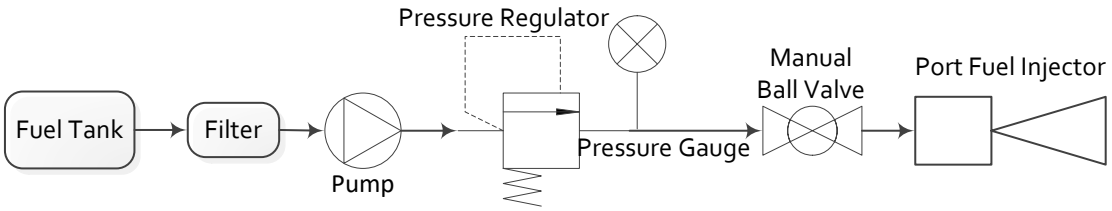

Figure 3-14: Schematic of the port fuel injector delivery system.

A port fuel injector was incorporated into the inlet tract, and the fuel spray was targeted at the back of the inlet valves to aid evaporation of the fuel and to improve the homogeneity of the charge. The PFI system included a Bosch EV6 type fuel injector with twin sprays (one for each inlet valve) and had a maximum mass flow rate of 349g/min at 380kPa gauge fuel rail pressure. Assuming an optimistic volumetric efficiency of 100% at full load and maximum engine speed (2000rpm), the engine was estimated to require a peak fuel mass flow rate of 70g/min to maintain stoichiometry.

3.3.7.2 Direct Injector

A direct injector was fitted to the side of combustion chamber in order to be able to run the engine on DI mode as well. As previously mentioned, it was possible to run the engine using port and direct fuel injectors at the same time.

To this end, a customised gasoline direct injector was selected to provide controlled oil and fuel injection. The fuel injector from a 2006 VW Golf 1.4 TSI (125kW) was selected due to its favourable packaging, both in terms of the injector body and multi-hole spray pattern.

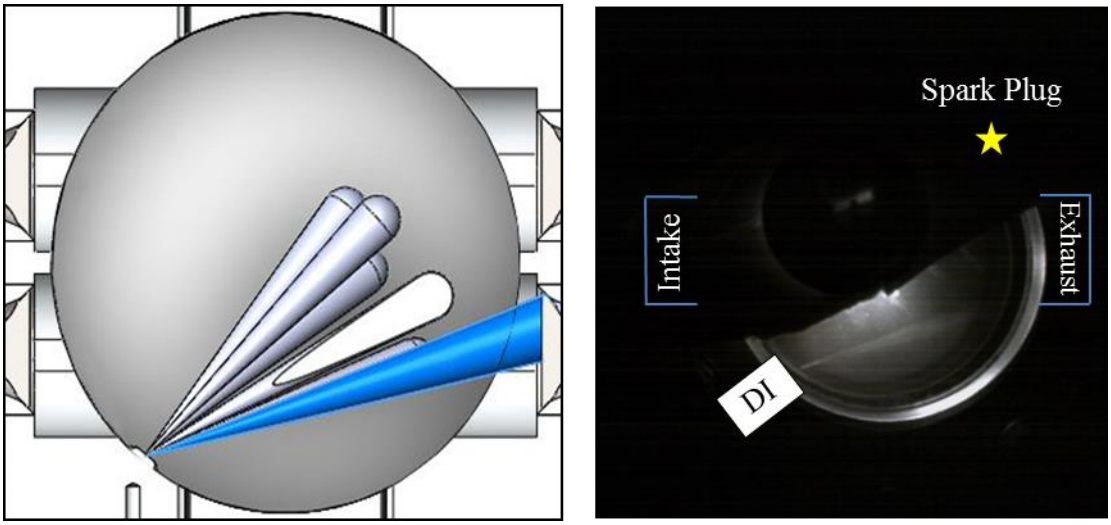

Figure 3-15: CAD images showing the spray pattern of the direct injector (blue for single hole injector).

An auxiliary adapted fuel supply system comprised of a PowerStar4 double-ended air driven pump with an amplification ratio of 64:1 was used for the DI system. The regulated air inlet pressure was ~5.5bar; this pump was able to generate rail pressures of up to ~340bar. Pressure variation in the fuel rail was recorded to be ±4bar at 200bar fuel pressure, with 0.5ms injection duration using iso-octane.

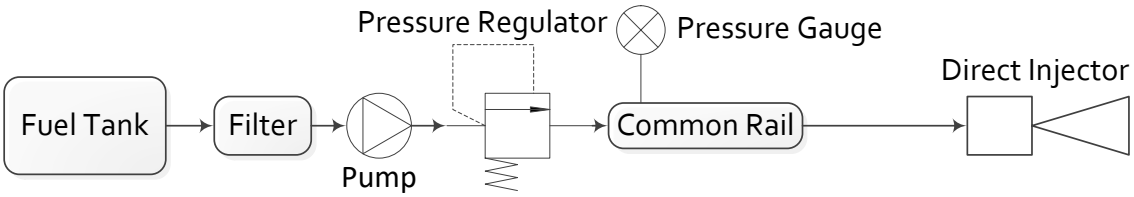

Figure 3-16: Schematic of the direct injector delivery system for fuel.

The location of the direct injector, close to the combustion chamber, meant that heat from the cylinder head would be transferred to the injector and therefore heat up the lubricant. Similarly, the rail was located on the side of the cylinder head, providing a significant amount of heat transfer to the lubricant inside the rail itself. As well as the heat conducted from the head, it was possible to further increase the lubricant temperature in the rail via a cartridge heater. The temperature control unit provided closed loop control of the lubricant temperature using an analogue voltage controller and a k-type thermocouple. The lubricant temperature within the rail was logged at all times, regardless as to whether or not the cartridge was in operation.

The DI was controlled using a MBE 959 ECU coupled to an MBE 9A1 amplifier (external injector driver), with full control over injection timing and pulse width. A current clamp was additionally fitted around the high voltage line to allow precise measurement of actual injection timing. . The minimum pulse width possible under this configuration was 1.0ms. In addition, a frequency divider was located between the ECU output and the MBE 9A1 voltage amplifier. The described circuit was based on a CMOS 4024 chip, and enable the DI to be skip-fired independently from the fuel injection and spark plug at rates of 2, 4, 8 or 16. The trigger signal from the divider was

recorded against CA through a data acquisition system to ensure accurate injection timing and durations were acquired.

3.4 Engine Control and Instrumentation

3.4.1 Engine Dynamometer

The engine was mounted on to an eddy-current dynamometer with a max power absorption of 10kW using a flexible coupling. The coupling is used to protect the dynamometer from peak engine torques. Engine speed and torque measurements attained from the dynamometer were logged using DAQ software and shown on the MBE ECU software.

3.4.1.1 Engine Calibration and Control

An MBE 959 ECU with custom firmware was used for engine control and calibration. This particular ECU relies on crank speed and cam position signals from a variable reluctance sensor (taken from a 2004 Ford Focus ST170), and a Hall Effect sensor (1GT101DC) respectively. The engine was fitted with two trigger discs, each with a 36-1 tooth pattern; one fitted to the exhaust camshaft and one to the crankshaft. The ECU uses the crankshaft trigger disc to measure engine speed and TDC timing, and the camshaft disc is used to synchronise the ECU with the engine phase.

3.4.1.2 Crank Position

Crank position was recorded in crank angle degrees using an incremental shaft encoder (EB58-S00040-2880). Due to the high frequency pressure oscillations during knocking combustion, a high angular resolution was required for accurately recording the pressure history of knocking combustion cycles. Although a high resolution of data sampling was wanted, this was limited by the sampling rates of available data acquisition systems. This trade off resulted in the selection of an incremental shaft encoder capable of 2880 samples per revolution. Due to difficulties in accessing and fitting a shaft encoder directly to the crankshaft, the shaft encoder was fitted to the inlet camshaft. With the camshaft rotating at half of the crankshaft rotational speed, the angular resolution was 4 samples per °CA.

3.4.1.3 Intake Conditions

The absolute pressure in the intake was recorded using a Gems 1200 series piezo resistive pressure transducer. This pressure transducer was used to peg the data from the dynamic pressure transducer in the cylinder to an absolute value at BDC prior to compression. It is generally considered best practice to fit an absolute pressure transducer to the cylinder liner that is exposed near BDC. However, [123] noted that it was possible that a drilling in the cylinder liner would inhibit the flow oil around the piston rings. Intake temperatures were measured using a k-type thermocouple fitted downstream of the inlet heater; this thermocouple was susceptible to electromagnetic interference due to the low voltage of the output signal. Where possible the cabling was located away from possible sources of noise.

3.4.1.4 In-Cylinder Conditions

The dynamic in-cylinder pressure was measured by an AVL piezoelectric pressure transducer (GH14DK). To reduce the minimum clearance height of the combustion chamber a particularly small pressure transducer was required. This requirement precluded the use of a water-cooled transducer and a pressure transducer with a 5mm thread diameter was selected. With a non-water-cooled transducer, thermal shock can affect the accuracy of the absolute pressure readings with the expansion stroke particularly affected [32]. Thermal shock only has a small effect on the absolute pressure measurement (< ±0.4bar in the model selected), but this error is amplified when deriving measurements of Mean Effective Pressure (MEP) and can result in errors in Indicated Mean Effective Pressure (IMEP) in excess of 10% [129]. However since increasing the compression ratio was a higher priority than accurate measurements of MEP, a non-water-cooled pressure transducer was selected.

3.4.2 Exhaust Conditions

A k-type thermocouple mounted in the exhaust port was used to measure exhaust gas temperatures. A Bosch LSU 4.2 Universal Exhaust Gas Oxygen sensor (UEGO) was located in the exhaust pipe to find the air-fuel ratio; the UEGO was connected to an ETAS LA4 lambda meter. The lambda meter used user input values of hydrogen to carbon ratio, stoichiometric air-fuel ratio, oxygen content and water content; Table 3-2 indicates the values used for each setting used for different fuels in this study. The water content is generally for use with external EGR systems and was assumed to be zero. However, high levels of internal EGR can also affect the overall water content of the charge; this represents a probable source of error in the lambda measurement.

Furthermore, it is probable that unburned lubricant was present in the exhaust gases. This has been analytically shown to produce significant errors in the measurement of lambda [130].

Table 3-2: Table of fuel properties for the lambda meter for the three fuels being used.

Property	Iso-Octane	Ethanol	Gasoline
Density at 1 bar and21 °C (kg/litre)	0.69	0.79	0.74
Lower Heating Value (Mj/kg)	44.3	26.8	44
Stoichiometric AFR	15.1	9	14.7
RON	100	109	97
Latent Heat of Vaporization (kj/kg)	308	840	305
Oxygen Content by Weight (%)	0	34.8	0
Volumetric Energy Content (Mj/litre)	30.6	21.2	31.6

3.4.3 Daily Checks and Ambient Conditions

A calibrated barometer and k-type thermocouple were used to record ambient pressure and temperature respectively in the lab each day. Figure 3-24 is an example plot of these daily pressure readings. In-cylinder motoring pressure was checked prior to each test in order to ensure there is no gas leakage through the optical accesses.

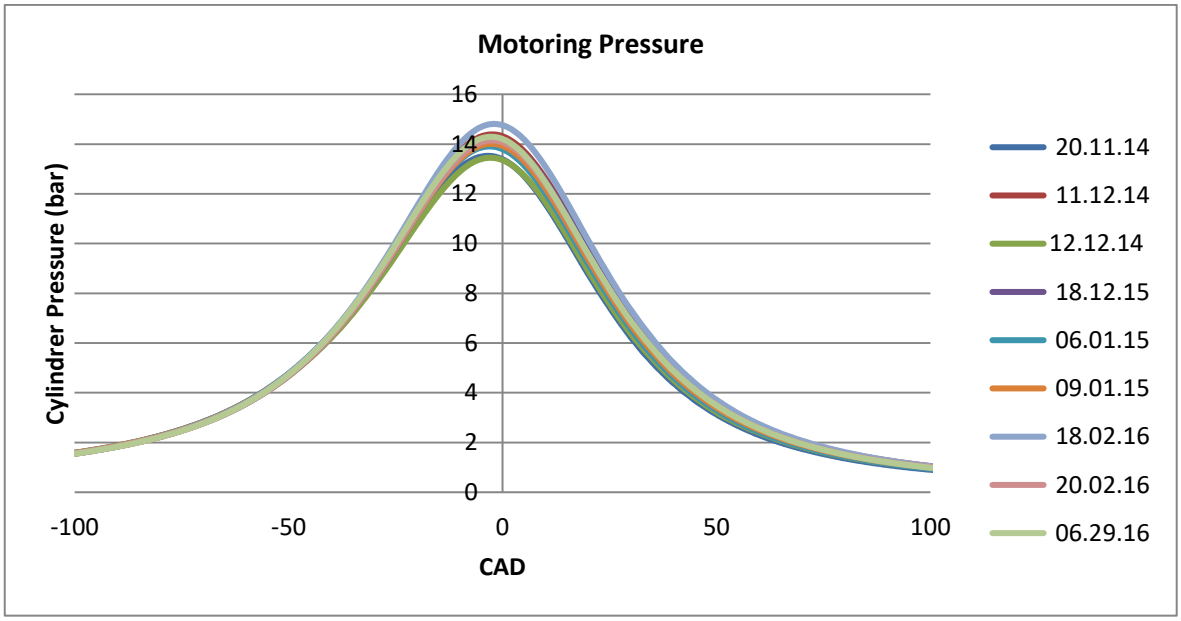

Figure 3-17: Daily motoring pressure check.

3.4.4 Engine Metal Temperature Measurement

Four different locations were used to measure the metal temperature within the engine using k-type thermocouples. As shown in Figure 3-18 and , these were: the liner, the exhaust bridge, the DI tip and the sampling valve tip. Such measurements were considered important for attempting to repeat knocking conditions.

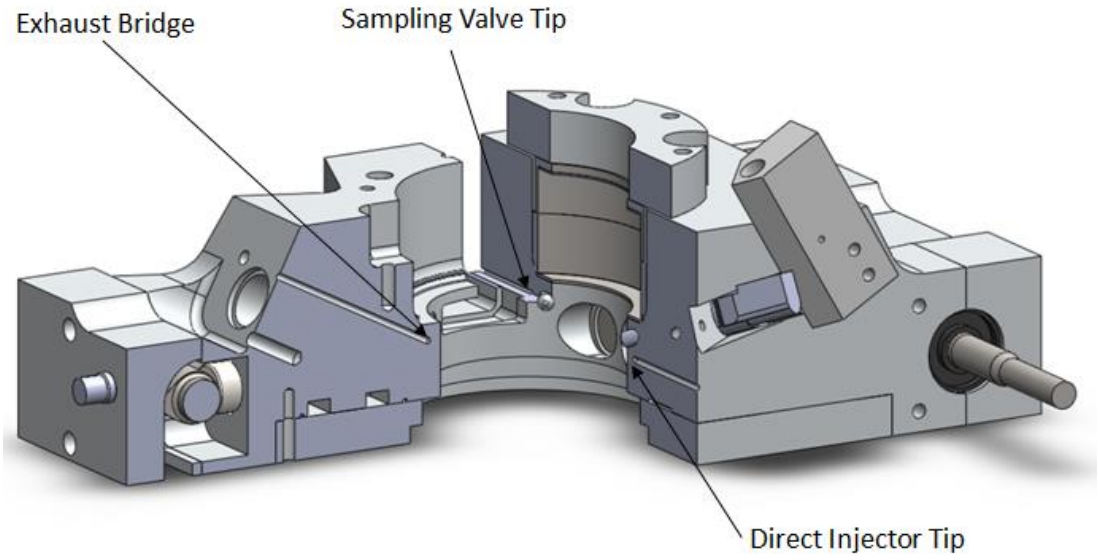

Figure 3-18: Section view of the cylinder head showing thermocouple locations.

Table 3-3: Table showing relative locations of cylinder head thermocouples.

Thermocouple	Distance from Cylinder Wall	Distance from Component Tip
Sampling Valve Tip	17.6mm	3.8mm
Exhaust Valve Bridge	5.3mm	n/a
Direct Injector Tip	5.6mm	4.9mm

3.4.5 Data Logging

Data was logged by a combination of two National Instruments data acquisition cards:

- USB-6353, with a high sample rate, 32 analogue channels and a maximum sample rate of 2MS/s, measurements were sampled at every increment of the digital shaft encoder

- USB-6210, with a low sample rate, sampled at approximately 3Hz; used to log temperature and lambda as the sensors didn't have a response time to warrant more frequent logging

Both acquisition cards were controlled over USB by an in-house Matlab program named "YanTech", which was developed by Dr. Yan Zhang and described by Coates [131]. The thermodynamic analysis of the pressure signal is described in the next chapter.

3.5 Combustion Imaging Instrumentation

Whilst Schlieren imaging is possible due to the design of the engine, the images in this study were captured using the natural light emitted by the combustion events themselves, this was down to the relative ease of setup when using natural light. Natural light imaging also has a number of advantages over Schlieren imaging:

- Natural light imaging is not affected by piston rock [98]
- Colour images can be produced if not using a light intensifier

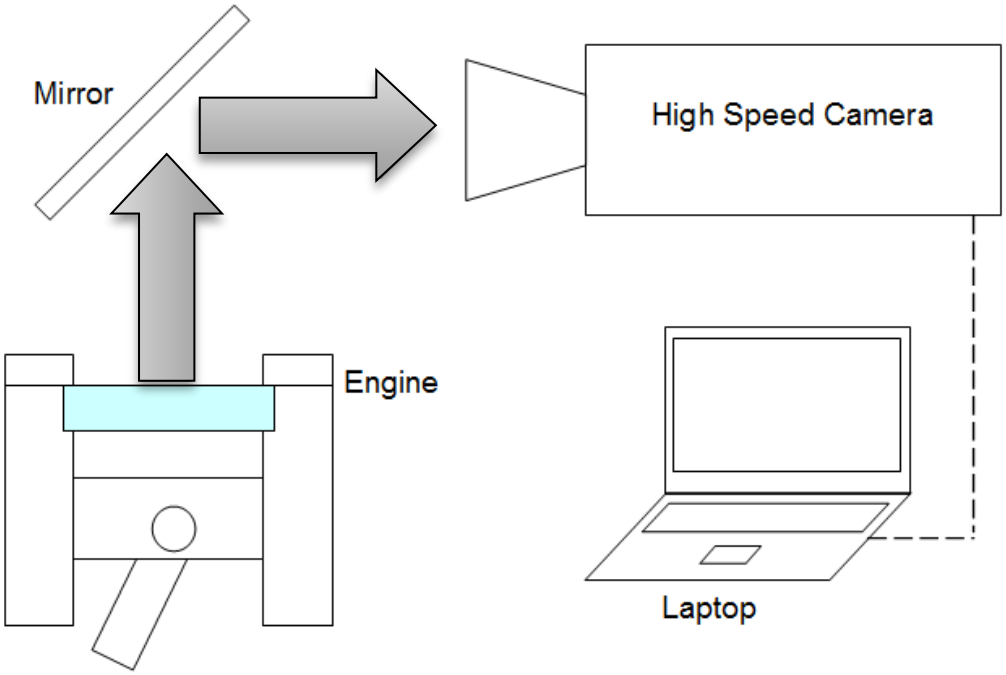

Figure 3-19: Schematic of combustion imaging setup.

The DRS Technologies ILS light intensifier operates by amplifying incoming light before it is enters the Memrecam fx6000 camera. Light enters the front of the intensifier via a standard camera lens, which focuses the light onto a photocathode. As packets of light, photons, contact the photocathode they are converted to electrons that are then accelerated by an electrical field before multiplying within micro-channels. Finally, the electrons impact a phosphor screen that releases photons to the high-speed camera; since the phosphor screen emits a green monochrome light, the colour is lost as the light is intensified. The light intensifier was used to boost low intensity light during engine characterisation tests, but not used when imaging lubricant induced pre-ignition.

The Memrecam fx6000 had a Complementary Metal Oxide Semiconductor (CMOS) sensor and a maximum resolution of 512x512 pixels, and a maximum frame rate of 240,000 fps. Since the frame rate, exposure and resolution were linked, images were

taken at either 8,000 or 6,000 fps contingent on the engine speed and imaging setup, see table 3.5 for details.

The camera had an on-board memory of 4GB to capture approximately 16,000 frames, therefore combustion cycles could be imaged in batches of approximately 50 cycles at the engine speeds and imaging frame rates used for testing. This creates an inconsistency between the number of cycles that were recorded thermodynamically, and the number recorded optically; for every 15 cycles that were recorded optically, there were 100 cycles recorded thermodynamically.

Table 3-4: Outlining of interdependence between image resolution, frame rate and maximum exposure time.

Frame Rate (fps)	Resolution (pixels)	Exposure Time (µs)
240,000	512x8	4
120,000	512x16	8
60,000	512x36	17
10,000	512x248	100
8,000	512x308	125
6,000	512x384	167
3,000	512x512	333

To synchronise the recorded images with thermodynamic measurements, an LED was fitted close to the upper optical window. The LED was linked to the encoder and programmed to flash at TDC firing. From the engine speed and imaging frame rate it was possible to calculate the CA between each frame. For an engine speed of 1200 rpm, and frame speed of 6000 fps, the crank angle between 2 frames was 1.2 CAD.

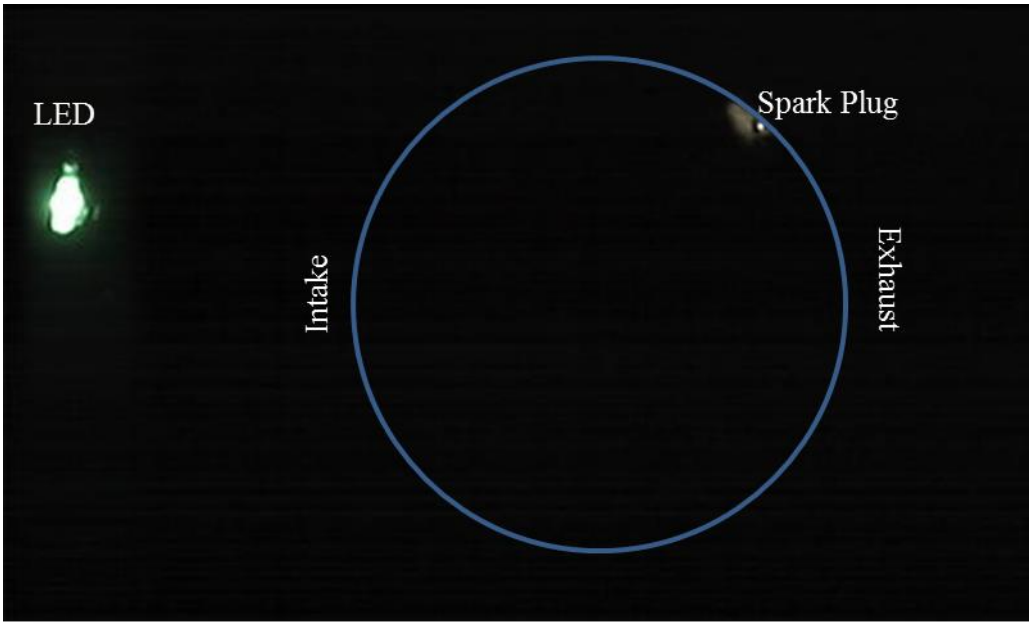

Figure 3-20: LED lamp blinks and spark plug ignition at TDC.

4 DATA ANALYSIS AND TECHNIQUES

4.1 Introduction

This chapter is divided into two main sections. The first section discusses the techniques used to analyse the thermodynamic data obtained from the in-cylinder pressure transducer. Within this section an appropriate sample size is established, followed by explanations of how critical information has been calculated such as indicated mean effective pressure, mass fraction burned and knock intensity. The data filtering techniques used have also been discussed. The second section outlines the techniques used to analyse the optical data collected during this study. This includes determination of the mean flame radius, the apparent flame speed and image presentation techniques.

4.2 Thermodynamic Analysis and Techniques

4.2.1 Sample Size

When the data sample is small, average values are strongly influenced by cyclic variation. The major cause of these cyclic variations is usually phenomena including differences in the charge air motion, inhomogeneity in the charge and differences in the exact fuelling amount and ignition timing and energy [6,13,132]. After conducting a study on the impact of sample sizes and engine cyclic variation on the preciseness of in-cylinder measurements of pressure and derived parameters, Lancaster et al. [133] suggested that the sample size should be 300 cycles for an SI engine, in order to

acceptable mitigate the risk of measurement error. In a similar study, Brunt and Emtage [129] concluded that the minimum number of cycles can be as low as 150 cycles. However, they still accept that 300 cycles would still be suitable for SI engine studies as has become the norm in the powertrain industry.

The equation below, where the standard deviation of the data set is σ and the sample size is represented by *n*, can be used to compute the 99 percent confidence interval for those measurements that are averaged across a number of cycles.

$$99\%\ Confidence\ Interval = \frac{2.5\sigma}{\sqrt{n}}$$

Equation 4-1

Shown in Figure 4-1 is a representation of the 99 percent confidence measurement of IMEP net calculation for data sets up to 600 cycles. The data displayed in Figure 4-1 shows that at 300 cycles, the 99 percent confidence interval was extremely low. In this case, the 99 percent confidence interval is 1.1 percent. Owing to the logarithmic character of the data, when the size of the data set was doubled, the confidence interval was only reduced by 0.3 percent. Hence, a sample size of at least 300 cycles was used to gather all thermodynamic data. It is also observed that a sample size of only 60 cycles was required to reduce the confidence interval to less than 2.5 percent. Hence, taking into account the fact that collecting optical data requires a lot of time and resources, this was considered the smallest suitable sample size for optical data sets. When combustion is studied optically, it is common that the sample size can be reduced to 50 cycles [134].

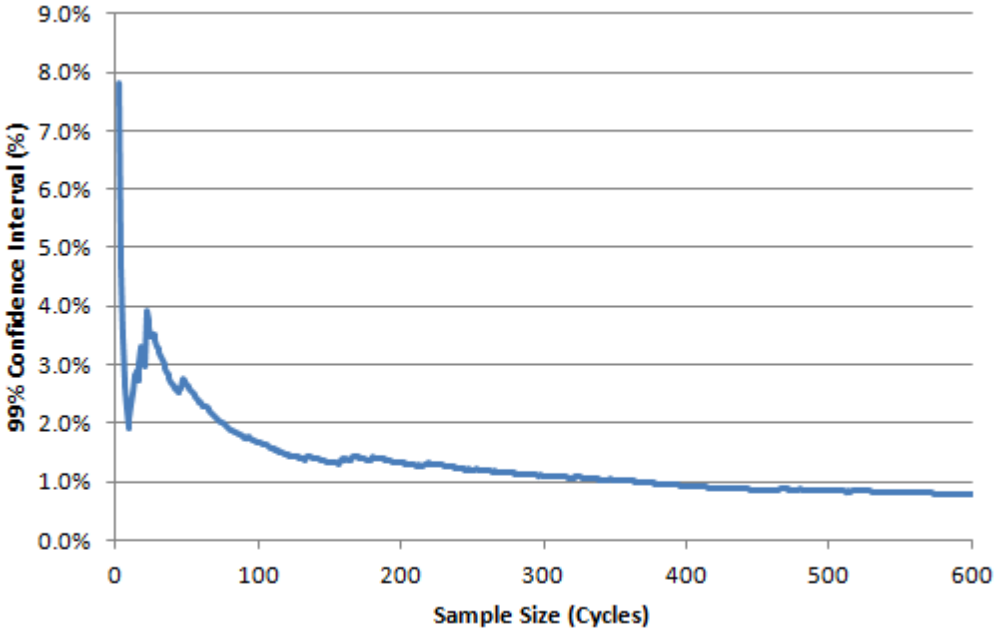

Figure 4-1: The 99% confidence interval for the measurement of average IMEPnet against sample size.

4.2.2 IMEP Calculation

During combustion, the IMEP net was calculated using the following formula [13], where *p* represents the in-cylinder pressure, V is the cylinder volume and *D*, the engine displacement.

$$\text{IMEPnet} = \frac{\oint p\, dV}{D}$$

Equation 4-2

4.2.3 Indices of Polytropic Compression and Expansion

During compression and expansion, the polytropic indices (n) were computed using a formula, where the terms are defined graphically in Figure 4-2 (for compression) and Figure 4-3 (for expansion).

$$n = \frac{\log(P_2/P_1)}{\log(V_2/V_1)}$$

Equation 4-3

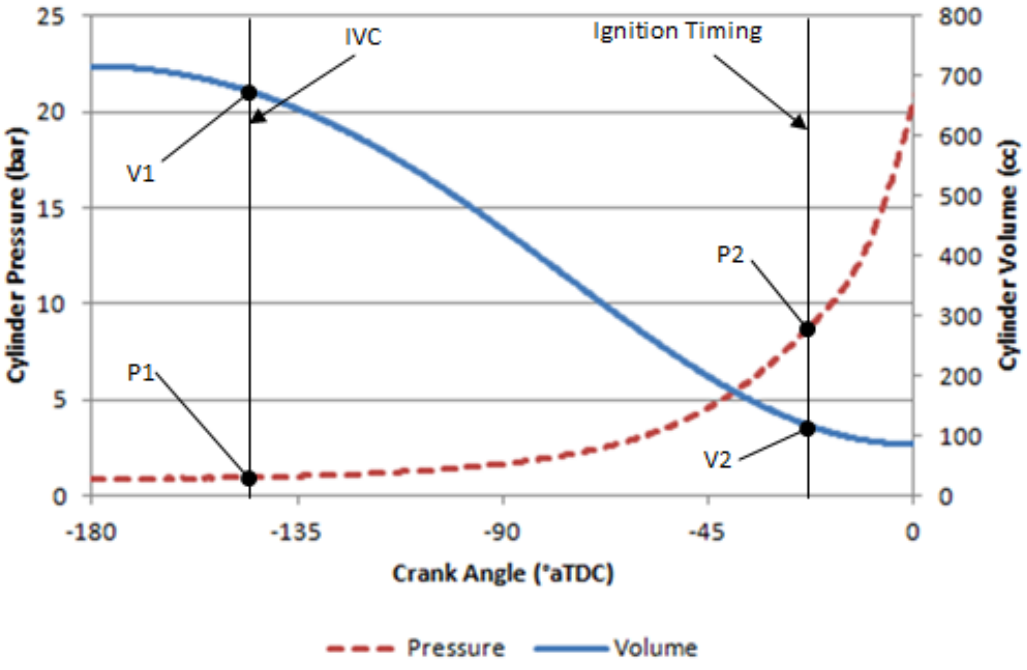

Figure 4-2: In-cylinder pressure and volume during the compression stroke

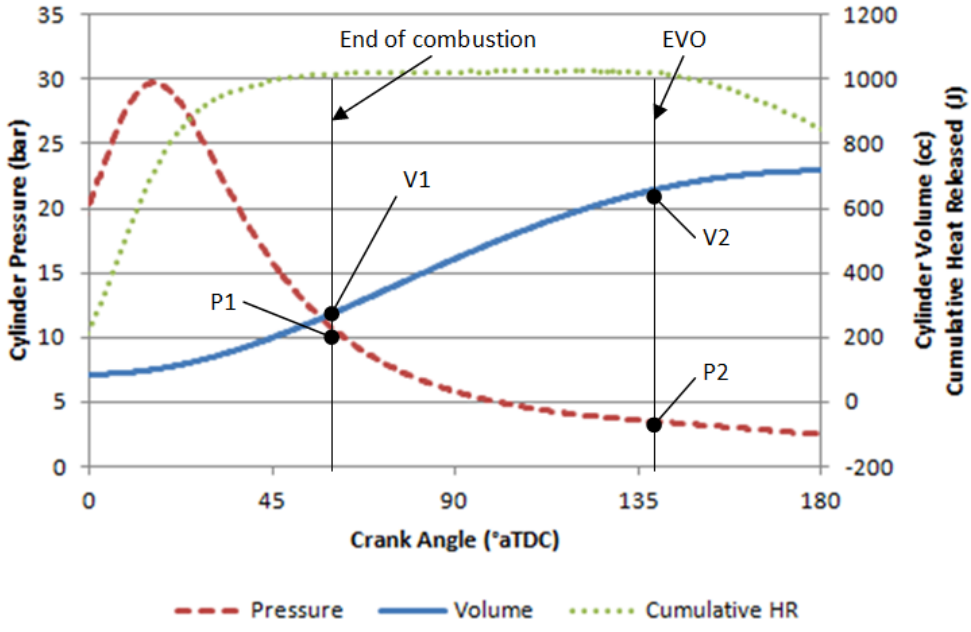

Figure 4-3: In-cylinder pressure, cylinder volume and cumulative heat released in the expansion stroke

During both expansion and compression, the polytropic condition needs the system to be closed with no energy or mass transfer. Hence, calculating polytropic indices should only be taken during a period when all valves are closed, either after or before combustion. In this case, the calculation of the index of polytropic compression was done at a point just after Intake Valve Closure (IVC) and the other reference point was taken ahead of the ignition point (this was confirmed by the examination of the pressure data). Brunt and Pond [135] have proven that when the intake valve closes, it can bounce and cause noise in the in-cylinder pressure signal leading to an error when measuring the index of polytropic expansion. Hence the region of noise was recognised and avoided. To reduce the effect of errors caused by low-level noise throughout the whole pressure signal, the measurement of P1 and P2 was averaged over 11 successive samples [135]. The index of polytropic expansion was calculated at a point once the combustion ended but before the Exhaust Valve Opened (EVO). It was easy to identify these points from the graph of cumulative heat release against crank angle as is illustrated in Figure 4-3.

4.2.4 Heat Release Analysis

4.2.4.1 Rate of Heat Release Calculation

The analysis of heat release was based on a comparison of the rate forecasted by the polytropic expansion and compression and the rate of change in the combustion chamber volume and pressure of a fired cycle. The rate of change in pressure and volume at each measurement interval was used to find the Rate of Heat Release (ROHR) for each cycle. This is illustrated in equation 4.4 [6].

$$\frac{\mathrm{dQ_n}}{\mathrm{d\theta}} = \frac{\gamma}{\gamma - 1} p \frac{dV}{d\theta} + \frac{1}{\gamma - 1} V \frac{dp}{d\theta}$$

Equation 4-4

The analysis using this equation is based on comparing the rate of change of pressure in the chamber during a fired cycle to that from a motored cycle with fuel injection. With the change in volume a known amount the net heat release for both fired and motored cycles is calculated and the motored heat release data is subtracted from the fired to provide only the heat released due to combustion. This is the ratio of the cumulative heat release to the total heat release in the event. While it may not take into account the differences in temperature between the burnt and unburnt, Yeliana et al. [136] showed that this Rassweiler and Withrow method produced comparable mass fraction burnt curves as both the single-zone and two-zone models while being easier to solve.

4.2.4.2 Motored Rate of Heat Release

Computing the rate of heat release was done on the assumption that the expansion and compression strokes are isentropic and polytropic. Practically, this was not possible considering that the average values for the expansion and compression strokes have differing average values for gamma. Also, the temperature during the expansion and compression would alter the gamma value [129]. To mitigate against these effects, the ROHR during motored engine cycle with the same operating conditions was calculated and then removed from RORH figures obtained during combustion. It can be presumed that no heat is released by the fuel during a motored engine cycle. Hence, the subtraction of the ROHR calculated during the motored cycle from that of a fired cycle can help to eliminate the amount of noise. Figure 4-4 summarises the average ROHR of 1200 cycles prior to and subsequent to the subtraction of the motored ROHR. It is

observed that there is a substantial improvement in the accuracy of ROHR during compression. This is especially vital in this study, where locating the ignition angle is important to the identification of pre-ignition.

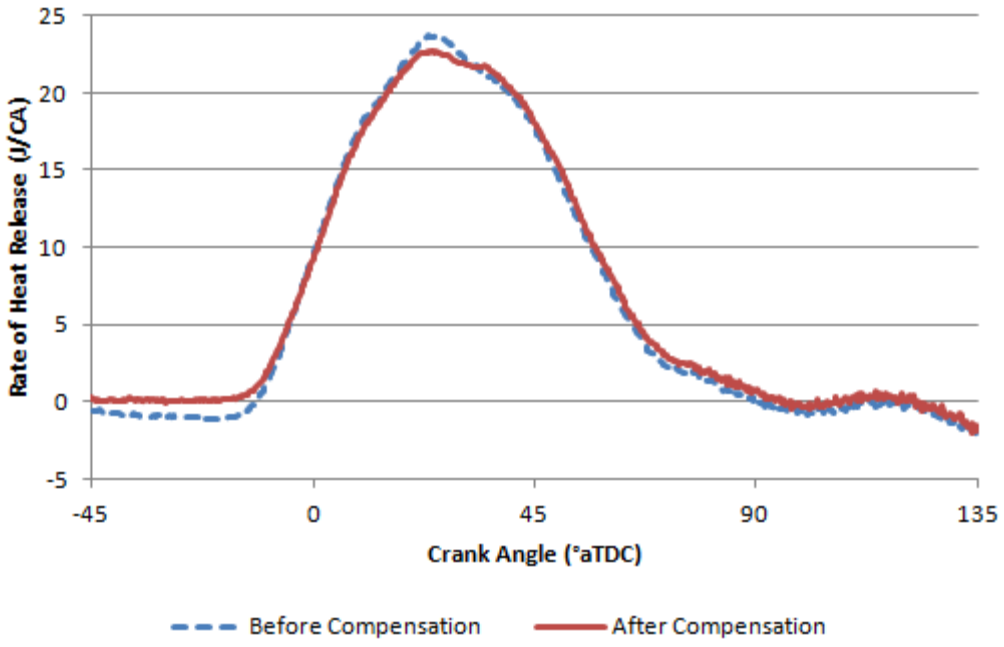

Figure 4-4: Average ROHR against crank angle for 300 cycles before and after compensating for the Filtering

With the aim of filtering the rate of heat release of individual cycles, two sample filters were tested so that noise could be reduced without the risk of losing information. Increasing the interval over which $\frac{dV}{d\theta}$ and $\frac{dp}{d\theta}$ are measured, is the first technique deployed in filtering. It can be indicated in Figure 4-5 with the increase of the interval, noise is greatly reduced. However, the signal shape also flattens significantly and this is noticeable particularly between 15 and 20°aTDC. An interval size of less than 2.5 crank angles should be used, owing to this flattening. The box filter was the second filter to be

trailed. To achieve this filter, each data point in the signal is changed to an average of all data points adjacent to it. Figure 4-6 illustrates that increases in the width of the box filter makes the noise reduction more pronounced with less flattening of the signal shape. However, when box widths are above 10, the true shape of the signal is still significantly flattened and this should be avoided.

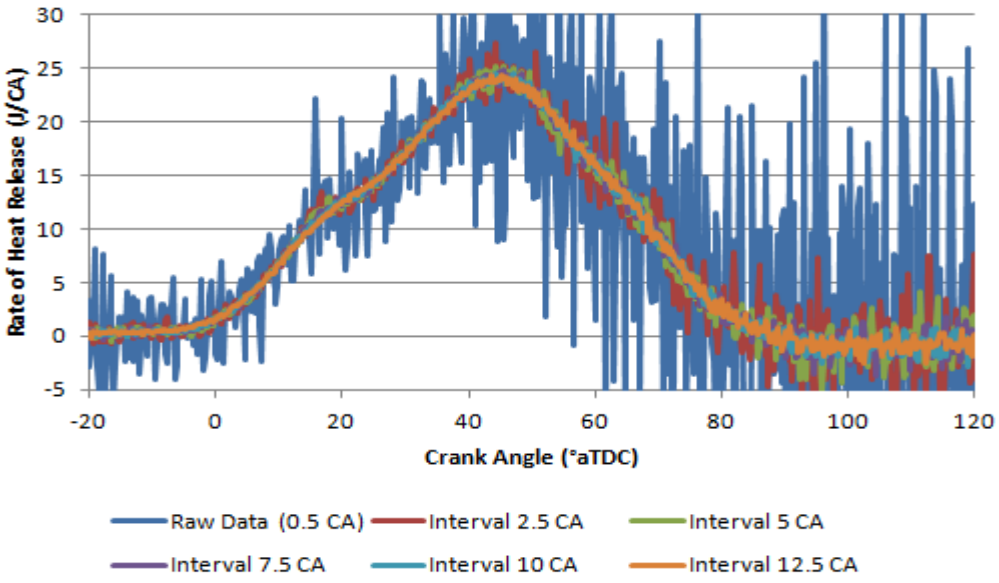

Figure 4-5: A graph showing the effect of varying interval sizes on the calculation of the net ROHR

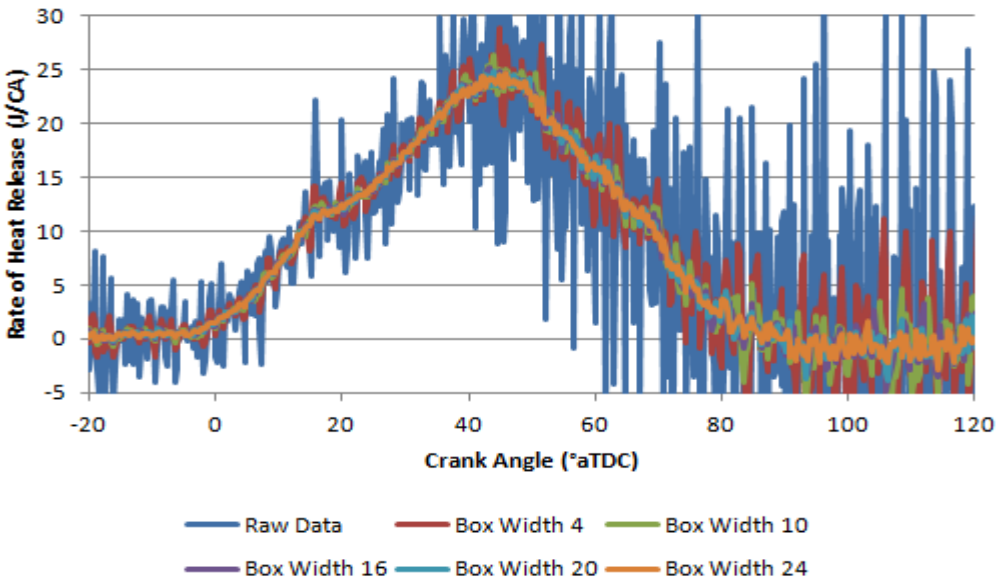

Figure 4-6: A graph showing the effect of different widths of box filter on the calculation of the net rate of heat release for a single cycle

With the aim of filtering the raw signal with heightened noise reduction but still ensuring the overall shape of the signal is maintained, the two filters were used in conjunction. The results are summarised in Figure 4-7. The focus of this figure is a region ranging between 10 and 20°aTDC which tends to be susceptible to distortion related to excessive filtering. It was observed that the 2-stage filter resulted in a very good reduction of noise without distorting the overall shape of the signal. As a result, crank angle interval of 2.5° with a further box-filter applied with a box width of 10 data points was used to present all heat release curves presented in this study.

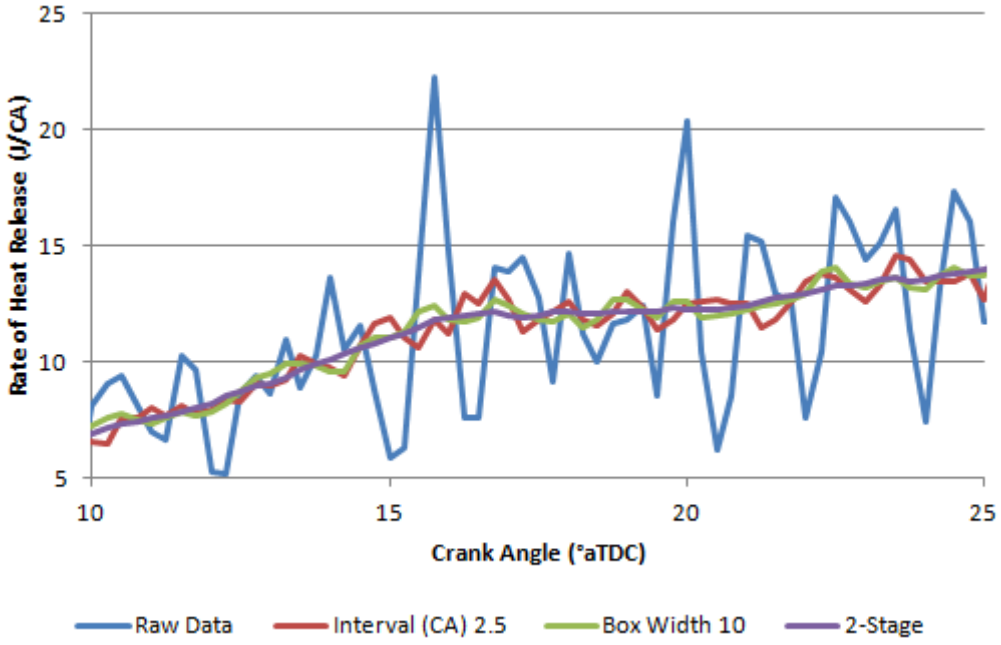

Figure 4-7: A graph showing a comparison between the interval filter, the box filter and a 2-stage combination filter

4.2.4.3 Pre-Ignition Detection

Shown in Figure 4-8 is a summary of 50 combustion cycles, with regards to their heat release. It can be observed that despite the filtering of signals, the noise was still significant enough leading to no useful information being used below 1J/CA. To detect the pre-ignition, the ROHR signals were used, with the threshold set above the noise level of 1J/CA. The ROHR of a cycle was considered to have been ignited once it had reached this threshold. In the event that the cycle reached this threshold ahead of the spark timing, it was considered to be a pre-ignitive cycle. From the data in Figure 4-8, it can also be observed that in spite of a spark timing of 10°aTDC, there are still a number of cycles that did not go beyond the 1J/CA threshold until after 10°aTDC; in one case being as late as 20°aTDC. What this illustrates is that the 1J/CA threshold was not a perfect description of the ignition timing and created the possibility of some pre-ignition

cycles being mistakenly classified as normal, spark-ignited cycles. Even though the exact number of pre-ignition cycles in a data may not have been totally accurate, the error was likely to be consistent across all test conditions given a sufficiently large sample size.

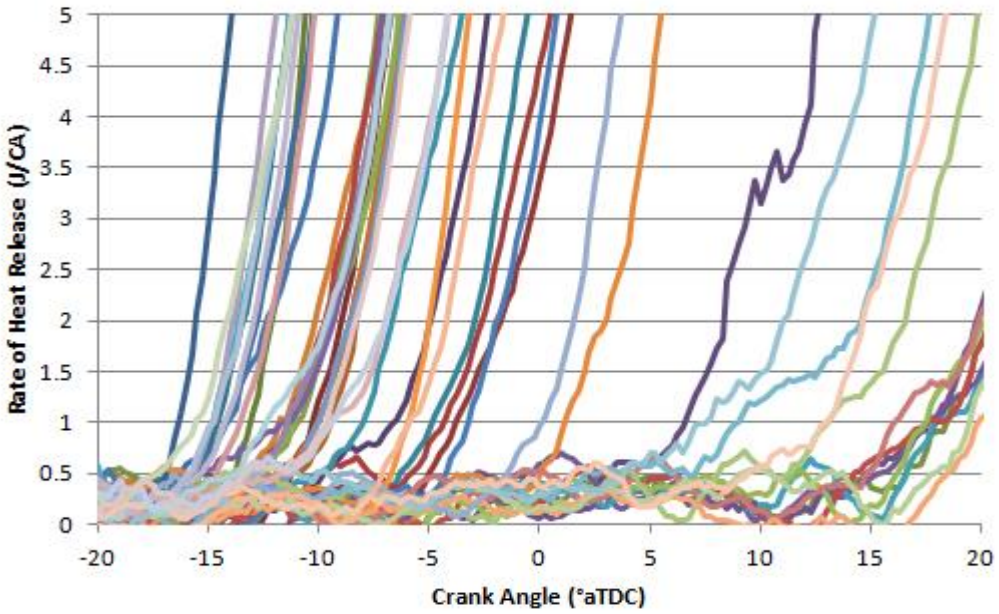

Figure 4-8: A graph of the ROHR against crank angle for 50 combustion cycles

4.2.4.4 Mass Fraction Burned Analysis

To compute the mass function of the fuel burned during a cycle, the cumulative heat released during combustion was normalised against the maximum heat release during the cycle. Figure 4-9 is a summary of both the average cumulative ROHR and average mass fraction burned against crank angle for a total of 1200 combustion cycles.

Usually, MFB data is used to characterise SI combustion when analysing combustion phasing and duration, and the parameters which follow, as represented in Figure 4-9 are normally used.

- CA0 is the crank angle location of the start of combustion.
- CA10 is the crank angle location of 10% MFB.
- CA50 is the crank angle location of 50% MFB.
- CA90 is the crank angle location of 90% MFB.
- CA0-10 is the crank angle duration for the first 10% of fuel mass to be burned.
- CA10-90 is the crank angle duration for the central 80% of fuel mass to be burned.

It has been illustrated that the CA50 location is a reliable measure of combustion phasing. It has also been indicated that (for SI engines) the optimum combustion phasing happens when CA50 is at around 10°aTDC (±2°CA) [13,132]. In the event that combustion is totally adiabatic, the optimum CA50 location would happen at TDC [6]. However, the release of heat via the combustion chamber walls and blowby past the piston rings prevent the combustion process from being adiabatic.

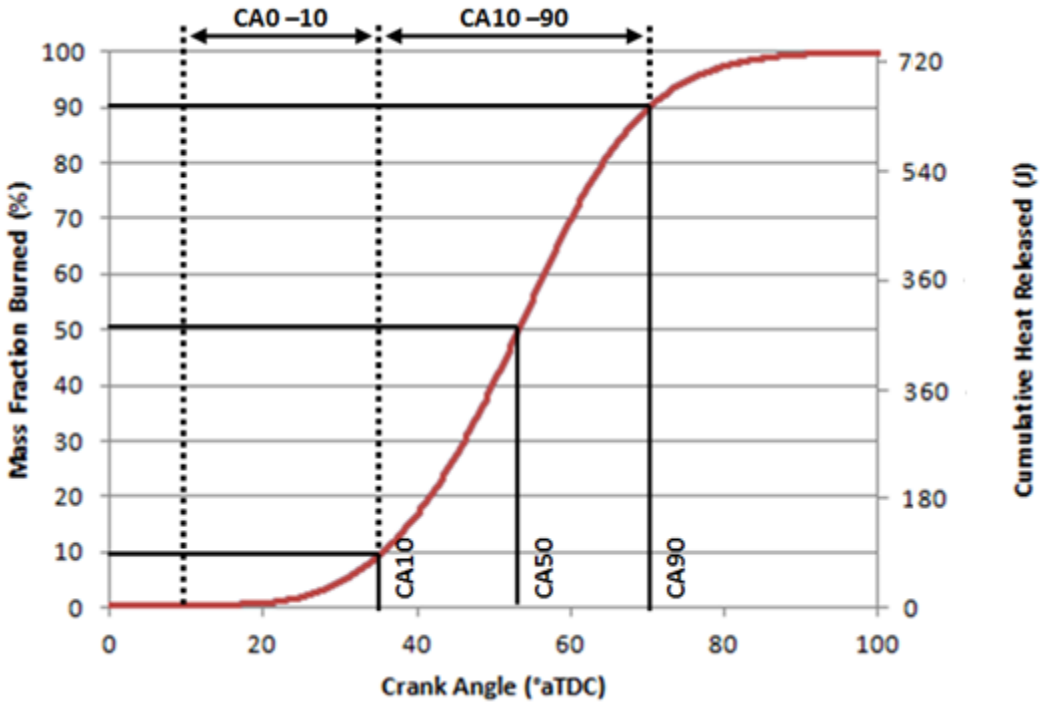

Figure 4-9: Energy released in terms of mass fraction burned and cumulative heat released against crank angle. Data averaged over 1200 cycles

4.2.5 Knocking Combustion Analysis

To calculate the knocking pressure signal of a combustion cycle, the filtering pressure signal is subtracted from the original pressure signal. To create the filtered pressure signal, a simple box filter was applied to the raw pressure signal with the objective of filtering out the high-frequency knock. For the filter, a box width of 10 was used. Figure 4-10 illustrates the raw in-cylinder pressure signal where the filtered signal is overlaid. In Figure 4-11 the resultant pressure signal can be observed when the filtered pressure signal was subtracted from the raw pressure signal. For purposes of this work, the knock intensity of a cycle was defined as the peak recorded absolute knocking pressure for the particular cycle. A value of 7.2bar is the recorded knock intensity for the cycle presented in Figure 4-11.

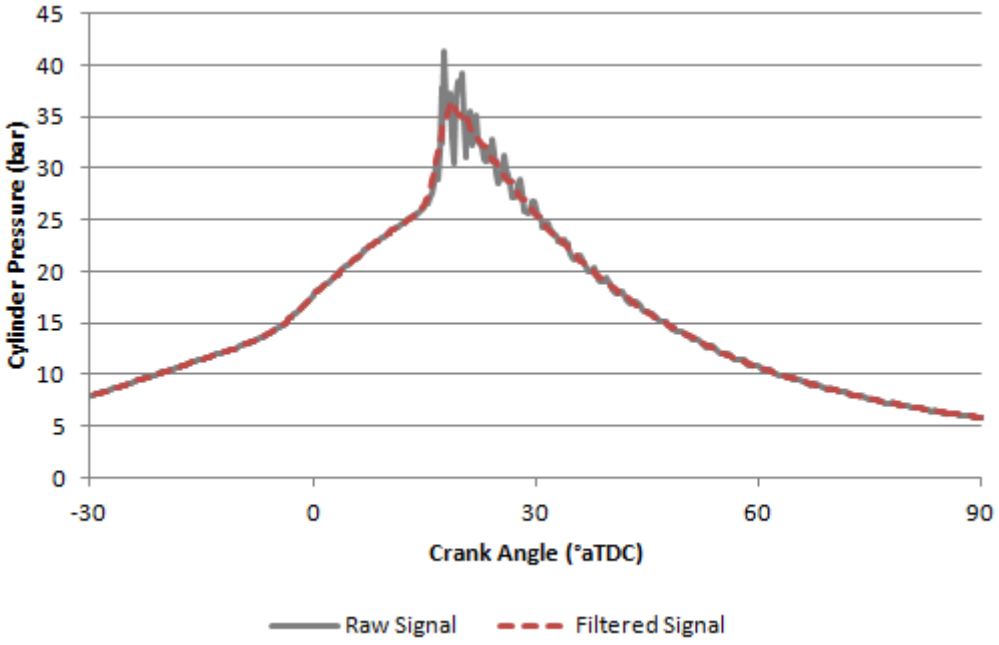

Figure 4-10: The raw and filtered pressure signals of a knocking combustion cycle.

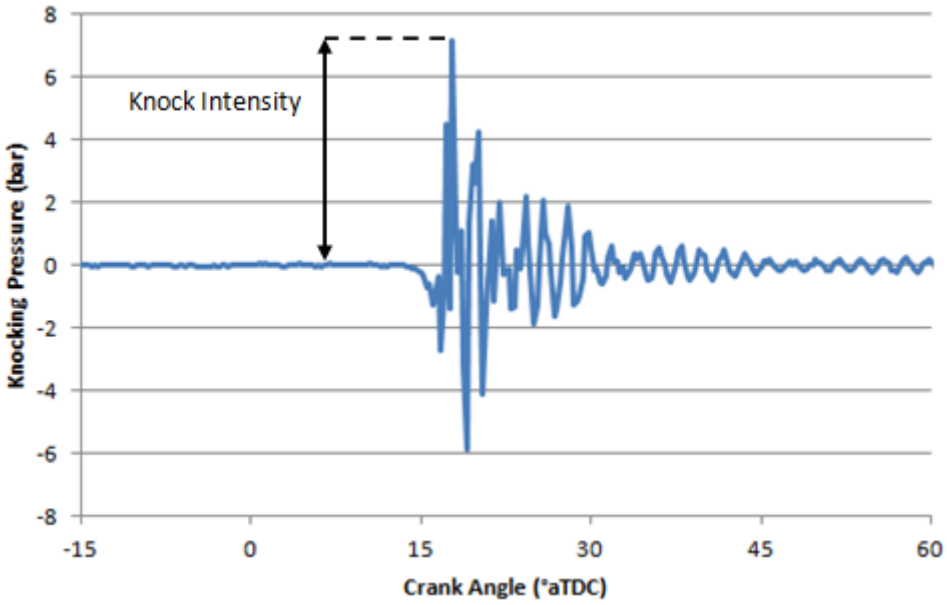

Figure 4-11: The calculated knock pressure signal and definition of knock intensity.

4.3 Operating Conditions

For all tests reported in this study, engine operating conditions were as presented in able 4-1.

Table 4-1: Table of key engine geometric parameters

Parameter (unit)	**Value**
Engine Speed (RPM)	1200±5
Relative AFR (λ) (PFI Only)	1±0.01
Ignition Timing (°bTDC)	17
COV of IMEP (%) (PFI Only)	5
Inlet Pressure (bar)	0.9±0.02
Inlet Air Temperature (°C)	66±2
Exhaust Bridge Temperature (°C)	130±2
DI Tip Temperature (°C)	102±4
Head Temperature (°C)	88±1

5 FLAME IMAGE TECHNIQUES AND ANALYSIS

5.1 Natural Light Flame Imaging

Natural light imaging is a kind of visualisation which employs the light obtained from the process of combustion itself. Ever since the optical engine was created, flame imaging and analysis has been attempted to improve insight into the nature of the turbulent premixed combustion event. From the 1980s, a period followed marked by the proliferation of research into the development of advanced laser based diagnostic tools such as the Planar Laser Induced Fluorescence (PLIF). The work of Rassweiler and Withrow [105,137] indicated that the use of natural light can be perceived as having been quite advanced for that period of time; they used a high-speed camera, managing to record up to 5000 frames per second (fps), resolving to 2.4 crank angle degrees for every image to capture the flame as it progressed across the cylinder. This was the basis from which the authors formulated the method, which would later become highly popular, for computing the mass fraction burned. The authors were able to project the photographs of the flame against a plaster cast of the complete chamber through an arrangement of probes within the cylinder walls, the cylinder pressure, and they also knew the aggregate combustion volume of the chamber. After removing the unburnt section of the cast, they would then weigh the remainder. In order to compute the mass fraction with a high degree of accuracy, it was known that the change in the cylinder pressure (ΔP) is a combination of the pressure rise resulting from combustion (ΔP_C)

and the pressure change resulting from the differences of the combustion chamber (ΔP_{υ}) resulting from the piston's motion:

$$\Delta P=\Delta P_C +\Delta P_{\upsilon}$$

Equation 5-1

in the event that the compression or expansion strokes are constant, the volume and pressure at the beginning and end of each crank angle interval could be represented by:

$$P_1V_1^n = P_2V_2^n$$

Equation 5-2

Hence the mass fraction burnt at the end of the n^{th} interval can be calculated using the following equation:

$$\frac{m_{b(n)}}{m_{b(total)}} = \frac{\sum_0^n \Delta P_C}{\sum_0^N \Delta P_C}$$

Equation 5-3

Where N, represents the total number of intervals. On a qualitative basis, this method is still broadly used and trusted [138]. However, from the quantitative perspective, this is a method that needs to be treated with caution owing to the fact that there are some elements such as mass blowby and heat transfer which are not accounted for.

Apart from being used for visualising the progress of flames as it passes through the cylinder, natural light imaging can also be employed to analysing the combustion products. Some molecules become raised to a state of excitement through exothermic

reactions as the flame spreads. Eventually, these molecules revert back to a state of balanced levels of energy resulting in release of wavelengths reliant on their chemical structure. This radiation is more resilient when compared to ordinary thermal radiation and makes detection easier. Chemiluminescence is the formal name given to the capture and analysis of this phenomenon. Figure 5-1 illustrates photon emission wavelengths of certain species.

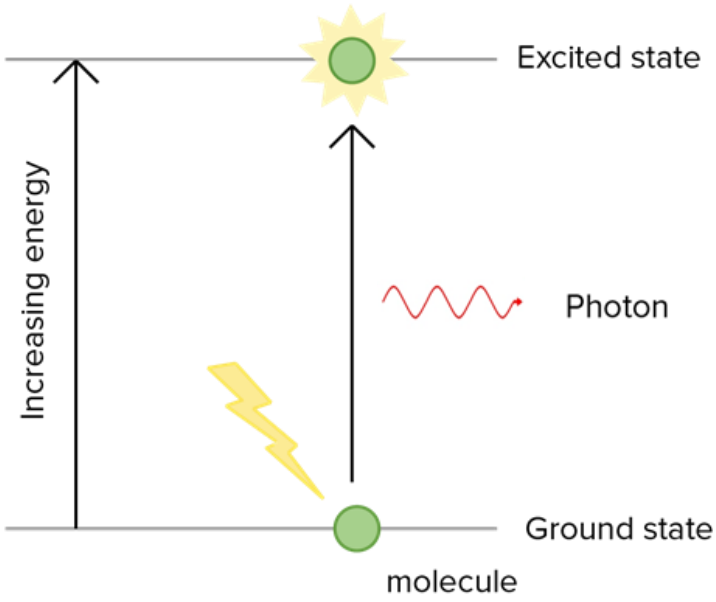

Figure 5-1: Molecules becoming excited by exothermic reactions which result in them moved to a state of excitement. The photon is then produced by their decay.

Chemiluminescence imaging allows a lot of information to be obtained by analysing the natural flame emission by some chemical species produced in the combustion process. Although many chemical species in the auto ignition and combustion processes can be present at the same time, each radical species emits a specific spectral profile so that some species can be captured individually with appropriate bandpass filters. Emission

and absorption of many combustion species are characterized by band spectra in the visible and UV regions. Table 5-1 shows prominent spectral peaks of intermediates and products of auto-ignition and combustion in the visible and UV regions. Imaging through appropriate filters of a particular spectral wavelength indicates the presence of the chemical species produced by the associated combustion reaction [139].

Table 5-1: Strong emission peaks of major combustion

Methane CH (nm)	Hydroxide OH (nm)	Formaldehyde CH_2O (nm)	Carbon Dioxide CO_2(μm)	C_2 (nm)	Aldehyde CHO (nm)
314-387	302-309	368-384	2.69-2.77	470-474	320-330
389-431		395-412	4.25-4.3	516-558	340-355
		457		563	360-3801
					385

Rassweiler and Withrow [137] showed that a flame front in the process of a knocking cycle releases photons which showed the presence of carbon dioxide, methane, and hydroxide. Chomiak [140] aimed to find the relations of these emission rates from the flame front to the Kolmogorov scale. He observed that the smallest extremely luminous objects within the combustion chamber could be around 1.5mm in size, which matches the Kolmogorov microscale within the regions.

Cool flame combustion has been a topic of study for a number of years. This type of combustion generally happens in the region of 600 to 800K and is a primary factor in auto-ignition. For instance, Dec and Espey [141] managed to illustrate that auto-ignition

was most likely to happen during times when photon discharge happened at ~430nm. From these experiments, it could be concluded that these emissions resulted from a cool flame and that mostly, it constituted of methane and formaldehyde. This flame chemistry is then engulfed and replaced; afterwards it was found that the soot combustion scale is at 310nm, which is an indication of hydroxide presence.

This conclusion was confirmed by Yang et al.[139], who studied the impact of injection timings of Controlled Auto-Ignition (CAI) combustion. He also arrived at the conclusion that the wavelength of a photon emitted during a cool flame is higher (in this particular case, the photon was an aldehyde) which is rapidly overtaken by a hydroxide species within the combustion as the cool flame comes towards the end. During the heat release, this hydroxide radical becomes not only stronger but also brighter. Since the OH radical is a major chemical intermediary of combustion, it is generally a suitable indicator of the flame front during the hot flame combustion. This has been the target of many PLIF methods [142,143].

One of the hardest challenges of working with natural light imaging involves the use of the OH radical as a flame front maker. Finding the precise front of the flame depends on identifying the UV light emitted from the hydroxide elements. In cool flame combustion, it is most probable that this will not be visible. It has been shown by Srinivasan and Saravanan [144] that owing to cooler combustion temperatures of ethanol, it possesses lower light intensity. By deploying the natural light technique for measurement, results rely on emissions produced by the combustion itself in order to identify the flame front. With the OH radicals being discharged in the form of UV light, it would be difficult to see the advancing flame using an ICCD camera. In order to

enhance the chances of seeing the flame front, an image intensifier or an appropriate external light source of chamber illumination will assist to distinguish between the burnt and unburnt regions owing to the variance in intensity. Schlieren is known as an excellent well-established alternative involving use of an internal light source.

5.2 Schlieren & Shadowgraph Flame Imaging

The technique of Schlieren was developed by Toepler in 1864, with the aim of detecting streaks in optical glasses. Mach later adapted this for further research and deployed the method in the photographing of Supersonic jets flying over Prague in the 1980s [145]. It was only after World War 2 that Schlieren started being used in automotive applications by Male (1949) who deployed the system in his efforts to detect auto-ignition inside the cylinder. Eventually, Smith [146] contributed a lot to this field through advancing the understanding of in-cylinder visualisation by passing a source of light (in this particular context, a laser beam) through the cylinder and then taking a photograph of the resulting images as is indicated in Figure 5-3.

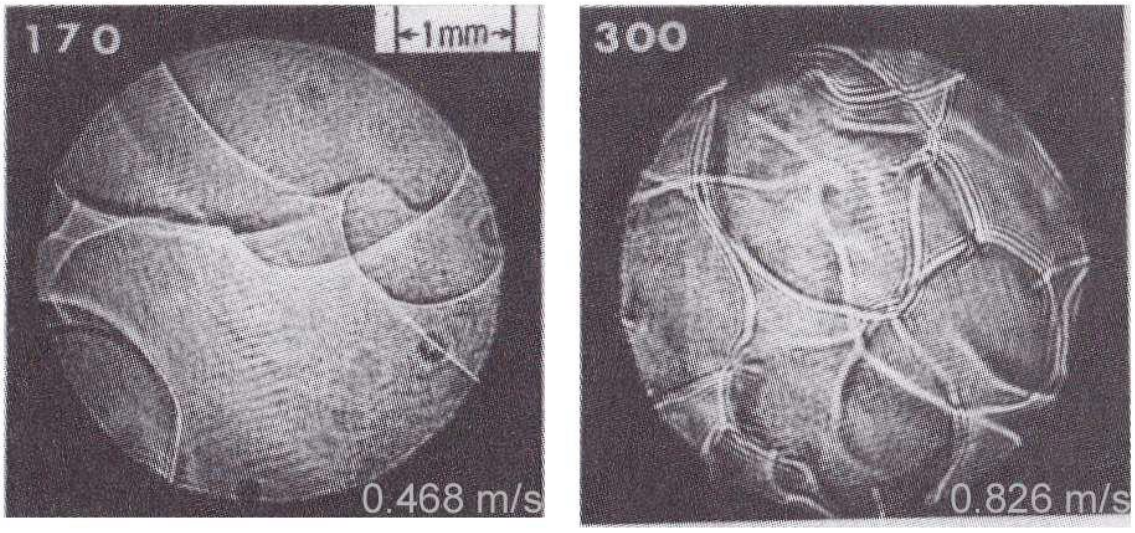

Figure 5-2: Shadowgraph images of flames propagating towards the camera [147]

The deployment of the laser in capturing shadowgraph images or schlieren has now generally become widespread[99,148].

Even though the setups of both schlieren and shadowgraph are nearly the same, there are still some clear differences between the techniques. Although both will report changes in the flow field, schlieren is generally more sensitive to the first derivation of density owing to the employment of aperture or knife-edge in the flow field [149]. The device for filtering is made with the aim of lessening the noise of light entering the image plane and thus resulting in a clearer image and better contrast in comparison to shadowgraph. However, shadowgraph delivers its own benefits, as it depends less on high-quality optics and labour intensive precision alignment.

5.3 Distinctions between Methods

Both schlieren and shadowgraph are techniques which are commonly used in the detection of knock due to the fact that they are sensitive to fluctuations in field density.

Owing to the reason that the refractive index can be different over the flame profile, as a result of either propagation of the front or the mixing of the burned and unburned gases, the output could be two areas with different intensities. When the refractive index gradient is normal to the light rays which are being transmitted through the test area, then the rays will be deflected in a certain pattern as the light particles move with slower speed where the index is larger. This deflection, which is the primary definition of schlieren imaging, is a measure of the first derivation of density [149]. When the light makes its way through the work area, it diverts in numerous directions and leaves an imprint in the profile of the beam that is then recorded using a high-speed camera. Ahead of the beam arriving at the camera, it goes through a knife edge (or adjustable aperture) to partially block some of the scattered light. Even though this will result in the end image being dimmer, it is required as the beam will lose focus as it passes through the flow. This will ensure images that are clearer and more focused.

However, in the event that there is variance in the index gradient across the field, the refraction of adjacent rays will vary, delivering either increased or decreased illumination on the camera lens or screen. The shadowgraph or “direct shadow” method is what these changes are known as and was firstly used by Dvorak in 1880 [145]. It is important to reiterate that in shadowgraph there is no knife-edge cut-off.

Since both shadowgraph and schlieren are highly sensitive to changes in density, they are suitable for use in the study of both auto ignition and flame development, with one not being seen as a replacement for the other. In an IC engine the application is complicated by the need for a reflective surface on the top of the piston, maintaining the cleanliness of which can be highly laborious.

5.4 Laser Sheet Flame Imaging

Laser sheet imaging is another laser method available for capturing flame propagation through the charge. Even although this method was not adopted in the currently reported work it may be useful in future related studies in the same engine. Compared to shadowgraph and schlieren, laser sheet presents a number of advantages. While the other techniques are able to create data directly along a defined line of sight, laser sheet has the ability to illuminate a fixed two-dimensional plane within the charge which results in spatially resolved information with additional temporal resolution. In the study by Hicks et al[150], he used four distinct sheets of four different wavelengths, to deliver the maximum possible information about the processes in the cylinder. Since combustion imaging is at all times an act of balancing between the spatial and temporal resolution types, this ‘middle ground’ of the laser sheet is seen by some as the better form of imaging [151]. Practically, laser sheet imaging analysis relates to a slice of the reaction front which is two dimensional, while the Chemiluminescence and schlieren methods have a closer relationship with the leading edge of the flame.

5.5 Mie Scattering

When it comes to implementing and analysing, the Mie scattering process is the simplest of laser sheet methods, involving transmission of a light source through the field of study from which the light particles are scattered. A standard high-speed camera is then used to capture these. The word "scatter" denotes the interface of the electromagnetic radiation between the laser light and the "seeded" charge. In the absence of the exchange of energy among the particles of the light and those of the mixture, all the light scatters. There are generally two types of scattering once this

happens: elastic and inelastic. When the frequency of the laser light and the scattered light is equal, elastic scatter occurs. Mie scattering is an elastic scattering process, where the scattering particle (d) diameter is equal to or greater than the laser light's wavelength (λ). One of the benefits of using the Mie scatter system is that, as opposed to other systems, it does not need a specialised ICCD or a fixed power rating of the light source, which makes it possible for the setup costs to be contained. However, the scattering of light only happens when the particle charge is big enough, in order of 0.5μm for visible light, to cause a disruption of the flow of light waves [149].When it comes to the pattern and type of scattering, diffraction happens in two ways from the seed particle.

In both scenarios, the scattering of light happens in a certain pattern as is illustrated in Figure 5-4. Most of the scattered light goes back to its source. At 90° from the original flow of direction directly above the cylinder head or the piston crown, which happens to be the area where the majority of researchers place their optics, is the easiest angle from which optical recording can be done. In the experiment by Hicks [150], a single camera was used to capture the four distinct laser sheets. This work was taken further by Gillespie et al. [152] who sent a pulsing (~20 kHz) copper vapour laser through a slow rotating mirror in order to come up with a 'swinging sheet'. From this, 25 simultaneous sheets where produced delivering either a three-dimensional flame front or collecting numerous multi-sheet images in one combustion event. Even though the information gathered was obtained through a spherical bomb chamber and the method is a challenge to implement, it is still a vital and cutting-edge tool that can possibly make the three-dimensional reconstruction of the flame possible.

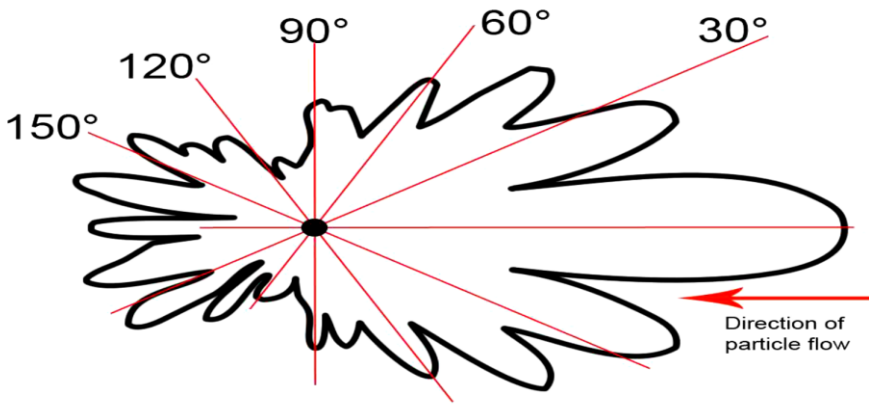

Figure 5-3: The calculated angular distribution of the light intensity scattered by a sphere, [153].

5.6 Planar Laser Induced Fluorescence (PLIF)

In respect to the production of a two-dimensional flame image, PLIF is similar to Mie scattering with regards to set up. A number of features of the charge can be determined using this method. Some of these are identified by Lozano [154]: flow patterns, velocity, species concentration, pressure and temperature. A laser that has been constructed into a sheet and passed through the engine using an optical window illuminates the in-cylinder charge. This window is often placed in the form of a collar between the head and the cylinder liner or in the form of two windows beside the head making it possible for the sheet to make its way through the head itself. Usually, the laser sheet is tuned and pulsed to a selected wavelength which will respond with a particular tracer within the prompted mixture. The tracer can either be artificially inserted into the mixture or occur naturally as a product of combustion (aldehydes or OH radicals) [155].

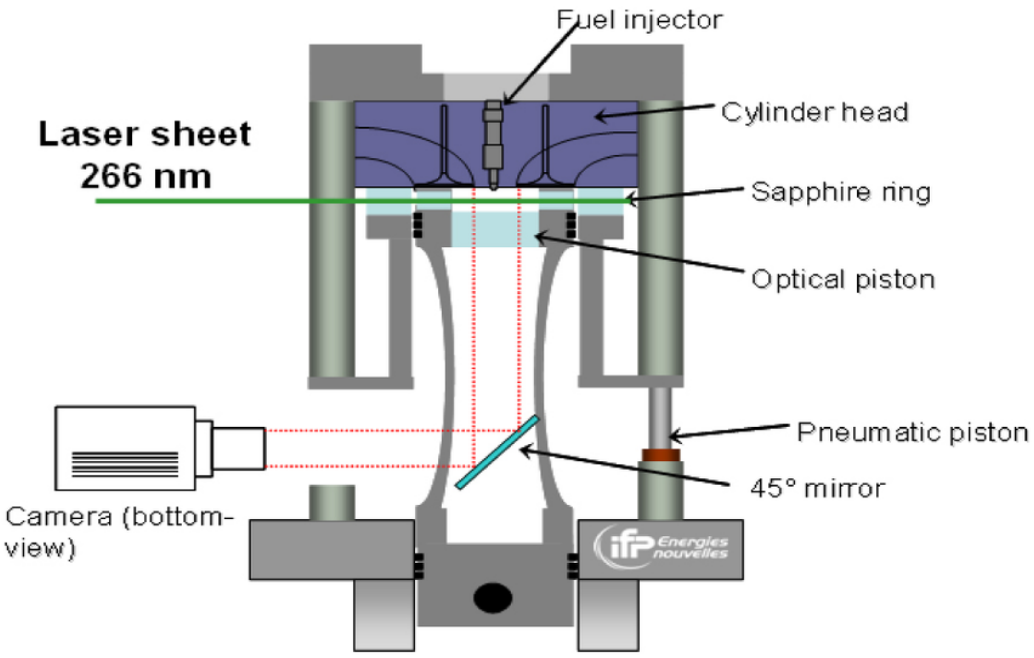

Figure 5-4: Sample of PLIF setup used for combustion optical investigations [156]

The energy of the laser will be absorbed by the tracer, which will excite the tracer, leading to decay and subsequent release of photons of light, which can then be recorded on an ICCD or comparable device. A potential similarity between Mie scatter and PLIF imaging is that the Mie scattering can result in interference and over-powering of the PLF signal. This depends to a large extent in the laser used and the dopant type. Even though PLIF gives a good flame front definition, it requires a lot of time to implement. The energy that is needed for the high-powered lasers can lessen the effectiveness of the data capture process to just a single image per cycle. Also fluorescence can be a challenge to image accuracy and correctly interpreting the signals. Pressure and temperature fluctuations can also have an impact on PLIF. Finally, a particular type of laser which relies on the selected dopant is required for PLIF.

5.7 Comparison of Imaging Methods

Set out in Table 5.2 is a detailed summary of the methods discussed. The different imaging techniques are also represented graphically in Figure 5-6.

Table 5-2: Comparison of the major methods of visualising flame propagation in the cylinder

Method	
Natural Light/ Chemiluminescence	
Advantages	**Disadvantages**
- Low in complexity to setup - Relatively inexpensive - Good measure of heat release fluctuations, both temporally and spatially - Alerts users to knocking regions - Allows user to spot species formation to analyse the chemical balance of the charge - Can visualise not only combustion, but 'cool-flame' combustion due to the emergence of a CHO radical	- Difficulties with identifying three dimensional structures - Signals must be interpreted carefully to ensure accuracy in assessment of emissions spectra - May not detect the flame front of cooler flames – particularly ethanol - Can be hard to detect all species due to varying wavelengths and with the spectrum of emissions being beyond visible light - Requires an image intensifier or an artificially boosted image – especially for alcohol fuels with less luminous flames
Schlieren	
- Very good contrast, especially compared to shadowgraph - Works with both laser and white visible light (like LEDs) - Due to its sensitivity to density changes, is suitable for detecting knock and for visualising the initiation and propagation of the flame - Provides an in-focus image, unlike shadowgraph	- Can only generate information along the line of sight of the light source - Not able to see mixing clearly - If the flow is in three dimensions the results can be misleading and the user is unable to integrate spatially throughout the flow - Requires the knife edge to be precisely placed - Requires a laser light source which could have a poor beam distribution - Double-pass can be very difficult to setup
Shadowgraph	

-Lower quality equipment required compared to schlieren – therefore lowering expense - Works with both laser and white laser light - Due to its sensitivity to density changes, is great for detecting knock and visualising the initiation and propagation of the flame	- Can only generate information integrated along the line of sight of the laser - Difficulties with identifying three dimensional structures - Unable to integrate spatially throughout the flow - Double-pass can be difficult to setup - Requires a laser light source which could have a poor beam distribution - Sensitive to piston motion meaning lower accuracy around bore perimeter
Laser Sheet-Mie Scatter	
- Can use any light source - Can use any type of camera (ICCD or high-speed) - Very strong signal - Clear distinction between the total burnt and unburnt gases - Good balance of spatially and temporal resolutions	- Unable to function with droplets less than 0.5µm in size because of its second order size dependence - Usually restricted to two dimensional (though swinging sheet techniques can be used to increase complexity)
Laser Sheet-Mie-PLIF	
- Very simple to set-up - Very high contrast as it is able to ignore irrelevant light scatters - Good balance of spatial and temporal resolutions	- Difficult to interpret signals - Must have an ICCD camera, thus raising costs - Requires a high-powered laser - Time-resolved images can take a long time to process, reducing the amount of optical work that can be completed in a day - Requires use of a dopant which may influence the in-cylinder mixture properties (such as the evaporation and the burn rates) - Requires a UV source to fluoresce the dopant

Natural light imaging was the method selected for this project based on the available technologies and the accuracy level required. A comparison between two-dimensional flame imaging employing natural light and schlieren was done by Murad [157] who

concluded that the development of flame radius and shape factor were not affected by the technique chosen as long as the available natural light was enough. Dingle and Moxey also recently deployed the technique of natural light imaging at Brunel University to measure flame propagation speed, auto ignition detection, and shape factor[5,123].

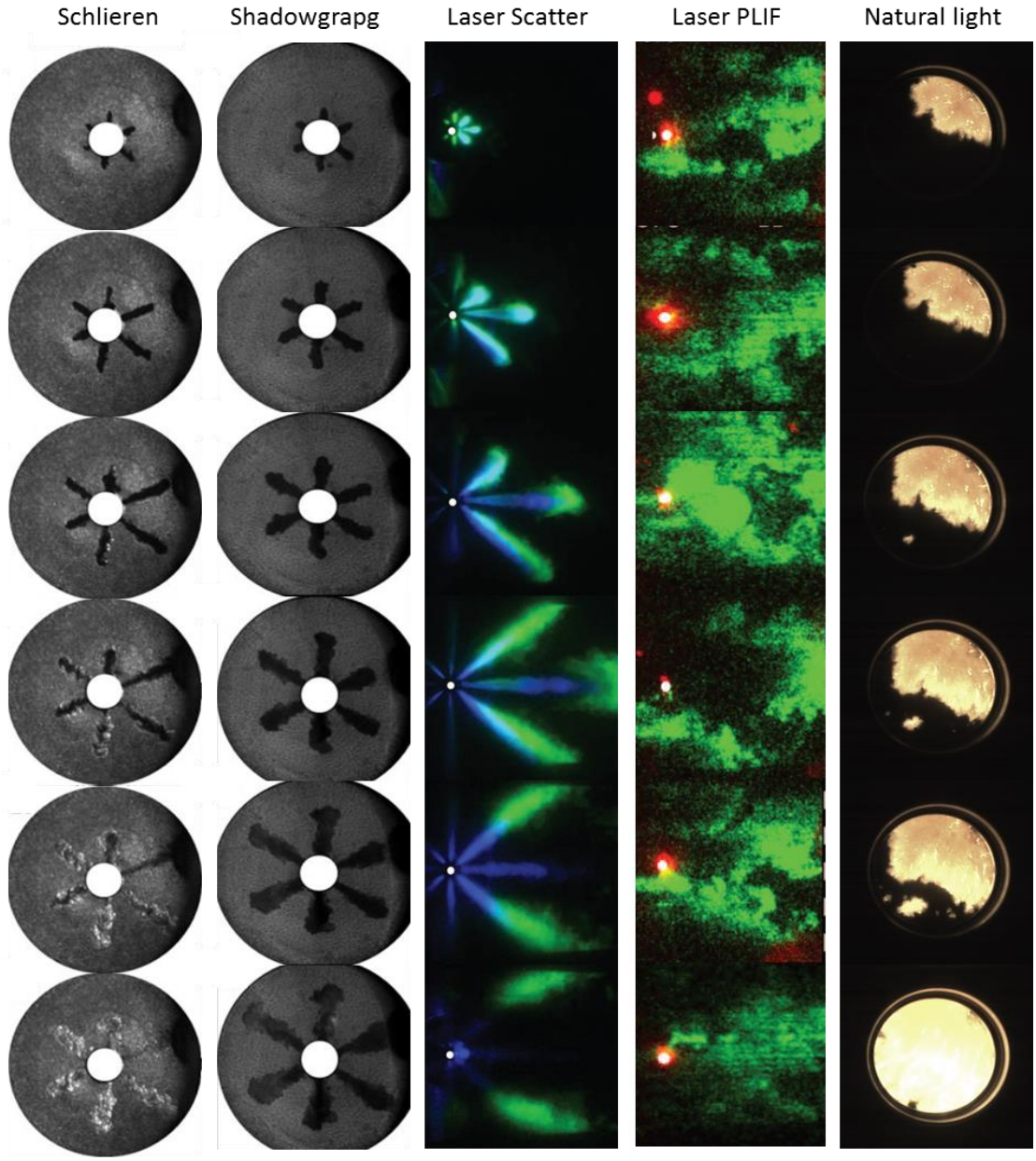

Figure 5-5: Visualised comparison of the major methods of flame propagation in the cylinder

5.8 Flame Image Processing

To aid the processing of the images a certain amount of automation (Matlab code) must be introduced. While this code itself will be discussed in greater detail later in this chapter, a brief overview may be found below.

Once the video file had been deconstructed into individual frames, with a resolution of one frame every 1.2° crank angle (engine speed of 1200 RPM and imaging speed of 6000 fps), these were then processed via in-house MATLAB coded software. The code analysed the pixel density of the image and assigned each a value between 0 and 1 as set by a pre-defined threshold value. The resulting image contained only white regions (pixels under that assigned value) and black regions (pixels over that assigned value). While the value requires initial calibration for each fuel concentration or equivalence ratio data set, this code saves time overall. From this binary image the program could identify the flame edge and the area of the white pixels, thus the area of the flame was calculated. The code then outputs not only the binary image of the flame for visual analysis but also it produced a spreadsheet of the flame speed, area, radius, wrinkle and shape.

5.9 Experimental Procedure

An NAC MEMRECAM fx 6000 high speed video camera coupled to a DRS Hadland Model ILS3-11 image intensifier was used to record all optical data for this experiment. The camera was triggered at the same time as the data acquisition card (DAQ) to record images simultaneously with the pressure and temperature data. The camera was set to record at 6000 fps at a resolution of 512 x 512 pixels (2.8 pixels per mm) meaning that

the time-resolved images acquired would be at 1.2° crank angles per image. While the desire will always be to capture the images 1:1 with the engine speed, this frame speed chosen was the quickest one available which still allowed full-bore optical capture at a resolution that allowed for early flame development to be identified accurately.

Figure 5-7, shows the engine with the optical head in place and also the camera and image intensifier secured to an optical table. A mirror positioned at 45° allowed the camera to capture images using only the natural light emitted from combustion. While pressure data for 300 thermodynamic cycles was obtained with each run, only 50 imaged cycles were obtained. This was due to the inherent data storage capacity issues and time-consuming nature of the optical imaging process. The error at 50 cycles was considered an acceptable compromise and it should be noted that several other authors have also shown that obtaining 50 optical cycles is sufficient to pick up key differences in flame development [134,158].

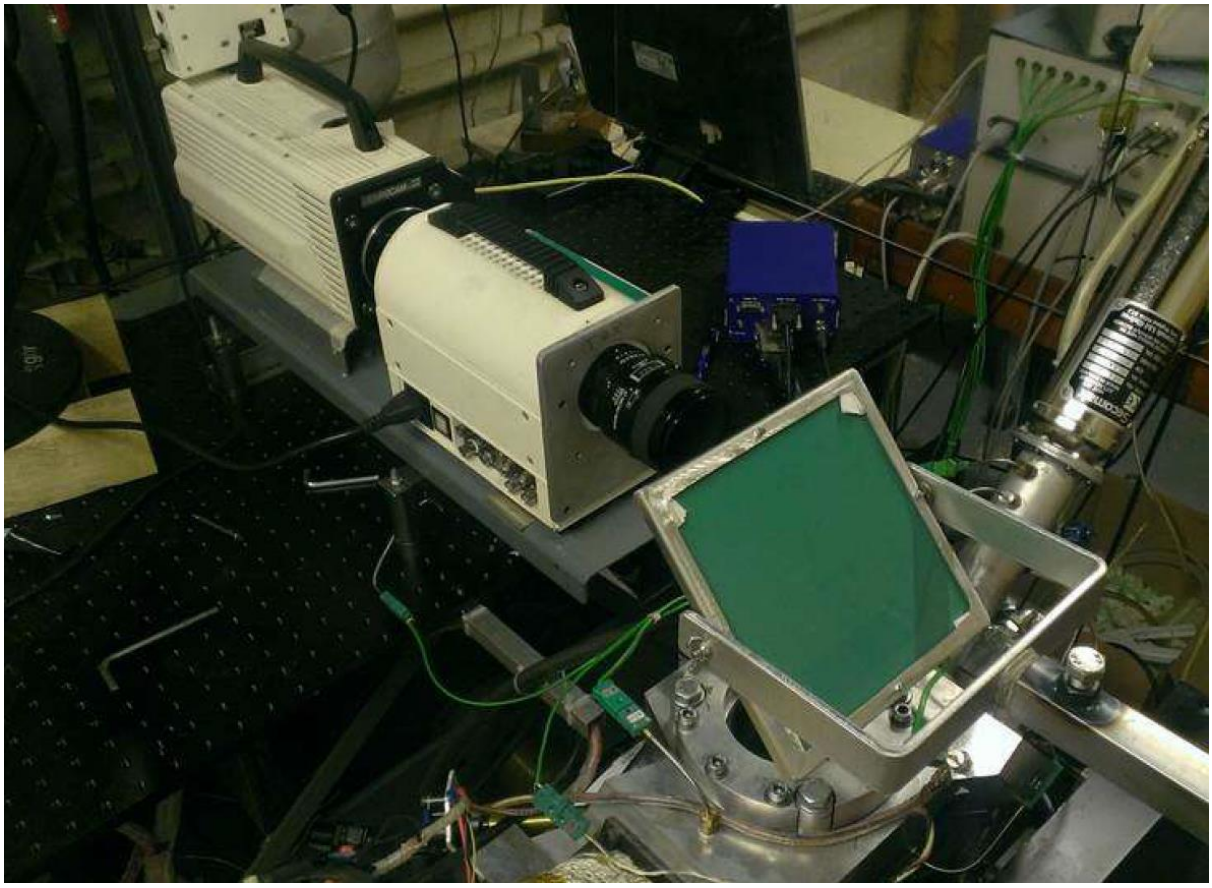

Figure 5-6: Photograph of the natural light imaging setup for this experiment showing the NAC MEMRECAM fx6000 joined to a DRS Hadland Intensifier position directly in front of the engine and aligned with the 45° mirror.

5.10 Intensifier

The images from the camera alone would be too dim for accurate analysis to be performed for normal flame propagation especially under lean conditions. The DRS intensifier was coupled to the camera and connected in such a way that when the camera's trigger was activated that, the intensifier's shutter opened.

It was important to set a right gain for intensifier; Too low an intensifier gain setting and the flame still would not be clear enough; too high and the photocathode and

phosphor screens in the device would be damaged due to excess light entering the shutter and effectively damaging the intensifier cells.

Unfortunately due to accidental improper use of the intensifier by previous users, the intensifier was damaged and some pixels were "burnt" (Figure 5-8, shown in red circles). In the photos captured using intensifier, there was black oval shape of burnt pixels causing problems during the image processing. Figure 5-8 shows the intensifier captured images and the image processing results.

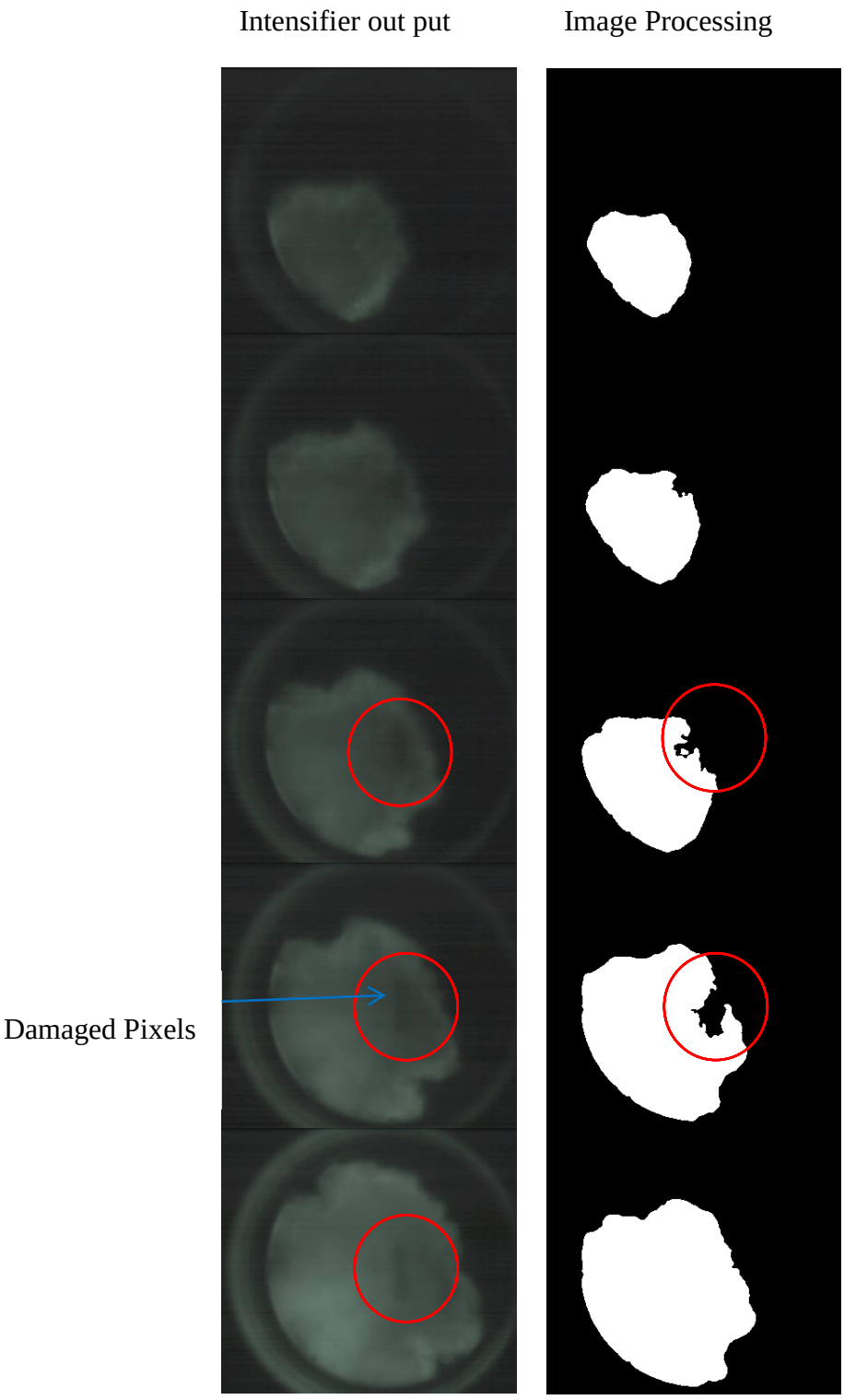

Figure 5-7: Shows the intensifier captured images and the image processing results.

During the knocking cycles, too much light emitted from combustion chamber toward the intensifier. So it was possible to damage the intensifier again and burn more pixels. As a result, it was decided not to use the intensifier for this study.

5.11 Image Capture Method

The most part this work focussed upon auto-ignition and knock. This included thermodynamic and optical observations. When the thermodynamic work was completed there was an opportunity to visit optically captured images of auto-ignition and pre-ignition in greater detail.

The availability of optical engine data provides the opportunity to better understand the causes and effects of auto-ignition and knock events on the pressure development and hence ultimately engine output. To this end a mirror was positioned over the optical cylinder head and angled so that the high-speed camera (set up at 90° to the engine) was able to record the resulting combustion.

5.12 Flame Image Post-Processing

As discussed previously, all flame images for this project were captured using a MEMRECAM fx 6000. The images were stored on the internal memory of the camera as a concurrent video file. These were then downloaded as TIFF files where each image represented 1.2 crank angle degrees. Each data point requires 50 individual cycles to be recorded (in order to reduce cyclic variation impacts), this means each data point could result in up to 15,000 images. Thus a process was created to batch process the images to allow for effective and quick analysis, while ensuring accuracy and continuity.

To do this a MATLAB code was written which would be able to compute the mean flame radius as it propagates, thus giving a mean flame speed [159]. In addition, the code could also calculate the perimeter length of the flame front, the 'shape factor' of the flame as well as the level of 'wrinkle' experienced. With these pieces of information it was then possible to determine the effects of both bulk and local distortion on the flame propagation event.

5.13 Flame Image Reading

The first segment of the code used the "imread" function of the MATLAB command library to import the digital images. This was performed by the user instructing the code to open the first image in the folder which contained the images for analysis. As the code ran through the processes and completed, it returned to the top of the code to select the next image until all have been processed. Once imported, the images were stored in the MATLAB workspace in matrices format that are the same size as the image (pixel by pixel).

5.14 Noise Suppression & Masking

Shown in Figure 5-9 is the initial image captured from the engine. It shows not only the flame kernel but also several elements of light pollution including reflecting light from the inside edges of the window and the TDC light probe which may affect the accuracy of the results. Firstly the image under analysis had a 'background image' subtracted from it. This was an image made of several points in a cycle overlaid on top of each other and common noises can be isolated leaving only the foreground of the bore.

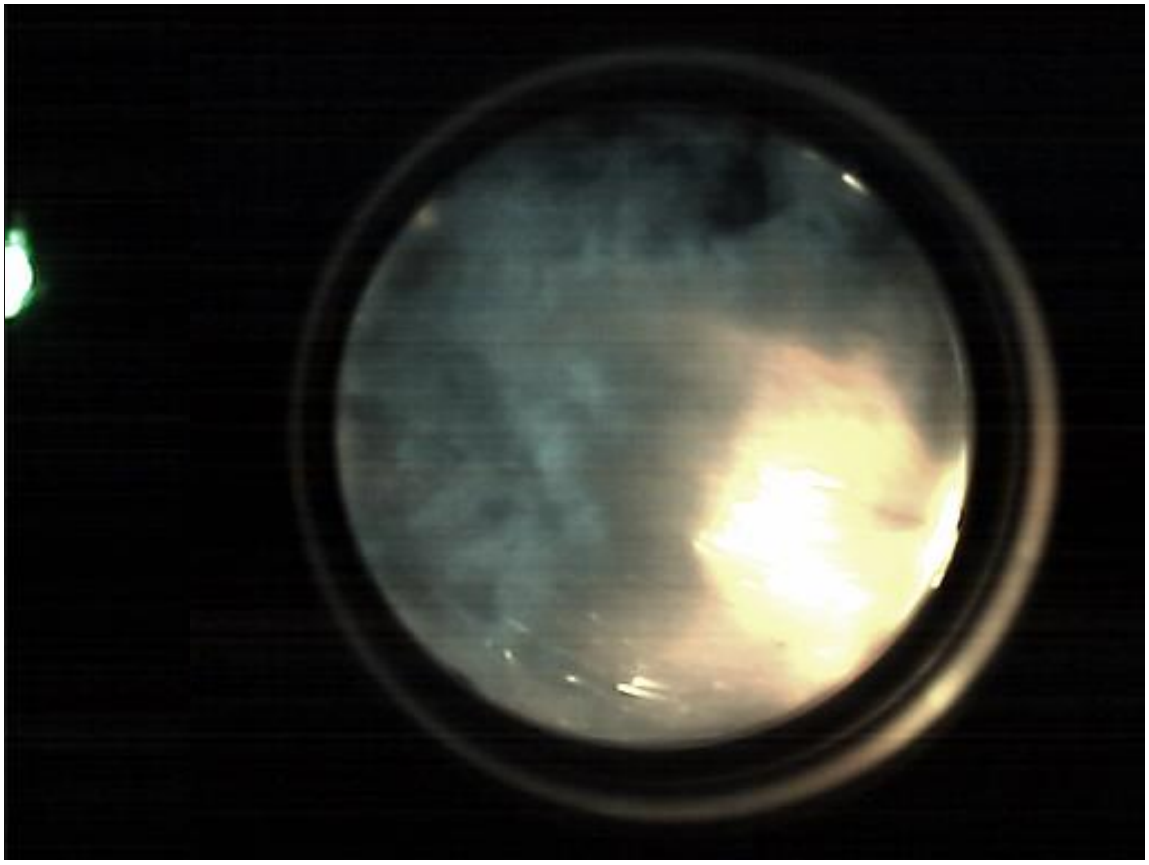

Figure 5-8: Raw image showing light pollution

The second stage was to apply a mask to crop out the cylinder wall noise (the ‘halo’ in Figure 5-10) and leave only the flame itself for analysis. This was accomplished by applying a binary matrix to isolate the bore and thus divide the image into ones and zeros, each representing the area inside the mask and outside the mask respectively. This had to be manually placed at the beginning of each processing run to account for camera movement or size of the bore. To aid in this mask creation, the code was able to select the image with the highest luminosity from the set to allow the user the best chance of placing the mask correctly. It was also here that the ratio of the image to the real world dimensions is created. This aided the correct calculation of the various analysis figures later (radius, area, etc.).

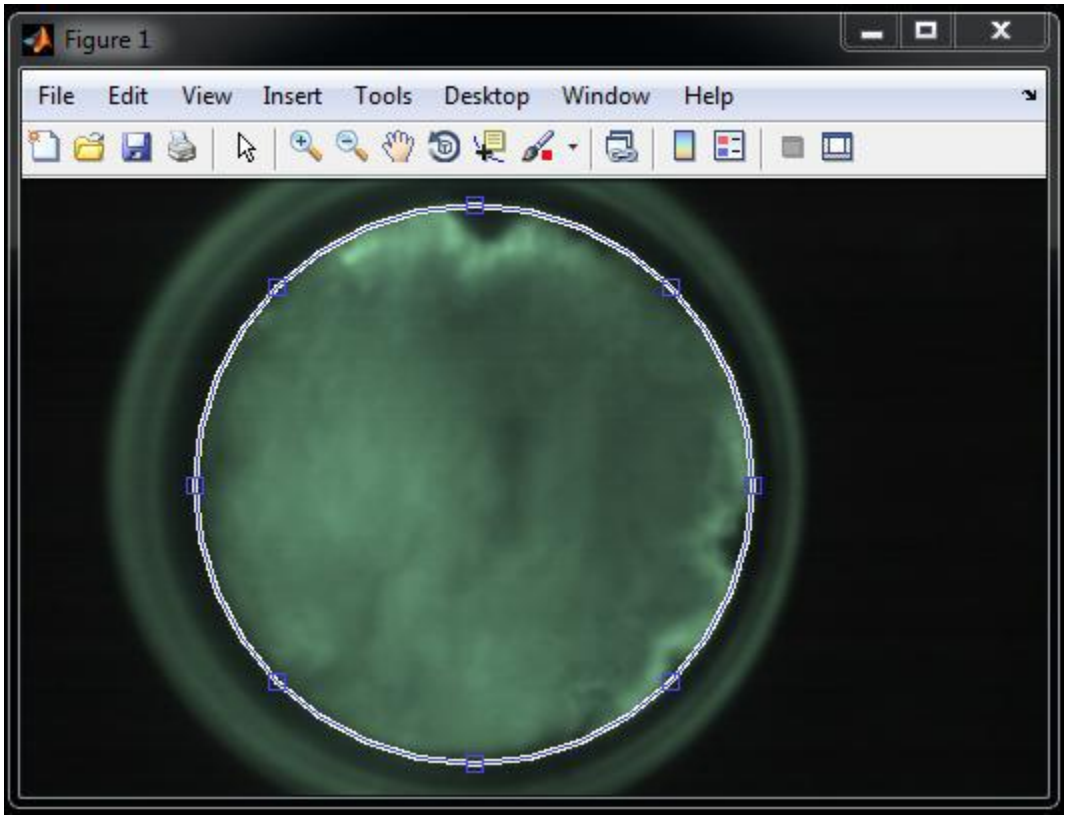

Figure 5-9: Application of the masking tool in MATLAB to designate the area of the bore.

5.15 Image Binarisation

This stage is represented visually in Figure 5-11. The code changed the image from RGB to black and white, where each pixel is represented by either a one or a zero, depending on it being white (of flame) or black (of unburnt gas). This binarisation has two stages:

- Greyscaling – The RGB image was turned to greyscale, transforming each region of the coloured image into shades of grey. This was vital as many binarisation codes require a thresholding value that decides which pixel is part of the flame or not and this value can accept only greyscale inputs. In

MATLAB, grayscaling of the image is done by eliminating the hue and saturation information while retaining the luminance.

- Application of the binarisation algorithm: The algorithm used initially was a threshold finding technique which depends on certain criteria. The one employed here was the Otsu method as it offered very accurate distinction between the flame and the bore with the least processing time.

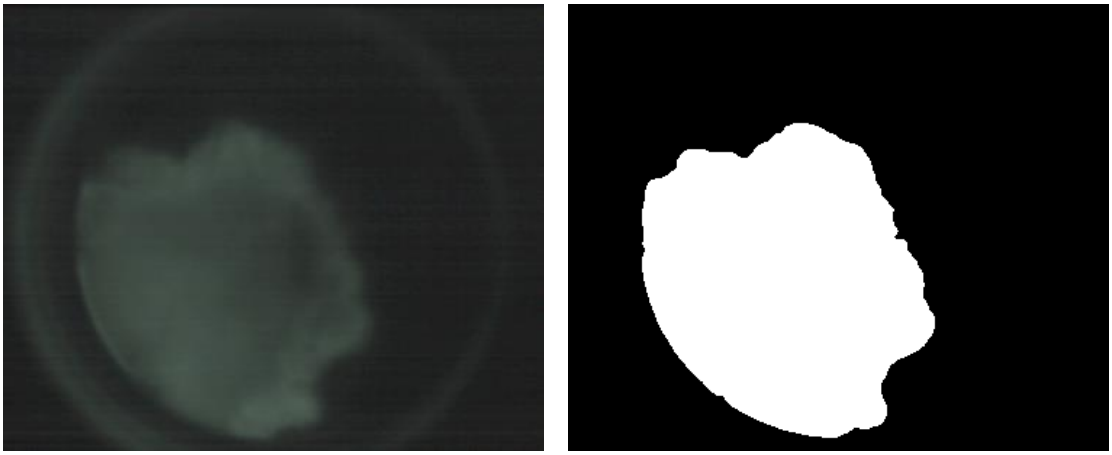

Figure 5-10: Original RGB image (Left), Binary image after processing (right)

The aim of this section of the code was to maximise the differentiation of the two regions (burnt and unburnt) and making it easier to separate the two, so the pixels of the image were divided into two classes depending on the intensity value. The spread between them could be minimised with a calculated threshold value, which was easily done by the code.

5.16 Calculations

Once the binarisation had taken place, the next stage of the code was to extract various items of data that would aid in accurate analysis of the flame including the flame area, speed, radius and flame centroid.

The centroid was identified by locating the point at which a centre of mass would be situated were the flame a solid object. So for a finite set of pixels (P_x) throughout the image, the centroid is:

$$C = \frac{\sum P_x}{K}$$

Equation 5-4

where K is the number of pixels selected in the image and $P_X = (x_i , y_i)$ represents the Euclidean co-ordinates of the pixels. Once this centroid had been identified all other calculations could be taken from here.

5.16.1 Flame Radius

This is one of the most important computed values of the flame analysis as from this many other values can be derived. Therefore obtaining the flame radius with the highest level of accuracy is a key.

The code used the best-fit circle method, an idea originally proposed by Keck [138], and used numerous times in the literature [138,150,152] to obtain the radius. This method seeks to find the flame's centre and radius by affixing a circle to the image. This

is done so that the amount of unburnt charge encompassed by the circle is equal to the amount of burnt charge.

This best-fit circle can be calculated by solving a non-linear, least-squares problem, in order to minimise the sum of the squares of the distances:

$$d_i^2 = (\|z - x_i\| - r)^2$$

Equation 5-5

where d_i is the distance between a point (x_i) and the centre of the best-fit circle (z) which possesses a radius of r. If $u = (z_1, z_2, r)^T$ this means that ũ needs to be determined so that:

$$\sum_{i=1}^{m} d_i(u)^2 = min$$

Equation 5-6

Here the Jacobian, defined by the partial derivatives $\frac{\partial d_i(u)}{\partial u_j}$ is given by:

$$\begin{pmatrix} \frac{u_1 - x_{11}}{\sqrt{(u_1 - x_{11})^2 + (u_2 - x_{12})^2}} & \frac{u_2 - x_{12}}{\sqrt{(u_1 - x_{11})^2 + (u_2 - x_{12})^2}} - 1 \\ \vdots & \\ \frac{u_1 - x_{m1}}{\sqrt{(u_1 - x_{m1})^2 + (u_2 - x_{m2})^2}} & \frac{u_2 - x_{m2}}{\sqrt{(u_1 - x_{m1})^2 + (u_2 - x_{m2})^2}} - 1 \end{pmatrix}$$

Equation 5-7

From this, using the Gauss-Newton method, the best-fit circle could be iteratively computed around a set of given points [160]. If those points are the flame front data,

then the calculated circle would equal one with a radius identical to that of the flame radius.

5.16.2 Flame Speed and Shape Factor

This value is also vital to the analysis of the flame development and the effects that charge motion or residual gas levels can have on a combustion event. As stated earlier, the flame speed is the expansion rate of the flame's radius over a set time frame – in reality it can be viewed as the radius growth rate. The time interval to analyse the two radii over was selected to be the interval between two flame images. As the camera was set to 6000 fps, this results in an interval of 125 μs. The difference between the two best-fit circle's radii could then be used to determine the speed.

The flame front analysis can be further enhanced by quantifying the developing flame front's distortion. This is referred to as the shape factor [153] and is defined as the ratio of the perimeter of the flame contour (P_c) to the perimeter of a circle whose radius is equal to that of the flame at a given crank angle (usually the radius of the best-fit circle,P_r):

$$SF = \frac{P_c}{P_r}$$

Equation 5-8

The perimeter of the flame contour was calculated via the commercially available photo-editing software Photoshop. Batch processing of the black and white images would entail importing the TIFF file, selecting the flame area and using the Measure tool within Photoshop to produce a count of the perimeter pixels of the flame shape.

Once this perimeter length had been converted to millimetres it became P_c and could be used in conjunction with the earlier calculated P_r to produce the shape factor.

5.17 Matlab Image Processing Results

Through the use of Matlab image processing, it was possible to calculate three things: flame radius, flame speed, and shape factor. Figure 5-12 illustrates the steps which led to the processing of images for a normal cycle using intensifier. During this time the intensifier was working without any burned pixels, so the results from Matlab image processing can be considered to have been reliable. As described previously, in the first step raw images convert to binary images. Then in order to find the flame radius and flame centre an imaginary circle is drawn around the flame area, which in figure illustrated by the red circle. Then, with the aim of defining the shape factor and flame wrinkle, a red line is used to highlight the flame front. Finally through the gathering together of visual data, the Matlab code makes some useful graphs like the ones which are presented in figure 5-13.

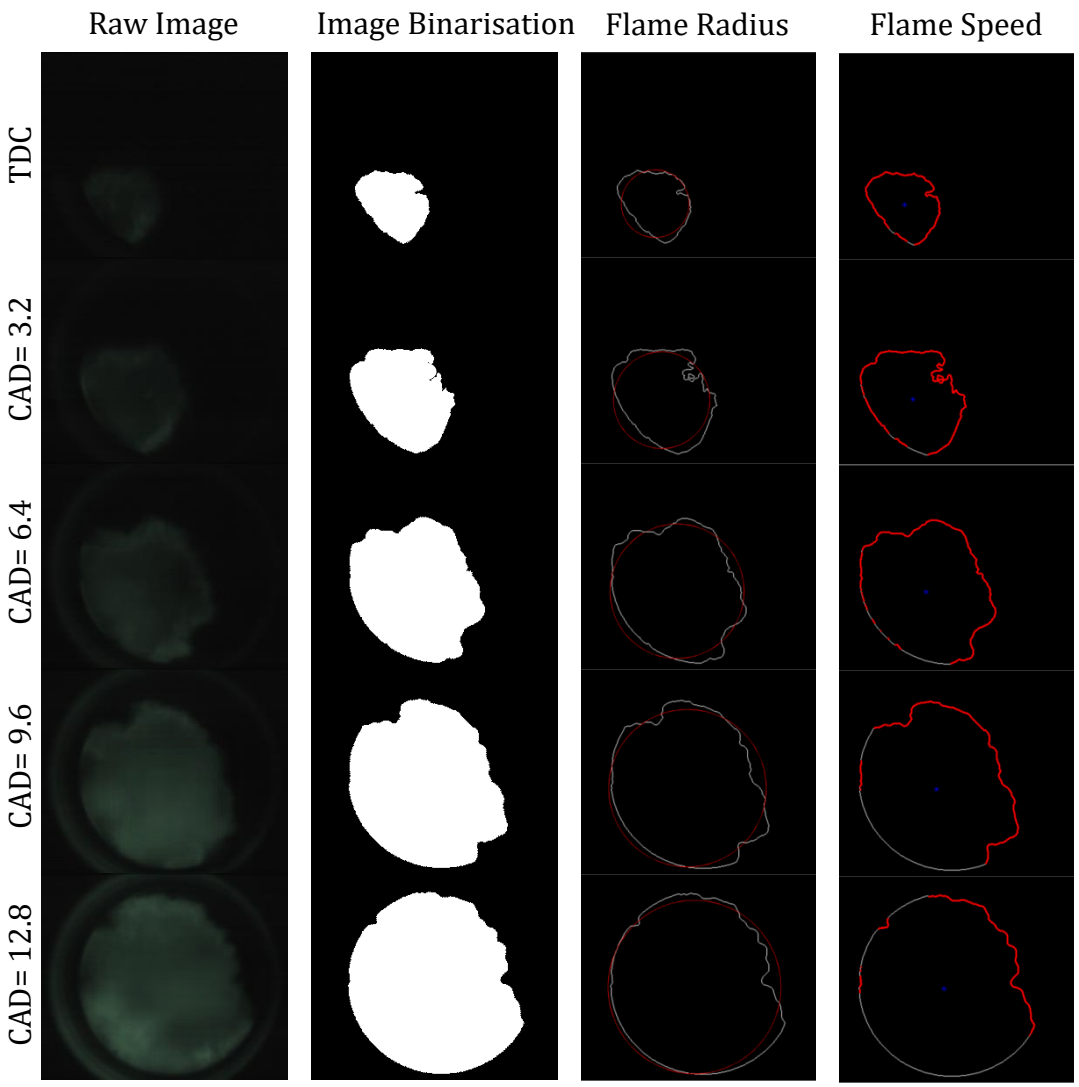

Figure 5-11: Matlab image processing

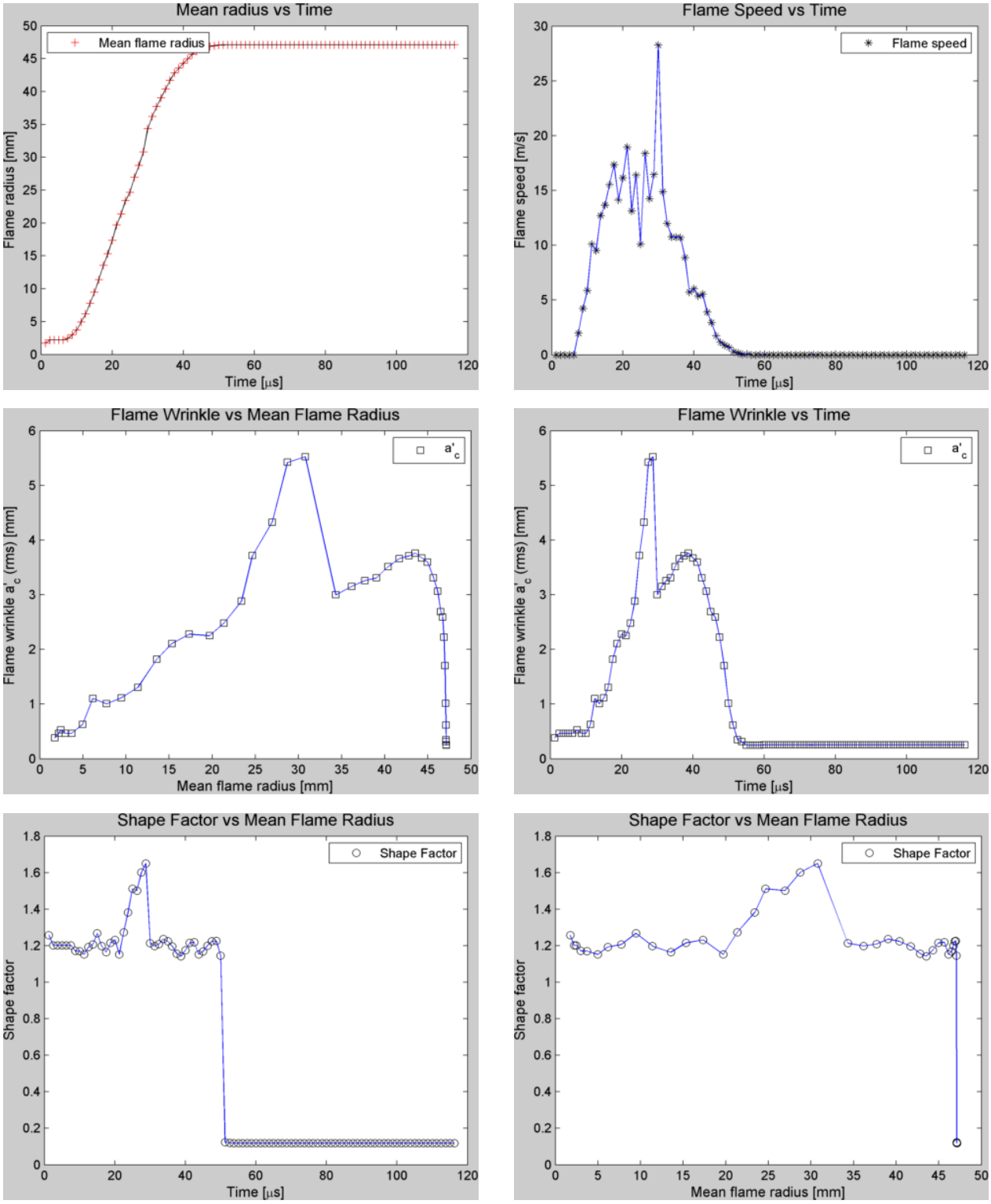

Figure 5-12: Matlab image processing graphs

5.18 Image Processing Errors

As described earlier in this chapter, it was not practical to use the intensifier in these experiments. The raw image from the camera was very dark, making it impossible to see the flame propagation in normal cycles. In cycles with pre-ignition and knock, the image was bright enough to see the flame propagation and all combustion events. The primary solution was to increase the gain in the camera settings. Figure 5-14 shows the images with different gains. At gain 0, the image was extremely dark and it was not possible for the Matlab code to recognise the flame. By increasing the gain to 3 and 6, the flame became apparent but also the horizontal noise lines were appearing on the image.

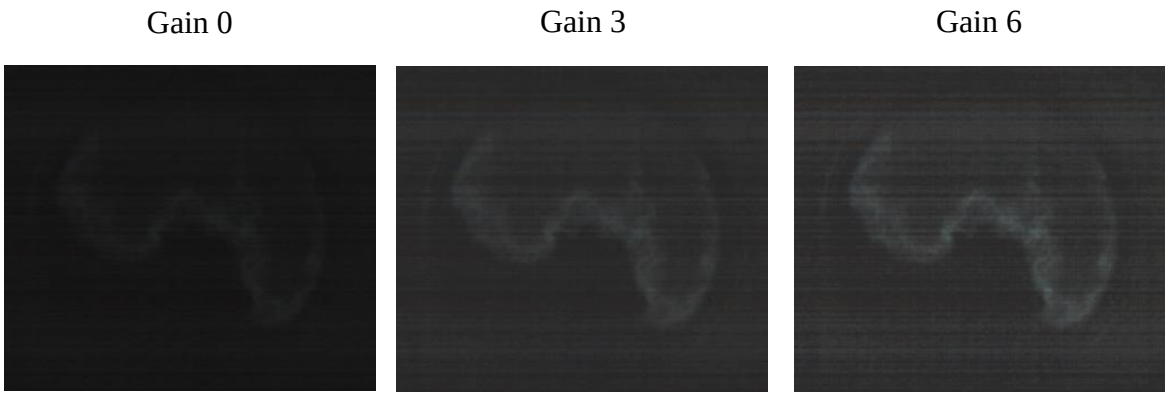

Figure 5-13: Different gain settings

Owing to noises which were apparent on the image, it was not possible to determine the flame area and the flame front clearly. In order to reduce the noise, many noise reduction technics have been tried, but they were not effective.

Figure 5-15 shows the image processing result from Matlab. As the noise level was high in the images, the code was not able to determine the flame front correctly.

Figure 5-16 shows the corresponding graphs based on the image processed earlier in Matlab. As it can be seen in this image, the results are not reliable. This is the reason why a decision was taken not to use Matlab image processing for this project.

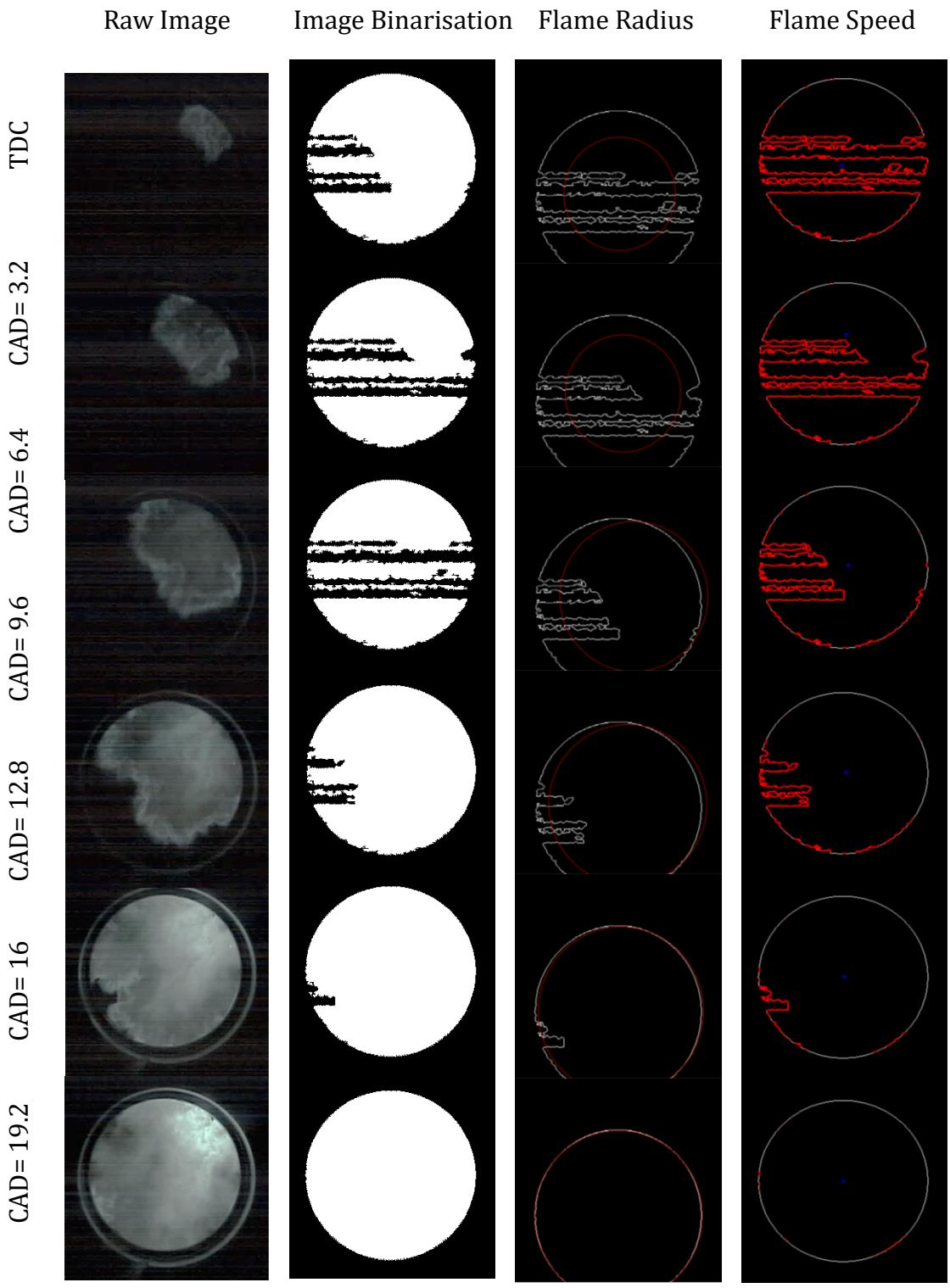

Figure 5-14: Errors in image processing

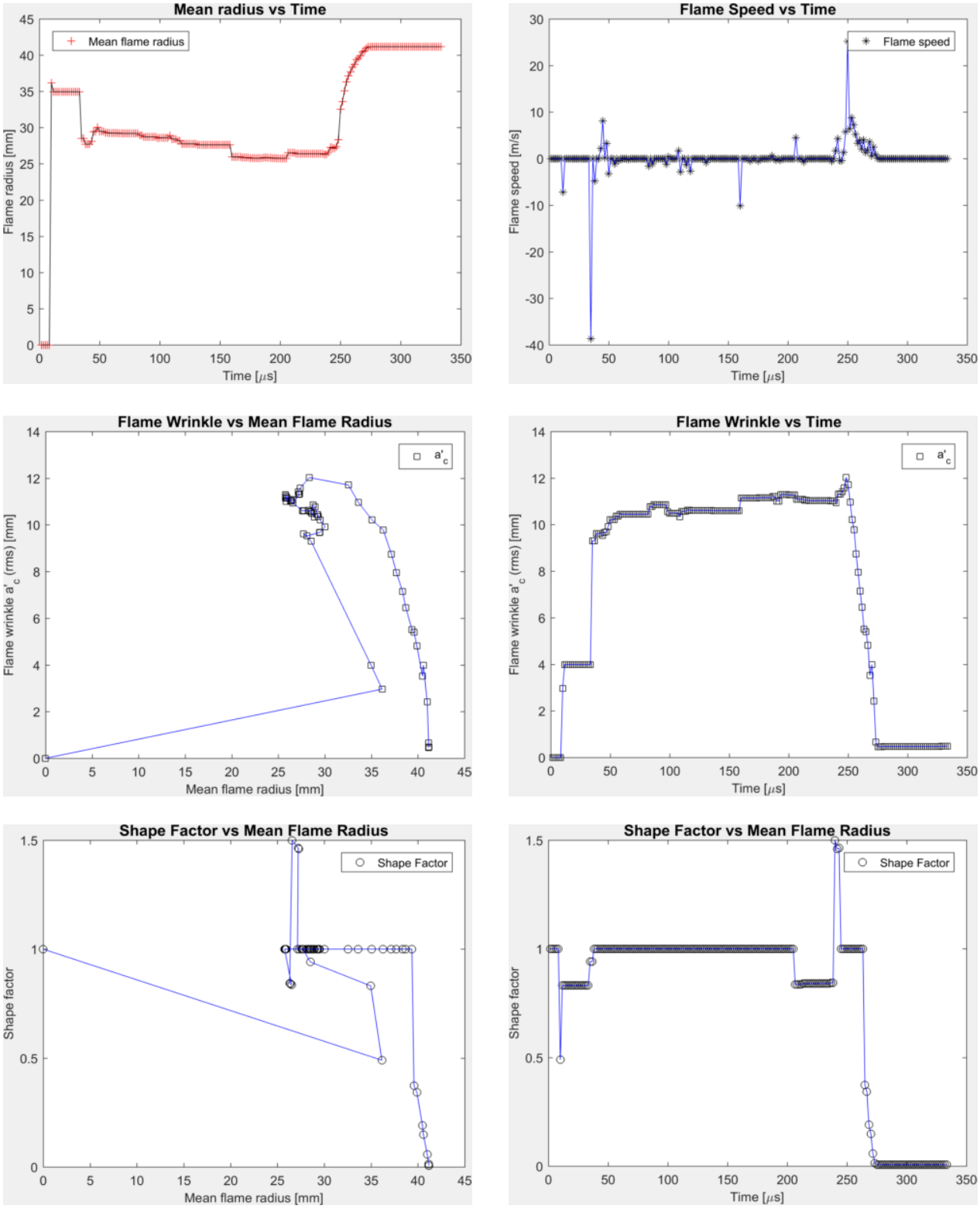

Figure 5-15: Errors in image processing

Many attempts were made to find the source of the noises on the camera. Firstly, all camera cables were isolated using aluminium foil, but the noise level was the same. Secondly, the camera was moved to other place in order to avoid any magnetic field around the engine as some high voltage cables passed over the engine cell. Again, this solution was not effective to reduce the noise. Finally it was concluded that this problem could be the result of camera age. For the last 20 years this camera was used in harsh conditions in a noisy environment. As this type of camera is so expensive, it was not possible to replace it with a new one or repair the current one. Consequently, it was decided not to use the Matlab code to analyse the images and only rely on visual analysis. Despite this limitation, considerable new information can be extracted regarding the nature of auto-ignition and knock, as will be shown in later chapters.

6 IMAGING AND ANALYSIS OF AUTO-IGNITION AND HEAVY KNOCK

6.1 Overview

This chapter involved fundamental study of auto-ignition under unusually high knock intensities. Heavy knock was deliberately induced under relatively low loads using inlet air heating and a primary reference fuel blend of reduced octane rating. Multiple centred auto-ignition events were regularly observed to lead in to violent knocking events, with knock intensities above 140 bar observed. The multiple centred events were in good agreement with the developing detonation theory proposed elsewhere to be the key mechanism leading to heavy knock in modern downsized SI engines. The accompanying thermodynamic analysis indicated lack of relation between knock intensity and the remaining unburned mass fraction burned at the onset of the auto-ignition. Spatial analysis of the full series of images captured demonstrated random location of the initial auto-ignition sites, with new flame kernels forming at these sites and initially growing steadily and suppressing further growth of the main flame front prior to violent detonation. Also the effect of oil droplets on pre-ignition and knock was examined. Analysis showed 54% of auto-ignitions initiated ahead of the flame front due to increasing temperature in this zone which was favourable to auto-ignition.

6.2 Introduction

Researchers at the University of Leeds and Shell [161] have recently postulated that Super-Knock events originate from a resonance between acoustic waves emitted by an auto-igniting hot spot and a reaction wave that propagates along negative temperature gradients in the fuel-air charge. The theory is based upon the assumption that the temperature gradient extends smoothly over sufficient length across the turbulent flow field. Subsequently, localised detonations may develop which are then able to violently ignite the remaining unburned charge in timescales of less than a millisecond. Ultimately, this can lead to catastrophic mechanical engine failure. Peters and co-workers[162,163] extended this theory developed at Leeds/Shell to at least partially attribute the random nature of the events to the stochastic nature of the in-cylinder turbulence. In the other study by Pan [164] the results show that as the decreases of octane number, knocking onset is significantly advanced due to the enhancement of low-temperature chemical reactivity. Consequently, more auto-ignition centres appear at hot exhaust valve side and even cool intake valve side at very low octane number. But for the knocking intensity, it does not always show a proportional correlation with octane number during super-knock. However, some uncertainty still remains around the triggering of these events. The pre-ignition typically occurs well below the auto-ignition temperature of the bulk charge, considered to be indicative of a deflagration caused by an exothermic centre with the high temperature gradient across it [101]. It has also been suggested that the auto-ignition might be caused by a localised volume of charge with particularly low auto-ignition temperature, such as an evaporating droplet of lubricant (or mixtures of fuel and oil due to wall impingement of a directly injected fuel spray). Such droplets, of relatively low octane number (and high cetane number), have been

suggested to cause the formation of the deflagration site(s) leading to pre-ignition and Super-Knock. To this end Dahnz et al. [165] produced a simple pre-ignition model to qualify the effects of a low-octane droplet within the main (high-octane) charge. It was found that a region existed where, given sufficient droplet temperature, ignition could be initiated below the bulk auto-ignition temperature of the main charge. When developing their theory Kalghatghi and Bradley [14] used pressure data from real engine Super-Knock cycles to show that gas-phase pre-ignition of an evaporating lubricant droplet could be possible, assuming that the lubricant droplet was substantially more reactive than n-heptane. In recent work by South-west Research Institute many lubricants were found to meet this condition [166].

With the complex nature of cyclic variations in SI engines influenced by varying turbulence, charge homogeneity, wall temperatures, deposit conditions, fuel and oil properties [102,163,165–167] it is quite probable that the stochastic pre-ignition event is caused by a combination of phenomena. However the theory of an increased likelihood of auto-ignition occurring due to suspended oil droplets has widely gained credibility. Amann et al. [168] found that, during a sequence of Super-Knock events in a multi-cylinder engine, the air-fuel ratio was significantly reduced compared to the calibrated air-fuel ratio. When extremely high intensity knocking combustion was artificially induced by intermittently advancing the spark timing, the same trend in air-fuel ratio was not observed. This observation was therefore attributed to the accumulation of lubricant during normal engine running and its subsequent release from the piston top-land crevice during Super-Knock events.

6.3 Effect of engine parameters on knock intensity

The engine geometry and in-cylinder thermodynamic characteristics have been related to auto ignition and knock intensity. The unburned zone thermodynamic characteristics can affect the onset of auto-ignition. Therefore the relationships between temperature and pressure of the unburned zone (end gas region) and the mass fraction burned (MFB) with knock intensity has been experimentally investigated and presented.

Shown in Figure 6-1 is the relationship between the knock intensity of each combustion cycle and the crank of the maximum in-cylinder pressure gradient on the upper part the graph, while trying to relate it to the lower part where heat release rate plotted against crank angle for 100 consecutive cycles. The ignition timing was set at 17° bTDC as shown by the blue vertical dotted line. In the lower part of the figure ROHR signals were used to detect pre-ignition by setting a threshold that was above the noise level. Once the ROHR of a cycle had reached this threshold it was considered to have ignited. If a cycle reached this threshold before the spark timing (-17°aTDC) then it was assumed to be a pre-ignitive cycle.

On the right-hand-side of the graph knock intensity is significantly low and the heat release rate starts climbing after spark plug ignited. In the left hand side of the figure (before ignition), as maximum heat release appears earlier, knock intensity is increased exponentially. In the right hand area, the obvious reason of knock onset is normal flame propagation followed by end gas deflagration a long time after ignition timing. Conversely on the left hand area, the knock source is related to pre-ignition happening before ignition as the heat release has rate gone up before the spark plug was energised.

The KI value variance can depict the stochastic behaviour of knock especially when it is a result of pre-ignition. Cycles 54 and 74 were selected to explain the main differences as shown in Figure 6-1. In Cycle 54, as the location of the maximum average in-cylinder pressure gradient (~14°aTDC) is closer to TDC, the related KI value is significantly higher than Cycle 74, which has a KI value of 0.7 at 26°aTDC.

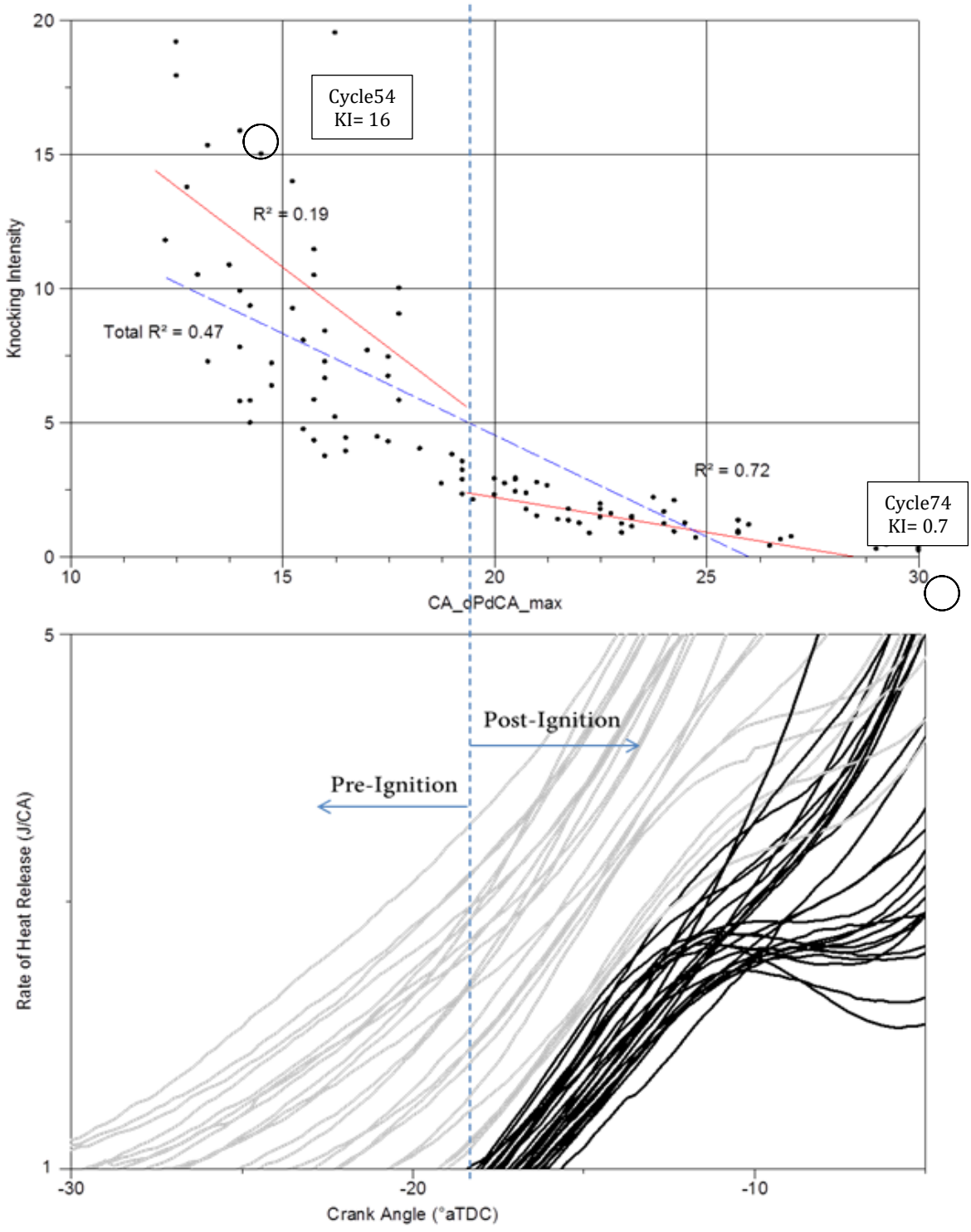

Figure 6-1 Knock intensity against location of maximum rate of change of pressure

As previously reported in the literature, knock intensity is strongly influenced by the crank angle at the onset of knock. This theory is completely in line with Figure 6-1,

where cycles with higher knock intensity are closer to TDC. Hence, it can be concluded that knock intensity correlates strongly with the temperature and pressure of the unburned gas at the onset of the auto-ignition. This dominated the effects of any other parameters. In order to investigate the effect of unburned mass on the knock intensity, from the data presented in Figure 6-1, various pre-ignited cycles with different knocking intensity (29 cycles), were selected. Figure 6-2 shows the knock intensity of these cycles plotted versus unburned mass fraction at the onset of auto-ignition for selected cycles. The method to calculate the mass fraction unburned was fully described by Karvountzis [169].

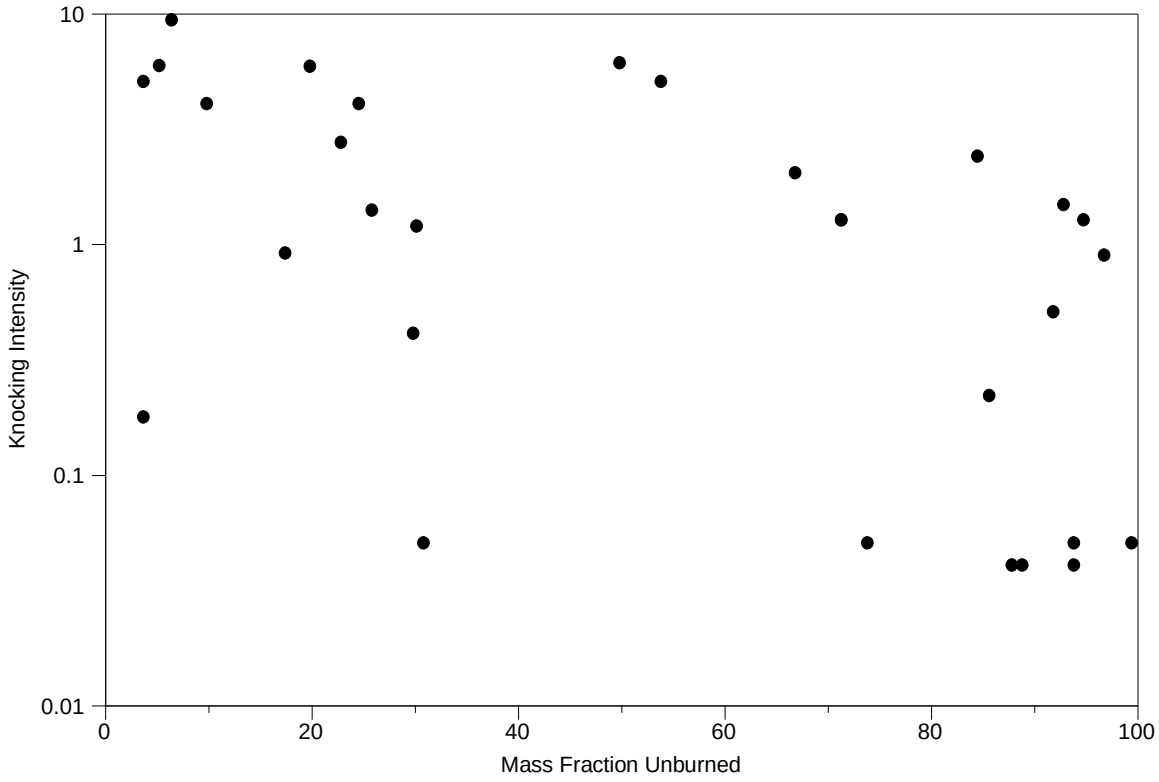

Figure 6-2 Knock intensity versus unburned mass at onset of auto-ignition

The figure clearly shows there is no relation and trend between KI and mass fraction unburned. These results are fully in agreement with the findings of Konig and Sheppard. They have shown experimentally, for a given engine running condition, that the knock intensity of a knocking combustion cycle was closely linked to the crank angle location of knock onset[98]. Also they concluded that knock severity was relatively independent

of the mass of unburned gas calculated to be available at the onset of auto ignition; increasing with the estimated unburned gas temperature upon auto ignition.

The crank angle location of knock onset may be approximated by the location of the maximum average in-cylinder pressure gradient (CA_dP/dCA_max).

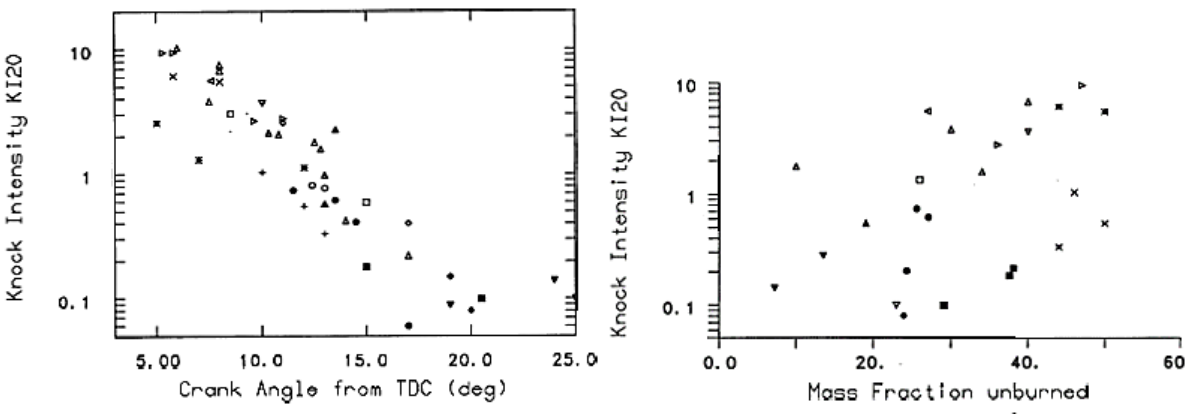

Figure 6-3 KI Vs. crank angle (left), KI Vs. mass fraction unburnd (right) adopted from [12]

More investigation on these cycles exposed the on-off behaviour of the knocking cycles. In this work 90% of heavy knocking cycles were followed by normal or light knocking cycles. Figure 6-4(A) presents a 'return map' of knock intensity. As highlighted on the graph, a cycle with a high KI value was followed by a cycle with notably lower knock intensity. Figure 6-4(B) demonstrates the KI for all selected cycles.

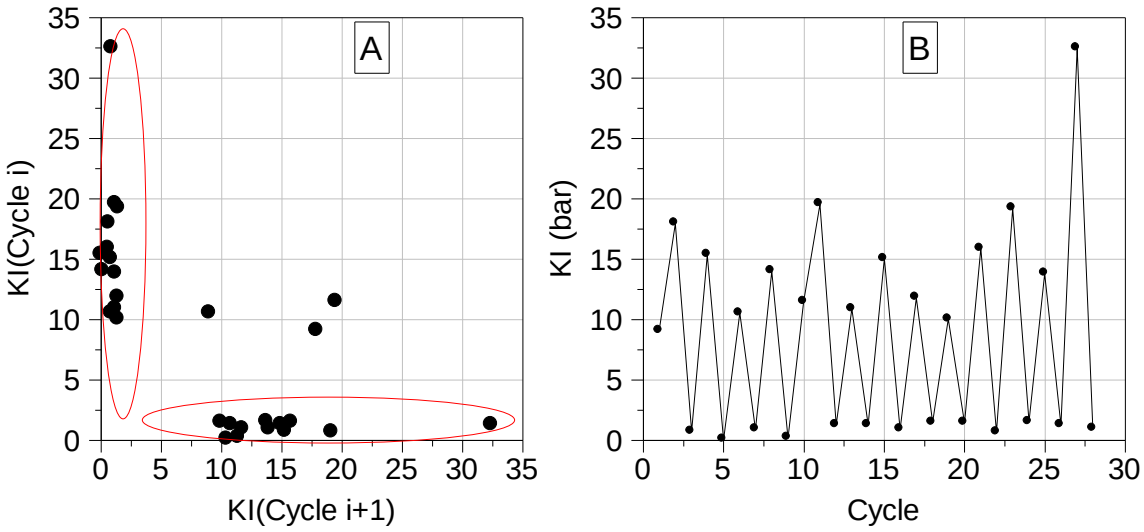

Figure 6-4 On-Off behaviour of heavy knocking cycles, a) return map, b) knock intensity vs cycle number

6.4 Optical Analysis of knocking combustion

6.4.1 Effect of auto-ignition onset on knock Intensity

Shown in Figure 6-5 is an optical analysis of light and heavy knocking cycles in different crank angles captured using the high speed camera at 6000 fps. As has been discussed previously, in a cycle with higher knock intensity (37 bar), the end gas auto-ignition occurred after 8.1 °aTDC. On the other hand, in the cycle with lower knock intensity (KI=3.2), the auto ignition started considerably later around 17°aTDC.

Also it is possible for cycles with the same KI values to have differing onset of pre-ignition as it is not a dominant factor. All of the evidence showed the stochastic nature of combustion and cycle-by-cycle variations in a spark ignition engine [38]. Shown in Figure 6-6 are three cycles with a KI around 16 bar. In Cycle A, detonation occurred at crank angle 8.1°aTDC while for Cycles B and C it happened at 13.5°aTDC and16.2°aTDC respectively.

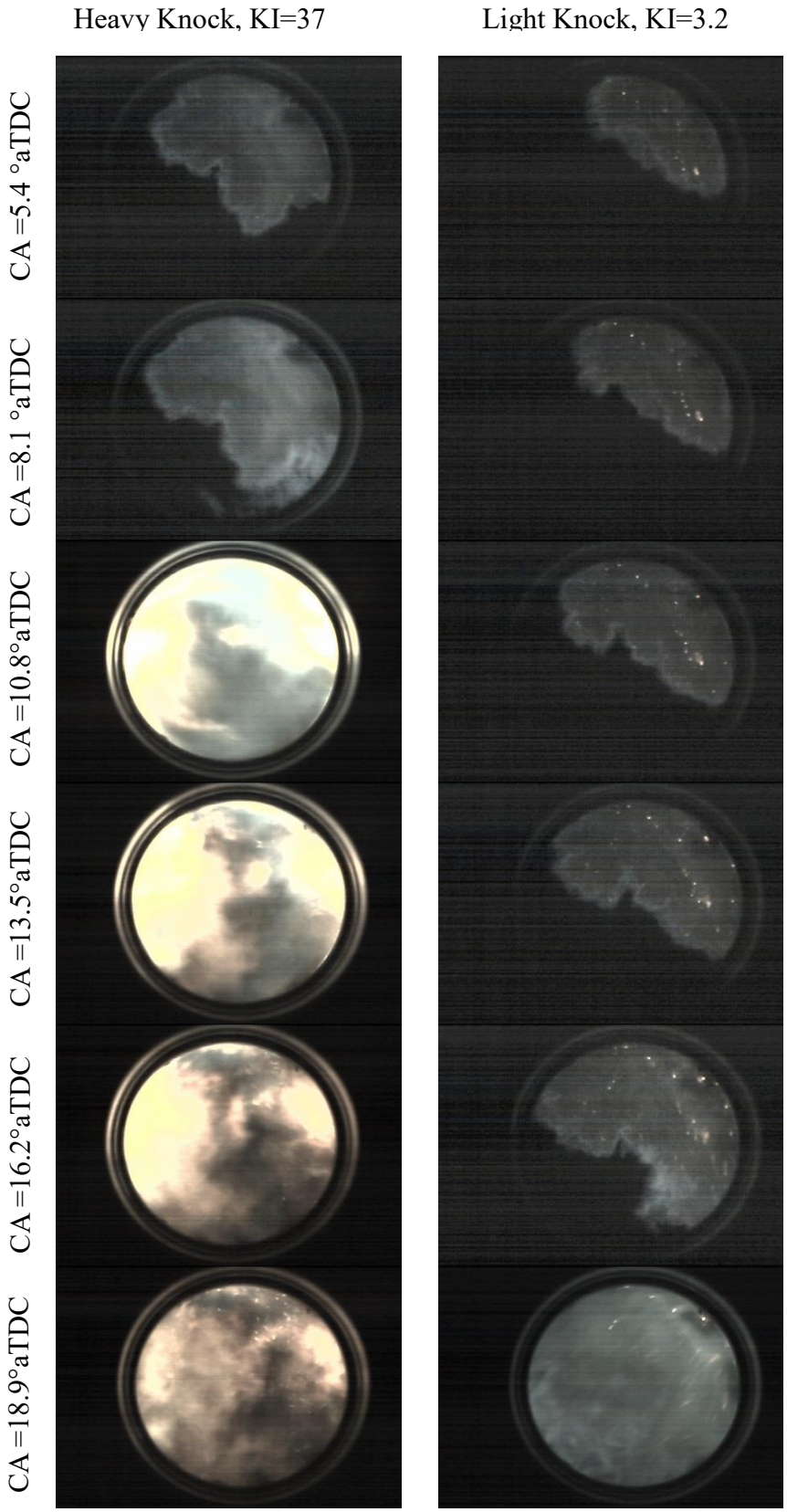

Figure 6-5 Optical analysis of heavy vs. light knock

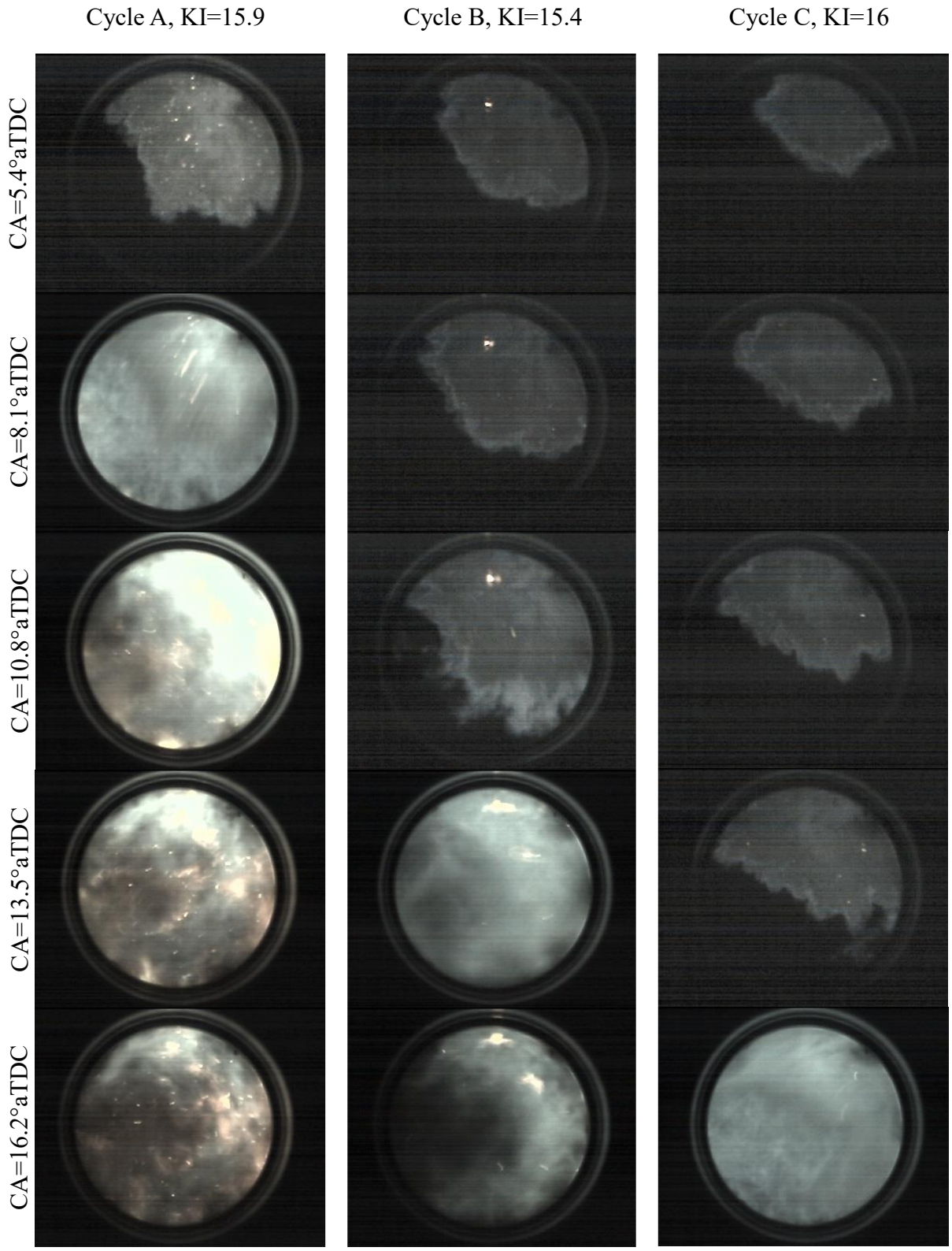

Figure 6-6 Cycles with same KI but different timing for onset of auto-ignition

6.4.2 Effect of oil droplets on pre-ignition and knock

During the heavy knock tests, there was some optical evidence showing burning oil could cause pre-ignition in the combustion chamber. There are many reasons for engine oil to become gas-borne in the combustion chamber naturally and one main reason could be release from the wall following dilution with fuel. Also ring malfunction or over filling the engine oil could result in the oil entering the combustion chamber. Figure 6-7 shows both thermodynamic and optical data for cycle with a huge amount of oil in the combustion chamber. The photo has been taken exactly at spark timing as shown on the top right corner of the frame. Remarkably, pre-ignition happened far before the spark plug ignited and the flame had propagated across almost one third of the combustion chamber by that time. The high pressure and temperature of this pre-ignition later led to heavy knock. As the graph shows both normal and heavy knocking cycle, the cycle with oil has higher in cylinder pressure and knock intensity.

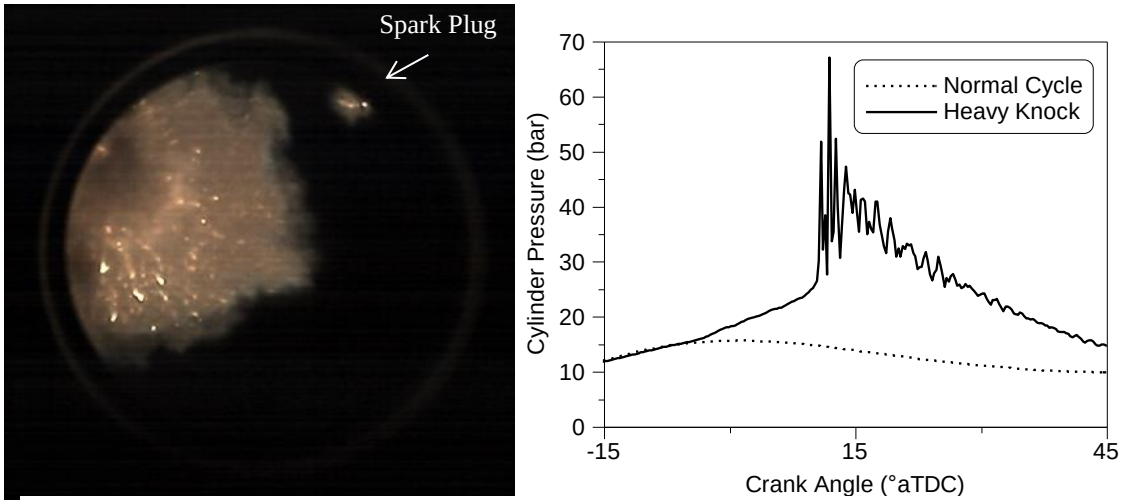

Figure 6-7 Heavy knock caused by oil in combustion chamber

In addition to above discussion about leakage of the engine oil into the combustion chamber, after considering more than 500 cycles with optical data another theory arose. A more detailed investigation showed a considerable amount of engine oil in the combustion chamber in the cycle immediately after heavy knock. Figure 6-8 shows some optical evidence of oil droplets present in the combustion chamber after heavy knock. As is clearly shown, all of the bright particles inside the flame front are burning

oil droplets. Interestingly, all cycles after heavy knock which have a huge amount of oil released, have lessen knock intensity in compare to previous cycle. The reason could be cooling effect of oil droplets in combustion chamber and lower pressure and temperature of unburned gas. In most samples, knock intensity reduced more than 50% in the next cycle.

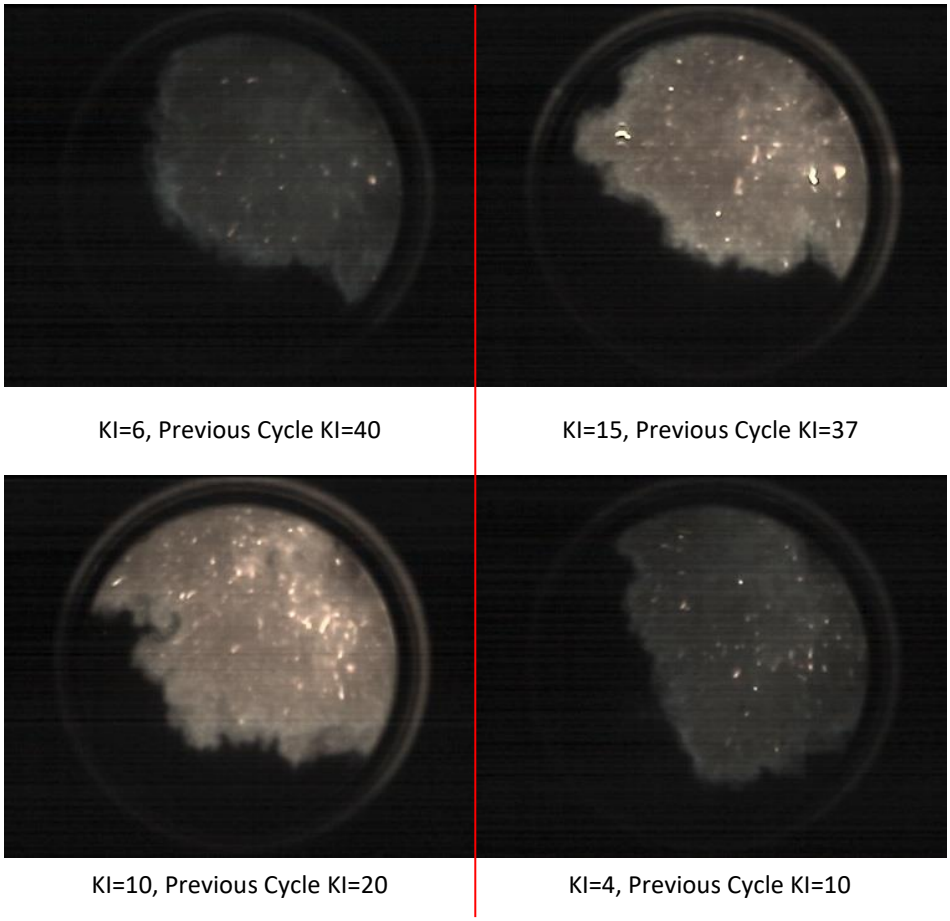

Figure 6-8 Optical evidence of oil existence in combustion chamber after heavy knock

It has been proved that heavy knock would make a pressure waves travelling at the speed of sound in combustion chamber [170][171]. Shown in Figure 6-9 is the in-cylinder pressure wave after heavy knocking cycle. The wave has frequency of 4.96 Hz which is in the boundary of sound wave frequency. These pressure waves may lead to vibration in the piston and piston rings, which might cause sealing issues. In consequence, significant of oil droplets would be exist in the next cycle. This observation is in agreement with recent study by Kawahara [172]. After visualization of

auto-ignition and the pressure waves that occurred during knocking, he noted that the auto-ignition and pressure waves caused the thermal boundary layer to breakdown near the cylinder wall and piston head, therefore combustion of the lubricant oil grease was visible inside burned gas region. In this work it was also noted that the oil would stay within the engine for multiple cycles and lead to successive on-off knocking events.

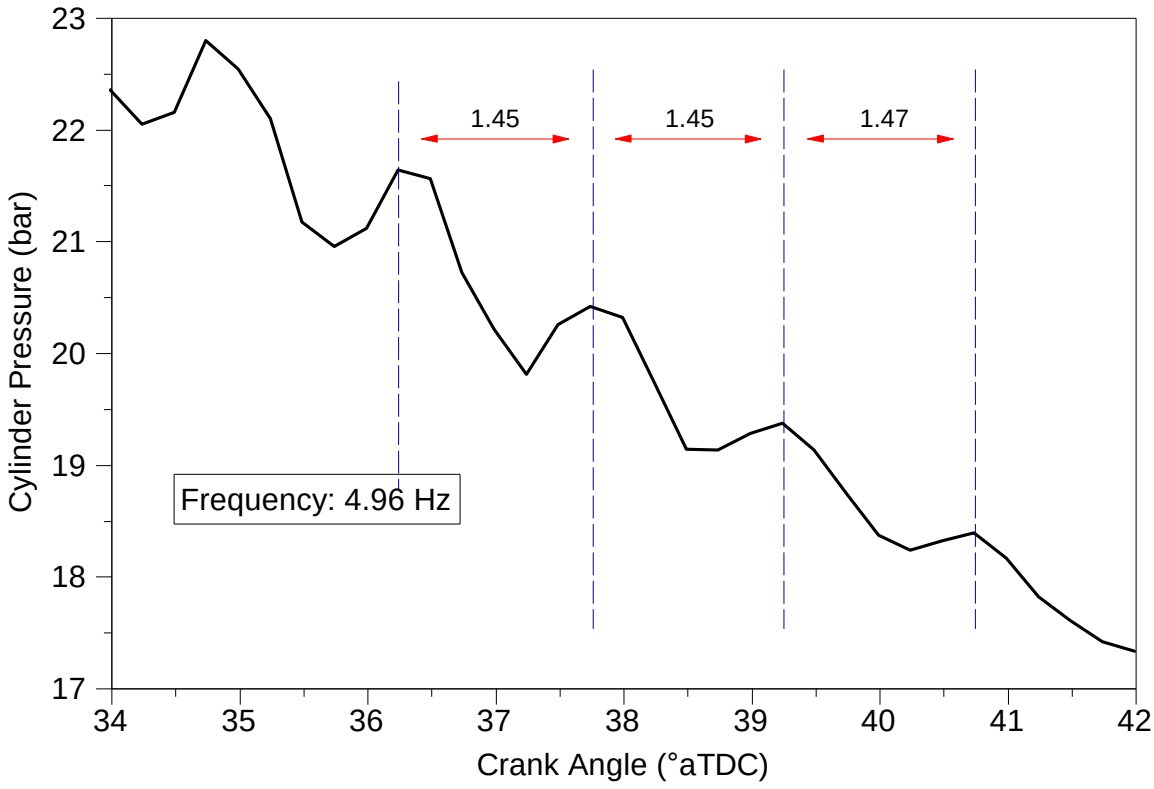

Figure 6-9 frequency of pressure waves after heavy knock

6.4.3 Locations of auto-ignition onset

In the experimental investigation more than 500 cycles were captured using natural light photography. Although the frame rate of the camera was not adequate to determine the knock inducing process, some indication of end-gas auto-ignition prior to knock could be observed in all knocking cycles. In most of the cycles multiple auto-ignition sites appeared as shown in Figure 6-10. This photo could prove the developing detonation theory optically for the first time.

Figure 6-10 Blown-up view of the multiple auto-ignition initiation sites observed during the tests

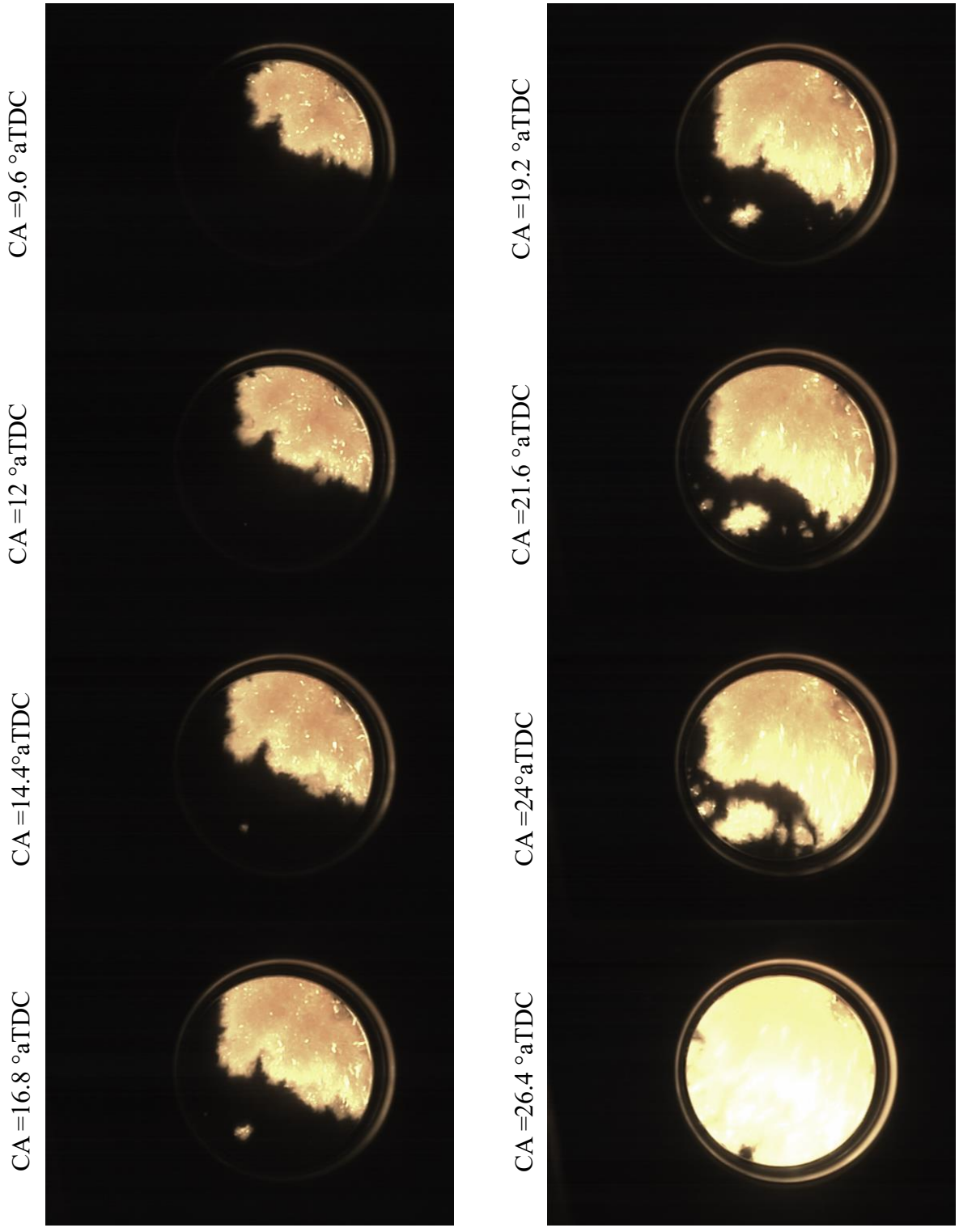

Figure 6-11 Knocking cycle showing the multiple auto-ignition initiation sites

Such multiple centres were regularly noted under heavy knocking conditions, in good agreement with prior developing detonation theory [14,99,102]. Also Kawahara [172]

noted that the explosive detonation reaction may be composed of many individual detonation reactions. Furthermore, the end zone becomes sufficiently conditioned or sensitive so that many seprate areas become centres for starting detonation reaction. Shown in Figure 6-12 is the relation between knock intensity and number of auto – ignition sites. It could be depicted from the graph that most of the heavy knocking cycles have multiple auto-ignition centroids. The cycle with highest knock intensity has one auto-ignition site. It could be end gas detonation where all of the unburned fuel exploded at once (or there were many different sites but the frame rate was not fast enough to capture them). Althogh Figure 6-12 shows the trend of lower knock intensity with more sites of auto-ignition, there is a possibility to observe different auto-ignition sites adjacent to each other as one or two sites.

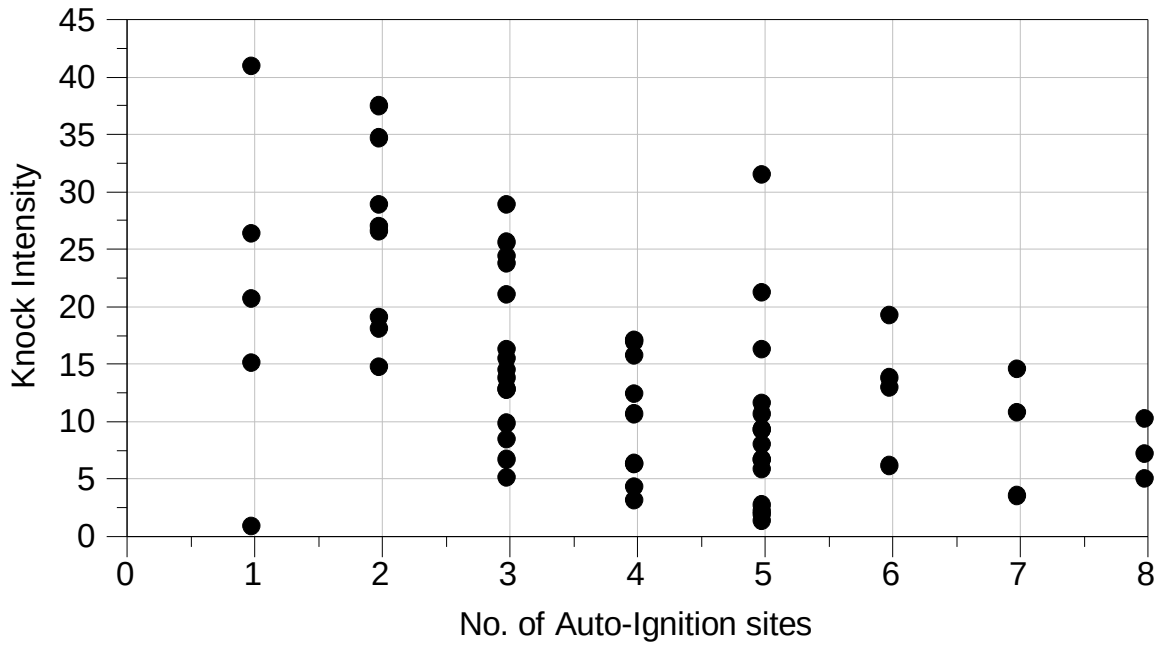

Figure 6-12: Relation between KI and auto ignition sites

The apparent initial locations of the auto-ignition were found to vary between cycles. All photos have been examined and classified in terms of three auto-ignition site locations:

a) Auto-ignition onset within the end-gas at a location between the flame front and the cylinder wall

b) Auto-ignition onset close the cylinder wall (more like end-gas auto-ignition)

c) Auto-ignition onset near the exhaust port

The examples in Figure 6-13 show the distribution of auto ignition onset locations for three different cases.

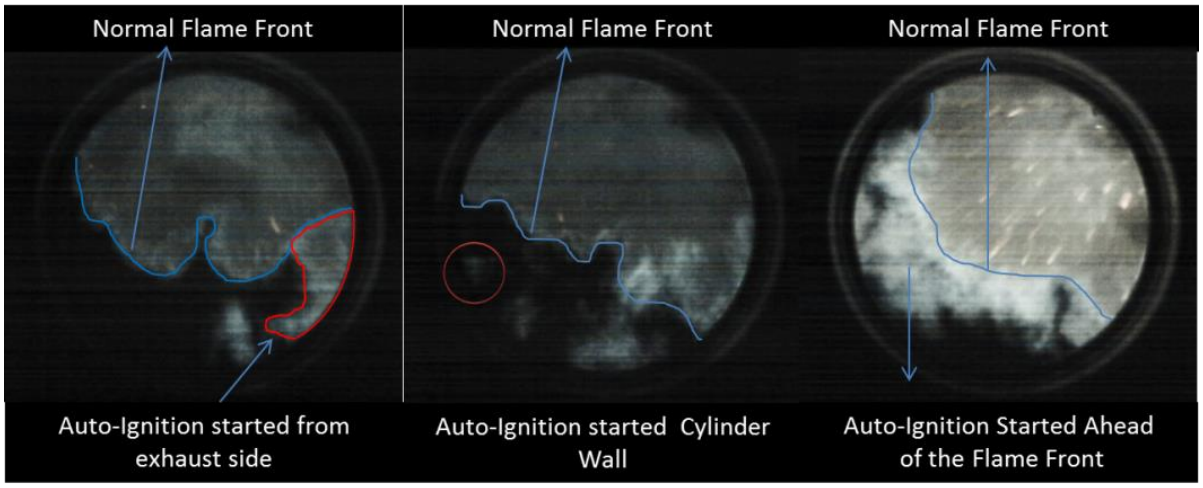

Figure 6-13 Demonstration of different auto-ignition site locations

Figure 6-14 illustrates the engine overhead schematic and percentage of auto-ignition in different locations. More than half of the auto-ignitions happened ahead of the flame front as pressure and temperature of the unburned gas are continuously increasing. Also end-gas knock was monitored in this section. The hot temperature of the exhaust port and the tendency of the air-fuel mixture to auto-ignite under higher temperatures was the reason for roughly one third of the cycles (32%) to have onset of auto-ignition close to exhaust port. The occurrence of auto-ignition near the walls is less likely. In the study

by Gerhard Konig[173] he noted this is possibly associated with a lessen concentration of reactant, due to boundary layer hydrocarbons and comparatively lower cylinder wall temperature.

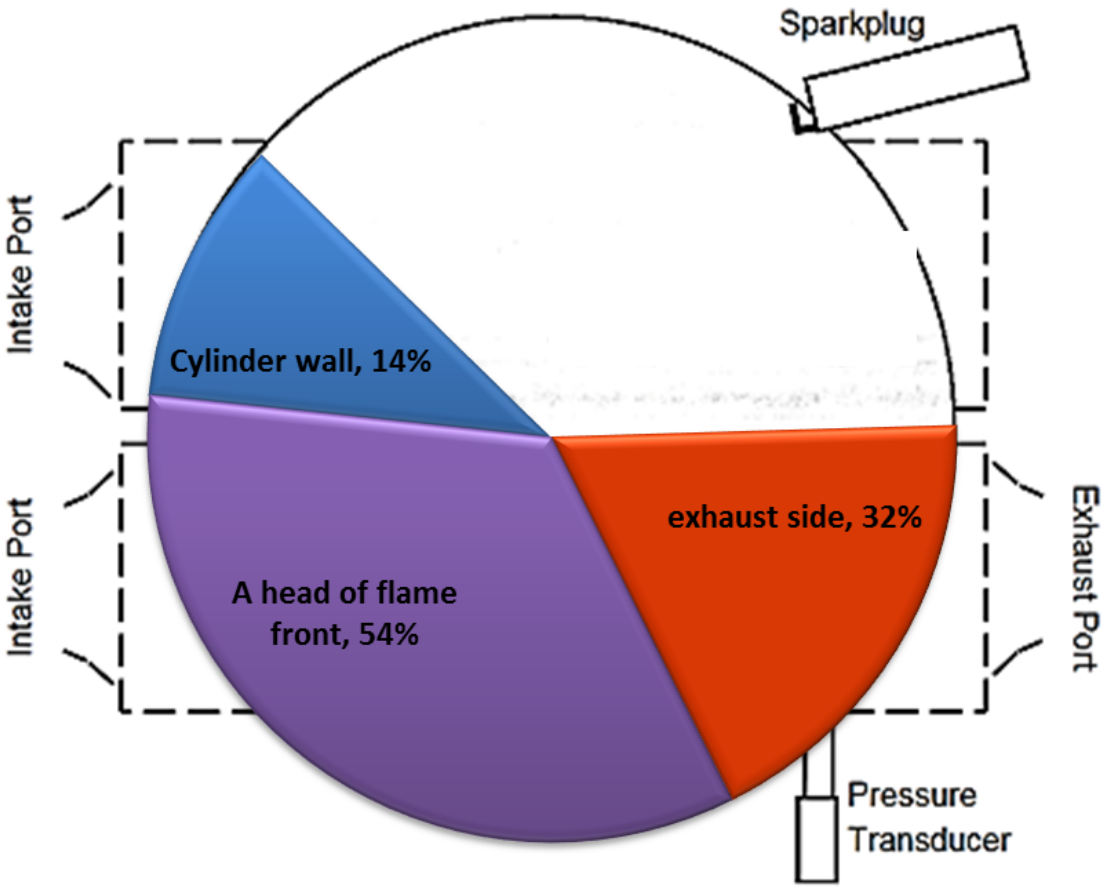

Figure 6-14 Overhead schematic of cylinder head, auto-ignition locations

6.5 Conclusion

The chapter involved the study of auto-ignition and heavy knock in an optical spark ignition engine.

It was observed that knock intensity is more affected by the crank angle of auto-ignition onset and that this is heavily dominant compared to other parameters. Also the results indicated 90% of heavy knocking cycles followed by normal or light knocking cycles, confirming the previously well reported 'on-off' nature of knocking combustion

Full bore chemiluminescence imaging confirmed multiple centred auto-ignition sites as a proof of developing detonation theory.

Also the optical analysis showed 54% of auto-ignitions initiated ahead of the flame front due to higher pressure and temperature in this zone which was favourable for auto-ignition.

Overall, the results highlight some key phenomena influencing the likelihood of auto-ignition and knock. However more investigation is needed on the auto-ignition sites and the sporadic natural release of oil droplets in the combustion chamber. Future work should consider the effects of heavy knock on exhaust temperature and emissions during heavy knocking cycles in real metallic engines.

7 THE COMPETING CHEMICAL AND PHYSICAL EFFECTS OF TRANSIENT FUEL ENRICHMENT DURING HEAVY KNOCK

7.1 Overview

The experimental work discussed in this chapter was concerned with improving understanding of the competing effects of the latent heat of vaporization and auto-ignition delay times of different ethanol blended fuels during heaving knocking combustion. Heavy knock was deliberately induced under moderate loads using inlet air heating and a primary reference fuel blend of reduced octane rating. High-speed chemiluminescence imaging and simultaneous in-cylinder pressure data measurement were used to evaluate the combustion events. Under normal operation the engine was operated under port fuel injection with a stoichiometric air-fuel mixture. Additional excess fuel of varied blend was then introduced directly into the end-gas in short transient bursts. As the mass of excess fuel was progressively increased a trade-off was apparent, with knock intensity first increasing by up to 60% before lower unburned gas temperatures suppressed knock under extremely rich conditions. This trade-off is not usually observed during conventional low intensity knock suppression via over-fuelling and has been associated with the reducing auto-ignition delay times outweighing the influence of charge cooling and ratio of specific heats. Ethanol has the highest latent heat of vaporization amongst the other fuels directly injected and was more effective to

reduce knock intensity albeit still aggravating knock under slightly rich conditions. Overall, the results demonstrate the risks in employing excess fuel to suppress knock deep within a heavy knocking combustion regime (potentially including a Super-Knock regime).

7.2 Introduction

Most of materials in this section have been discussed extensively in chapter 2and here are a quick review and some additional point.

One of the most promising methods from improving gasoline engine efficiency is engine downsizing. The basic principle is to reduce the capacity of the engine and hence enforce a large proportion of operation to higher loads. As a result of the under wider open throttle conditions the pumping losses are reduced for a given road load requirement. In order to maintain adequate vehicle acceleration and top speed, the smaller engine must be pressure-charged and still produce acceptable transient response.

Such downsizing clearly yields significant part-load fuel consumption benefits, but significant challenges remain including problematic combustion. Downsizings (and “downspeeding”) enforce a considerable proportion of "real world" operation to the low speed high load regime. Under such conditions the increased energy density of a highly pressure charged mixture leads to an increased tendency for the fuel and air to auto-ignite. This phenomenon sometimes referred to as Low Speed Pre-Ignition (LSPI) and "Super-Knock", has been associated with low-to-moderate thermal gradients within the unburned charge leading to developing detonation events. Ultimately, this may produce multiple high frequency and intensity pressure waves within the cylinder that may

interact and ultimately destroy the engine. In existing downsized engines the phenomenon is avoided by running fuel rich, where the charge cooling properties of the excess fuel reduce pre-ignition tendency at the expense of poor fuel consumption and vastly increased tailpipe emissions (given the three-way catalyst is no longer effective). Such operation is clearly not sustainable, particularly in light of the real world driving cycles currently being proposed with the EU and elsewhere to cover a wider area of engine operation in the future. Hence the current Chapter was concerned with evaluation of the transient effects of intra-cycle overfuelling as a potential method to allow improved efficiency in future real world cycles. In addition the work was intended to demonstrate the trade-off between increased charge cooling and reducing ignition delay when suppressing knock by varying rich conditions in a real engine.

7.3 Direct Fuel Injection Optimization

In order to optimize the injection strategy for direct injection, Start of Injection (SOI) and Injection Duration (ID) sweeps were undertaken using 75RON fuel only. Set out in Figure 7-1 are the cycle by cycle values of average knock intensity with and without additional direct fuel injection, with the Direct Injection Start of Injection (DI SOI) timing set to 60°bTDC and DI pulse width set to 7ms.

In Figure 7-1, the red dashed line superimposed represents the activation signal sent to the DI injector. The average values of Knock Intensity (KI) before and after the direct injection were 7.7 bar and 0.48 bar respectively. It can be seen that knock was largely suppressed and returned to similar levels when the over-fuelling was deactivated after

~30 cycles, albeit marginally lower in magnitude (KI ~6.3bar). This was associated with the lower peak gas temperatures during non-knocking combustion and differences in wall heat transfer. The differences in the in-cylinder pressure development are more apparent when observing the waterfall plot in Figure 7-3, which shows a cropped selection of cycles immediately before, during and after the over-fuelling event. Overall, the result confirmed the experimental setup, with the elimination of knock associated with the previously well reported charge cooling effect of a relatively high amount of excess fuel introduced within the cylinder [60].

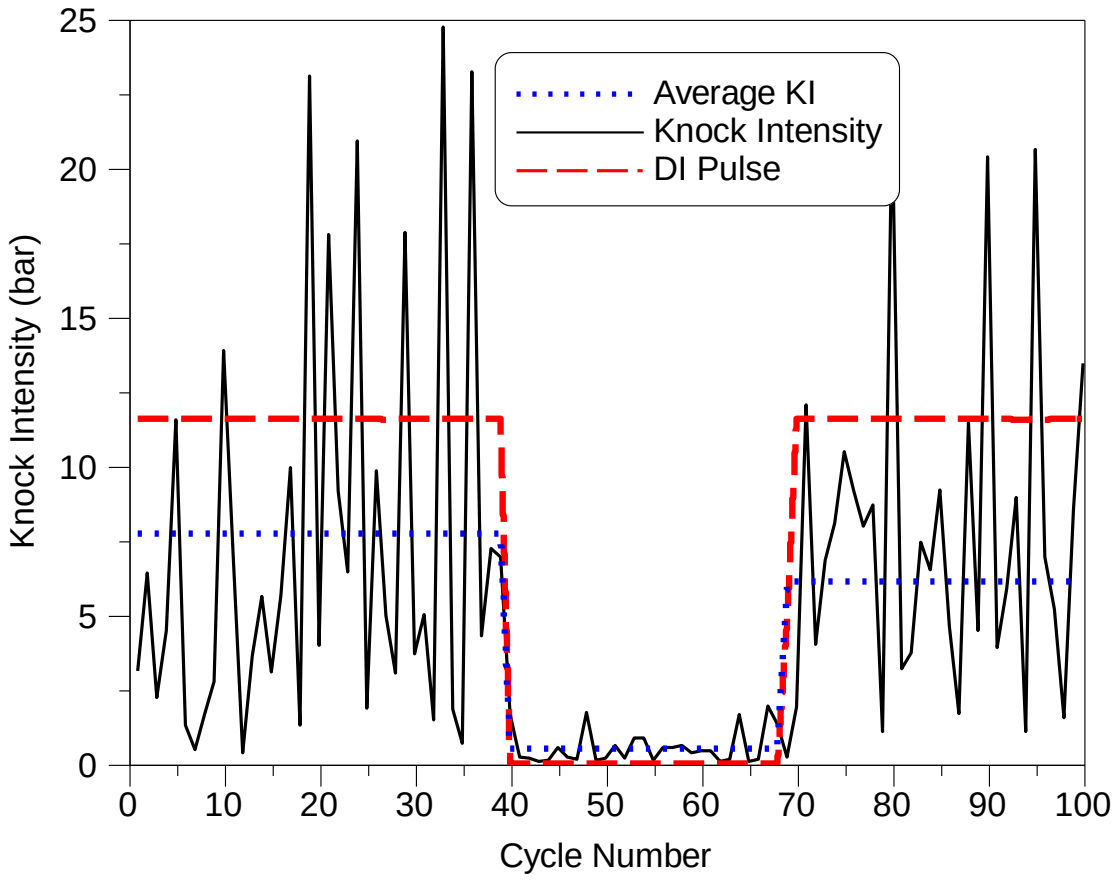

Figure 7-1 Knock intensity versus engine cycle number before, during and after the fast over-fuelling

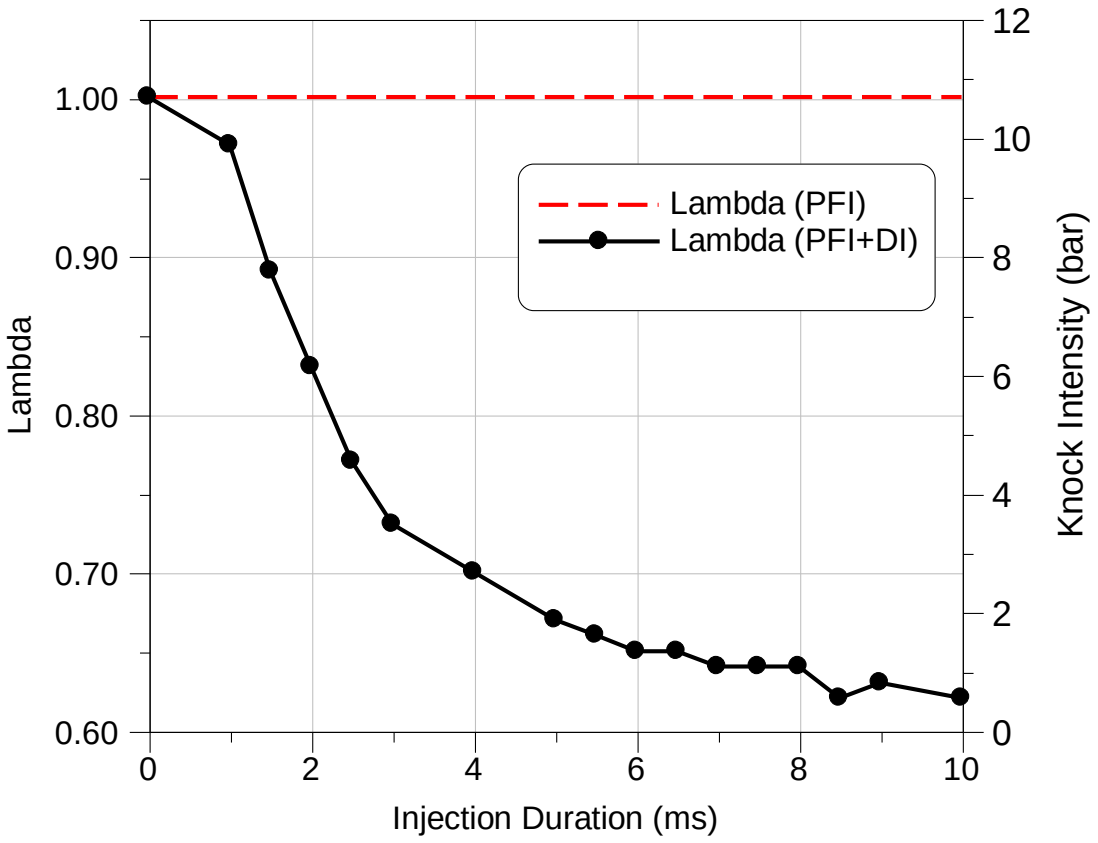

Figure 7-2 Injection duration sweep for different cycles during the PFI + DI for 75 Ron fuel

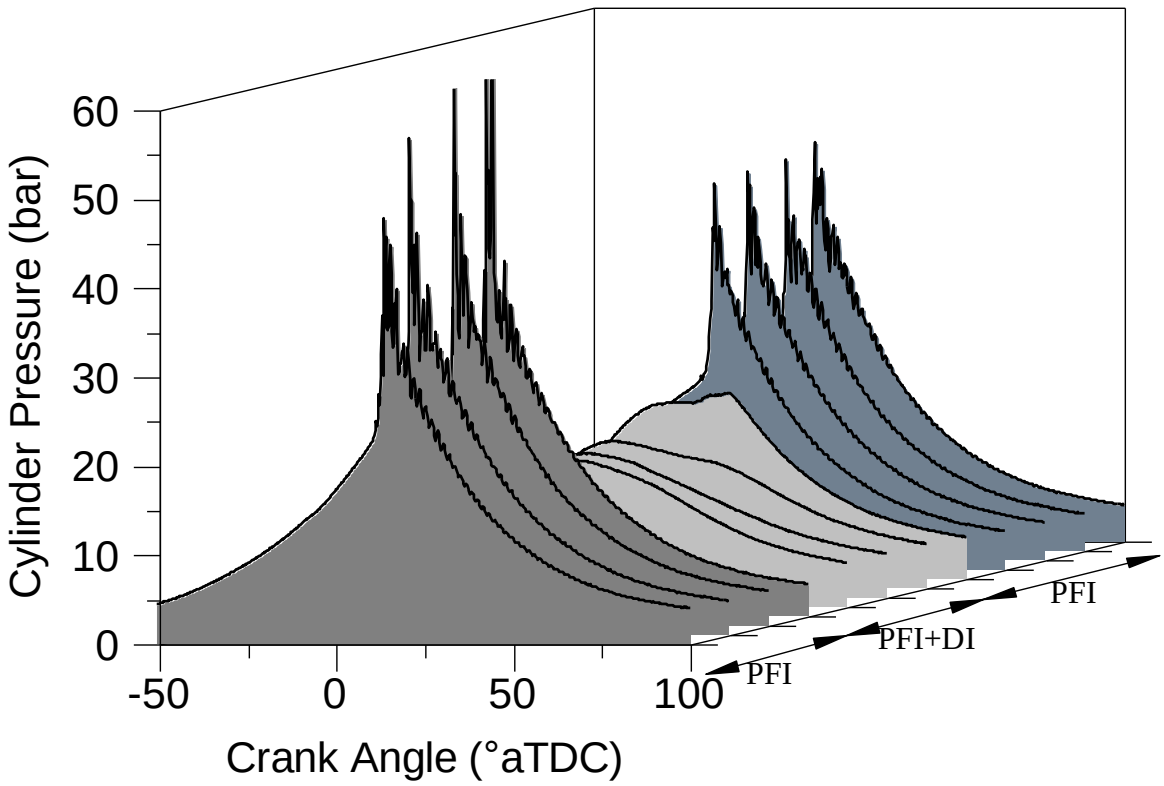

Figure 7-3 Waterfall plot showing the differences in the in-cylinder pressure development before, during and after additional direct fuel injection

7.4 Start of Injection Timing Sweep

A DI SOI timing sweep was undertaken to establish response to varying fuel stratification, as might be experienced during real transient engine operation and/or advanced knock control in modern DI engines. As reported in [18], the earlier the injection timing, the more homogeneous the fuel/air equivalent ratio field. The resultant effect is usually lower CO emissions and higher combustion efficiency when operating at stoichiometric conditions. It is also important to note that the mixture formation homogeneity, bulk fluid motion and turbulence intensity during the compression stroke

can be strongly affected by direct injection. During direct injection, the induced fluid motion interacts with the bulk air motion.

Throughout the sweep the DI fuel pressure was left fixed at 65bar. This left two variables; injection timing and additional fuel mass (or pulse width). In initial work, the pulse width was fixed to a relatively high value of 7ms (estimated to be an upper limit given the above result) and the SOI timing swept from 120° to 20°bTDC firing in intervals of 5° crank. The results are set out in Figure 7-4, where the solid black dots denote the value of average KI measured immediately prior to each DI activation (i.e. PFI only, included to show the consistency of the baseline knocking cases) and the stars denote the average KI when the direct injection was activated. When the direct injection was advanced to 60°bTDC or earlier the knock was appropriately suppressed, with sufficient time remaining for the additional fuel mass to mix into the end gas region (albeit the remaining degree of stratification was unknown). With later injection timings the knock intensity progressively increased, with average KI values as high as ~3bar but with some individual cycles exhibiting knock intensities of up to 12 bar at the latest injection timings studied. The excess fuel suppresses the knock via two well-known mechanisms. Firstly, the charge cooling effect associated with evaporation of the fuel and secondly the reduced ratio of specific heats under richer conditions leading to lower end-gas temperatures after compression, as previously demonstrated in a real multi-cylinder DI engine [175]. However, it is important to note that auto-ignition delay times reduce under rich conditions, which becomes more important when using excess fuel under severe knocking conditions as discussed in more detail below.

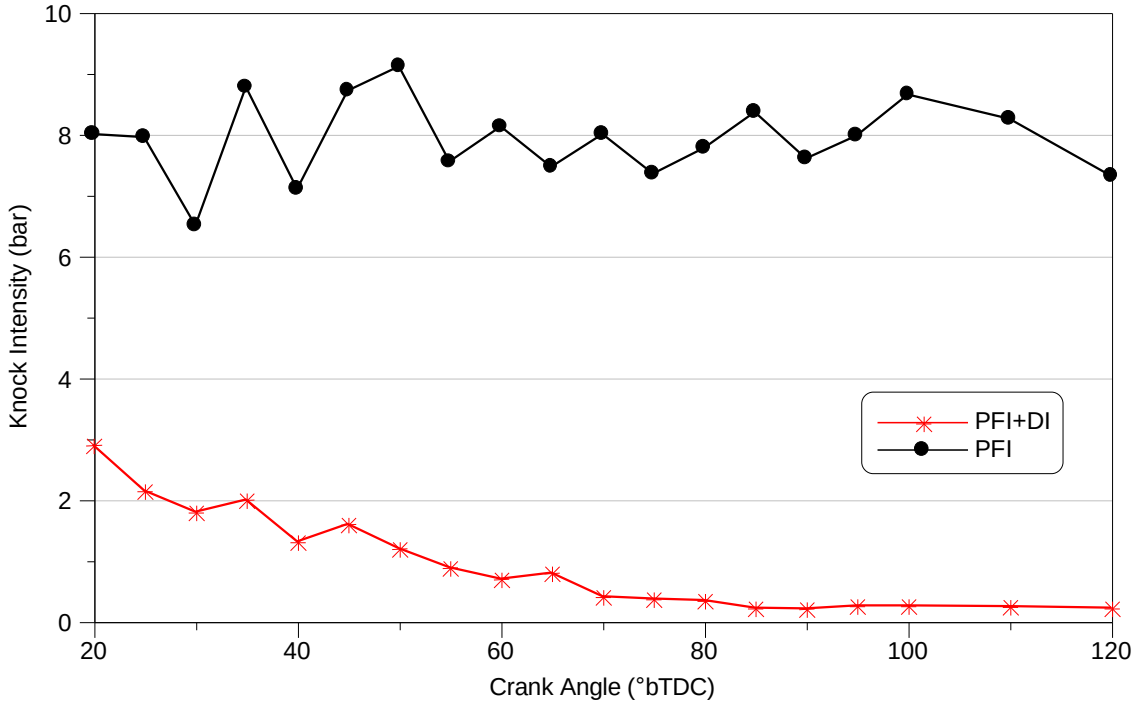

Figure 7-4 Start of direct injection timing sweep under fixed direct injection pulse width and rail pressure

Shown in Figure 7-5 are key thermodynamic values during the injection timing sweep. It should be acknowledged that the engine was operating at the stability limit under PFI only, due to the running conditions necessary to invoke heavy knock. As the DI was introduced it can be seen that the stability fell well below the COV of IMEP threshold. This was associated with advanced and faster combustion. In turn the output of the engine increased. Clearly some stratification in the DI fuel was favorable to burning rate and knock suppression, presumably due to richer local conditions in the end gas prior to the onset of auto-ignition. These observations appear to be in good agreement with those of Wang et al. [176], who employed split (double) direct injection to suppress Super Knock in a modern downsized DI engine. However, some caution is required as the exact mechanisms of Super-Knock suppression (i.e. stratification, reduced wall wetting) were unknown.

Considering all results presented in figure7-5, it was decided to choose start of injection at 60° bTDC as an optimum start of injection for these set of tests.

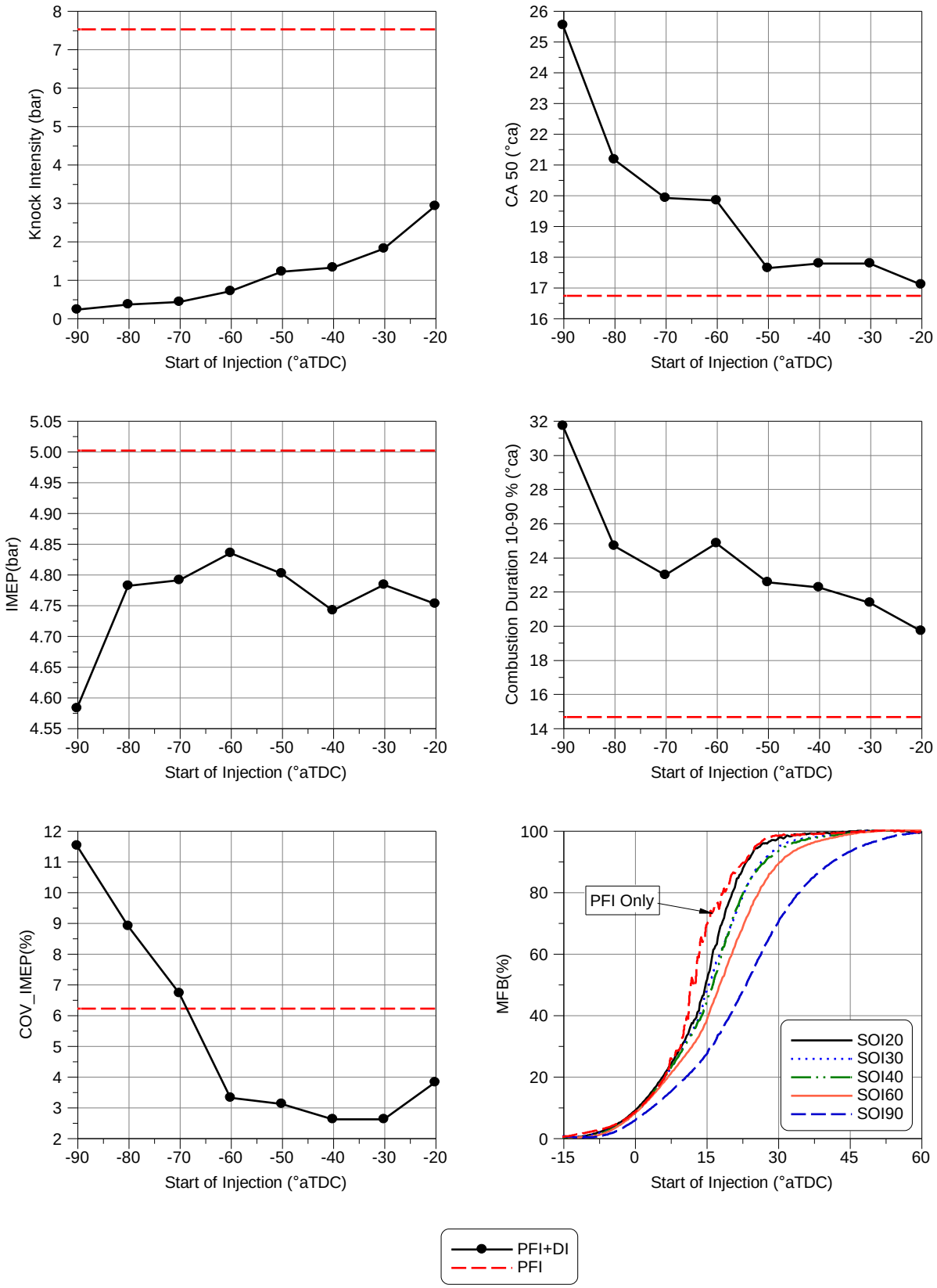

Figure 7-5 Thermodynamic operating parameters during the SOI timing sweep (75 RON fuel)

7.5 Direct Fuel Injection Duration Sweep

A direct fuel injection duration sweep was undertaken to establish the response to progressively increasing fuel mass, as might be experienced during real transient engine operation and/or advanced knock control strategies. During the experiment the SOI timing was left fixed at 60°bTDC and the fuel rail pressure set to 65 bar. Set out in Figure 7-6 are the values of average knock intensity. Shown in Figure 7-7 are the corresponding measured values of relative air to fuel ratio (via a wide band sensor fitted in the exhaust). Contradictory to the charge cooling and ratio of specific heat effects, it can be seen that with small additional DI fuel mass the knock intensity increases by ~65% at 1.5ms compared to the baseline PFI only case. This has been associated with reducing auto-ignition delay times under rich conditions, which under heavy knock with low additional fuel mass outweighs any charge cooling and/or changes in ratio of specific heats.

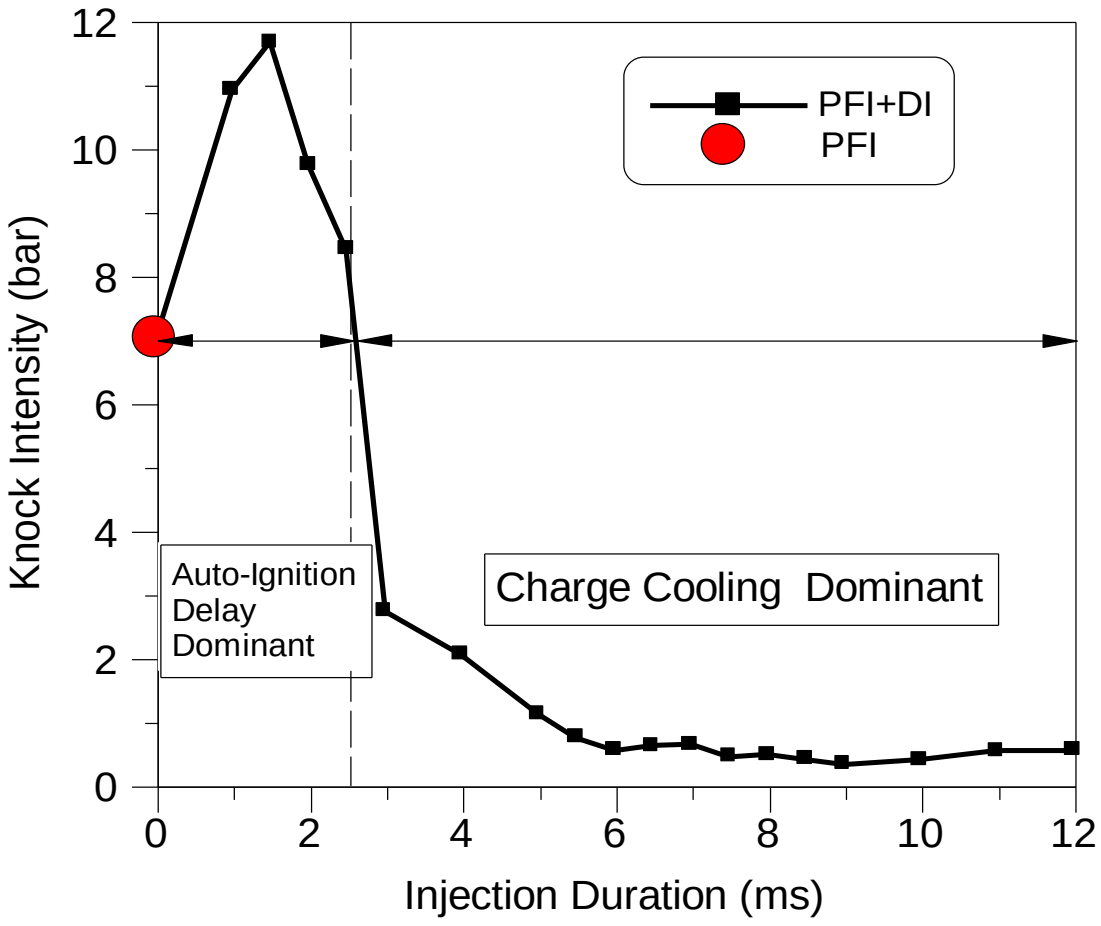

Figure 7-6 : Average knock intensity versus direct fuel injection duration (75 RON Fuel)

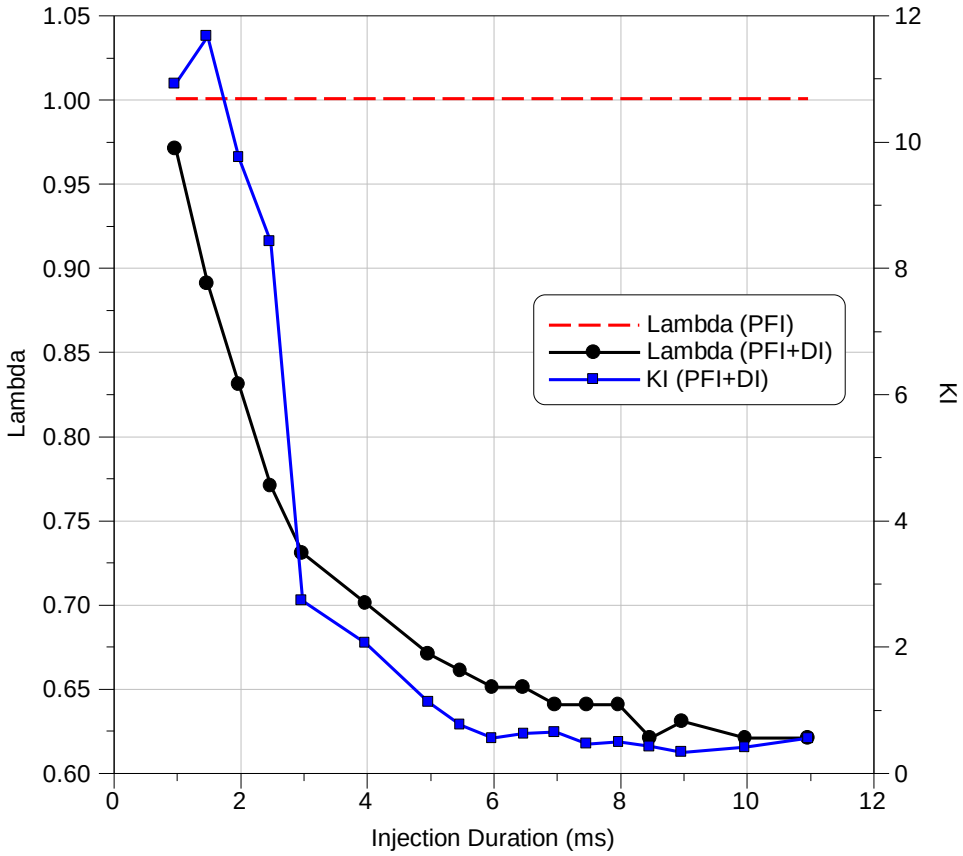

Figure 7-7 Injection Duration Sweep for different cycles during the PFI + DI with the average superimposed

Finally by considering the results from SOI and duration sweeps, when using 75RON PRF and a fixed DI rail pressure of 65 bar, the "optimum" knock suppression was obtained with an SOI of 60 °bTDC and pulse width of 7ms.

7.6 Knock reduction results

Numerous previous publications have considered knock reduction when combining direct fuel injection and ethanol [177][178]. However, the potential trade-off between chemistry (lower auto-ignition temperature) and physics (charge cooling) is not as well reported. The current work was primarily concerned with establishing such effects when

using ethanol. Of additional interest is hydrous ethanol, which has attracted additional interest in recent years due to potential vast reductions in the energy required to purify ethanol. Shown in Figure 7-8 are corresponding values of KI when additionally directly injecting pure ethanol (E100) and hydrous W5E10 (containing 5% volume water within the ethanol). Again, the baseline case (without DI) utilised 75RON PRF only. At the start of each sweep there was some variation in KI, with the relative influence of the hydrous ethanol not as clear due to lower starting KI. Firstly, considering the baseline case (75RON only), the knock intensity first increases by ~65% for at 1.5ms. In other words, adding a small additional mass of fuel resulted in vastly increased knock, which is perhaps initially surprising in the backdrop of over-fuelling being a well-established method to reduce knock when operating close to borderline detonation. Under richer conditions it has been previously reported for both iso-octane and heptane that the auto-ignition delay time is reduced. This observation was validated by reviewing the auto-ignition delay times for the two components of the fuels, with an example set out in Figure 7-9. This figure has been directly reproduced from recent simulation work by Stapf and Reis [179], where the solid lines denote their own predictions and the data points experimental shock tube measurements made elsewhere [180,181]. The predictions were determined using a simple Livengood-Wu integral model linked to a zero-dimensional engine code fed with experimental in-cylinder pressure. For both primary reference fuel components there is good agreement between the simulated and experimental results in that the auto-ignition delay time reduces under richer operating conditions (notably more so in the case of n-heptane). As the fuel mass is increased charge cooling and/or stratification effects dominate, with the knock thereafter suppressed albeit under significantly richer conditions. The key point in this work is that

the engine was initially operating under relatively heavy knock, with KI values much higher than usually encountered when mapping real engines near borderline detonation. In terms of the relative fuel effects, in the case of pure ethanol and W5E10, the knock intensity also initially increased by 42% and 55% respectively. This increase was associated with reducing auto-ignition delay times under rich conditions, which under heavy knock with low additional fuel mass outweighs any charge cooling and reduction in the ratio of specific heats when rich. Again, to understand the result the ignition delay of ethanol was also reviewed. In recent work elsewhere, Syed and co-workers reported on the results of a numerical simulation of auto-ignition of gasoline-ethanol/air mixtures, performed using a closed homogeneous reactor model in CHEMKIN to compute the dependence of auto-ignition time with ethanol concentration, pressure, temperature, dilution and Lambda values [182]. Figure 7-10 has been reproduced directly from this report, and shows the effect of lambda value on auto-ignition time for E40 under stoichiometric, lean and rich conditions. Overall, the effects of auto-ignition delay are in good agreement with the experimental results presented earlier on in this chapter.

To summarise the fuel effects, using pure ethanol or ethanol blends still leads to the observed trade-off between auto-ignition delay and charge cooling, despite the significant charge cooling benefit of the ethanol. The late injection leads to high stratification of the fuel, and less time for charge cooling effects to occur. If such stratification was to occur in a real engine the results indicate the remaining potential dangers from reducing auto-ignition delay time under heavy knocking conditions (potentially including Super-Knock regimes of operation).

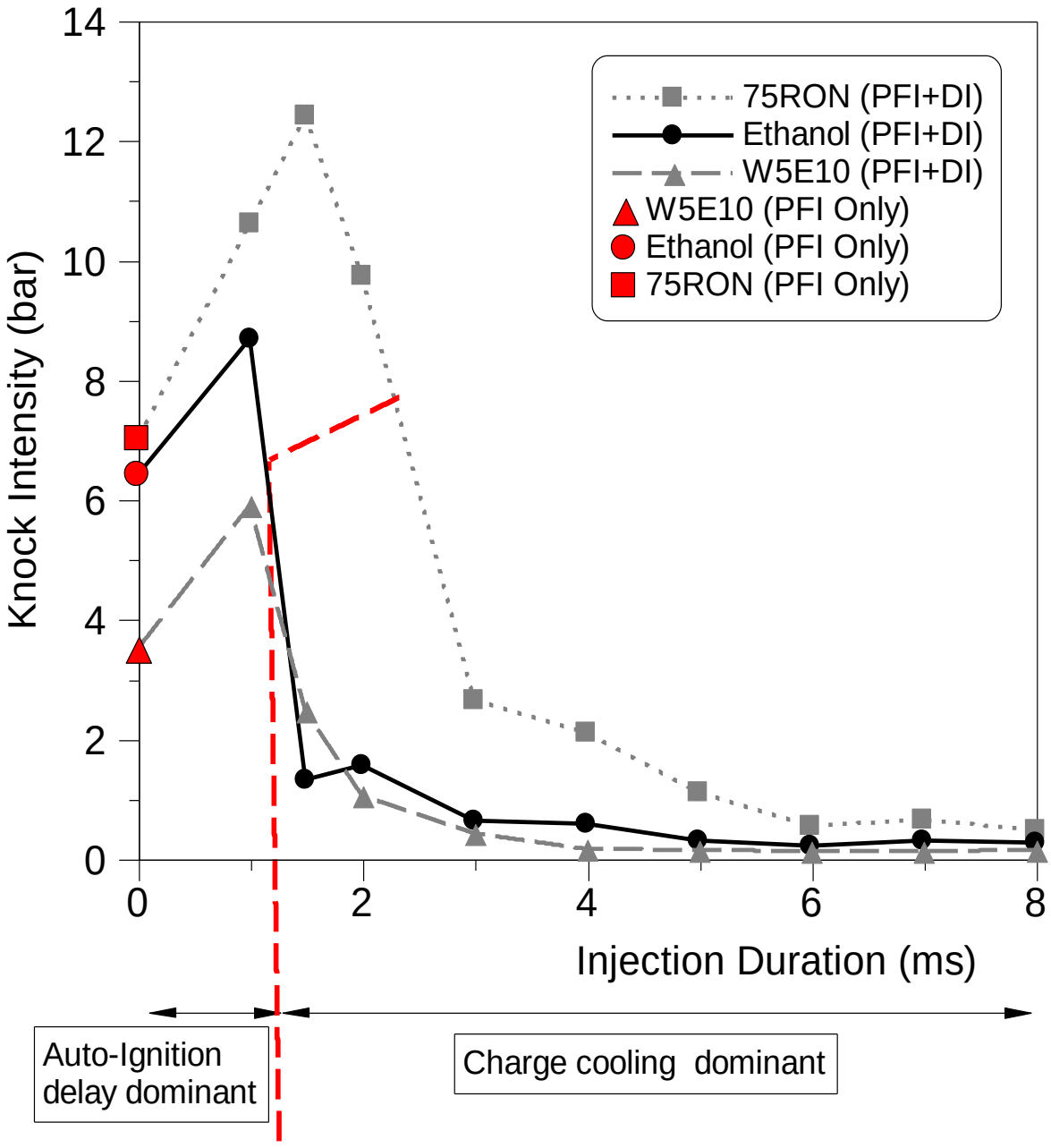

Figure 7-8 Average knock intensity versus direct fuel injection duration

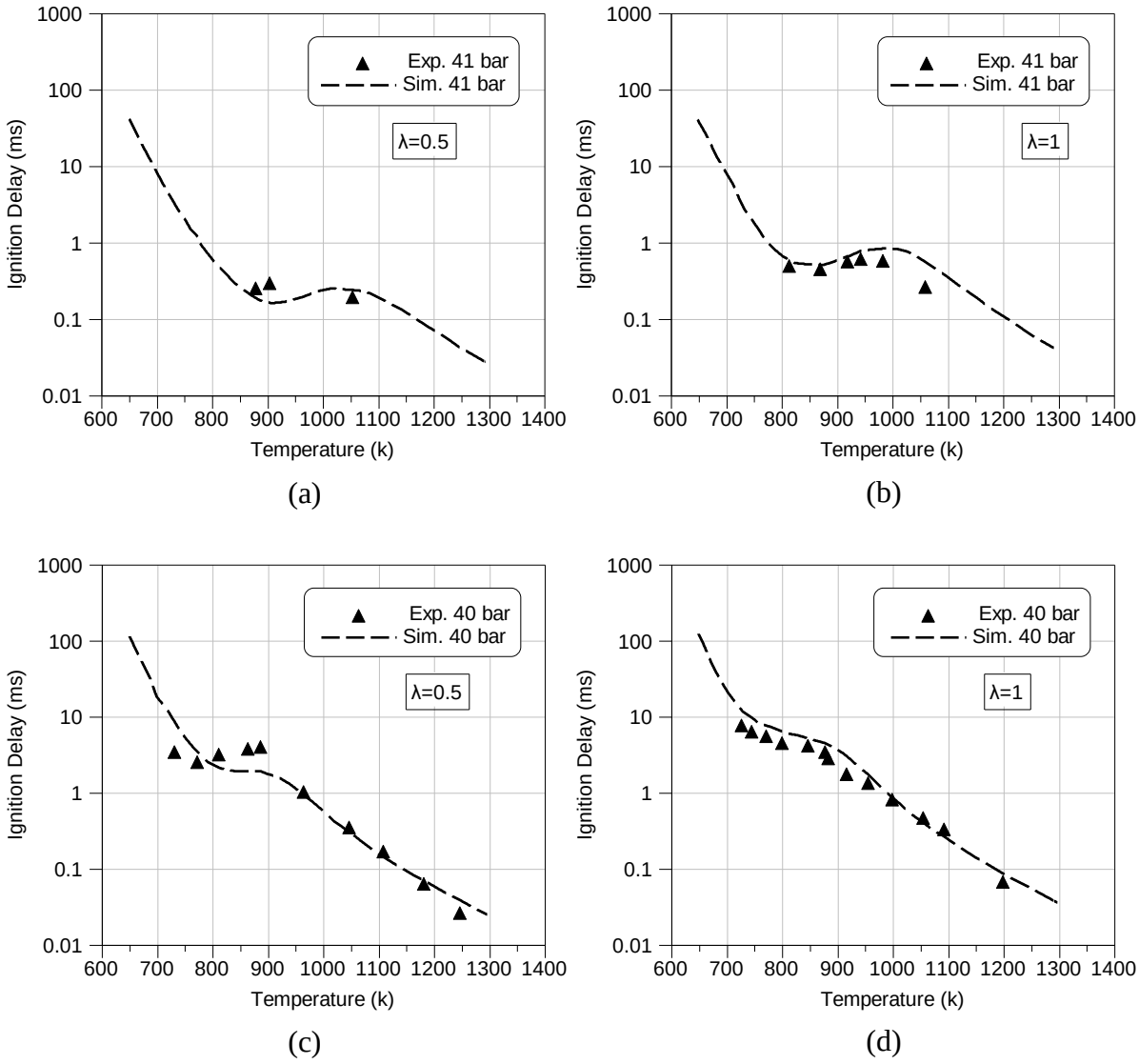

Figure 7-9: Predictions and measurements of auto-ignition delay versus gas temperature for iso-octane under a) rich and b) stoichiometric conditions compared to equivalent values for n-heptane (c, d). Reproduced from [20].

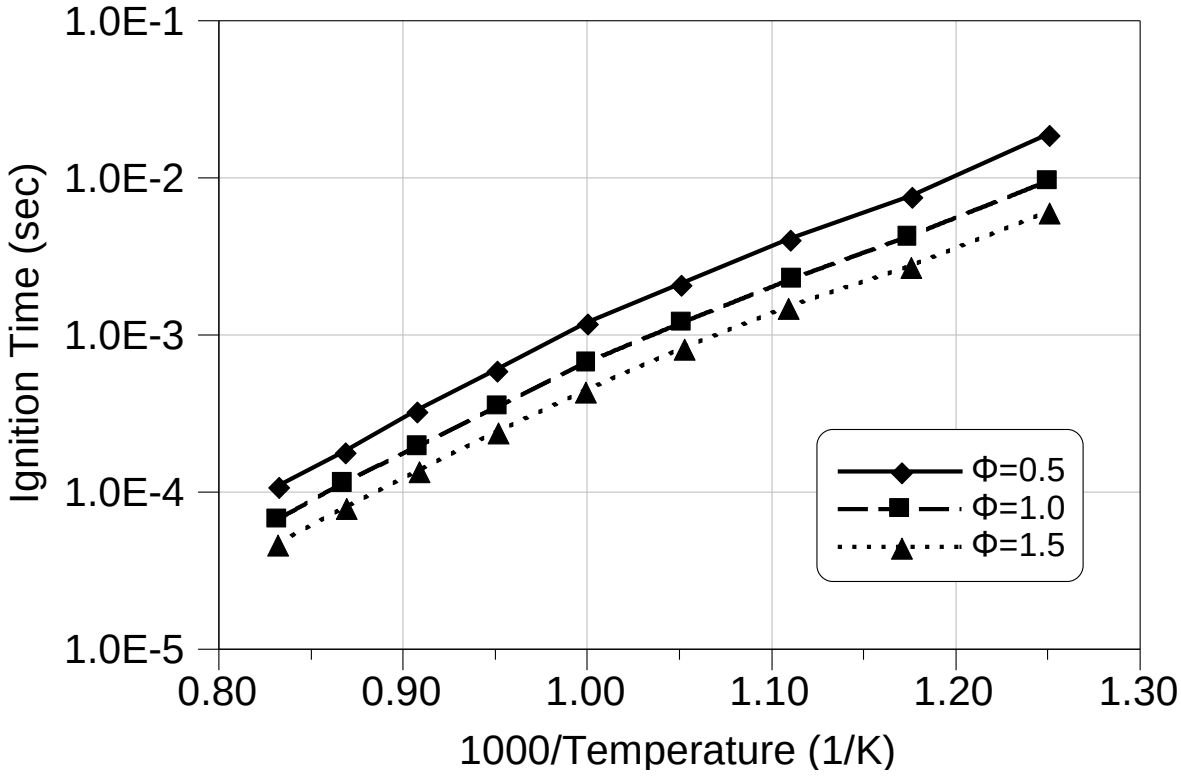

Figure 7-10 Effect of equivalence ratio on auto-ignition time for E40

The above results show the key data, however the following section provides the accompanying detailed thermodynamic analysis. Set out in Figure 7-11(a) is the net IMEP versus Start of Injection (SOI). As might be expected, introducing a higher degree of stratification leads to lower engine output, which is in good agreement with Wallner and Miers [183]. Such stratification leads to slower combustion, as denoted by the retarded MFB set out in Figure 7-11(b) which shows MFB for different fuels at optimum condition (SOI at 60°bTDC and 7ms of injection). Although ethanol has a faster laminar burning velocity compared to gasoline [184], the present study has shown the CA50 of ethanol and 75RON do not follow this trend during over-fuelling experiments. This has been associated with varied stratification and charge cooling effects in the case of the ethanol fuels.

Schifter et al. performed some experiments on burning duration of ethanol content fuels at different lambda values [185] . These workers concluded that the combustion duration has an inverse relationship with ethanol content, which held true for a wide range of lambda values.

In Figures 7-11 (b and c), both the mass fraction burned and CA50 support the fact that 75RON has a faster laminar burning velocity compared to ethanol and W5E10. This is not well aligned with the theory in [184], however, due to the higher latent heat of vaporization and/or stratification effects. Some stratification in the DI fuel was favourable to the mass burning rate and knock suppression, presumably due to preferential local conditions in the end-gas leading to lower temperature and/or prolonged auto-ignition delay. These observations appear to be in good agreement with those of Wang et al. [175], who employed split (double) direct injection to suppress Super-Knock in a modern downsized DI engine. However, some caution is required in this comparison as the exact mechanisms of Super-Knock suppression (i.e. stratification, reduced wall wetting) were unknown. In future work it is intended to study such effects under elevated injection pressures with different fuels.

The fact that ethanol allows for a more optimal combustion phasing at high engine loads without knocking indicates the necessity to design and calibrate an engine specifically for ethanol operation. This would permit taking full advantage of the promising combustion properties of ethanol and compensate for the lower volumetric energy content of ethanol compared to gasoline.

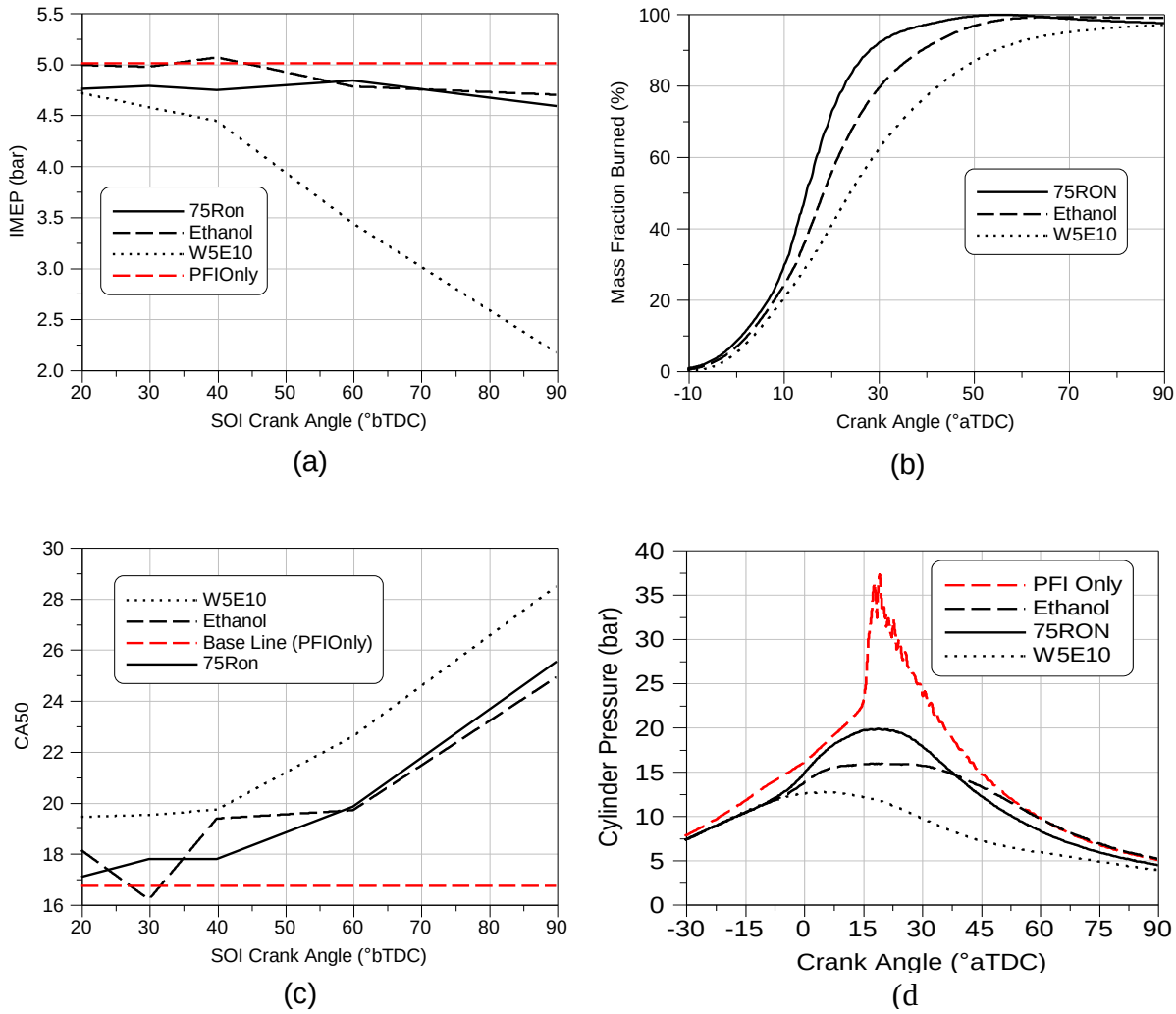

Figure 7-11: Thermodynamic operating parameters during over-fuelling

7.7 Optical Analysis

Shown in Figure 7-12 are flame images from three cycles selected to show "typical" events under varied start of injection timings for the transient DI events. Each horizontal strip denotes a different cycle and SOI setting, as marked on the figure. The fuel injection pulse width and DI rail pressure remained fixed at 7ms and 65bar respectively.

The bright yellow-ish light omission denotes local sooty combustion in the end-gas region, with the phenonenon exacerbated as the DI timing was retarded. As the first and second strips show, by setting the start of injection later than 30°bTDC, the excess fuel injected from DI will start to burn after flame propagation coverd the bore.

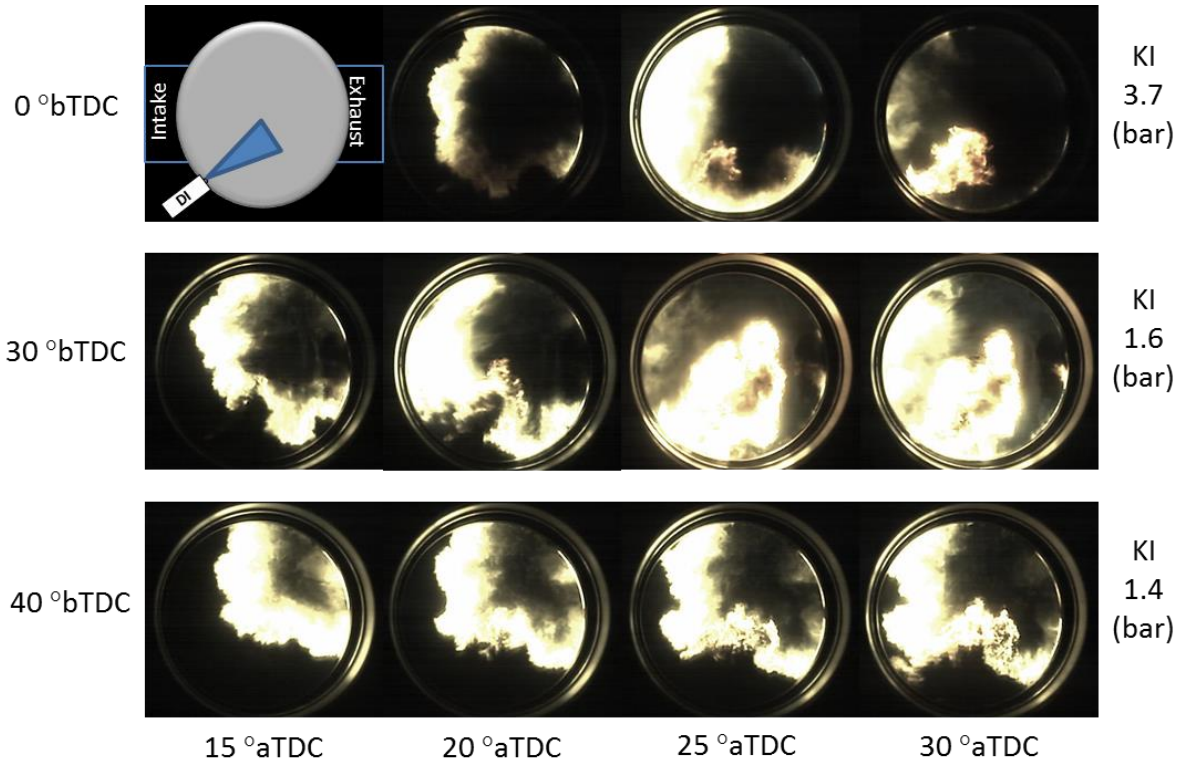

Figure 7-12: Flame images under varied direct injection SOI timings. Each horizontal strip shows a different cycle obtained at different DI SOI timing (marked on the left).

Set out in Figure 7-13 are flame images from four cycles selected to show “typical” events under varied fuel injected from the direct injector. Corresponding strips show the "optimum" PFI+DI cases versus PFI-only. Each vertical strip denotes a different fuel. Excluding the first strip on the left (PFI only), the fuel injection pulse width, Start of Injection and DI rail pressure remained fixed at 7 ms, 60 °bTDC and 65 bar respectively and ignition timing was fixed to 15 °bTDC.

As the PFI-only strip shows, auto-ignition occurred between 4.8 and 10.8 °aTDC. The bright yellow-ish light omission denotes local sooty combustion in the end-gas region. In the other strips, when the flame propagated to roughly one third of the bore, the kernel encroached the extra fuel injected from the direct injector. It is apparent that the combustion slows down and ultimately cannot proceed directly in this vicinity.

Set out in Figure 7-14 is an illustration of the DI fuel targeting, with this direction of injection confirmed in earlier work by Dingle and co-workers [12] . It is clear that the local fuel-air mixture is so rich that flame propagation cannot proceed in this zone, with the oxygen deficiency also preventing auto-ignition and knock albeit at the likely expense of very poor combustion efficiency.

The flames in Figure 7-14 with the DI active exhibit similar behaviour. Overall, the results show that knock is suppressed but by very inefficient means. Overall, transient additional direct injection would appear to be a very high risk strategy in the presence of heavy knock, due to the observed competing chemical and physical effects.

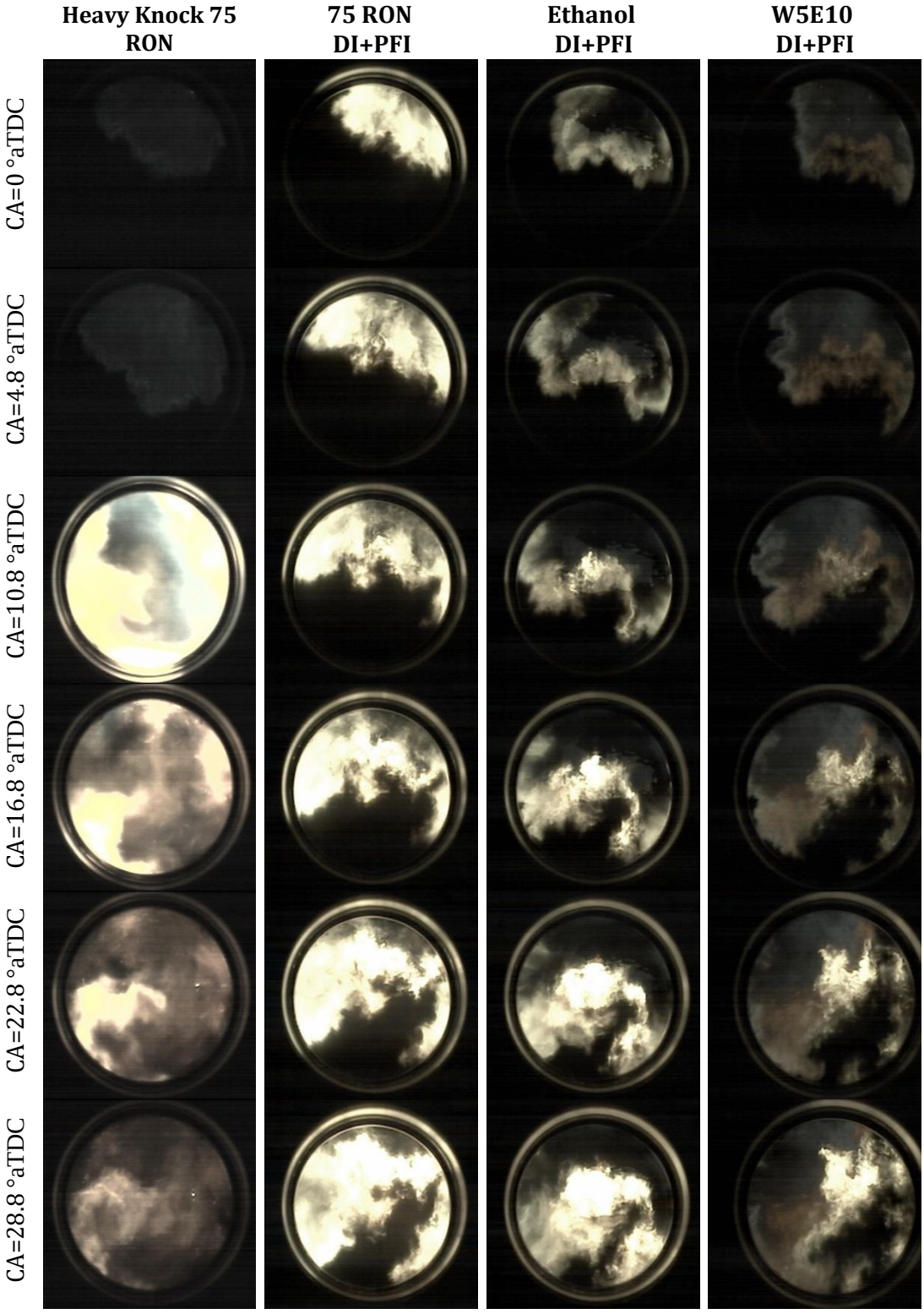

Figure 7-13: A comparison of a typical baseline heavy knocking cycle versus a typical "optimum" over fuelling cycles for all fuels

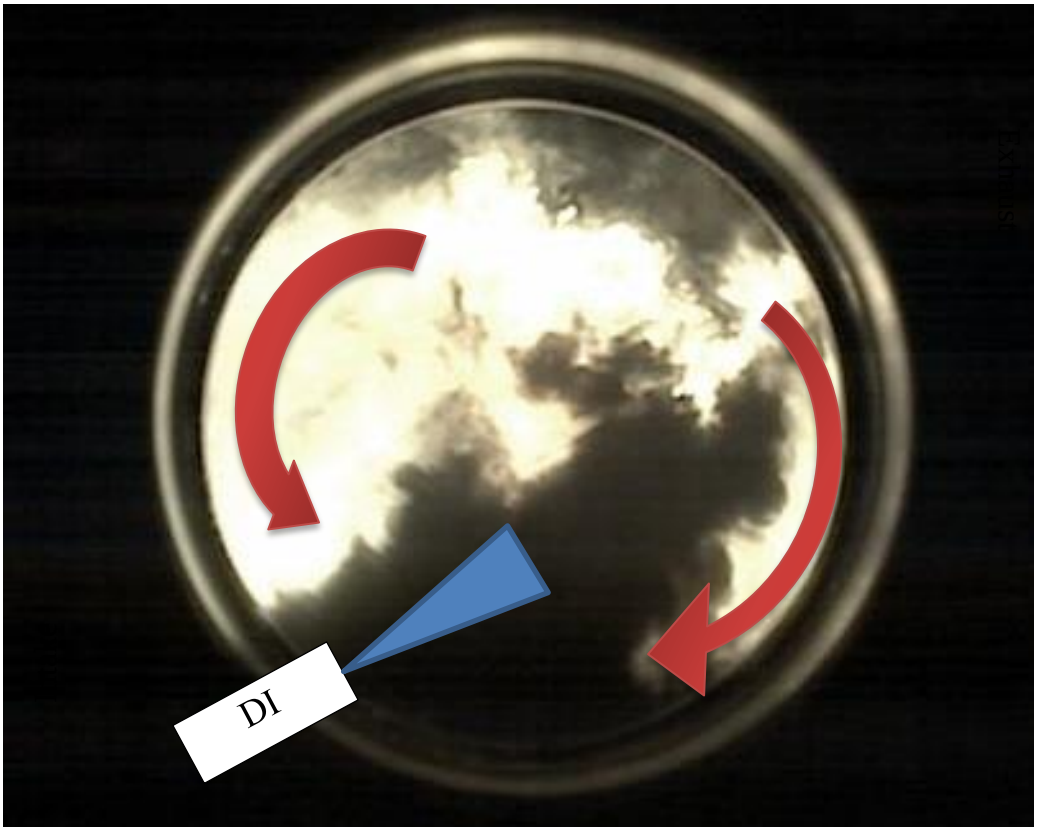

Figure 7-14Flame image under over-fuelling

7.8 Summary/Conclusions

The work presented in this chapter involved study of over-fuelling using additional direct fuel injection during heavy knocking PFI engine conditions. It was observed that directly injecting a small-to-moderate additional mass of fuel would exacerbate knock, with reducing auto-ignition delay time leading to higher peak in-cylinder pressures and knock intensities elevated by 40-65%, with the pure ethanol case leading to slightly lower aggravation. As the additional mass of excess fuel was further increased, the effects of charge cooling and reducing ratio of specific heats began to dominate and ultimately eliminated knock, albeit requiring extremely rich conditions. It was also apparent that some stratification in the fuel-air charge was favourable to burning rate

and knock suppression, associated with favourable local conditions in the end gas prior to the onset of auto-ignition. Full bore chemiluminescence imaging confirmed slower flame propagation during the over-fuelling and the tendency of the flame to ignore the rich area in front of the direct injector.

Overall, the results highlight the potential risks in transient over-fuelling under heavy knocking conditions, where an unexpected violent knocking event (e.g. Super-Knock) might be exacerbated by the presence of excess fuel leading to reduced auto-ignition delay. The observations demonstrate that traditional over-fuelling may be an unreliable method of Super-Knock suppression in modern downsized spark ignition engines operating with ethanol blends, even without considering the other detrimental effects of rich combustion on thermal efficiency and tailpipe pollutant emissions. However, some caution is recommended given the simple nature of the fuels adopted and future work should consider the effects of a wider suite of fuels.

8 CONCLUSION AND RECOMMENDATIONS

8.1 Summary of Results

The work reported in this study has been concerned with thermodynamic and optical investigations of pre-ignition and heavy knock in a novel full bore optical SI engine. The research involved different number of investigations including:

- Optical and thermodynamic study of the pre-ignition and resultant knock using a 75 RON gasoline surrogate blend
- Study of the relationship between the knock intensity and the crank angle of the maximum in-cylinder pressure gradient
- Investigation of the heat release rate of the pre-ignitive cycles
- Verifying any relationships between mass fraction unburned at the onset of auto-ignition and resultant knock intensity (contradictorily reported in prior literature)
- Direct optical investigations of knocking cycles
- Categorising the locations of auto-ignition initiation sites
- The competing chemical and physical effects of transient fuel enrichment during heavy knock using ethanol blends
- Study of the potential risk of over-fuelling during super knock

The following section is an overview of the main conclusions achieved within this study.

8.1.1 Baseline Engine Heavy Knock

This section of the work involved study of auto-ignition and heavy knock in an optical spark ignition engine. Heavy knock was deliberately induced under relatively low loads using inlet air heating and a primary reference fuel blend of reduced octane rating. High speed chemiluminescence natural light imaging was used together with simultaneous heat release analysis to evaluate the combustion events

It was observed that knock intensity is more effected by the crank angle of auto-ignition onset. Cycles with Pre-ignition (and/or auto-ignition) onset closer to TDC have higher knock intensity due to higher pressure and temperature. Analysis of the unburned mass fraction at the beginning of the pre-ignition showed no relation to knock intensity under any of the conditions studied.

Naturally released lubricant droplets were observed in cycles following high knock and appeared to initiate pre-ignition in subsequent cycles. The results showed that 90% of heavy knocking cycles were followed by normal or light knocking cycles which presented characteristics of the previously reported “on-off-on” nature of super-knock [165,186,187].

Full bore chemiluminescence imaging confirmed multiple centred auto-ignition sites and the relationships between the location of the auto-ignition sites and knock intensity. The optical analysis showed 54% of auto-ignition events initiated ahead of flame front due to higher pressure and temperature in this zone, which is favourable for auto-ignition. Also 32% of auto ignitions happened near the exhaust side due to higher temperature of this area.

8.1.2 Transient Over-fuelling

The section involved study of over-fuelling (fuel enrichment) using additional direct fuel injection during heavy knocking PFI engine conditions. The effects of different fuels including 75 RON and ethanol blends were examined.

It was observed that during heavy knocking cycles, directly injecting a small-to-moderate additional mass of fuel (up to 2 ms of injection) would exacerbate knock, with reducing auto-ignition delay time (rich areas) leading to higher peak in-cylinder pressures and knock intensities (elevated by 40-65%). The pure ethanol case led to slightly lower aggravation of knock. For this fuel results showed better knock suppression due to higher latent heat of vaporisation. As the additional mass of excess fuel was further increased, the effects of charge cooling and reducing ratio of specific heats began to dominate and ultimately eliminated knock, albeit requiring extremely rich conditions.

Also it was apparent that some stratification in the fuel-air mixture was favourable to burning rate and knock suppression, associated with favourable local conditions in the end gas prior to the onset of auto-ignition. Full bore chemiluminescence imaging confirmed slower flame propagation during the over-fuelling and the tendency of the flame to avoid the rich area in front of the direct injector.

Overall, the findings highlighted the potential risks in transient over-fuelling under heavy knocking conditions, especially where an unexpected violent knocking event (e.g. Super-Knock) might be exacerbated by the presence of excess fuel as a result of reduced auto-ignition delay time. The observations demonstrate that traditional fuel enrichment method may be an unreliable strategy of Super-Knock suppression in

modern downsized spark ignition engines operating with ethanol blends, even without considering the other detrimental effects of rich combustion on thermal efficiency and tailpipe pollutant emissions.

8.2 Recommendations for Future Work

The contents of this study have provided a valuable insight into the understanding the pre-ignition and knock in SI engine. To gain a greater understanding of these issues and improve the quality of the results, recommendations suggested for future work in the next section.

8.2.1 Experimental setup modification

Having one active exhaust valve limited the maximum engine speed to 1200 rpm. Therefore it is suggested that for future work, activation of both exhaust valves is achieved to increase the range of engine speed. Also, it is recommended to use the external EGR system to understand the interaction of EGR with pre-ignition and knock. Additionally, it is highly recommended that an intake air supply boosting be installed to allow the engine to operate at higher loads and lean conditions as it would be more indicative of a real downsized engine (and potentially allow more stable baseline combustion). In order to avoid inlet air temperature fluctuations while using heater, it is suggested to improve the intake air heating automation and control.

In terms of the camera and optical equipment, it is recommended to design a new window that incorporates a central spark plug in order to study the influence of the spark plug location on pre-ignition and knock. Also employing a more up-to-date or

new camera is essential as there were many problems regarding the age and memory capacity of the camera.

It is also recommended that a water cooling system to be installed to allow collecting the data in 300 consecutive cycles and no waiting for engine cool down (the waiting time was approximately 12 mins for each run).

8.2.2 Future studies on Pre-ignition and Knock

Pre-ignition and auto-ignition sites were reported near the area directly surrounding the active exhaust valve. Therefore it is recommended that the effect of the exhaust valve temperature be further investigated.

In many cycles the presence of oil droplets (or potentially soot particles) followed pre-ignition and led to knock. It is highly recommended for future work to put more effort in droplet tracking by increasing the number of optical samples. The droplets could intentionally be introduced to the combustion chamber using the direct injector. .

In the literature, there is not enough investigations on mass fraction burned analysis of the knocking cycles. More attention is needed on the chemistry of pre-ignition and MFB analysis during super knocking cycles in real engines in which the chemistry freezes due to fast chemical reactions. It is also therefore recommended to evaluate the fast emissions of hydrocarbons (HC) during heavy knock but with the knock induced under more stable engine conditions.

8.2.3 Fuel enrichment

The effect of over-fuelling on knock reduction was investigated and reported in this thesis. The trade-off between ignition delay and charge cooling has not been well correlated in modern down sized engines. In an ideal situation a shock tube would be commissioned that is capable of operating at the typical high pressures and temperatures experienced at the onset of super knock.

REFERENCES

1. Change, C., “Science and Impacts CLIMATE CHANGE 101,” *Science (80-.).*, 2009, doi:20.2029/2005JD006548.Ocean.

2. IPCC, “Climate change 2014: Synthesis Report,” ISBN 9789291691432, 2014, doi:10.1017/CBO9781107415324.

3. United Nations Framework Convention on Climate Change, “Summary of the Paris Agreement,” *United Nations Framew. Conv. Clim. Chang.*, 2016.

4. We’re now breaking global temperature records once every three years, https://www.theguardian.com/environment/climate-consensus-97-per-cent/2017/jan/23.

5. Moxey, B.G., Cairns, A., and Zhao, H., “A Study of Turbulent Flame Development with Ethanol Fuels in an Optical Spark Ignition Engine,” *SAE* (2014-01–2622), 2014, doi:10.4271/2014-01-2622.

6. Stone, R., “Introduction to internal combustion engines,” 2012.

7. EU new car CO2 emissions Landmark, www.smmt.co.uk.

8. Reducing CO2 emissions from passenger cars, https://ec.europa.eu/clima/policies/transport/vehicles/cars_en, 2004.

9. E10 compatibility issues.

10. Dresner, T. and Barkan, P., “A Review of Variable Valve Timing Benefits and Modes of Operation,” *SAE Tech. Pap.*, 1989, doi:10.4271/891676.

11. Amann, M., Alger, T., and Mehta, D., “The Effect of EGR on Low-Speed Pre-Ignition in Boosted SI Engines,” *SAE Int. J. Engines* 4:235–245, 2011, doi:10.4271/2011-01-0339.

12. Dingle, S.F., Cairns, A., Zhao, H., Williams, J., Williams, O., and Ali, R., "Lubricant Induced Pre-Ignition in an Optical SI Engine," (2014-01–1222), 2014, doi:10.4271/2014-01-1222.

13. Heywood, J.B., "Internal Combustion Engine Fundamentals," ISBN 007028637X, 1988.

14. Kalghatgi, G.T. and Bradley, D., "Pre-ignition and 'super-knock' in turbo-charged spark-ignition engines," *Int. J. Engine Res.* 13(4):399–414, 2012, doi:10.1177/1468087411431890.

15. Cairns, A., Stansfield, P., Fraser, N., Blaxill, H., Gold, M., Rogerson, J., and Goodfellow, C., "A Study of Gasoline-Alcohol Blended Fuels in an Advanced Turbocharged DISI Engine," *SAE Int. J. Fuels Lubr.* 2(1):41–57, 2009, doi:10.4271/2009-01-0138.

16. Balat, M. and Balat, H., "Recent trends in global production and utilization of bio-ethanol fuel," *Appl. Energy*, 2009, doi:10.1016/j.apenergy.2009.03.015.

17. Ozdor, N., Dulger, M., and Sher, E., "Cyclic Variability in Spark Ignition Engines A Literature Survey," *SAE Tech. Pap.*, 1994, doi:10.4271/940987.

18. Renault, G.I.E.P.S.A., Cheng, W.K., and Heywood, J.B., "The Effects of Initial Flame Kernel Conditions on Flame Development in SI Engine," (912402), 1991.

19. Lord, D.L., Anderson, R.W., Brehob, D.D., and Kim, Y., "The Effects of Charge Motion on Early Flame Kernel Development," *SAE Tech. Pap.* (930463), 1993, doi:10.4271/930463.

20. Aleiferis, P.G., Taylor, A.M.K.P., Ishii, K., and Urata, Y., "The nature of early flame development in a lean-burn stratified-charge spark-ignition engine," *Combust. Flame*, 2004, doi:10.1016/j.combustflame.2003.08.011.

21. Lee, K., Bae, C., and Kang, K., "The effects of tumble and swirl flows on flame propagation in a four-valve S.I. engine," *Appl. Therm. Eng.* 27(11–12):2122–

2130, 2007, doi:10.1016/j.applthermaleng.2006.11.011.

22. Benjamin, S.F., “A phenomenological model for ‘barrel’ swirl in reciprocating engines,” *Arch. Proc. Inst. Mech. Eng. Part D J. Automob. Eng. 1989-1996 (Vols 203-210)* 206(14):63–71, 1992, doi:10.1243/PIME_PROC_1992_206_161_02.

23. Kang, K.Y. and Baek, J.H., “Tumble Flow and Turbulence Characteristics in a Small Four-Valve Engine,” *SAE Pap. 960265* (960265), 1996, doi:10.4271/960265.

24. Coz, J.-F. Le, Henriot, S., and Pinchon, P., “An experimental and computational analysis of the flow field in a four-valve spark ignition engine - Focus on cycle-resolved turbulence,” *SAE Tech. Pap. 900056* (900056), 1990.

25. Floch, A., Frank, J. Van, and Ahmed, A., “Comparison of the Effects of Intake-Generated Swirl and Tumble on Turbulence Characteristics in a 4-Valve Engine,” *SAE Tech. Pap.* (952457), 1995, doi:10.4271/952457.

26. Urushihara, T., Murayama, T., Lee, K.-H., and Takagi, Y., “Turbulence and Cycle Variation of Mean Velocity Generated by Swirl and Tumble Flow, and Their Effects on Combustion.,” *Trans. Japan Soc. Mech. Eng. Ser. B* 60(580):4280–4286, 1994, doi:10.1299/kikaib.60.4280.

27. Pischinger, S. and Heywood, J.B., “How Heat Losses to the Spark Plug Electrodes Affect Flame Kernel Development in an SI-Engine,” *SAE Pap.* (900021), 1990, doi:10.4271/900021.

28. Wang, Z., Qi, Y., He, X., Wang, J., Shuai, S., and Law, C.K., “Analysis of pre-ignition to super-knock: Hotspot-induced deflagration to detonation,” *Fuel* 144:222–227, 2015, doi:10.1016/j.fuel.2014.12.061.

29. Taylor, J., Fraser, N., and Wieske, P., “Water Cooled Exhaust Manifold and Full Load EGR Technology Applied to a Downsized Direct Injection Spark Ignition Engine,” *SAE Int. J. Engines* (2010-01–0356), 2010, doi:10.4271/2010-01-0356.

30. Turner, J.W.G., Pearson, R.J., Curtis, R., and Holland, B., “Improving Fuel Economy in a Turbocharged DISI Engine Already Employing Integrated Exhaust Manifold Technology and Variable Valve Timing,” *Engineering*, 2011, doi:2008-01-2449.

31. Ayala, F. a, Gerty, M.D., and Heywood, J.B., “Effects of Combustion Phasing, Relative Air-fuel Ratio, Compression Ratio, and Load on SI Engine Efficiency,” *SAE Tech. Pap. 2006-01-0229* (01–0229), 2006, doi:10.4271/2006-01-0229.

32. Dingle, S.F., “LUBRICANT INDUCED PRE-IGNITION IN AN OPTICAL SPARK-IGNITION ENGINE,” Brunel University, 2013.

33. Hires, S.D., Tabaczynski, R.J., and Novak, J.M., “The Prediction of Ignition Delay and Combustion Intervals for a Homogeneous Charge , Spark Ignition Engine,” *SAE Tech. Pap. 780232* (780232), 1979, doi:10.4271/780232.

34. Chu, S., & Majumdar, A., “Opportunities and challenges for a sustainable energy future,” *Nature*, 2012, doi:10.1038/nature11475.

35. Valve, V. and Engine, T., “930878 Development of a New Multi-Mode Variable Valve Timing Engine,” *SAE* (930878), 2013.

36. Dugdale, P.H., Rademacher, R.J., Price, B.R., Subhedar, J.W., and Duguay, R.L., “Ecotec 2 . 4L VVT : A Variant of GM ’ s Global 4-Cylinder Engine,” *SAE Tech. Pap.* (2005-01–1941), 2005, doi:10.4271/2005-01-1941.

37. Gentile, I., Pirelli, M., and Mastrangelo, G., “PAPER SERIES The New FIRE 1 , 4 8v and 16v VVT Engine Family : an The New FIRE 1 , 4 8v and 16v VVT Engine Family : a n Unique Approach to Reduce Fuel Consumption,” *SAE Pap.* (2005-24–076).

38. hakariya, M., Toda, T., and Sakai, M., “The New Toyota Inline 4-Cylinder 2.5L Gasoline Engine,” (2017-01–1021), 2017, doi:10.4271/2017-01-1021.

39. Brüstle, C. and Schwarzenthal, D., “VarioCam Plus - A Highlight of the Porsche

911 Turbo Engine," *SAE Tech. Pap. 2001-01-0245* 2001(724), 2001, doi:10.4271/2001-01-0245.

40. Vent, G. and Enderle, C., "The new 2.0 l turbo engine from the Mercedes-Benz 4-cylinder engine family," *2nd Aachen Colloquium China*, 2012.

41. Honda, "New 1 . 0L I3 Turbocharged Gasoline Direct Injection Engine," *SAE Tech. Pap.*, 2017, doi:10.4271/2017-01-1029.Copyright.

42. Flierl, R. and Kluting, M., "The third generation of valvetrains – New fully variable valvetrains for throttle-free load control," *SAE Tech. Pap.* 2000-01–1227, 2000, doi:10.4271/2000-01-1227.

43. Luttermann, C., Schueenemann, E., and Klauer, N., "Enhanced VALVETRONIC technology for meeting SULEV emission requirements.," *Soc. Automot. Eng. [Special Publ. SP*, 2006, doi:10.4271/2006-01-0849.

44. Takemura, S., Aoyama, S., and Sugiyama, T., "A Study of a Continuous Variable Valve Event and Lift (VEL) System," *SAE* (2001-01–0243), 2013, doi:10.4271/2001-01-0243.

45. Sugiyama, T., Hiyoshi, R., Takemura, S., and Aoyama, S., "Technology for Improving Engine Performance using Variable Mechanisms," *SAE* (2007-01–1290), 2007, doi:10.4271/2007-01-1290.

46. Fujita, T., Onogawa, K., Kiga, S., Mae, Y., Akasaka, Y., and Tomogane, K., "Development of Innovative Variable Valve Event and Lift (VVEL) System," *Sae Sp* 2174(724):47, 2008, doi:10.4271/2007-01-3548.

47. Gottschalk, W., Lezius, U., and Mathusall, L., "Investigations on the Potential of a Variable Miller Cycle for SI Knock Control," (2013-01–1122), 2013, doi:10.4271/2013-01-1122.

48. Trevas, I., Baeta, A.J., Pimenta, C., Fernandes, H., Carvalho, M., and Montemor, R., "Combustion Analysis on a Variable Valve Actuation Spark Ignition Engine

Operating with E22 and E100," *SAE Tech. Pap.* (2017-01–1069), 2017, doi:10.4271/2017-01-1069.

49. Titolo, A., "The Variable Valve Timincl - System - Application on a V8 Engine," *SAE Tech. Pap.* (910009), 1991.

50. Gould, L.A., Richeson, W.E., and Erickson, F.L., "SA E TECHNICAL Performance Evaluation of a Camless Engine Using Valve Actuators with Programmable Timing," *Ind. Electron.*, 2011, doi:10.4271/910450.

51. Pischinger, M., Salber, W., Staay, F., Baumgarten, H., and Kemper, H., "Benefits of the Electromechanical Valve Train in Vehicle Operation," *Sae 2000-01-1223* (2000-01–1223), 2000, doi:10.4271/2000-01-1223.

52. Allen, J. and Law, D., "Production electro-hydraulic variable valve-train for a new generation of IC engines," *Sae Trans.* (2002-01–1109), 2002, doi:10.4271/2002-01-1109.

53. Milovanovic, N., Blundell, D., Gedge, S., and Turner, J., "Cam Profile Switching (CPS) and phasing strategy vs Fully Variable Valve Train (FVVT) strategy for transitions between spark ignition and controlled auto ignition modes," *SAE Tech. Pap.* 2005-01–0766, 2005, doi:10.4271/2005-01-0766.

54. RICARDO, "Case Study: Stroke of genius for gasoline downsizing."

55. Shao, D., Sichuan, X., and Du, A., "Research on a New Electromagnetic Valve Actuator Based on Voice Coil Motor for Automobile Engines A New Design of Voice Coil Electromagnetic Valve," (2017-01–1070), 2017, doi:10.4271/2017-01-1070.Copyright.

56. Freevalve, "Freevalve Technology," http://www.freevalve.com/., 2017.

57. Zhang, Y. and Zhao, H., "Investigation of combustion, performance and emission characteristics of 2-stroke and 4-stroke spark ignition and CAI/HCCI operations in a DI gasoline," *Appl. Energy*, 2014, doi:10.1016/j.apenergy.2014.05.036.

58. Haase, M. and Piecyk, T., “Get ready for the combustion strategies of tomorrow: Variable Valvetrain.”

59. Zhao, F., Lai, M., and Harrington, D., “A review of mixture preparation and combustion control strategies for spark- ignited direct-injection gasoline engines,” *SAE Tech. Pap. 970627* (970627), 1997.

60. Advanced Direct Injection Combustion Engine Technologies and Development, Volume 2: Diesel Engines (Woodhead Publishing in Mechanical Engineering): H Zhao.

61. Types of engines and their advancements., http://ibnox.com/read/7eapnzt/engines-advancements-advantages-and-disadvantages.

62. stratified charge vs homogeneous charge, https://knowicengine.wordpress.com/2016/04/10/fuel-injection-in-si-engine/.

63. Benson, J.D., “The Influence of Engine and Fuel Factors on After-Run,” *1972 Automot. Eng. Congr. Expo.* (720085), 1972, doi:10.4271/720085.

64. Ingamells, J.C., “Effect of Gasoline Octane Quality and Hydrocarbon Composition on Afterrun,” *1979 SAE Int. Fall Fuels Lubr. Meet. Exhib.* (790939), 1979, doi:10.4271/790939.

65. Lavy, J., Dabadie, J.-C., Angelberger, C., Duret, P., Willand, J., Juretzka, A., Schäflein, J., Ma, T., Lendresse, Y., Satre, A., Schulz, C., Krämer, H., Zhao, H., and Damiano, L., “Innovative Ultra-low NOx Controlled Auto-Ignition Combustion Process for Gasoline Engines: the 4-SPACE Project,” (2000-01–1837), 2000, doi:10.4271/2000-01-1837.

66. Koopmans, L. and Denbratt, I., “A four-stroke camless engine, operated in homogeneous charge compression ignition mode with commercial gasoline,” *SAE Trans.* 110(3):2324–2337, 2001, doi:10.4271/2001-01-3610.

67. Li, J., Zhao, H., Ladommatos, N., and Ma, T., “Research and Development of Controlled Auto-Ignition (CAI) Combustion in a 4-Stroke Multi-Cylinder Gasoline Engine,” *SAE Tech. Pap.* (01–3608), 2001, doi:10.4271/2001-01-3608.

68. Zhao, H., Li, J., Ma, T., and Ladommatos, N., “Performance and Analysis of a 4-Stroke Multi-Cylinder Gasoline Engine with CAI Combustion,” (2002-01–0420), 2002, doi:10.4271/2002-01-0420.

69. Cao, L., Zhao, H., Jiang, X., and Kalian, N., “Mixture formation and controlled auto-ignition combustion in four-stroke gasoline engines with port and direct fuel injections,” *Int. J. Engine Res.* 6(4):311–329, 2005, doi:10.1243/146808705X30611.

70. Cao, L., Zhao, H., Jiang, X., and Kalian, N., “Investigation into the Effect of Injection Timing on Stoichiometric and Lean CAI Operations in a 4-Stroke GDI Engine,” *Sae* (2006-01–0417), 2006, doi:10.4271/2006-01-0417.

71. Wang, H., DelVescovo, D., Yao, M., and Reitz, R.D., “Numerical Study of RCCI and HCCI Combustion Processes Using Gasoline, Diesel, *iso* -Butanol and DTBP Cetane Improver,” *SAE Int. J. Engines* 8(2):2015-01–0850, 2015, doi:10.4271/2015-01-0850.

72. Alexandros G. Charalambides (2013). Homogenous Charge Compression Ignition (HCCI) Engines, Advances in Internal Combustion Engines and Fuel Technologies, Dr. Hoon Kiat Ng (Ed.), InTech, DOI: 10.5772/55807. Available from: https://www.intechopen.com/books/.

73. Dimopoulos, P., Rechsteiner, C., Soltic, P., Laemmle, C., and Boulouchos, K., “Increase of passenger car engine efficiency with low engine-out emissions using hydrogen-natural gas mixtures: A thermodynamic analysis,” *Int. J. Hydrogen Energy*, 2007, doi:10.1016/j.ijhydene.2006.12.026.

74. Qi, D., Leick, M., Liu, Y., and Lee, C.F.F., “Effect of EGR and injection timing on combustion and emission characteristics of split injection strategy DI-diesel engine fueled with biodiesel,” *Fuel*, 2011, doi:10.1016/j.fuel.2011.01.016.

75. Zhao, H., Hu, J., and Ladommatos, N., “In-cylinder studies of the effects of CO2 in exhaust gas recirculation on diesel combustion and emissions,” *Proc. Inst. Mech. Eng. - Part D J. Automob. Eng.*, 2000, doi:10.1243/0954407001527727.

76. Jääskeläinen, H. and Khair, M.K., “EGR Systems & Components,” 2012.

77. Osborne, R.J., Li, G., Sapsford, S.M., Stokes, J., and Lake, T.H., “Evaluation of HCCI for future gasoline powertrains,” *SAE 2003 World Congr. Exhib.* (2003-01–0750), 2003, doi:10.4271/2003-01-0750.

78. Atkins, M.J. and Koch, C.R., “A Well-to-Wheel Comparison of Several Powertrain Technologies,” *SAE Tech. Pap. Ser.* (2003-01–0081), doi:2003-01-0081.

79. Cairns, A. and Blaxill, H., “Lean Boost and External Exhaust Gas Recirculation for High Load Controlled Auto-Ignition,” *SAE Tech. Pap.* 2005013744(724), 2005, doi:10.4271/2005-01-3744.

80. Schmidt, L., Seabrook, J., Stokes, J., Ahmad Zuhdi, M.F., Begg, S., Heikal, M., and King, J., “Multiple Injection Strategies for Improved Combustion Stability under Stratified Part Load Conditions in a Spray Guided Gasoline Direct Injection (SGDI) Engine,” *SAE* (2011-01–1228), 2011, doi:10.4271/2011-01-1228.

81. Stephenson, M. and Powertrain, M., “Engine Downsizing - An Analysis Perspective,” 2009.

82. Bandel, W., Fraidl, G.K., Kapus, P.E., Sikinger, H., and Cowland, C.N., “The Turbocharged GDI Engine: Boosted Synergies for High Fuel Economy Plus Ultra-low Emission,” (2006-01–1266), 2006, doi:10.4271/2006-01-1266.

83. Fraser, N., Blaxill, H., Lumsden, G., and Bassett, M., “Challenges for Increased Efficiency through Gasoline Engine Downsizing,” *SAE Int. J. Engines* 2(1):2009-01–1053, 2009, doi:10.4271/2009-01-1053.

84. Lumsden, G., OudeNijeweme, D., Fraser, N., and Blaxill, H., “Development of a Turbocharged Direct Injection Downsizing Demonstrator Engine,” *SAE Int. J. Engines* 2(1):1420–1432, 2009, doi:10.4271/2009-01-1503.

85. Eichhorn, A., Lejsek, D., Hettinger, A., and Kufferath, A., “Challenge Determining a Combustion System Concept for Downsized SI-engines - Comparison and Evaluation of Several Options for a Boosted 2-cylinder SI-engine,” (2013-01–1730), 2013, doi:10.4271/2013-01-1730.

86. Turner, J.W.G., Popplewell, A., Patel, R., Johnson, T.R., Darnton, N.J., Richardson, S., Bredda, S.W., Tudor, R.J., Bithell, C.I., Jackson, R., Remmert, S.M., Cracknell, R.F., Fernandes, J.X., Lewis, A.G.J., Akehurst, S., Brace, C.J., Copeland, C., Martinez-Botas, R., Romagnoli, A., and Burluka, A.A., “Ultra Boost for Economy: Extending the Limits of Extreme Engine Downsizing,” *SAE Int. J. Engines* 7(1):387–417, 2014, doi:10.4271/2014-01-1185.

87. Martin, S., Beidl, C., and Mueller, R., “Responsiveness of a 30 Bar BMEP 3-Cylinder Engine: Opportunities and Limits of Turbocharged Downsizing,” *SAE Tech. Pap.*, 2014, doi:10.4271/2014-01-1646.Copyright.

88. Lewin, T., “HyBoost: the win-win option.”

89. Baêta, J.G.C., Pontoppidan, M., and Silva, T.R.V., “Exploring the limits of a down-sized ethanol direct injection spark ignited engine in different configurations in order to replace high-displacement gasoline engines,” *Energy Convers. Manag.*, 2015, doi:10.1016/j.enconman.2015.08.041.

90. Remmert, S., Campbell, S., Cracknell, R., Schuetze, A., Lewis, A., Giles, K., Akehurst, S., Turner, J., Popplewell, A., and Patel, R., “Octane Appetite: The Relevance of a Lower Limit to the MON Specification in a Downsized, Highly Boosted DISI Engine,” *SAE Int. J. Fuels Lubr.* 7(3):2014-01–2718, 2014, doi:10.4271/2014-01-2718.

91. Cruff, L., Kaiser, M., Krause, S., Harris, R., Krueger, U., and Williams, M., “EBDI® - Application of a Fully Flexible High BMEP Downsized Spark Ignited

Engine," (2010-01–0587), 2010, doi:10.4271/2010-01-0587.

92. Hancock, D., Fraser, N., Jeremy, M., Sykes, R., and Blaxill, H., "A New 3 Cylinder 1.2l Advanced Downsizing Technology Demonstrator Engine," (2008-01–0611), 2008, doi:10.4271/2008-01-0611.

93. Dalla Nora, M., "EXPERIMENTAL AND NUMERICAL STUDY OF A TWO-STROKE POPPET VALVE ENGINE FUELLED WITH GASOLINE AND ETHANOL," Brunel University London, 2015.

94. Rightsizing vs. Downsizing, https://hubpages.com/autos/Rightsizing-vs-Downsizing, 2016.

95. Dunham, B., "Automatic on/off switching gives 10-percent gas saving," *Pop. Sci.* 205,.

96. Mazda i-Stop, Idling Stop Technology, http://www.mazda.com/mazdaspirit/env/engine/siss.html/.

97. Miller, C.D., "Relation between spark-ignition engine knock, detonation waves, and autoignition as shown by high-speed photography," *NACA Report,* 1946.

98. Konig, G. and Sheppard, C.G.W., "End Gas Autoignition and Knock in a Spark Ignition Engine," *SAE Technical Paper*, SAE International: 902135, 1990, doi:10.4271/902135.

99. König, G., Maly, R.R., Bradley, D., Lau, a K.C., and Sheppard, C.G.W., "Role of Exothermic Centres on Knock Initiation and Knock Damage," 902136, 1990, doi:10.4271/902136.

100. Maly, R., Klein, R., Peters, N., and Kŏnig, G., "Theoretical and Experimental Investigation of Knock Induced Surface Destruction," *SAE Tech. Pap.* 41, 1990.

101. Pan, J. and Sheppard, C.G.W., "A Theoretical and Experimental Study of the Modes of End Gas Autoignition Leading to Knock in S. I. Engines," (942060), 1994, doi:10.4271/942060.

102. Pan, J., Sheppard, C.G.W., Tindall, A., Berzins, M., Pennington, S. V., and Ware, J.M., "End Gas Inhomogeneity, Autoignition and Knock," *SAE* (982616), 1998, doi:10.4271/982616.

103. Ricardo, H.R., "Paraffin as Fuel," *Automob. Eng.*, 1919.

104. MillerC.D., "Relation Between Sprak-Ignition Engine Knock, Detonation Waves, and Auto-Ignition as Shown by High-Speed Photography," National Advisory Committee for Aeronautics.

105. Withrow, L. and Rassweiler, G.M., "Slow Motion Shows Knocking and Non-Knocking Explosions," *Semi-Annual Meet. Soc.* (360126), 1936, doi:10.4271/360126.

106. Nates, R.J. and Yates, A.D.B., "Knock Damage Mechanisms in Spark-Ignition Engines," (942064), 1994.

107. Fitton, J. and Nates, R., "Knock Erosion in Spark-Ignition Engines," *SAE Tech. Pap.* (962102), 1996.

108. Spark Knock (Detonation): Engine Knock Under Acceleration, www.autorepairpit.com/spark-knock-detonation/.

109. Zahdeh, A., Rothenberger, P., Nguyen, W., Anbarasu, M., Schmuck-Soldan, S., Schaefer, J., and Goebel, T., "Fundamental Approach to Investigate Pre-Ignition in Boosted SI Engines," *SAE Int. J. Engines* 4(1):246–273, 2011, doi:10.4271/2011-01-0340.

110. One Stop Auto. What causes spark knock and how do you get rid of it, www.onestopauto.com/What-causes-spark-knock.html.

111. Gupta, H.N., "Fundamentals of Internal Combustion Engines.," PHI Learning Pvt. Ltd, 2012.

112. International Energy Agengy, "Global EV Outlook 2015," *Glob. EV Outlook*, 2015, doi:EIA-0383(2016).

113. Bishop, J.D.K., Axon, C.J., Tran, M., Bonilla, D., Banister, D., and McCulloch, M.D., "Identifying the fuels and energy conversion technologies necessary to meet European passenger car emissions legislation to 2020," *Fuel*, 2012, doi:10.1016/j.fuel.2012.04.045.

114. Kim, N., Moawad, A., Shidore, N., and Rousseau, A., "Fuel Consumption and Cost Potential of Different Plug-In Hybrid Vehicle Architectures," *SAE Int. J. Altern. Powertrains* (2015-01–1160), 2015, doi:10.4271/2015-01-1160.

115. Fraidl, G.K., Beste, F., Kapus, P.E., Korman, M., Sifferlinger, B., and Benda, V., "Challenges and Solutions for Range Extenders - From Concept Considerations to Practical Experiences," (2011-37–19), 2011, doi:10.4271/2011-37-0019.

116. Mock, P., "EU CO2 standards for passenger cars and light-commercial vehicles," *Int. Counc. Clean Transp.*, 2014.

117. Ricardo, "Delivering Excellence Through Innovation & Technology: Driving automotive electrification," 2017.

118. Zhao, H., Hu, J., and Ladommatos, N., "Spray and diesel combustion studies in a specially designed single cylinder engine," *J. KONES* 6(1–2):193–203, 1999.

119. Peng, Z., Zhao, H., and Ladommatos, N., "Effects of Air / Fuel Ratios and EGR Rates on HCCI Combustion of n-heptane , a Diesel Type Fuel Reprinted From : Homogeneous Charge Compression Ignition," 2003(724), 2003, doi:10.4271/2003-01-0747.

120. Tsolakis, A., Megaritis, A., Wyszynski, M.L., and Theinnoi, K., "Engine performance and emissions of a diesel engine operating on diesel-RME (rapeseed methyl ester) blends with EGR (exhaust gas recirculation)," *Energy* 32(11):2072–2080, 2007, doi:10.1016/j.energy.2007.05.016.

121. Bai, S., Li, G., Hua, Z., and Williams, D.J.R., "Experiment study of stratified combustion at different boost pressure," *Asia-Pacific Power Energy Eng. Conf. APPEEC* 1–4, 2009, doi:10.1109/APPEEC.2009.4918350.

122. Williams, D.J.R., “The effect of charge stratification on the combustion and emissions of a spark-ignition internal combustion engine,” Brunel University London, 2002.

123. Dingle, S.F., “LUBRICANT INDUCED PRE-IGNITION IN AN OPTICAL SPARK-IGNITION ENGINE,” Brunel University London, 2013.

124. Gatowski, J.A., Heywood, J.B., and Deleplace, C., “Flame photographs in a spark-ignition engine,” *Combust. Flame* 56(1):71–81, 1984, doi:10.1016/0010-2180(84)90006-3.

125. Vafamehr, H., Cairns, A., Sampson, O., and Koupaie, M.M., “The competing chemical and physical effects of transient fuel enrichment on heavy knock in an optical spark ignition engine,” *SAE* (2017-01–0665):687–697, 2017, doi:2016.07.038.

126. Vafamehr, H. and Cairns, A., “The Effects of Transient Over-Fuelling on Heavy Knock in an Optical Spark Ignition (SI) Engine,” *3rd Biennial International Conference on Powertrain Modelling and Control*, 2016.

127. Vafamehr, H., Cairns, A., Sampson, O., and Koupaie, M.M., “The competing chemical and physical effects of transient fuel enrichment on heavy knock in an optical spark ignition engine,” *Appl. Energy* 179(March):687–697, 2016, doi:10.1016/j.apenergy.2016.07.038.

128. WANG, “Introduction to engine valve trains,” *Multibody Syst. Dyn.* 1987:1, 2007.

129. Brunt, M.F.J. and Emtage, A.L., “Evaluation of IMEP Routines and Analysis Errors,” *SAE Tech. Pap.* (960609), 1996, doi:10.4271/960609.

130. Welling, O. and Collings, N., “UEGO Based Measurement of EGR Rate and Residual Gas Fraction,” *SAE* (2011-01–1289), 2017, doi:10.4271/2011-01-1289.

131. Cotes Barnaby, “Investigation of Engine Design Parameters on the Efficency and

Performance of the High Specific Power Downsized SI Engine," Brunel University London, 2012.

132. Sztenderowicz, M.L. and Heywood, J.B., "Cycle-to-Cycle IMEP Fluctuations in a Stoichiometrically-Fueled S.I. Engine at Low Speed and Load," *Int. Fuels Lubr. Meet. Expo.* (902143), 1990, doi:10.4271/902143.

133. Lancaster, D.R., Krieger, R.B., and Lienesch, J.H., "Measurement and Analysis of Engine Pressure Data," *1975 Automot. Eng. Congr. Expo.* (750026), 1975, doi:10.4271/750026.

134. Cairns, A. and Sheppard, C.G.W., "Cyclically Resolved Simultaneous Flame and Flow Imaging in a SI Engine," *SAE Technical Paper*, 2000, doi:10.4271/2000-01-2832.

135. Brunt, M.F.J. and Pond, C.R., "Evaluation of Techniques for Absolute Cylinder Pressure Correction," *SAE Tech. Pap.* (970036), 1997, doi:10.4271/970036.

136. Yeliana, Y., Cooney, C., Worm, J., and Naber, J., "The Calculation of Mass Fraction Burn of Ethanol-Gasoline Blended Fuels Using Single and Two-Zone Models," *SAE* (2008-01–0320), 2008, doi:10.4271/2008-01-0320.

137. Rassweiler, G.M. and Withrow, L., "Motion Pictures of Engine Flames Correlated with Pressure Cards," 1938, doi:10.4271/380139.

138. Beretta, G.P., Rashidi, M., and Keck, J.C., "Turbulent flame propagation and combustion in spark ignition engines," *Combust. Flame*, 1983, doi:10.1016/0010-2180(83)90135-9.

139. Yang, C., Zhao, H., and Megaritis, T., "In-Cylinder Studies of CAI Combustion with Negative Valve Overlap and Simultaneous Chemiluminescence Analysis," *SAE* (2009-01–1103), 2009, doi:10.4271/2009-01-1103.

140. Chomiak, J., "Application of chemiluminescence measurement to the study of turbulent flame structure," *Combust. Flame* 18(3):429–434, 1972.

141. Dec, J.E. and Espey, C., “Chemiluminescence Imaging of Autoignition in a DI Diesel Engine,” *SAE Tech. Pap.* (982685), 1998, doi:papers://B3F20CA2-9ACD-4BA1-A510-19A2EC38FE78/Paper/p1008.

142. Tanaka, T., Fujimoto, M., and Tabata, M., “Planar Measurements of NO in an S . I . Engine Based on Laser Induced Fluorescence,” (940477), 1997.

143. Zhao, H., Peng, Z., and Ma, T., “Investigation of the HCCI / CAI Combustion Process by 2-D PLIF Imaging of Formaldehyde,” *SAE Tech. Pap. 2004-01-1901* (2004-01–1901), 2004, doi:10.4271/2004-01-1901.

144. SRINIVASAN, C. and SARAVANAN, C., “Emission Reduction on Ethanol–Gasoline Blends using 1, 4 Dioxan,” *Lect. Notes Eng. …* II:2–5, 2010.

145. Settles, G. and Covert, E., “Schlieren and Shadowgraph Techniques: Visualizing Phenomena in Transport Media,” ISBN 3540661557, 2002, doi:10.1115/1.1483362.

146. Johnston, S.C., Robinson, C.W., Rorke, W.S., Smith, J.R., and Witze, P.O., “Application of Laser Diagnostics to an Injected Engine,” *SAE Tech. Pap.* (790092), 1979, doi:10.4271/790092.

147. Smith, J.R., “Turbulent Flame Structure in a Homogeneous-Charge Engine,” *SAE Int. Congr. Expo.* (820043), 1982, doi:10.4271/820043.

148. Pickett, L.M., Kook, S., and Williams, T.C., “Visualization of Diesel Spray Penetration, Cool-Flame, Ignition, High-Temperature Combustion, and Soot Formation Using High-Speed Imaging,” *SAE Int. J. Engines* 2(1):439–459, 2009, doi:10.4271/2009-01-0658.

149. Zhao, H. and N, L., “Engine Combustion Instrumentation and Diagnostics,” SAE: Warrendale, USA. ISBN 978-0-76-800665-0.

150. Hicks, R.A., Lawes, M., Sheppard, C.G.W., and Whitaker, B.J., “Multiple Laser Sheet Imaging Investigation of Turbulent Flame Structure in a Spark Ignition

Engine," (941992), 1994.

151. Kurada, S., Rankin, G.W., and Sridhar, K., "Particle-imaging techniques for quantitative flow visualization: a review," *Opt. Laser Technol.*, 1993, doi:10.1016/0030-3992(93)90116-W.

152. Gillespie, L., Lawes, M., Sheppard, C.G.W., and Woolley, R., "Aspects of Laminar and Turbulent Burning Velocity Relevant to SI Engines," *Sae Tech. Pap. Ser.* (2000-01–0192), 2000, doi:10.4271/2000-01-0192.

153. Cairns, A., "Turbulent Flame Development in a Spark Ignition Engine," University of Leeds, 2001.

154. Lozano, A., Yip, B., and Hanson, R.K., "Acetone: a tracer for concentration measurements in gaseous flows by planar laser-induced fluorescence," *Exp. Fluids*, 1992, doi:10.1007/BF00223244.

155. Hanson, R.K., Seitzman, J.M., and Paul, P.H., "Planar laser-fluorescence imaging of combustion gases," *Appl. Phys. B Photophysics Laser Chem.*, 1990, doi:10.1007/BF00408770.

156. Dronniou, N., Kashdan, J., Lecointe, B., Sauve, K., and Soleri, D., "Optical Investigation of Dual-fuel CNG/Diesel Combustion Strategies to Reduce CO_2 Emissions," *SAE Int. J. Engines* 7(2):2014-01–1313, 2014, doi:10.4271/2014-01-1313.

157. Murad, A., "Flow and Combustion in disc and pent-roof SI engines," Leeds University, 2006.

158. Aleiferis, P.G., Malcolm, J.S., Todd, A.R., Cairns, A., and Hoffmann, H., "An Optical Study of Spray Development and Combustion of Ethanol, Iso-Octane and Gasoline Blends in a DISI Engine," *SAE World Congr. Exhib.* (2008-01–0073), 2008, doi:10.4271/2008-01-0073.

159. Moxey, B., "A STUDY OF FLAME DEVELOPMENT WITH

ISOOCTANEALCOHOL BLENDED FUELS IN AN OPTICAL SPARK IGNITION ENGINE," Brunel University London, 2014.

160. Gander, W., Golub, G.H., and Strebel, R., "Fitting of circles and ellipses-least squares solution," *SVD Signal Process. III*, 1994, doi:10.1007/BF01934268.

161. Welling, O., Moss, J., Williams, J., and Collings, N., "Measuring the Impact of Engine Oils and Fuels on Low-Speed Pre-Ignition in Downsized Engines," *SAE Int. J. Fuels Lubr.* (2014-01–1219), 2014, doi:10.4271/2014-01-1219.

162. Peters, N. and Kerschgens, B., "Super-Knock Prediction Using a Refined Theory of Turbulence," *SAE Int. J. Engines* 6(2013–01–1109.), 2013, doi:10.4271/2013-01-1109.

163. Bates, L., Bradley, D., Paczko, G., and Peters, N., "Engine Hot Spots: Modes of Auto-ignition and Reaction Propagation," *Combust. Flame*, 2015.

164. Pan, J., Wei, H., Shu, G., Pan, M., Feng, D., and Li, N., "LES analysis for auto-ignition induced abnormal combustion based on a downsized SI engine," *Appl. Energy* 191:183–192, 2017, doi:10.1016/j.apenergy.2017.01.044.

165. Dahnz, C., Han, K.-M., Spicher, U., Magar, M., Schiessl, R., and Maas, U., "Investigations on Pre-Ignition in Highly Supercharged SI Engines," *SAE Int. J. Engines* 3(1):214–224, 2010, doi:10.4271/2010-01-0355.

166. Amann, M., Alger, T., Westmoreland, B., and Rothmaier, A., "The Effects of Piston Crevices and Injection Strategy on Low-Speed Pre-Ignition in Boosted SI Engines," *SAE Int. J. Engines* 5(3):1216–1228, 2012, doi:10.4271/2012-01-1148.

167. Griffiths, J.., MacNamara, J.., Sheppard, C.G.., Turton, D.., and Whitaker, B.., "The relationship of knock during controlled autoignition to temperature inhomogeneities and fuel reactivity," *Fuel* 81(17):2219–2225, 2002, doi:10.1016/S0016-2361(02)00134-5.

168. Amann, M., Mehta, D., and Alger, T., "Engine Operating Condition and Gasoline

Fuel Composition Effects on Low-Speed Pre-Ignition in High-Performance Spark Ignited Gasoline Engines," *SAE Int. J. Engines* 4(1):274–285, 2011, doi:10.4271/2011-01-0342.

169. Karvountzis-Kontakiotis, A. and Ntziachristos, L., "Improvement of NO and CO predictions for a homogeneous combustion SI engine using a novel emissions model," *Appl. Energy* 162:172–182, 2016, doi:10.1016/j.apenergy.2015.10.088.

170. Lightfoot, N.S. and Negus, C.R., "Investigation of the 'knock' phenomenon in an optically-accessed engine," *Symp. Combust.* 20(1):111–122, 1985, doi:10.1016/S0082-0784(85)80494-X.

171. Yang, F., Zhang, H., Chen, Z., and Kong, W., "Interaction of pressure wave and propagating flame during knock," *Int. J. Hydrogen Energy* 38(35):15510–15519, 2013, doi:10.1016/j.ijhydene.2013.09.078.

172. Kawahara, N. and Tomita, E., "Visualization of auto-ignition and pressure wave during knocking in a hydrogen spark-ignition engine," *Int. J. Hydrogen Energy* 34(7):3156–3163, 2009, doi:10.1016/j.ijhydene.2009.01.091.

173. G., K., "Autoignition and Knock Aerodynamics in Engine Combustion.," Leeds, UK : Department of Mechanical Engineering, The University of Leeds, 1993.

174. Knop, V. and Essayem, E., "Comparison of PFI and DI Operation in a Downsized Gasoline Engine," *SAE Int. J. Engines* 6(2):941–952, 2013, doi:10.4271/2013-01-1103.

175. Wang, Z., Liu, H., Song, T., Xu, Y., Wang, J.-X., Li, D.-S., and Chen, T., "Investigation on Pre-ignition and Super-Knock in Highly Boosted Gasoline Direct Injection Engines," *SAE Tech. Pap.* (2014-01–1212), 2014, doi:10.4271/2014-01-1212.

176. Qi, Y., Wang, Z., Wang, J., and He, X., "Effects of thermodynamic conditions on the end gas combustion mode associated with engine knock," *Combust. Flame* 162(11):4119–4128, 2014, doi:10.1016/j.combustflame.2015.08.016.

177. Stein, R. a, Polovina, D., Roth, K., Foster, M., Lynskey, M., Whiting, T., Anderson, J.E., Shelby, M.H., Leone, T.G., and VanderGriend, S., "Effect of Heat of Vaporization, Chemical Octane, and Sensitivity on Knock Limit for Ethanol - Gasoline Blends," *SAE Int. J. Fuels Lubr.* 5(2):823–843, 2012, doi:10.4271/2012-01-1277.

178. Kasseris, E. and Heywood, J., "Charge Cooling Effects on Knock Limits in SI DI Engines Using Gasoline/Ethanol Blends: Part 2-Effective Octane Numbers," *SAE Int. J. Fuels Lubr.* 5(2):844–854, 2012, doi:10.4271/2012-01-1284.

179. Stapf, K.G. and Reis, B., "'Simulation of Auto-Ignition Behaviour for Varying Gasoline Engine Operating Conditions', Proceedings of the 2nd Conference on Engine Processes: July 2--3, 2015, Berlin, Germany," Universit{ä}tsverlag der TU Berlin, 2015.

180. Fieweger, K., Blumenthal, R., and Adomeit, G., "Self-ignition of S.I. engine model fuels: A shock tube investigation at high pressure," *Combust. Flame* 109(4):599–619, 1997, doi:10.1016/S0010-2180(97)00049-7.

181. Ciezki, H.K. and Adomeit, G., "Shock-tube investigation of self-ignition of n-heptane-air mixtures under engine relevant conditions," *Combust. Flame* 93(4):421–433, 1993, doi:10.1016/0010-2180(93)90142-P.

182. Syed, I.Z., Mukherjee, A., and Naber, J.D., "Numerical Simulation of Autoignition of Gasoline-Ethanol/Air Mixtures under Different Conditions of Pressure, Temperature, Dilution, and Equivalence Ratio," *SAE Tech. Pap.* (2011-01–0341), 2011, doi:10.4271/2011-01-0341.

183. Wallner, T. and Miers, S. a, "Combustion Behavior of Gasoline and Gasoline / Ethanol Blends in a Modern Direct-Injection 4-Cylinder Engine," *SAE Tech. Pap.* 2008(2008-01–0077), 2008, doi:10.4271/2008-01-0077.

184. Broustail, G., Seers, P., Halter, F., Moréac, G., and Mounaim-Rousselle, C., "Experimental determination of laminar burning velocity for butanol and ethanol iso-octane blends," *Fuel* 90(1):1–6, 2011, doi:10.1016/j.fuel.2010.09.021.

185. Schifter, I., Diaz, L., Rodriguez, R., Gómez, J.P., and Gonzalez, U., “Combustion and emissions behavior for ethanol-gasoline blends in a single cylinder engine,” *Fuel* 90(12):3586–3592, 2011, doi:10.1016/j.fuel.2011.01.034.

186. Inoue, T., Inoue, Y., and Ishikawa, M., “Abnormal Combustion in a Highly Boosted SI Engine - The Occurrence of Super Knock,” (2012-01–1141), 2012, doi:10.4271/2012-01-1141.

187. Takeuchi, K., Fujimoto, K., Hirano, S., and Yamashita, M., “Investigation of Engine Oil Effect on Abnormal Combustion in Turbocharged Direct Injection - Spark Ignition Engines,” *SAE Int. J. Fuels Lubr.* 5(3):1017–1024, 2012, doi:10.4271/2012-01-1615.